On-ground characterization of the cold atoms space clock PHARAO

Igor Moric

On-ground characterization of the cold atoms space clock PHARAO

Igor Moric

Observatoire de Paris - SYRTE, CNES

Université Pierre et Marie Curie

A thesis submitted for the degree of

Docteur

December 2014

Soutenue le 19/12/2014 devant le jury composé de :

Mme. JULIEN Lucile - **Président du Jury**

M. SZYMANIEC Krzysztof - **Rapporteur**

M. VERNOTTE Franois - **Rapporteur**

Mme. AMY-KLEIN Anne

M. WEYERS Stefan

M. SALOMON Christophe

M. LAURENT Philippe

Contents

List of Figures

LIST OF FIGURES

List of Tables

Glossary

AC Stark effect splitting of atomic spectral lines due to a presence of a static electric field.

ACES Atomic Clock Ensemble in Space.

ACT Automatic Cavity Tuning.

Active compensation system a feed-forward system composed of a magnetic sensor and a compensating coil (BT) controlled by a computer.

AOM acousto-optic modulator.

ASTRIUM today Airbus Defence and Space.

Atomic fountain an atomic clock using the Ramsey interrogation where the atoms are tossed upwards passing the same interaction zone twice; resembling a fountain.

AVAR Allan variance.

B1, B2, B3 PHARAO magnetic shields.

BCPC coil used to improve internal magnetic field homogeneity around the interaction cavity apertures.

BCPD coil used to improve internal magnetic field homogeneity around the interaction cavity apertures.

BCSC coil used to improve field homogeneity near capture.

BEC computer on the detection side that controls the thermal probe.

BEDET computer on the capture side that controls the thermal probe.

BIPM Bureau International des Poids et Mesures.

Black body radiation atomic clock frequency shift due to black body radiation of the cavity pertrubing the cesium atoms energy levels (Stark effect).

BP a large solenoid responsible for providing a static electric field.

BS L6 coil used to improve field homogeneity inside the preparation and detection cavit.

BS L7 coil used to improve field homogeneity inside the preparation and detection cavity.

BT coil used for active compensation.

CADMOS Centre d'Aide au Dévelopement de la Microgravite et aux Operations Spatiales.

CEPF Columbus External Payload Facility; two identical L-shaped consoles attached to the starboard cone of the ISS Columbus science laboratory.

Clock accuracy describes the frequency shift of an atomic clock.

Clock stability describes the temporal stability of an atomic clock using the Allan deviation.

CNES Centre National d'Etudes Spatiales; French space agency.

Cold collision atomic clock frequency shift due to low velocity atomic collisions.

DCP or Doppler effect atomic clock frequency shift due to the microwave cavity phase gradient.

DDF detection zone thermal regulation.

DDS Direct Digital Synthesizer; frequency synthesizer used for creating arbitrary waveforms from a single, fixed-frequency reference clock.

Detection laser noise atomic clock noise due to laser power fluctuations.

Detection system noise atomic clock noise due to the photodiode photon → electron conversion, the pre-amplifier current → voltage conversion and the voltage amplifier.

Detection zone atomic hyperfine state detection zone.

DLL Delay-Locked Loop.

Domain wall layers of finite thickness separating magnetic domains.

Doppler cooling method of laser cooling of atoms.

Doppler effect or DCP atomic clock frequency shift due to the microwave cavity phase gradient; the shift is proportional to atomic velocity.

Dragon SpaceX developed capsule that will be used for ACES.

DTU PHARAO magnetometer.

Duralumin aluminium alloy.

ECDL Extended Cavity Diode Laser.

ELT European Laser Timing; time and frequency transfer link in the optical domain developed for the ACES mission.

EM engineering model, used to test performances.

End-to-end DCP contribution DCP frequency shift contribution due to the phase gradient between the two interaction zones.

ESA European Space agency.

ESATAN software for thermal analysis / heat transfer.

Falcon 9 v1.1 SpaceX developed launcher that will be used for ACES.

FCDP Frequency Comparison and Distribution Package; the central node of the ACES signal management also responsible for signal distribution to the time and transfer link.

FFT Fast Fourier Transform.

Fictitious spin representation Ramsey interrogation representation combining the classical, semi-classical and the quantum representation.

FM flight model; full space qualified mode.

FOM SYRTE mobile atomic fountain.

FPGA Field Programmable Gate Array; programmable integrated circuits.

FWHM Full Width at Half Maximum.

GALILEO a global navigation satellite system currently being built by the European Union (EU) and European Space Agency (ESA).

GCRS Geocentric Celestial Reference System.

GNSS Global Navigation Satellite System.

GPA or GP-A Gravity Probe A; a space-based experiment to test the theory of general relativity.

Helmholtz coils a device for producing a region of nearly uniform magnetic field.

Hysteresis loop branch the ascending or descending part of a hysteresis loop.

I-DEAS software used to construct a FM thermal model and verify its performances.

IEN Instituto Elettrotecnico Nazionale.

INRIM Istituto Nazionale di Ricerca Metrologica, Torino, Italy.

IRCOM Institut de Recherche en Communications et Micro-onde (Limoges).

ISS International Space Station.

JAXA The Japan Aerospace Exploration Agency.

JILA Joint Institute for Laboratory Astrophysics.

JLP Jet Propulsion Laboratory (USA).

Local oscillator noise atomic clock oscillator noise.

LSA Low Sensitivity to Acceleration.

LTF Laboratoire temps-fréquence - Université de Neuchtel.

Magnetic domains packages of uniform magnetization separated by layers of finite thickness called domain walls.

Magnetic permeability the degree of magnetization that a material obtains in response to an applied magnetic field.

Magnetocrystalline anisotropy energy necessary for changing the magnetization direction.

Major loop hysteresis loop containing a minor loop.

Microwave cavity cavity where the Ramsey interrogation occurs.

Minor loop hysteresis loop contained inside a major loop.

MSTH mechanical and thermal model; equivalent to STM (in English).

Mumetal a nickel-iron alloy.

MWL two way time and frequency transfer link in the microwave domain developed for the ACES mission.

NICT National Institute of Information and Communications.

NIST National Institute of Standards and Technology (USA).

Nodal regression westward deflection of the ISS every time it crosses the equatorial bulge.

NPL National Physical Laboratory (UK).

NRC National Research Council (Canada).

NRLM National Research Laboratory of Metrology (Japan).

OBT mechanical shutter.

OI optical isolator.

OP200AZ amplifier model used for the primary and secondary PHARAO thermal regulation amplifiers.

Permalloy a nickel-iron magnetic alloy.

PFS Primary Frequency Standard; a cesium atomic clock used for the definition of the second in SI.

PHARAO Projet d'Horloge Atomique par Refroidissement d'Atomes en Orbite.

PIF package induced failure.

PM polarisation maintained fiber.

PTB Physikalisch Technische Bundesanstalt (Braunschweig Germany).

Quantum projection noise atomic clock noise originating from atomic superposition.

Rabi interrogation one zone method of invoking atomic hyperfine transition.

Ramsey interrogation two zone method of invoking atomic hyperfine transition.

Recoil effect atomic clock frequency shift due to the fact the atom's recoil is less than the photon energy.

Relative frequency shift atomic clock frequency shift divided by the clock frequency.

Sensitivity function function introduced to evaluate effects of small perturbations on the clock signal.

SHM Space Hydrogen Maser; active space hydrogen maser developed for the ACES mission by Spectratime (Switzerland) based on the 1,420,405,752 Hz transition between two ground state hyperfine levels in hydrogen.

SL slave diode laser.

SME Standard Model Extension.

SNR signal to noise ratio.

SODERN French space instrumentation and optics development company.

SpaceX Space Exploration Technologies Corporation; a private space transport service company headquartered in Hawthorne, California..

STM structural and thermal model; equivalent to MSTH (in French).

sub-Doppler or Sisyphus cooling a type of laser cooling of atoms used to reach temperatures below the Doppler cooling limit.

Switching point the field value where the magnetic field amplitude exceeds the current hysteresis bounds and switches trajectory to its major loop ascending or descending branch.

SYRTE Systèmes de Référence Temps-Espace.

Systematic effects pertrubations causing a clock frequency shift.

TAI Temps atomique international or International Atomic Time; a time scale produced from a weighted average of the time kept by over 200 atomic clocks in over 50 national laboratories worldwide.

TC cesium tube.

TEC Total Electron Content; measured by MWL S-band.

TM/TC Télémesure/Télécommande.

TOF Time of flight.

TRP bottom of the cesium tube support.

Turning point the field value where the magnetic field is reversed creating a reversal curve.

TWSTFT Two-way satellite time and frequency transfer; a high-precision long distance time and frequency transfer mechanism.

UGB PHARAO on-board computer.

USO Ultra Stable Oscillator.

USOC ACES User Support and Operation Center at CNES.

UWA The University of Western Australia.

VCXO Voltage Controlled Crystal Oscillator.

VNA Vector Network Analyzer; used to measure the interrogation cavity resonance frequency.

XPLC eXternal PayLoad Computer; responsible for telecommand, telemetry, data handling for all ACES instruments and short and long-term servo loop.

Zeeman effect effect of spectral line splitting in the presence of a static magnetic field.

Zeeman levels atomic energy levels present in a static magnetic field.

Zeeman wire wire placed along the atom path used to degauss the cesium tube.

ZI1 zone interaction 1.

ZI2 zone interaction 2.

"There was a man who sat each day looking out through a narrow vertical opening where a single board had been removed from a tall wooden fence. Each day a wild ass of the desert passed outside the fence and across the narrow opening - first the nose, then the head, the forelegs, the long brown back, the hindlegs, and lastly the tail. One day, the man leaped to his feet with the light of discovery in his eyes and he shouted for all who could hear him: It is obvious! The nose causes the tail!"

-Stories of the Hidden Wisdom, from the Oral History of Rakis

1

Introduction

Operation of any clock is based on counting the frequency of some oscillation. Earth's rotation around its axis and around the Sun constitute the most simple examples available to man. These oscillations created the concepts of days and years. To better divide the motion of the Sun across the sky, hours and seconds were introduced.

In 1960 at the "Conférence Générale des Poids at Mesures" the International System of units (SI) was established. The second was defined as "the fraction 1/31,556,925.9747 of the tropical year for 1900 January 0 at 12 hours ephemeris time."

With the development of quantum mechanics, atomic hyperfine transition based clocks were introduced in the 1950s (2). Their operation is based on inducing hyperfine transitions in atoms and measuring the resonance frequency.

Technology advances led to the redefinition of the second in 1967 at the 13th "Conférence Générale des Poids et Mesures" as the "the duration of 9,192,631,770 periods of the radiation corresponding to the transition between the two hyperfine levels of the ground state of the caesium-133 atom".

Cesium clocks have been continuously improved with the progress of technology such as the introduction of Doppler cooling (3). This allowed atoms to be cooled to only a few μK in the 1990's. Today, cesium fountain clocks are the best primary frequency standards.

However, cesium atomic fountains seem to have reached a frequency stability and accuracy plateau (Figure 1.1). The most accurate and stable cesium atomic clock today are at NIST (4), NPL (5), SYRTE (6) and PTB (7) with a relative accuracy better than 3×10^{-16} and stability of $10^{-13} - 10^{-14}$ at 1 s.

Recent advances in the development of optical clocks offer a possibility of redefining the second with the accuracy of about 10^{-17} and very high stability (8). For example, in August 2013 NIST ytterbium optical clocks achieved a frequency stability of 2×10^{-18}. Figure 1.1 shows the evolution of accuracy of cesium and optical clocks.

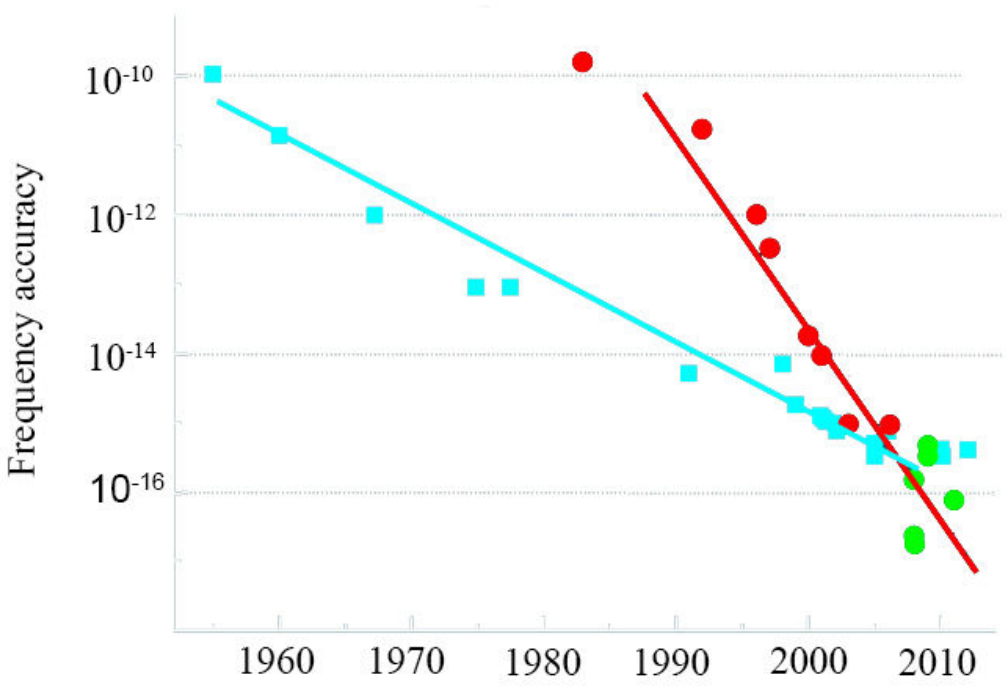

Figure 1.1: Atomic clock accuracy evolution. Cesium atomic clocks are in blue. Red and green circles represent optical frequency standards uncertainties determined by referencing to the cesium clock and by estimation, respectively. Figure from (1)

Atomic clocks are not only useful for metrology, but also for the study of quantum mechanics (for instance high accuracy spectroscopy) and general relativity (by comparing different clocks). General relativity and quantum field theory are incompatible and their unification attempts have proven unsuccessful so far. The validity domain of general relativity can be explored with the atomic clocks by testing different aspects of general relativity such as variation of fundamental constants, measuring of the gravitational redshift and verifying the space-time isotropy.

Atomic clock technology transfer to space has opened up new possibilities of usage and significantly improved the science and technology performance levels previously attained on Earth. For example, atomic clocks are very important for GNSS systems

(GPS, GALILEO (9)...) as time signal triangulation enables ground users to poinpoint their location. Currently, GPS satellites are calibrated from ground and depend on cesium or rubidium clocks having a stability of 10^{-14} per day and accuracy at the order of 10^{-13}. A dedicated space clock having a high performance time transfer link could considerably enhance the capabilities of GNSS systems. Clocks are also crucial for high-speed communication and radio astronomy (synchronization for very-long-baseline interferometry).

This thesis deals with the development of a new high performance space clock called PHARAO (Projet d'Horloge Atomique par Refroidissement d'Atomes en Orbite) (10), which is being developed by the French space agency CNES. PHARAO is the first cold atoms Primary Frequency Standard (PFS) specially designed for operation in space. PHARAO is part of the space mission ACES (Atomic Clock Ensemble in Space) that is being managed by the European space agency ESA (11). The payload will be installed on the external pallet of the European Columbus laboratory on-board the International Space Station (ISS) in 2016. The expected frequency accuracy is less than 3×10^{-16} in relative value. Expected frequency stability is 10^{-16} in relative frequency after 10 days of integration.

Low velocity of cooled atoms and long interaction times in microgravity will allow a series of experiments to be performed, both in the scientific and the technological domain. By varying the atomic velocity, systematic effects perturbing clock frequency will be analyzed. Studies of the PHARAO optimization and performances that will be performed are crucial for future space application and design of new atomic quantum sensors for acceleration and rotation (atom interferometers) and other instruments using cold atoms (future space optical clocks, atom lasers, etc). Expertise obtained from the ACES mission will also be useful for development of a more accurate next generation of space clocks operating in the visible domain. A time transfer link will enable distant ground clocks time comparison at the unprecedented level of 10^{-17}.

The thesis is organized as followed.

Chapter 2 deals with atomic clock and atomic fountain operation generalities. The properties of the PHARAO clock are very similar to the fountain clocks. Concepts of clock accuracy (Section 2.1.1) and clock stability (Section 2.1.2) will be introduced. In Section 2.1.3, the cesium clock development and the cesium atom benefits are briefly

overviewed. This leads to Section 2.2 which details the typical atomic fountain operation cycle containing atom cloud capture, cooling, preparation, interrogation and detection phases. Finally, Ramsey interrogation is explained in Section 2.2.1.2.

Chapter 3 will introduce the ACES mission. The environment on the International Space Station where the instruments will operate will be presented (Section 3.1). The payload (Section 3.2) consists not only of the PHARAO atomic clock, but also of a maser developed for space operation. Their signals will be merged (Section 3.2.3) to improve medium term stability and disseminated by time and frequency transfer links (Section 3.2.5). Finally, an overview of the scientific objectives will be given in Section 3.3.

Chapter 4 is dedicated to the PHARAO space clock description. Its main components the microwave (Section 4.3) and the laser source (Section 4.4) are discussed. The electronic control system is examined in Section 4.5. PHARAO cesium tube and its operation phases are explored in detail in Section 4.6. Magnetic shields surrounding the tube are introduced in Section 4.6.6. The experimental setup (Section 4.6.7.1) and the system initialization, optimization and operation (Section 4.6.7.2) are given.

Chapter 5 analyzes the sources of noise on PHARAO and their effect on stability: quantum projection in Section 5.1.1, detection system noise in Section 5.1.2, detection laser noise in Section 5.1.3, microvibration in Section 5.1.5 and the local oscillator noise in Section 5.1.4). In Section 5.2 the experimental results are given.

Chapter 6 details the most important systematic effects that shift the hyperfine resonance frequency. These include the second order Zeeman effect in Section 6.1, the cold collision in Section 6.3, the Doppler effect in Section 6.4 and the black body effect in Section 6.2.

Finally, in Chapter 7 the results are summarized and a conclusion is given. The same Chapter gives an overview of the activities I performed during the thesis and the experiments I worked on. I was heavily involved in the work presented in Section 6.1, made a significant contribution to Section 6.2 and worked on results of Section 6.3. Papers I authored or co-authored during the thesis are: (12, 13, 14, 15, 16).

2

Atomic clocks

2.1 Principle and performances

A diagram explaining microwave atomic clock principle is presented on Figure 2.1. The periodic signal provided by a macroscopic oscillator is sent to the atoms to excite the transition between two energy levels. From the detection of the resulting resonance signal a frequency correction is sent to the oscillator to lock the frequency of the oscillator on the atomic frequency resonance.

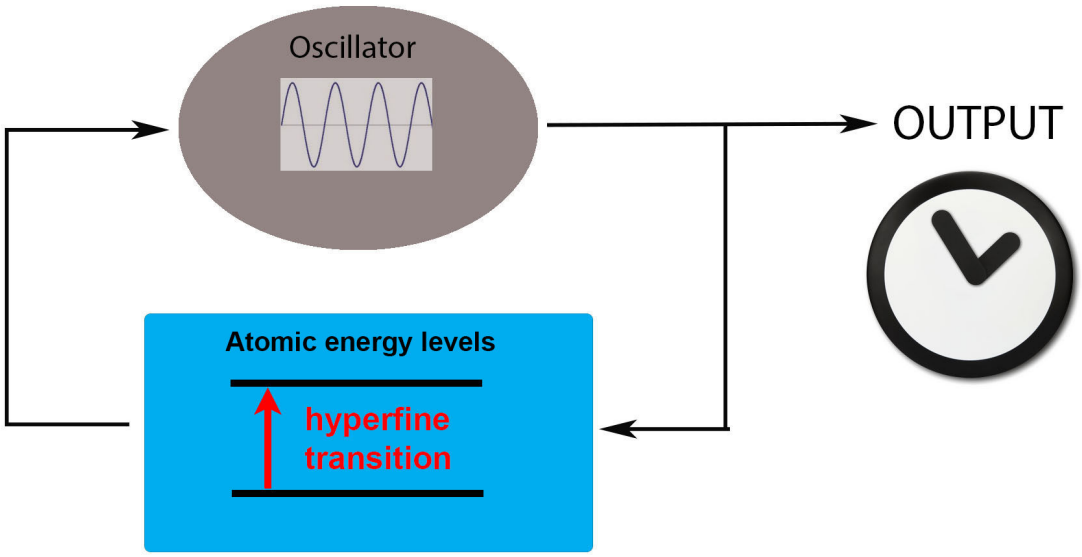

Figure 2.1: Scheme of microwave clock principle.

Clock performances are characterized by two physical quantities: frequency accuracy and frequency stability. The frequency ν delivered by the locked oscillator is not the actual Bohr frequency ν_0 but is shifted:

$$\nu(t) = \nu_0(1 + y(t) + \varepsilon), \tag{2.1}$$

where $y(t)$ represents the noise of the frequency measurement and ε is the frequency shift.

2.1.1 Clock accuracy

In Equation 2.1, ε represents the frequency shift originating from the multiple systematic effects perturbing the atoms during their interrogation (see, for example, (17)). The total uncertainty on ε at 1σ defines the frequency accuracy of the clock.

The most important systematic effects on a cold cesium atomic clock are the second order Zeeman effect (Section 6.1), cold collision effect (Section 6.3) and the black body effect (6.2). The Zeeman effect is due to the interaction of atoms with the magnetic field with a quadratic dependency. Cold collisions are low velocity interatomic collisions dependent on atomic density and relative kinetic energy. The black body effect is caused by the atomic interaction with the thermal photons emitted by the cavity walls.

Another relevant effect is the Doppler effect. The effect is due to the microwave field gradient inside the interrogation cavity inducing a frequency shift with a linear dependency on atomic velocity.

2.1.2 Clock stability

Temporal frequency stability of clocks depending on the noise processes is evaluated by phase or frequency comparison with a reference clock. It can be characterized by the Allan variance (AVAR) (17, 18, 19):

$$\sigma_y(\tau)^2 = \frac{1}{2}\langle(\bar{y}_{k+1} - \bar{y}_k)^2\rangle = \frac{1}{2}\lim_{n\to+\infty}\frac{1}{n}\sum_{k=1}^{n}(\bar{y}_{k+1} - \bar{y}_k)^2, \tag{2.2}$$

where $\bar{y}_k$ are the average values of the $y(t)$ relative (divided by the clock frequency) frequency fluctuations between successive intervals $t_k \to t_{k+1}$:

$$\bar{y}_k = \frac{1}{\tau}\int_{t_k}^{t_{k+1}} y(t)dt, \tag{2.3}$$

where $\tau = t_{k+1} - t_k$ is the duration of the measurement.

Allan variance allows estimation of stability for sampled measurements of individual duration τ and total measurement duration of $N \times \tau$. For an illustration see Figure 2.2.

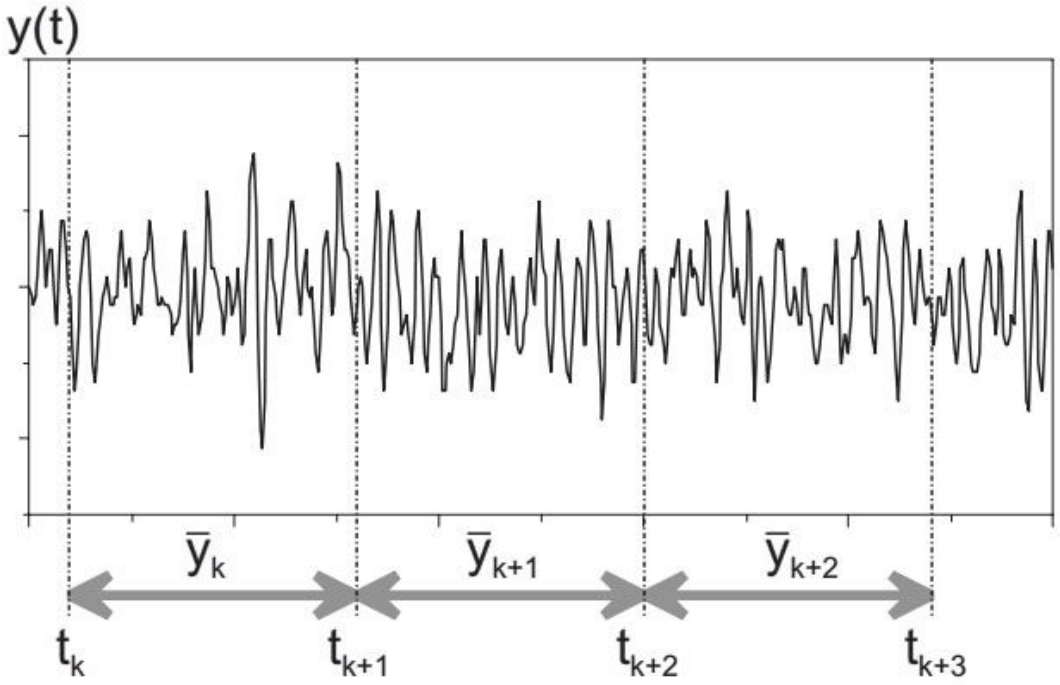

Figure 2.2: Frequency dispersion of successive intervals.

From the log-log power-law of $\sigma_y(\tau)$ it is possible to separate noise contributions (Figure 2.3): white phase noise or flicker phase noise (slope -1: Allan variance cannot distinguish between them [1]), white frequency noise (slope -1/2), flicker frequency noise (slope 0) and random walk frequency noise (slope 1/2).

Dominant stability impairing source on an atomic clock is the white frequency noise. At long term a stability floor is reached defined by the flicker frequency noise.

[1] with the modified Allan variance they can be distinguished and have slopes -3/2 and -1, respectively.

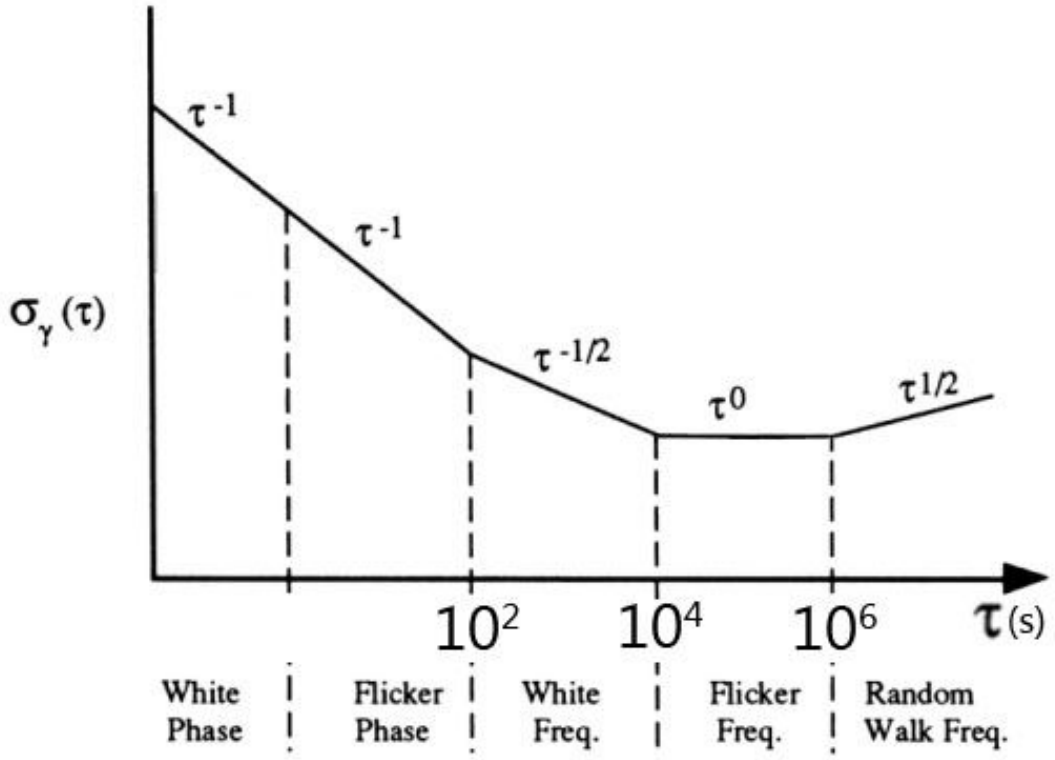

Figure 2.3: Example of a spectral distribution of noise.

2.1.3 Clock development

In 1945. during a meeting of the American Physical Society, Rabi proposed a technique of detecting magnetic resonance. This was used to build the first atomic clock based on an ammonia maser by the US Narional Bureau of Standards (now National Institute of Standards and Technology or NIST). In 1950. Ramsey proposed an improved technique (20, 21) based on separated oscillating fields that has a number of advantages over the Rabi method (22). A few years later, the National Physical Laboratory (NPL) in the UK constructed the first cesium clock (23) based on the ^{133}Cs transition and the combined Rabi and Ramsey method (Figure 2.4). The development of cesiums clock has lead to a new definition of the second in 1967. and replaced the previous definition which was based on Earth's rotation.

In 1980, the optical pumping technique and a GaAs laser were used to select ground hyperfine levels of cesium in an atomic clock (24). In 1988. sub-Doppler process was used to cool atoms in an atomic clock. This was a breakthrough in quantum mechanics

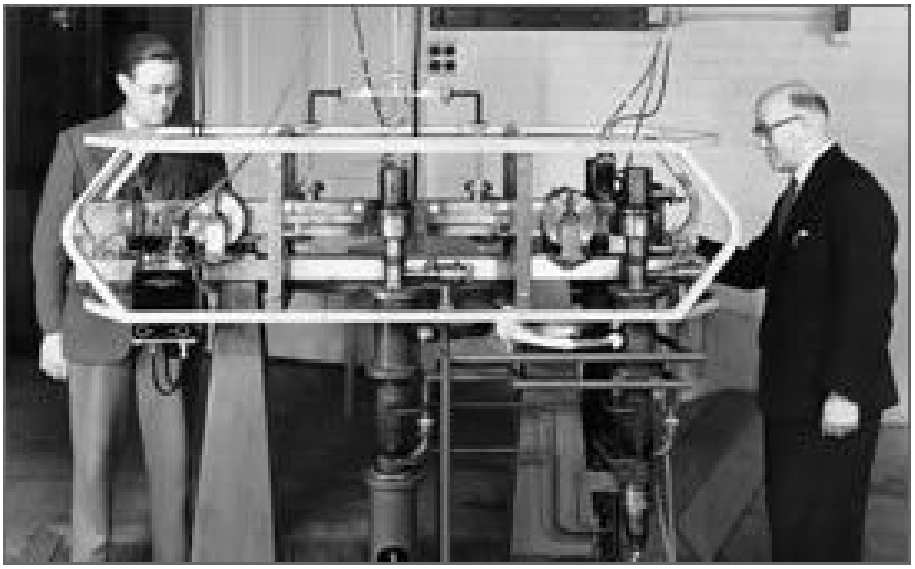

Figure 2.4: First cesium clock built in 1953. at the NPL by Louis Essen and Jack Parry.

for which a Nobel prize was given to Steven Chu, Claude Cohen-Tannoudji, and William D. Phillips (25). The first cold atom fountain as a primary frequency standard has been developed at SYRTE in 1993 (26). Today, several fountains are in operation in the world. The main fountains that contribute to TAI (International Atomic Time) are the FO1, FO2 and FOM at Syrte (6), CsF1 and CsF2 at PTB (7), CsF2 (5) at NPL and F1 at NIST (4).

2.1.3.1 Selection of cesium and alternatives

The transition in ^{133}Cs was selected at the "General Conference on Weights and Measures in 1967" as a basis for a definition of a second. ^{133}Cs is the only stable Cs isotope, and it offered the following advantages:

- high transition frequency means a larger quality factor of the central resonance pattern $Q = \frac{\nu_0}{\Delta\nu_0}$ (where ν_0 is the transition frequency and $\Delta\nu_0$ the resonance central fringe linewidth) and the fact the transition can be only weakly affected by electric fields (27),

- the isotope is abundant and easily isolated,

- a cavity that resonates at the selected transition frequency can be manufactured with a reasonable size,
- due to massive atom size, ^{137}Cs has lower thermal velocity and thus the resonance peak is narrower (larger Q).

The selection makes the cesium atomic clock the primary standard for time and frequency measurements (28).

By definition, the second is "the duration of 9,192,631,770 periods of the radiation corresponding to the transition between the two hyperfine levels of the ground state of the ^{133}Cs. The frequency value of the $F = 3, \rightarrow F = 4$ transition is then fixed by definition. The Figure 2.5 shows the cesium transitions used in a cold atomic clock.

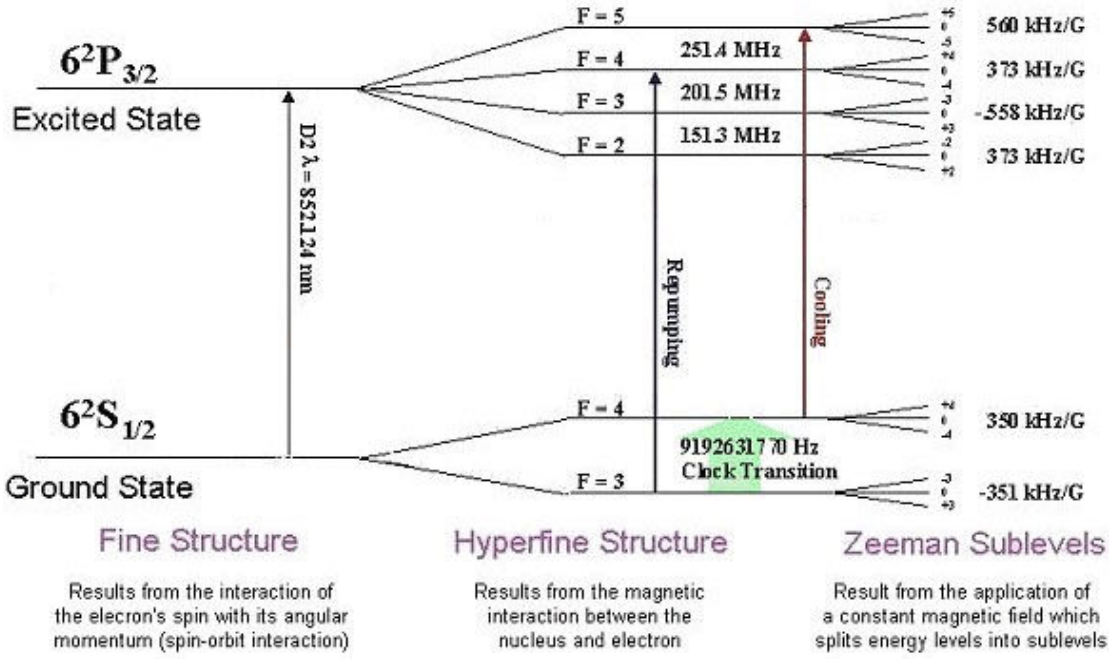

Figure 2.5: The energy levels of cesium: energy level used for clock transition and cooling.

2.2 Atomic fountain - primary frequency standard

In 1953, one of Rabis's students, Zacharias performed the first experiments using a prototype of an atomic fountain where the thermal atomic beams were directed upwards towards the apogee and return back through the same cavity thanks to gravity. The

idea of Zacharias was to increase the interaction time and improve clock performance. The two passages through the same cavity constitute the Ramsey method of measuring atomic transition frequency. The assumption was that the atoms at the low velocity end of the Maxwell-Boltzmann distribution would have a sufficiently low energy to successfully complete a parabolic trajectory. However, the experiments were unsuccessful because of a high rate of atom loss due to collisions between returning slow atoms and faster atoms being launched.

In the next forty years the development of atomic clocks continued with increased accuracy and decreased size and cost. In 1989. the first successful atomic fountain was tested. Kasevich et al. (29) used the newly introduced laser cooling techniques to cool the atomic sample of around 5×10^7 sodium atoms and launch them in an atomic fountain. The first cesium fountain geometry was demonstrated by Clairon et al. (30) in 1991. The first cesium fountain as a frequency standard was developed at SYRTE (Observatoire de Paris) in 1993. This was followed by the construction of other fountain clocks at SYRTE, NIST, Physikalisch-Technische Bundenstag (PTB) in Germany, Instituto Elettrotecnico Nazionale (IEN) in Italy, NPL and NMIJ in Japan. Besides the first clock FO1, SYRTE is currently operating FO2, a dual fountain that can operate with ^{87}Rb and ^{133}Cs simultaneously and FOM (Figure 2.6). FOM is the only transportable primary frequency standard. It was originally constructed in 1999 at LNE-SYRTE Paris as a prototype for the space clock PHARAO.

2.2.1 Cesium atomic fountain operation

The hyperfine levels of cesium are degenerated states. The Zeeman level degeneracy is lifted by applying a static magnetic field.

For every cycle of operation of an atomic fountain (typically, an atomic clock cycle lasts 1-2 s), a cloud of atoms is captured, cooled and launched upwards by laser beams provided by a laser source. Using the 3D optical molasses technique consisting of Doppler and sub-Doppler cooling via 3 pairs of counter-propagating laser beams the atomic cloud is cooled to a temperature of $\sim 1\ \mu K$.

After cooling, the atoms are launched vertically and enter the preparation cavity. In the preparation cavity the atoms are prepared in the energetically lower hyperfine fundamental state $|F = 3, m_F = 0\rangle$. Next they pass through the interrogation cavity, reach an apogee and return along the same path downwards passing through the same

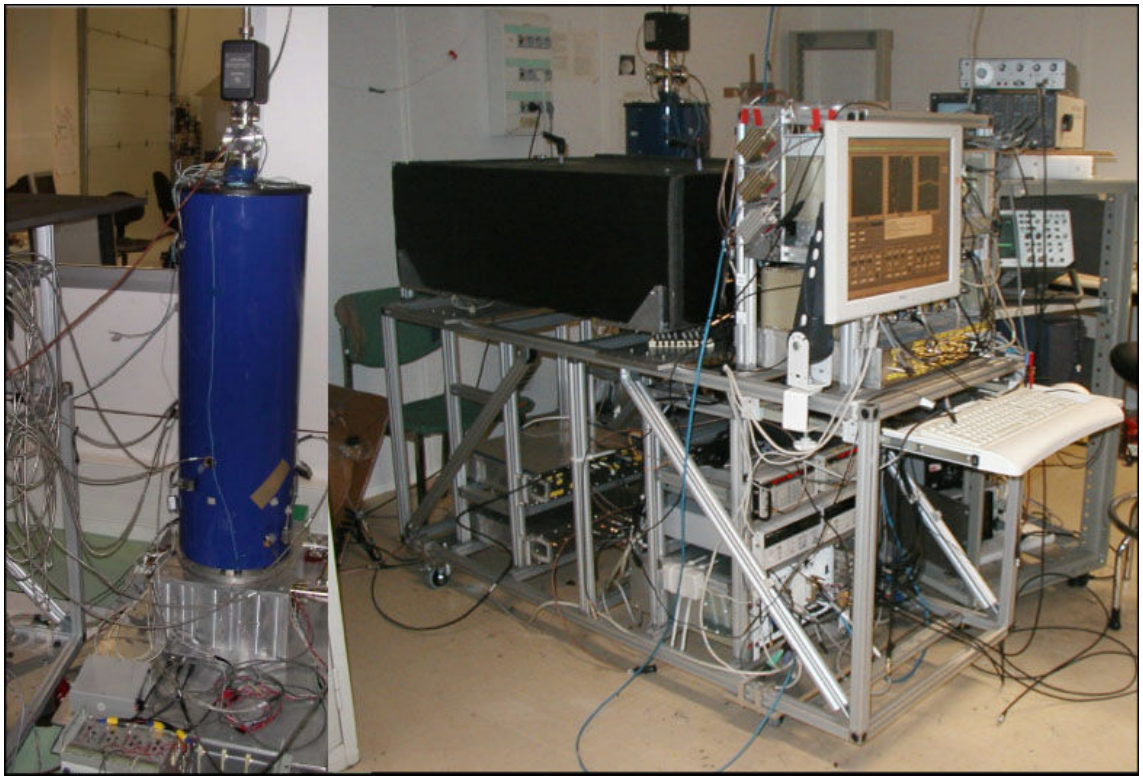

Figure 2.6: The vacuum cavity (on the left), the laser system (black box on the right) and the microwave source (below the black box in the right) of the FOM atomic fountain

cavity. In that way the atoms are submitted twice to the same microwave field. This is called Ramsey interrogation.

Near the bottom of the fountain the atoms are detected and the probability of transition as a function of microwave oscillator frequency is calculated, thus ending the cycle. The transition probability is determined by measuring the total number of atoms in the $|F = 4\rangle$ and in the $|F = 3\rangle$ state (31):

$$P = \frac{N_4}{N_3 + N_4} = \frac{1}{2}(1 + cos\pi\Delta\nu t_0), \tag{2.4}$$

The probability varies with the frequency difference $\Delta\nu$ between the atomic resonance frequency and the oscillator frequency. The width of the central resonance is inversely proportional to the transit time t_0 and is about 1 Hz. The measurement is based on the atomic fluorescence induced by laser beams.

To lock the microwave oscillator, the frequency is modulated around the atomic

resonance frequency. After each cycle the frequency of the microwave field is corrected in order to reduce $\Delta\nu$. For a graphical representation of a ground based atomic fountain cycle see Figure 2.7.

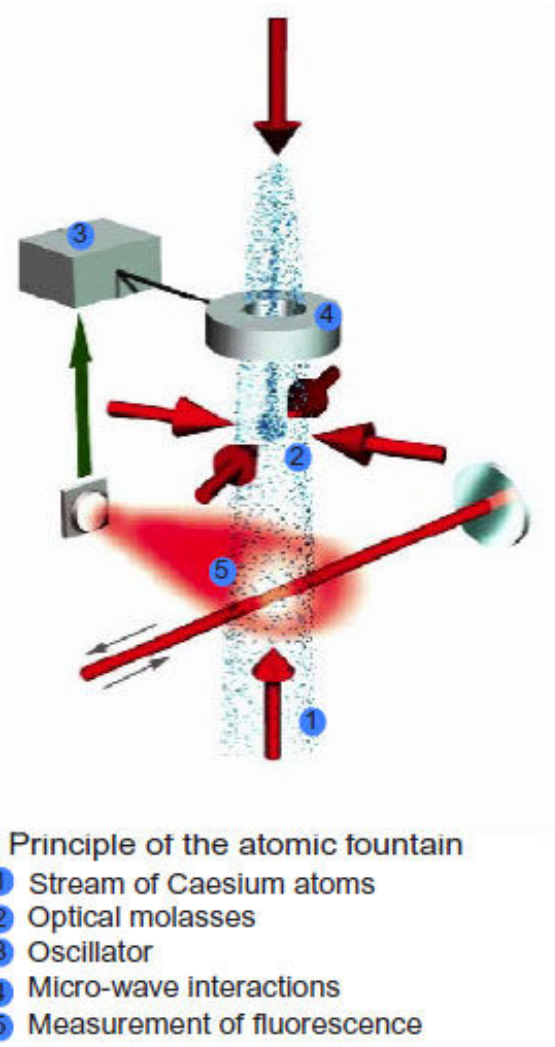

Figure 2.7: Principle of atomic fountain operation. Atoms are relased from a reservoir (1). Atoms are cooled using the optical molasses technique (2). A microwave oscillator (3) interrogates the atoms (4). Next, by measuring fluorescence, the number of atoms in each hyperfine level is determined (5). The frequency of the microwave field is corrected in order to achieve a higher probability of transition. New cycle begins with (1).

2.2.1.1 Atom cooling (Doppler and sub-Doppler cooling) and the launch

Doppler cooling (32, 33, 34, 35, 36) is based on the Doppler effect. Three pairs of laser beams are positioned in opposite directions and tuned a little below the transition frequency of $6S_{1/2}(F=4) \rightarrow 6P_{3/2}(F=5)$. Due to the Doppler effect, atoms moving inside the laser beams in the counter propagating direction absorb more photons and their momentum is decreased.

However, the atoms can also be excited in the $6S_{1/2}(F=4) \rightarrow 6P_{3/2}(F=4)$ (every ≈ 1000 transitions) and can decay in the $6P_{3/2}(F=4) \rightarrow 6S_{1/2}(F=3)$ transition. In that case the atoms are no longer submitted to the laser cooling process. That is why another laser beam tuned to the $6S_{1/2}(F=3) \rightarrow 6P_{3/2}(F=4)$ transition pumps them to the $6S_{1/2}(F=4)$ level.

Using the optical Bloch equations (37), the scattering rate for atoms is:

$$\Gamma_{sc} = \frac{\Gamma}{2} \frac{I/I_s}{1 + I/I_s + 4(\Delta/\Gamma)^2} \tag{2.5}$$

where Γ is the natural linewidth, $\Delta = (\omega - \omega_0 - k \times v)$ is the frequency detuning, I is the photon intensity and I_s is the saturation photon intensity ($1.1 - 1.6 mW/cm^2$ depending on the beam polarization).

After time τ, inversely proportional to the natural linewidth Γ ($3.3 \times 10^7 s^{-1}$) of the excited state, the state $6P_{3/2}(F=5)$ decays and emits a photon. This emission has an isotropic angular distribution so the overall result after many recoil events is the reduction of average atom velocity, and therefore its kinetic energy and temperature.

The laser beam intensity needs to be large in order to be able to decelerate a wide range of initial velocities. The maximum recoil impulse amounts to $\hbar\vec{k_l} \times \Gamma/2$ per unit of time, where $\hbar\vec{k_l}$ is the momentum of a photon. The force a cesium atom experiences is $\frac{d\vec{p}}{dt} = \hbar\vec{k_l}\frac{\Gamma}{2}$. From that the acceleration can be calculated:

$$\vec{v}_{rec} = \frac{\hbar\vec{k_l}}{m} = 3.52 mm/s. \tag{2.6}$$

The recoil velocity the atom experiences when it absorbs or emits a photon is:

$$\vec{a} = \frac{1}{m}\frac{d\vec{p}}{dt} = \frac{\hbar\vec{k_l}}{m}\frac{\Gamma}{2} = \vec{v}_{rec}\frac{\Gamma}{2} = 6 \times 10^4 m/s^2 \tag{2.7}$$

Depending on the 6 beam intersection size d (typically $\approx 20mm$) the maximum velocity of atoms that can be captured is then (from kinematic equations):

$$v \approx \sqrt{2 \times a \times d} = 48.99m/s. \tag{2.8}$$

The lowest temperature, limited by the spontaneous emission rate (velocity random walk), that can be achieved by Doppler cooling depends on the natural linewidth and is called the Doppler limit (38):

$$T_D = \frac{\hbar\Gamma}{2k_B} \tag{2.9}$$

For cesium $T_D = 127\mu K$.

At low temperatures another cooling mechanism can be used. Sub-Doppler or Sisyphus cooling (from Greek mythology) is based on the AC stark shift of the Zeeman sub-levels of $F = 4$. It was introduced by Chu (39), Cohen-Tannoudji (38) and Phillips (40).

Counter propagating lasers with the same amplitude and perpendicular polarizations along the x and y axis ($lin \perp lin$ configuration) create a position dependent polarization field along the z-axis. Polarization varies cyclically in space between linear σ_+ and linear perpendicular σ_- for every $\lambda/8$. This creates a proportional gradient force pattern along z. Laser tuning and the polarisation variations have been arranged in a way that a propagating atom is always rolling on the potential hill thus loosing kinetic energy due to the energy conservation law.

With Sisyphus cooling the spontaneous decay rate becomes much smaller and the temperature can reach a very low value. The final temperature is proportional to the laser beam intensity and inversely proportional to the detuning between the laser frequency and the atomic frequency (36):

$$T_{min} \approx \frac{1}{k_b}\frac{I}{\delta} + T_L \tag{2.10}$$

where k_b is the Boltzmann constant and T_L is the temperature limit of Sisyphus cooling set by the recoil limit due to photon scattering.

Efficiency of sub-Doppler cooling depends on the relative phase noise between the counter propagating laser beams. Therefore, the beams need to be coherent.

More details on the sub-Doppler cooling are given in Appendix 2 (Section 9.1).

After cooling, the atoms are trapped in the standing wave of counter propagating laser beams pointing upwards and downwards $e^{i(k\bar{a}-\omega t)} - e^{-k\bar{a}-\omega t)}$. If the frequencies of the beams are shifted by $-\Delta\omega$ and $+\Delta\omega$, the standing wave moves at a velocity given by $\frac{dz}{dt} = \frac{\Delta\omega}{k}$ and the atoms are launched.

Therefore, the Doppler and sub-Doppler processes steer the atomic velocities at the velocity of the standing wave. This is called the moving molasses technique and it allows for precise control of the launch velocity.

To launch the atoms a large number of absorbed photons are needed. To increase sub-Doppler cooling efficiency (reach minimum temperature) after the launch it is necessary to decrease the beam intensity and increase the laser detuning. Sub-Doppler with the new parameters is repeated after launch.

The minimum temperature reached for ^{133}Cs is $T_L \leq 1\mu K$.

2.2.1.2 Ramsey interrogation

A method of atomic interaction was introduced by Norman Ramsey in 1949, for which he was awarded the Nobel Prize in Physics in 1989 (41). The atoms are submitted to a microwave field in the two smaller interaction zones separated by a relatively long distance. The Ramsey method is an advance over the Rabi method, which uses a single interaction zone. The resonance peaks when using Ramsey interrogation are typically 40% narrower that those measured after the Rabi method due to the introduction of the free evolution region. The width of the peaks is inversely proportional to the duration of the free evolution flight time between the two interaction zones. This is explained using an analogy from optical physics where a double-slit experiment creates an interference pattern whose peaks are narrower than in a single-slit experiment.

The Ramsey interrogation is explained in much more detail in the Appendix 1 (Section 8.1).

2.3 Perspective and other clocks

Other atoms besides cesium are also studied to use as a secondary standard. For example, a ^{87}Rb clock (42) is physically similar to a cesium clock and has an electronic structure favourable for laser cooling. Due to a lower cross section of ^{87}Rb atoms, the frequency shift due to cold collision is reduced by a factor of 15. Based on the

work on the double cesium-rubidium FO2 clock at LNE-SYRTE in Paris over several years, the secondary representation of the definition of the second is given by the hyperfine transition of frequency $f(^{87}Rb)$ = 6 834 682 619. 904 312 with a relative standard uncertainty of 1.3×10^{-15} (43). Another alternative for a frequency standard are optical clocks. Optical frequency standards are based on an optical electronic transition with narrow bandwidth that stabilizes the frequency of the laser. The atoms are trapped using the Penning trap or optical trap and laser cooled. Optical clocks can be constructed using atoms (for example Ca, Rb, Sr, Yb, Mg or H), ions (Hg^+, Sr^+, Yb^+, In^+, Al^+) or molecules (I_2, CH_4, C_2H_2). Some of the advantages of optical clocks are higher accuracy and stability due to the higher frequency of the resonance.

In 2001, femtosecond laser techniques (44) broke the gap between frequency comparisons in the optical and microwave domains. The development of laser locking on a high finesse cavity (to provide very low noise optical oscillators), atom cooling and trapping processes have lead to a significant optical clock technology advancement. In July 2013, two optical lattice strontium clocks were able to stay in synchrony at 1.5×10^{-16} (45) at 1s. In August of the same year NIST ytterbium optical clocks achieved a frequency stability of 2×10^{-18} (46) at 1s, a new record in atomic clock stability.

Transfer of atomic clocks to space will open new possibilities in clock development and usage. The scientific and technological performances will be improved because of the microgravity environment, the possibility of additional fundamental physics test, possibility of high performance intercontinental clock comparison, etc. Next chapter introduces the ACES mission which is dedicated to high space clock performances and fundamental physics.

3

ACES mission

In December 1996, ESA issued an Announcement of Opportunity for Externally Mounted Payloads during the Early Space Station Utilisation Period. This announcement was based on the ESA/NASA Agreement that allows European payloads access to the US-provided external Truss attach sites. 102 proposals had been received by the April 1997 closing date. Five payloads have been selected and among them the ACES (47, 48) mission proposed by LKB (principal investigator: Christophe Salomon) and SYRTE.

ACES (Atomic Clock Ensemble in Space) is an ESA mission in fundamental physics based on time/frequency comparisons of ground and space clocks. The flight segment is to be installed on the NASA developed External Payload Facility pallet of the Columbus laboratory (CEPF) on-board the ISS (International Space Station) in 2016. The launcher is the SpaceX Falcon 9 v1.1 (49) with the SpaceX Dragon capsule (50) that will be used to transport the ACES payload. SpaceX is a privately owned US based space transport company providing launch services to NASA, but also to non-American governments and private sector companies. Falcon 9 v1.1 offers 60% more thrust than the previous SpaceX Falcon 9 v1.0. It is a two stage vehicle using liquid oxygen and rocket-grade kerosene propellants and offering a lift of 13.150 kg to LEO (low Earth orbit). SpaceX Dragon has been used since October 2012 to deliver cargo to ISS with a crewed variant currently in development. It offers a maximum payload weight of 3.110 kg with a choice of pressurization.

ACES payload will operate two new types of space atomic clocks: the active hydrogen maser (SHM) and the cold cesium clock (PHARAO). By combining stabilities of the two on board clocks ACES will distribute a stable and accurate timescale by a two

way time and frequency transfer links in the microwave (MWL) and optical domain (ELT). The generated timescale will be used for space to ground and ground to ground timescale comparisons. From these comparisons information on general relativity, atmosphere, clocks performances and other scientific aspects will be derived.

Ground terminals will mainly be located in time and frequency laboratories. The mission will be operated from the ACES User Support and Operation Center (USOC), installed at CADMOS (Centre d'Aide au Developement de la Microgravite et aux Operations Spatiales) in France. Operation of the system is controlled by adjusting parameters relevant to the clock signal characteristics (linewidth, S/N ratio, etc.).

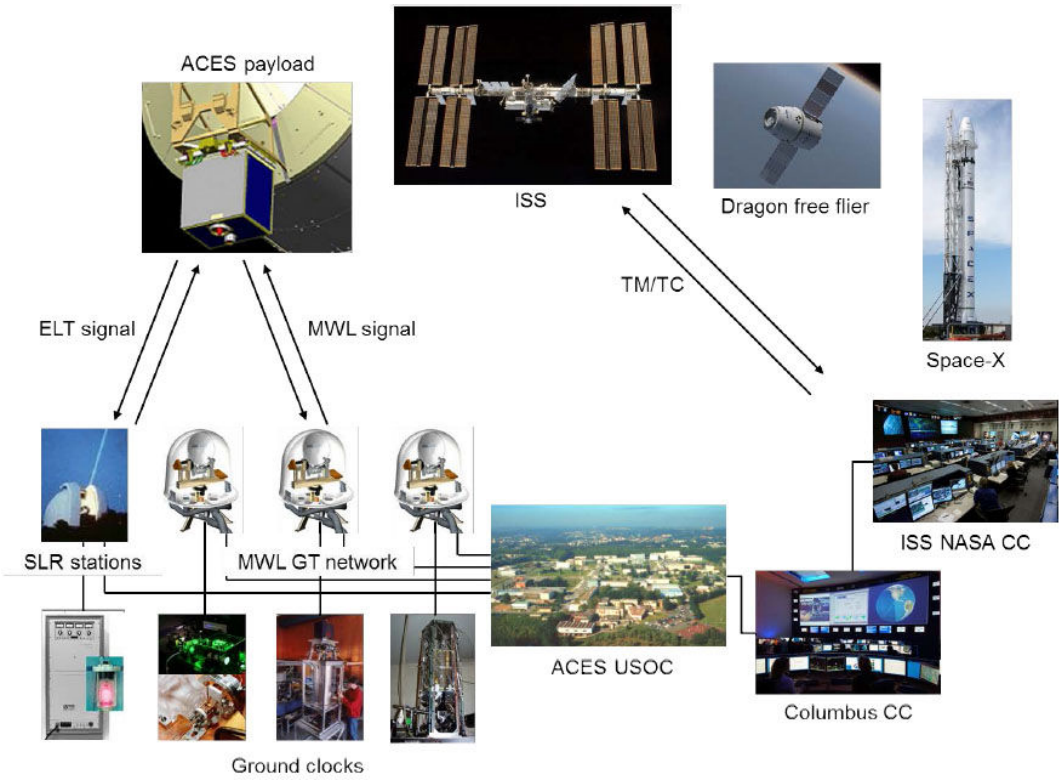

Figure 3.1: The ACES mission. Placed on the ISS, the signal will be disseminated by the microwave (MWL) and optical (ELT) link to ground stations. The mission will be controlled from CADMOS, Toulouse. A SpaceX launcher will be used

It is expected the ACES signal will provide a 1-2 orders of magnitude more stable and accurate signal compared to existing clocks developed for space applications (GPS and GALILEO) and reach a frequency stability floor of 10^{-16} and frequency accuracy lower then 3×10^{-16}.

Planned duration of the mission is 18 months with a possible extension to 36 months. First 6 months are reserved for functionality verification of instruments and performance evaluation. After the initial two months dedicated to flight commissioning ground users will be provided by a signal with a frequency accuracy of 10^{-15}. In the second part of the mission the clocks will reach optimum performance and be compared to ground clocks operating both in the microwave and optical domains.

3.1 International Space Station

The station (51, 52, 53) is normally managed by a crew of six and is used as a microgravity multi-purpose research facility. Its mass is $\approx$ 450 000 kg, length 72.8 m, width 108.5 m and height 20 m. Its pressurized volume is 837 m^3. The first component was launched in 1998. The station is currently funded until 2020 with operation prolongation proposal to 2028.

Elements of the ISS are shown on Figure 3.2.

3.1.1 Orbit and environments

The ISS is orbiting inside the ionosphere in low Earth orbit at a mean elevation of 400 km with about a 90 min rotation period and an inclination angle of 51.6 degrees to the equator. Due to the equatorial bulge and the resulting westward nodal precession the ISS daily passes occur approximately 20 minutes earlier every day. The orbital altitude varies between 330 km and 460 km due to aerodynamic drag of 0.6 km/day. To regain altitude small reboosts are performed every 10 to 45 days depending on the atmospheric profile. Large reboosts are performed about every 90 days. If the reboots do not perturb the clock operation, it would be possible to measure the gravitational redshift modulation. An altitude difference of 40 km corresponds to a frequency modulation of about 4×10^{-12} in relative frequency. Figure 3.3 shows the evolution of the ISS orbit altitude over 7 years.

The position accuracy of ISS is better than 75 m for each axis measured by four GPS receivers placed at different positions of the station. The velocity and attitude determination accuracy is better than 0.2 m/s and $\pm 3°$, respectively. Star tracker measurements show that the attitude stability is actually typically better than specifications; the attitude has a sinusoidal variation with an amplitude of $< 1°$ in each axis.

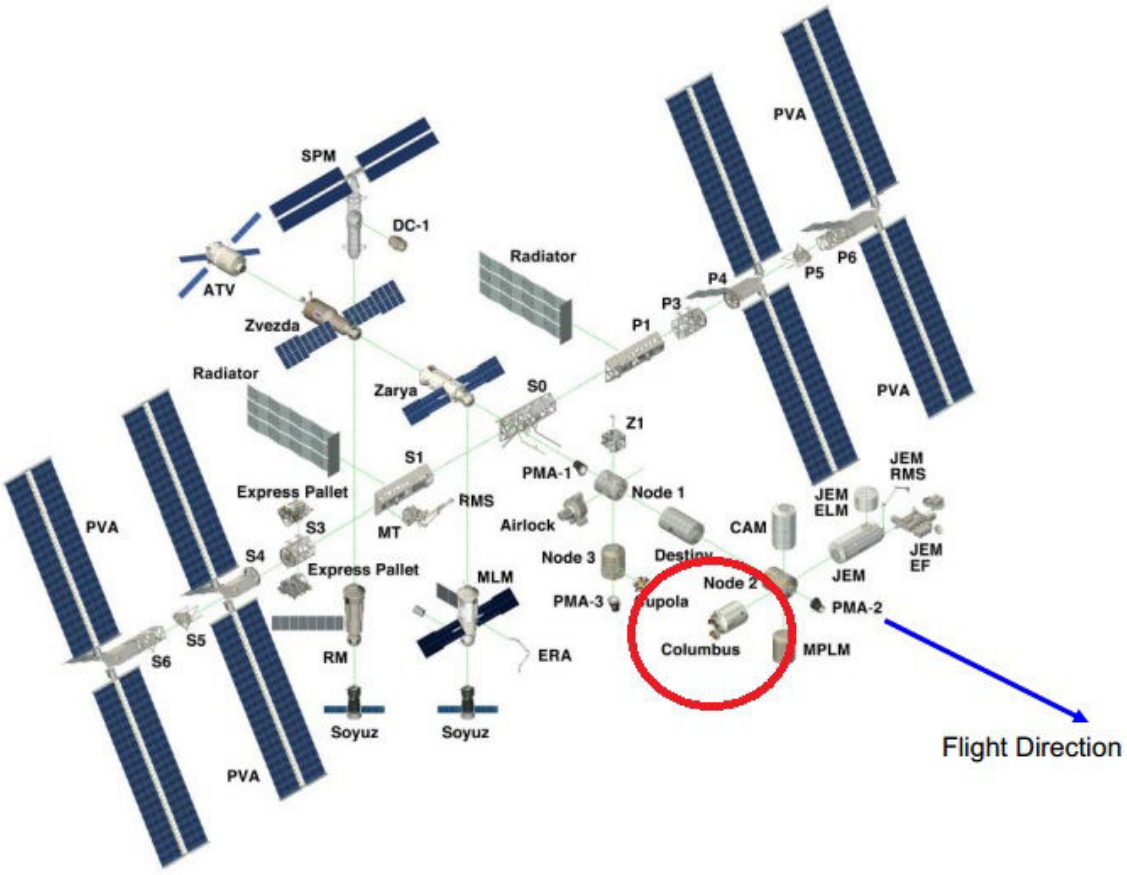

Figure 3.2: Elements of the ISS. Red circle marks the position of the Columbus laboratory where the ACES package is to be installed.

Docking of vehicles and reboosts result in the attitude variation of $3-4°$ and $2-3°$, respectively.

The station orbit flys over 85% of Earth's surface which includes 95% of its population. The environment has minor quasi-steady accelerations of $< 10^{-5}g$ and frequency $< 0.01Hz$ due to air drag and vibratory accelerations resulting from crew and ISS operations (such as reboosts and docking).In the 1-100 Hz range the acceleration levels could be an issue on the stability performance of the PHARAO clock as will be explained later.

Due to the angle between the ISS and the solar orbit, the instruments experience varying solar illumination. The accumulated heat of the Columbus external payloads can only be dissipated by radiation. Some of the environmental characteristics at the

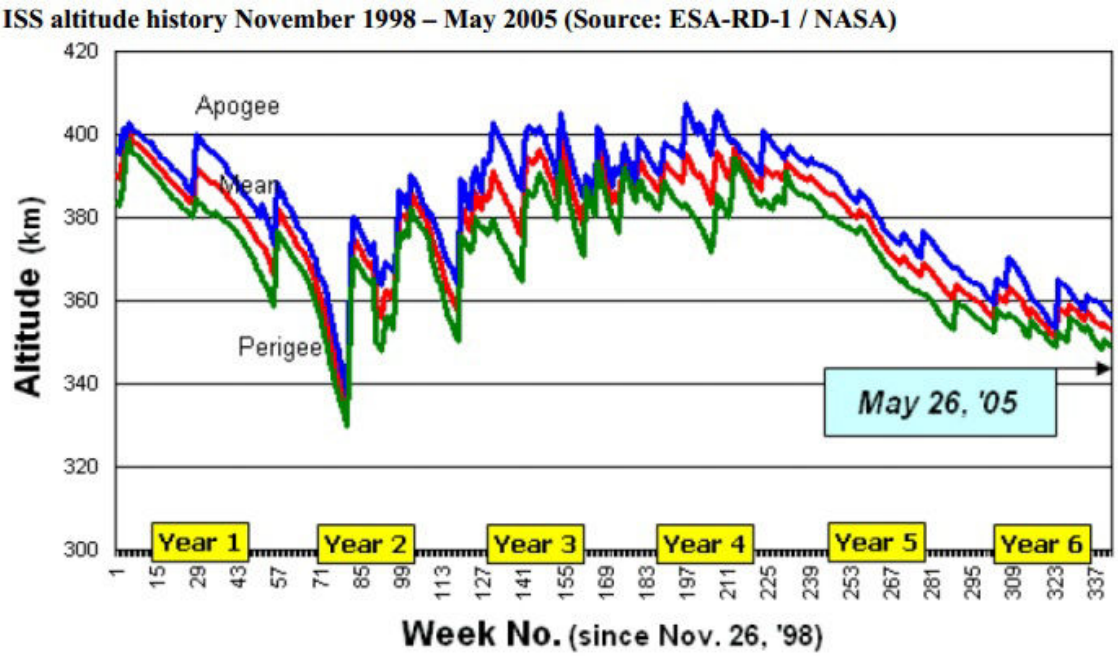

Figure 3.3: 7 year ISS altitude profile.

position of the ISS orbit are shown on Figure 3.4.

The Earth's magnetic field extends about 95 000 km from the surface towards the sunward direction and several times more in the antisunward direction. This defines the magnetosphere. Above this region the interplanetary space is not affected by its field. The magnetic field acts on the ISS by creating local electric field gradients inside the station and the payloads. Above 2000 km, the interaction of charged particles with the magnetosphere causes significant deviations to the magnetic field. Its distribution can be presented as a dipole tilted 11.5 degrees from the rotation axis of the Earth and offset from the geometric centre of the Earth by 430 km in the direction of southeast Asia. The strength of the field is not constant and changes cyclically. Currently, it is decreasing by about 0.1% per year. The South Atlantic anomaly is an area of a weak magnetic field where the increased flux of trapped particles causes high levels of radiation. Additionally, geomagnetic storms resulting from increased solar activity can change its amplitude by a few hundred nT. For the shape and amplitude of the magnetic field experienced by the ISS during rotation see Section 6.1. The magnetic field variations are large and have an important impact on PHARAO operation.

Natural External Environment	
Parameter	Value / Remarks
Atmospheric Pressure	~3.6 x 10^{-11}kPa
Thermal Environment	Max: ~+120°C Min: ~ -120°C
• Cold Natural Thermal Environment	Solar Constant: 1321 W/m^2 Earth Albedo: 0.2 Earth OLR*: 206 W/m^2
• Hot Natural Thermal Environment	Solar Constant: 1423 W/m^2 Earth Albedo: 0.4 Earth OLR*: 286 W/m^2
Humidity	0% relative humidity
Atomic Oxygen	Up to 4.4x1019 atoms/cm^2/day
Electromagnetic radiation spectrum	Exposure to full electromagnetic spectrum from X-rays to long wave radio. Intense solar ultraviolet radiation
Plasma	Plasma environment of ionosphere. ISS surface has an equilibrium potential of a few negative volts with respect to external plasma environment
Ionizing radiation	Trapped electrons, protons, solar and galactic cosmic rays
Meteoroids and orbital debris	Weak flux of small orbital debris and micrometeroid particles which cause cumulative surface damage and degradation over time
Induced External Environment	
Quiescent periods = standard operations outside of visiting vehicle operations and reboosts	
Molecular Column Density from ISS contamination sources	1x 10^{14} molecules/cm^2 (Excludes ram wake effects)
Particulate background	Limited 1 particle (<100μm) per orbit
Molecular disposition	Less than 1x10-^{14}g/cm^2
Non Quiescent periods *(e.g. docking / undocking of visiting vehicles, reboosts)*	
Molecular disposition	Less than 1x10-^{6}g/cm^2
Plume Impingement	Maximum 0.16kPa direct, Maximum 0.038kPa indirect (shear)

* Earth Outgoing Long-Wave Radiation

Figure 3.4: External environment of the ISS orbit.

3.1.2 Instrument positions

The on-board instruments can be placed either internally (view through windows) or externally (exposed to space). External mounting locations are the ESA Columbus External Payloads Facility (CEPF), JAXA Kibo Exposed Facility (Kibo-EF), US Truss and the Russian Segment URM-D.

CEPF mounting structure has 2 adaptor plates that can fit a total of 4 large payloads allowing nadir, starboard and zenith viewing (Figure 3.5). This is where ACES will be placed (nadir).

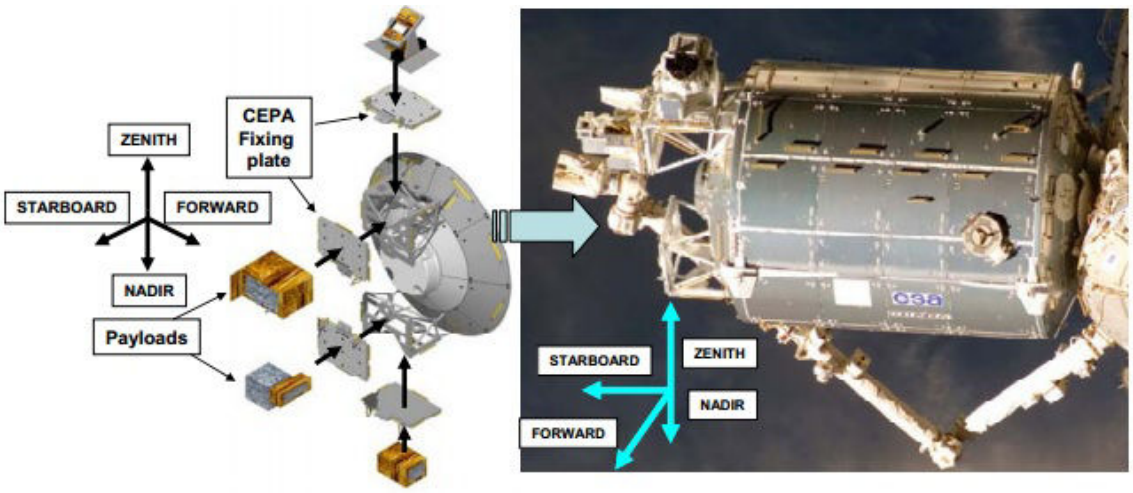

Figure 3.5: CEPF orientations.

The maximum weight of the payload is 230 kg with a volume of 1.39 m^3 (width = 1168 mm, height = 1375 mm and depth = 864 mm). The thermal environment can vary between $-62°C$ and $+36°C$. The maximum available power is 1.25 kW per location. For an illustration of the Columbus module configuration and the position of the external payloads see Figure 3.6.

The internal mounting locations are the NASA Destiny Module Nadir Window, NASA Cupola Module and the Russian Segment Zvezda Window. Positions of the external and internal mounting locations can be seen on Figure 3.2.

3.1.3 Vehicle support

At the moment, the rotation of crews is performed mostly by Russian Soyuz vehicles (average of 4 dockings per year), while the resupply is mainly performed by the Russian

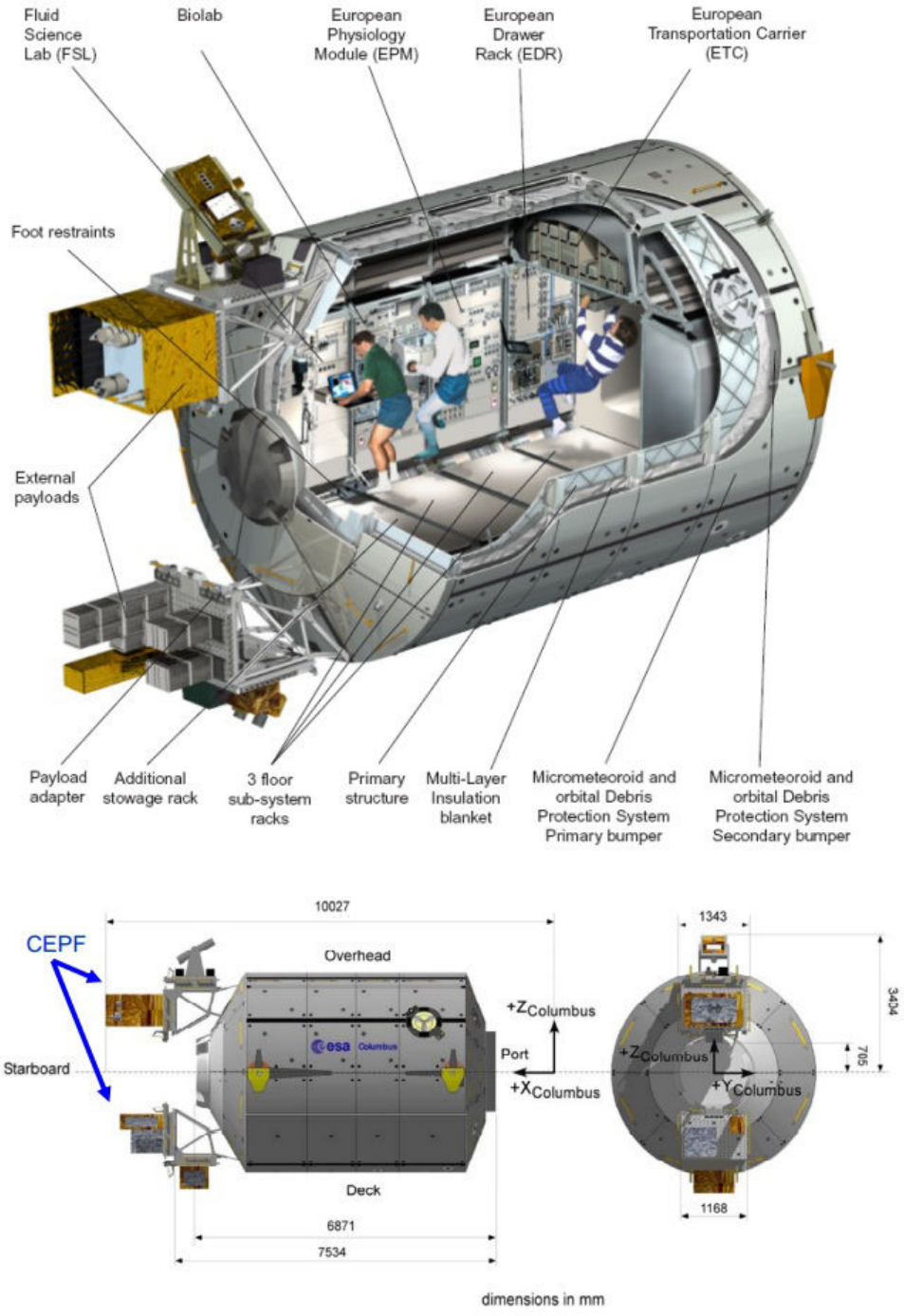

Figure 3.6: General arrangement and dimensions of the Columbus module.

Progress (4-5 dockings per year) with the tendency to replace both with commercial flights. As the Soyuz can carry only three crew members at a time, there are brief periods when the station is operated with only three crew members. Other resupply vehicles are the ESA ATV (flight frequency 12-18 months), Japanese HTV (flight frequency 12 months) and the recent NASA financed commercial vehicles OSC Cygnus and SpaceX Dragon. The vehicles dock at various docking ports present on the station.

External payloads can be transported in an unpressurised compartment by the JAXA HTV, a variant of the OSC Cygnus and the SpaceX Dragon (Figure 3.7) which will be used for ACES.

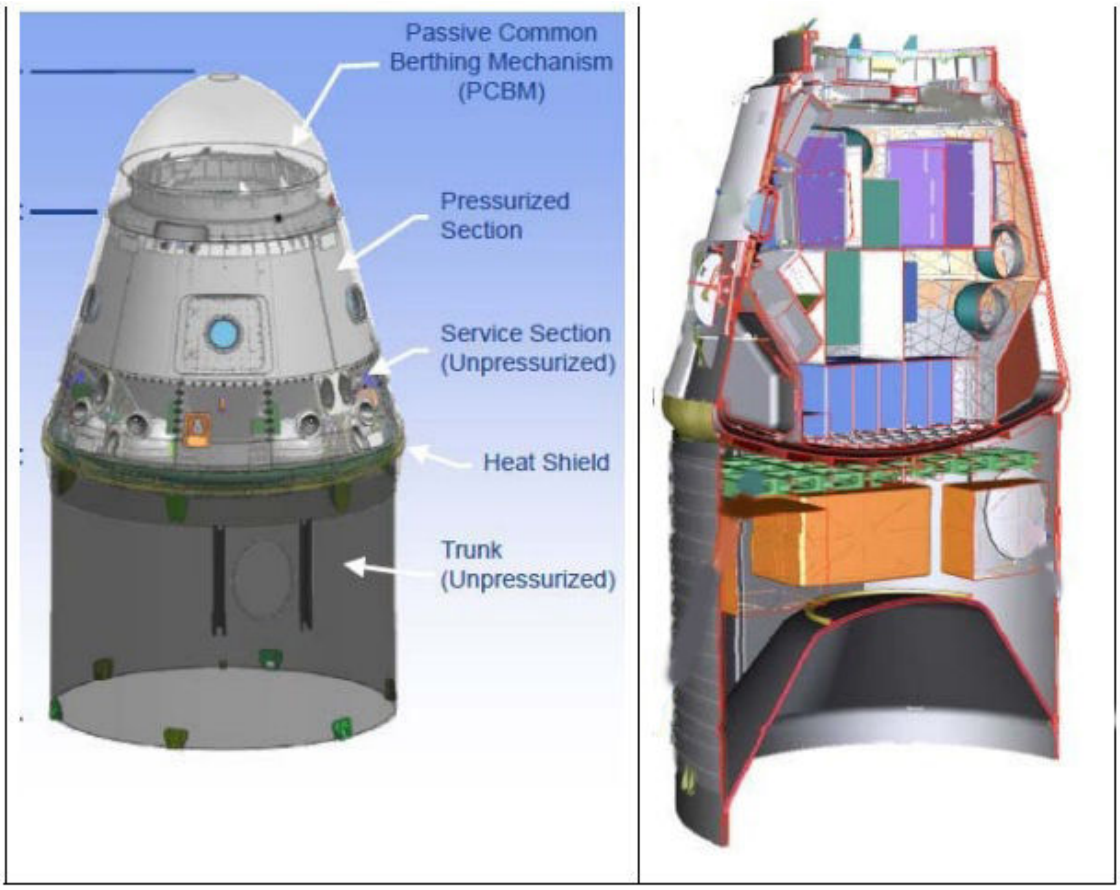

Figure 3.7: General configuration of SpaceX Dragon.

Installation of the payloads from the vehicles is performed by the robotic arm Canadarm-2 which can be operated by the crew or from ground.

3.2 ACES payload and requirements

The ACES payload (shown on Figure 3.8) has a volume of about $1m^3$, a total mass of 230 kg and a power consumption of 450 W (11). It includes the hydrogen maser SHM, the cold cesium clock PHARAO, a GPS/GALILEO receiver, a two way time transfer in the S and Ku band MWL and a two way time transfer in the optical band (500nm) ELT. The FCDP measures the phase/frequency difference between PHARAO and SHM and distributes the reference signal to the transfer links. XPLC is the payload computer.

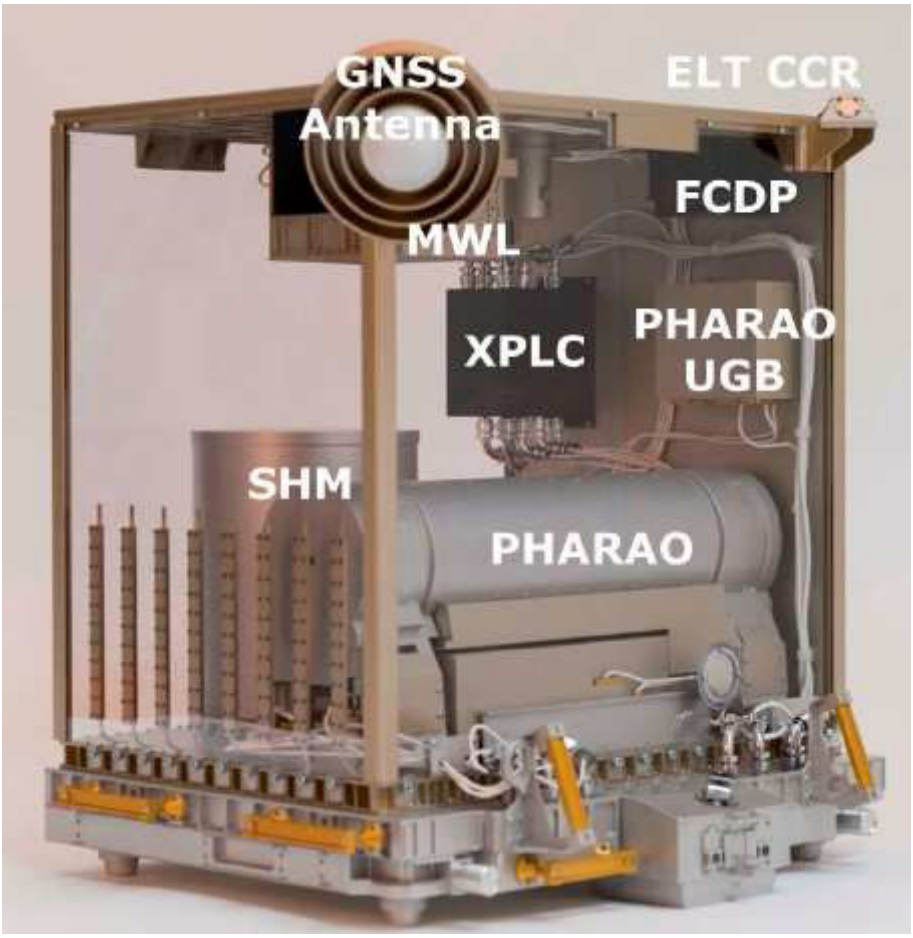

Figure 3.8: The ACES payload: main parts of ACES are the atomic clocks PHARAO, SHM and the MWL used for signal transfer.

3.2.1 SHM

SHM (Space Hydrogen Maser) (54) is being developed in Switzerland by Spectratime. It is an atomic clock based on the 1,420,405,752 Hz transition between two ground state hyperfine levels in hydrogen. An atomic beam of dissociated H2 molecules is created and directed towards a storage bulb (teflonized quartz) placed inside a microwave cavity whose resonant frequency is tuned on the hydrogen atomic resonance. By using state selection magnets in the entry, only the atoms in m = 0 Zeeman sublevel are selected. In the storage bulb some atoms spontaneously decay to the lower level emitting microwave radiation which simulates other atoms to do the same. The microwave cavity around the bulb stores the photons and amplifies the emission on every subsequent atom pass thus creating maser action. The generated energy is very low, but is detected by an antenna, converted into electrical energy and amplified. A quartz oscillator is phase locked on this signal to synthesize a 100 MHz signal which can be tuned through a DDS.

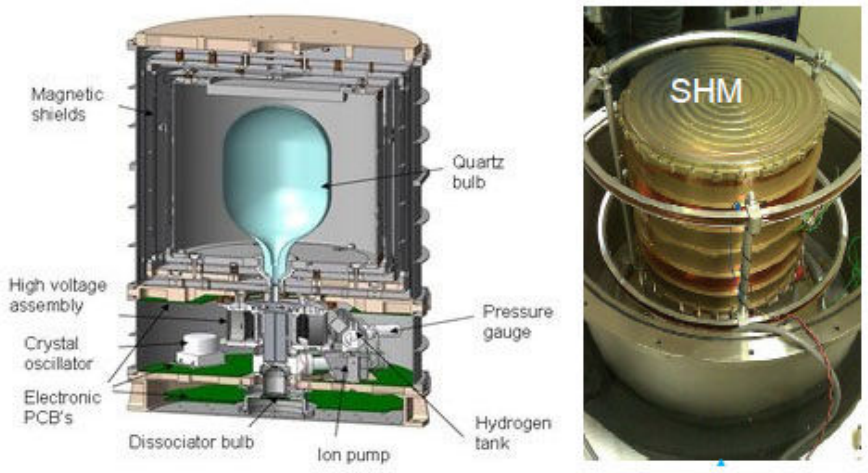

Figure 3.9: Schematics and a photo of the SHM.

Compared to the first maser used for space application in the GPA (Gravity Probe A) experiment in 1976 weighing 200 kg (55), SHM is much lighter (at 38 kg) providing high reliability, simplicity, good short and medium stability and improving on the performance of existing GALILEO passive masers by at least one order of magnitude. Due to the low weight requirement, the number of thermal shields has been reduced and

the Automatic Cavity Tuning (ACT) system has been designed to partially compensate for the effect of thermal drifts on cavity resonance which degrade SHM stability at longer integration time. The specifications for the frequency instability as a function of time for the SHM is:

$$\sigma^{SHM}(\tau = 1s) = 1.5 \times 10^{-13}$$
$$\sigma^{SHM}(\tau = 10s) = 2.1 \times 10^{-14}$$
$$\sigma^{SHM}(\tau = 100s) = 5.1 \times 10^{-15}$$
$$\sigma^{SHM}(\tau = 1000s) = 2.1 \times 10^{-15}$$
$$\sigma^{SHM}(\tau = 10000s) = 1.5 \times 10^{-15}$$

3.2.2 PHARAO

PHARAO (Projet d'Horloge Atomique par Refroidissement d'Atomes en Orbit) clock, which is being developed by the French space agency CNES, is the first Primary Frequency Standard (PFS) specially designed for operation in space. A PFS is a cesium atomic clock which realizes the unit of time, the second, with high accuracy. PFS operation is based on the measurements of the hyperfine transition of cold cesium atoms at the frequency 9,192,631,770 Hz. Its operation is similar to ground based atomic fountains but optimized for microgravity operation. Main components of PHARAO are the cesium tube, the laser source, the microwave source and the computer.

3.2.2.1 Operation

Cesium atoms are captured and cooled by laser beams to form an optical molasses (38). The atomic cloud is launched using the same laser beams. The atoms are selected in a pure hyperfine state before they interact with a 9.2 GHz field injected in the Ramsey cavity. At the end, the atomic population in each hyperfine state is measured to deduce the transition probability.

In nominal operation the PHARAO oscillator is phase locked on the 100 MHz signal of the SHM and synthesizes the 9.2 GHz field. Consequently, the PHARAO measures the frequency difference between the hyperfine resonance and SHM. The difference is used to lock the SHM frequency (through its DDS).

The advantage of microgravity is that the launch velocity of the atoms can be varied by two orders of magnitude to study and optimize the clock performances. A drawback

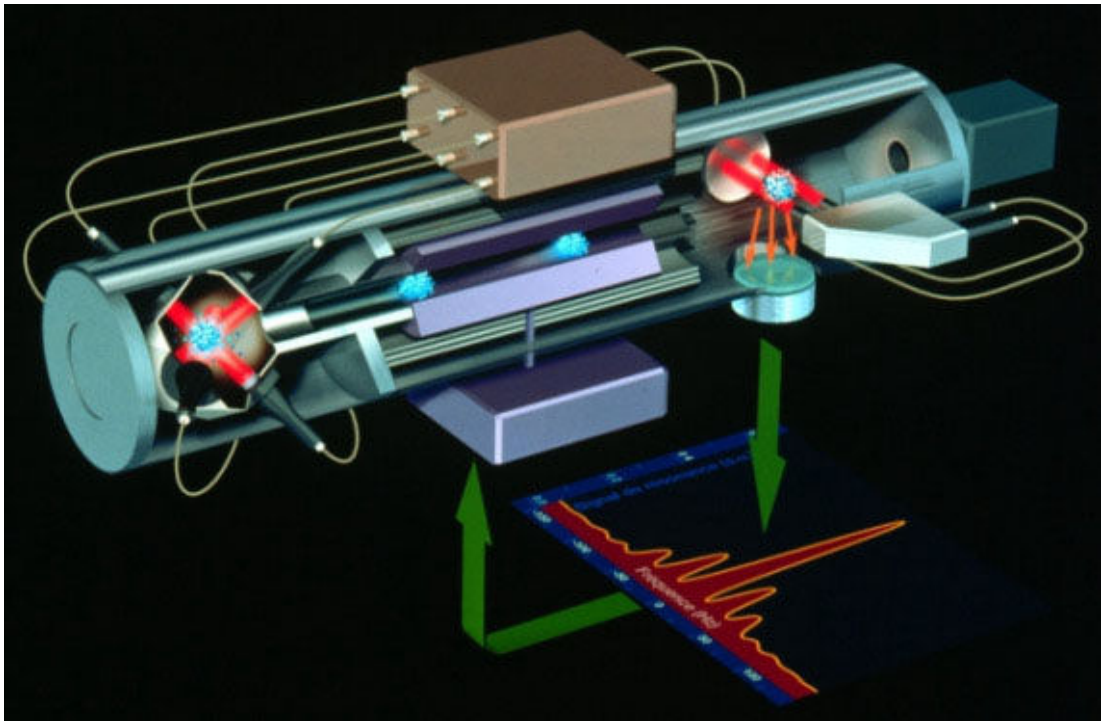

Figure 3.10: Illustration of PHARAO and its operation. Details will be explained later.

is that the Ramsey interaction symmetry is lost due to the existence of two different interaction zones.

Expected performances of PHARAO are fractional instability in Allan deviation below the $10^{-13} \times \tau^{-1/2}$ level (where τ is integration time in seconds and $1s \leq \tau \leq 10$ day) and accuracy better than 3×10^{-16} (11).

3.2.3 Signal merging and data handling

Telecommand, telemetry and data handling for all ACES instruments and short and long-term servo loop is ensured by the eXternal PayLoad Computer (XPLC), developed by ASTRIUM under ESA responsibility.

ACES will operate a phase locked loop which will stabilize the medium term stability of the PHARAO local oscillator on the clock signal generated by SHM which has a better medium term stability (Figure 3.11). Data corrections are sent every 250 ms. Short, medium and long term stability are defined on time intervals of 0.0001s to 1s, 1s to 1000s and 1000s to ∞, respectively. In order to compare the 100 MHz signals of SHM

and PHARAO the Frequency Comparison and Distribution Package (FCDP) is used. It was developed by ASTRIUM and TimeTech under ESA responsibility. FCDP is the central node of the ACES signal management also responsible for signal distribution to the time and transfer link.

Instability of the hydrogen maser for $\tau > 3000s$ will be measured and corrected by a second servo loop. XPLC receives the PHARAO measurements and sends the correction to SHM at a rate of several hundreds seconds. Resulting fluctuations of the ACES timescale based on the SHM signal are expected to be around 10 ps per day.

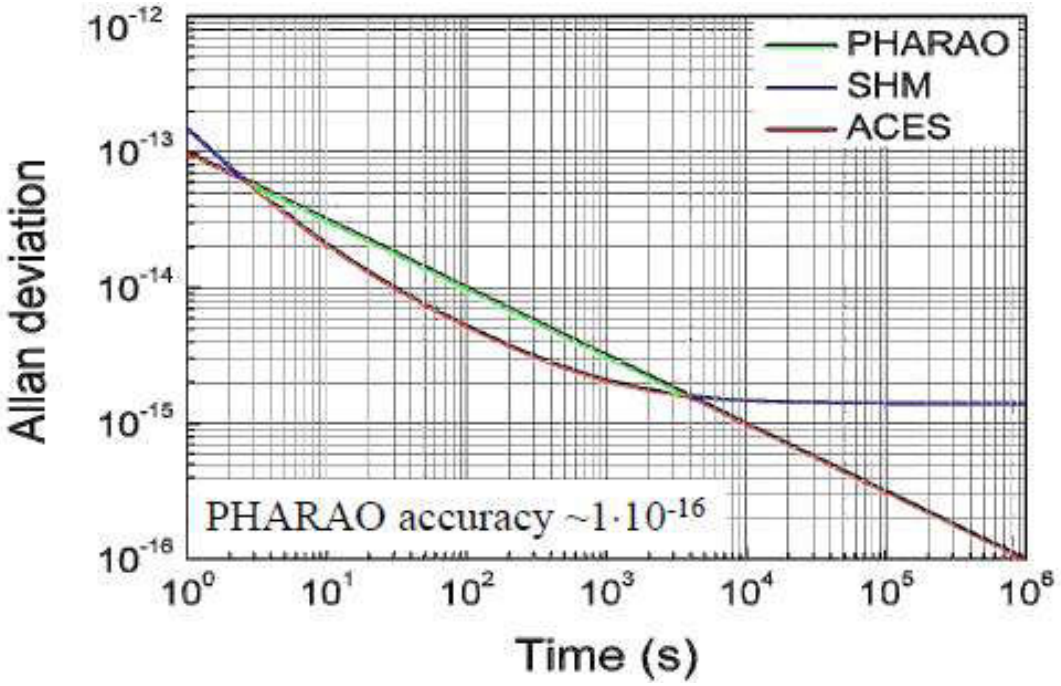

Figure 3.11: Stability of the PHARAO, SHM and final ACES signal: the ACES signal combine short and medium term stability of SHM with long term stability of PHARAO

3.2.4 Operation modes

PHARAO modes (56) define the data exchange configuration with ACES (Technological and Operational mode) and the physical configuration states (OFF, Stay Alive, Low Power, Configuration, Demagnetisation).

The **Technological mode** is used by PHARAO to prepare and test its sub-assemblies. During **Operational mode** PHARAO provides data based on ACES input and ACES

PHARAO data management. The 4 Operational modes are autonomous, evaluation, nominal and back up.

During the **autonomous mode** all functions are operating and the atomic cycle is active. The frequency corrections are directly applied to the 100 MHz PHARAO oscillator. This mode is used in case of SHM failure and during the initial optimization. During the **evaluation mode** the atomic cycle is active with all the functions implemented. Internal 9.2 GHz is the frequency locked on the atomic resonance and the atomic resonance frequencies for different clock parameters are compared. This mode is used to evaluate the systematic effects of PHARAO. The **back up mode** is used as a degraded mode in case of the PHARAO 100 MHz signal failure or for testing. PHARAO directly uses the 100 MHz maser signal to synthesize the 9.2 GHz (or another signal during ground testing). In the **nominal mode** the 100 MHz PHARAO signal is phase locked on the 100 MHz SHM signal. The frequency difference between atoms and SHM is used to lock SHM frequency on long term. This is the main operational mode with the best performances.

Other modes are the **Off mode** (PHARAO functions are not powered), **Stay Alive mode** (only the ion pump is powered), **Low Power mode** (provided power is reduced in case of ISS power reductions or in case of PHARAO software anomalies), **Configuration mode** (PHARAO subsystems and initializations are prepared) and **Demagnetization mode** (used to perform cesium tube demagnetization).

3.2.5 Time and frequency transfer: MWL and ELT

The implemented microwave link MWL (57), developed by ASTRIUM, Kayser-Threde and TimeTech, is one of the key elements of ACES surpassing the performances of the currently used transfer links (TWSTFT and GPS) by one to two orders of magnitude. It is a two-way system with two different frequencies that allows both space to ground and ground to ground clock comparisons. It has 4 channels allowing 4 simultaneous ground users. MWL has a high carrier upload and download frequencies (13.5 and 14.7 GHz, respectively). Another frequency in the downlink S-band (2.2 GHz) is used to correct the ionosphere time delay by measuring Total Electron Content (TEC). A code phase measurement removes the phase ambiguity between separated ground space clock comparisons.

To evaluate instrumental errors, ground MWL stations will have electronics similar to the on-board MWL.

Medium term stability after $\approx 300s$ is driven by the noise performance of the DLL (Delay-Locked Loop) boards, while the long term stability is provided by continuous calibration by a built-in test-loop translator.

Figure 3.12: MWL electronics, antenna and the ground station.

ACES will also accommodate a GALILEO/GLONASS/GPS receiver as part of the payload directly connected to the ACES signal. It will provide orbit determination and payload positioning information.

Comparison of ground clocks is possible using the common view and the non-common view technique. Common view technique is used when both clocks are geographically close enough to be in view of ACES. Two channels of the MWL are used simultaneously. By comparing two clocks, common-mode noise from the space clock is rejected and a direct comparison between ground clocks provided. The instability is only due to the noise of the time and frequency link. Due to low orbit height of the ISS, this technique can be utilized for comparing clocks over distances within a continent

and for periods of short duration ($\sim$ 300-400 s) for 3-5 comparisons per day on average. Example of the ISS number of passes over Paris is given on Figure 3.13.

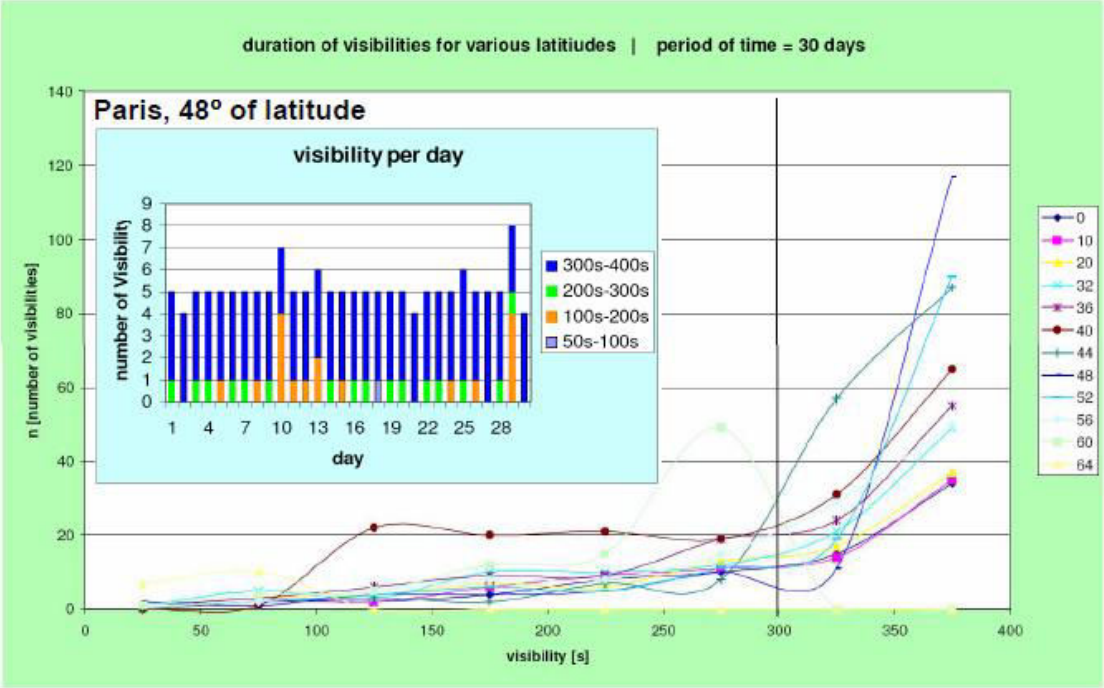

Figure 3.13: Number of passes of the ISS as a function of visibility time for different latitudes of ground stations performed over 30 days. Average pass over has a length of 300-400 seconds. Inset represents ISS pass overs for ground station at Paris over the same time interval.

Medium term time instability between on-board and a ground clock (including clock noise and MWL noise contribution) is expected to reach $\sqrt{2} \times 0.3$ps for a typical ISS pass corresponding to a frequency resolution of $\sigma_y(\tau = 300s) \leq 1.4 \times 10^{-15}$. With longer integration time, the uncertainty decreases and reaches a level of 10^{-17} in relative frequency or 7 ps after one day of integration time, almost two orders of magnitude below the GPS Carrier Phase and TWSTFT (58).

Non-common view technique is used for larger intercontinental distances between ground clocks when they are not in optical visibility with the space station at the same time. First ground clock is compared to the ACES scale followed by dead time needed for the ISS to be in visibility of the second clock when the next comparison is made. The reliability of the comparison depends on the total error created by the space clock

which adds up during dead time and the link noise.

Currently, the plan is to have MWL ground stations in the United States (JPL and NIST), Europe (SYRTE and PTB), Japan (NICT) and Australia (UWA) as seen on Figure 3.14. Additionaly, two transportable units will be available. One transportable MWL terminal with clock will be used to perform calibration and establish zero baseline and the other is to be shared among institutions in Europe.

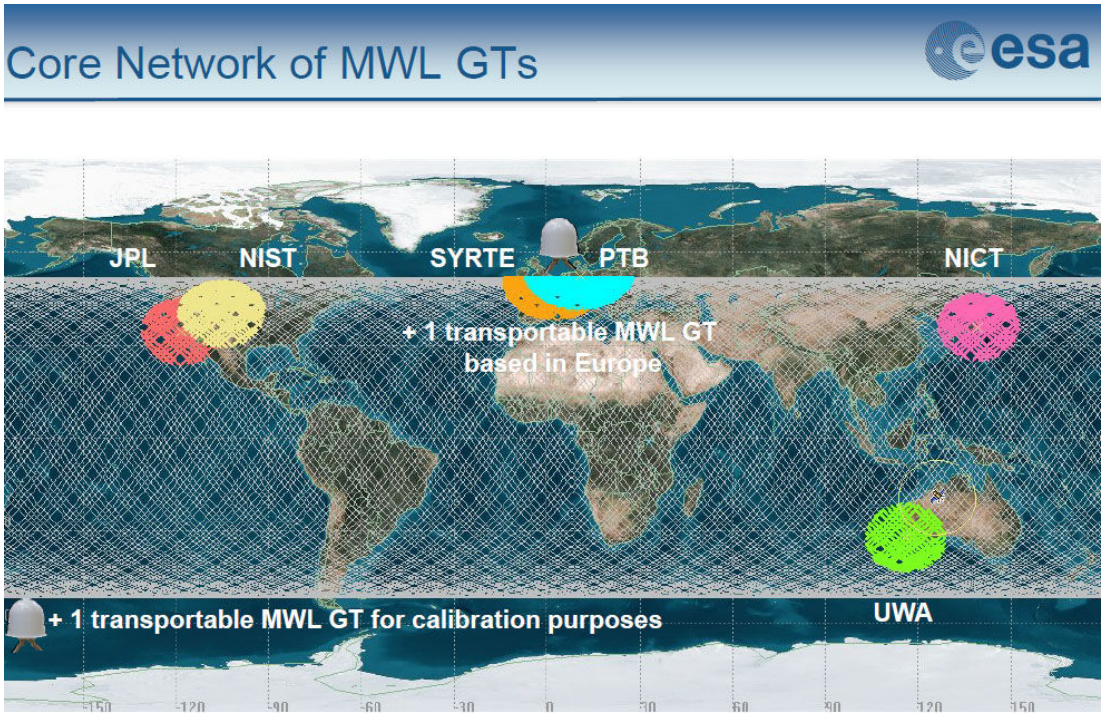

Figure 3.14: Core network of MWL ground stations: currently planned distribution of ACES MWL ground stations.

ACES will also use European Laser Timing (ELT) (59), a second transfer link, which will allow for time transfer, clock comparison and ranging in the optical domain. ELT is being developed by the Czech Space Research Center. Ranging experiments will be performed by firing light pulses towards ACES from laser ranging ground station. These pulses will be detected by the ELT Single-Photon Avalanche Diode (SPAD), time tagged in the ACES time scale and redirected by the Corner Cube Retro-reflector (CCR) to ground thus providing ranging information. An orbit prediction of the ELT on-board antenna with an uncertainty of 300 m is necessary for night time ELT operation, while 15 m of uncertainty is necessary for day time operation (because of SNR degradation

due to stray light). Space to ground comparison via ELT will have a time stability, expressed in time deviation, better than:

$$\sigma(\tau = 100s) = 6ps$$
$$\sigma(\tau = 300s) = 4ps$$
$$\sigma(\tau = 10^3 s) = 4ps$$
$$\sigma(\tau = 10^4 s) = 4ps$$
$$\sigma(\tau = 10^5 s) = 7ps$$
$$\sigma(\tau = 10^6 s) = 7ps$$

Using the common view technique the expected time stability is better than 6 ps for 300 s of integration time during one ISS pass. The laser link will demonstrate a time accuracy of 50 ps (25 ps as target) for distributing the ACES signal to ground users and ground clock synchronization.

For a time deviation comparison of the signal provided by ACES and the MWL and ELT links see Figure 3.15.

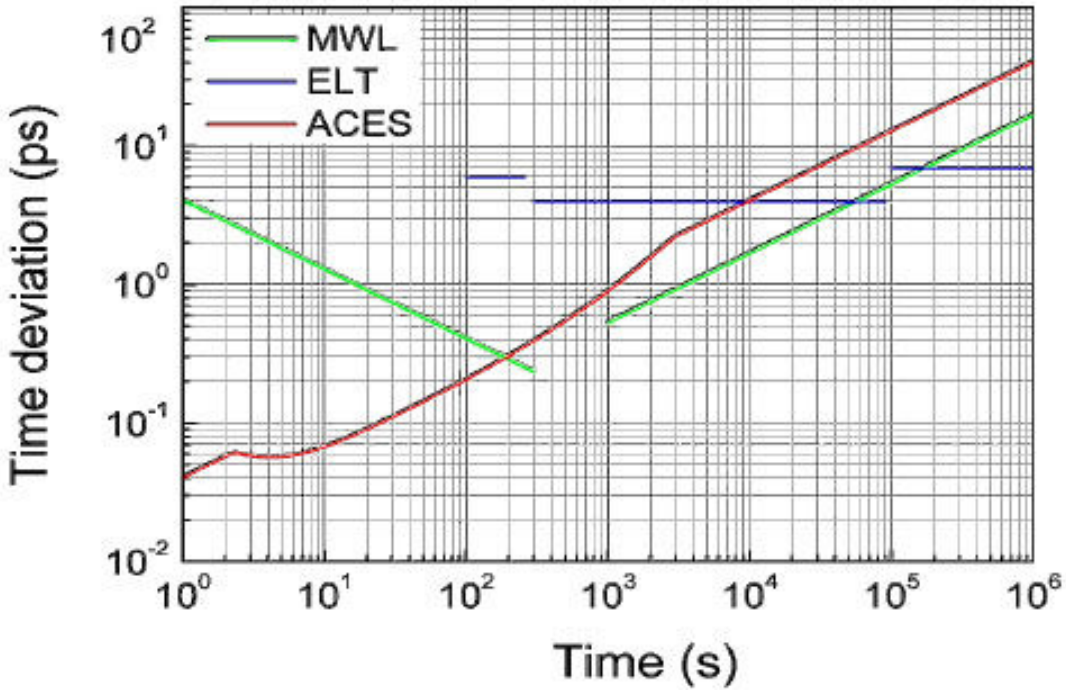

Figure 3.15: Time deviation comparison of the ACES output signal and time and transfer links.

3.3 Scientific objectives

3.3.1 Fundamental physics

One of the primary objectives of the ACES mission are three fundamental physics experiments which rely on comparisons between space and ground clocks. The high accuracy ACES clock signal will put the General Relativity, Special relativity and Standard Model Extension through a stringent test. See Figure 3.16 fo a summary.

ACES Mission Objectives	ACES performances	Scientific background and recent results
Fundamental physics tests		
Measurement of the gravitational red shift	Absolute measurement of the gravitational red-shift at an uncertainty level $< 50 \cdot 10^{-6}$ after 300 s and $< 2 \cdot 10^{-6}$ after 10 days of integration time.	Space-to-ground clock comparison at the 10^{-16} level, will yield a factor 35 improvement on previous measurements (GPA experiment).
Search for time drifts of fundamental constants	Time variations of the fine structure constant α at a precision level of $\alpha^{-1} \cdot d\alpha / dt < 1 \cdot 10^{-17}$ year $^{-1}$ down to $3 \cdot 10^{-18}$ year $^{-1}$ in case of a mission duration of 3 years	Optical clocks progress will allow clock-to-clock comparisons below the 10^{-17} level. Crossed comparisons of clocks based on different atomic elements will impose strong constraints on the time drifts of α, m_e / Λ_{QCD}, and m_u / Λ_{QCD}.
Search for violations of special relativity	Search for anisotropies of the speed of light at the level $\delta c / c < 10^{-10}$.	ACES results will improve present limits on the RMS parameter α based on fast ions spectroscopy and GPS satellites by one and two orders of magnitudes respectively.

Figure 3.16: Fundamental physics ACES mission objectives

3.3.1.1 Gravitational red-shift

A space based atomic clock frequency compared to a ground-based atomic clock frequency can be used to measure the gravitational red-shift (60, 61). As stated by General Relativity, a frequency shift of emitted radiation occurs when a source is placed in a gravitational field. The frequency appears reduced, or redshifted, when the observer is positioned in a weaker gravitational field. This is equivalent to a Doppler shift of an object placed in an accelerating frame. Therefore, the frequency comparison of identical clocks placed in different gravitational fields gives a frequency shift of (for example

(62)):

$$\frac{\Delta f}{f} = \frac{\Delta U}{c^2} \tag{3.1}$$

where f is the radiation frequency, U is the Newtonian potential (by convention $U \geq 0$) and $\delta U = U_S - U_O$ is the difference in gravitational potential between source S and observer O. At 400 km the gravitational frequency shift is 4.6×10^{-11}

Using the Earth-centered inertial coordinate frame Geocentric Celestial Reference System (GCRS), the shift in frequency between ground and space is (63):

$$\frac{d\tau^g}{dt} - \frac{d\tau^s}{dt} = \frac{1}{c^2}[U(t, \vec{x_s}) - U(t, \vec{x_g}) + \frac{v_s^2}{2} - \frac{v_g^2}{2}] + O(\frac{1}{c^4}) \tag{3.2}$$

where τ^g and τ^s are proper times on ground and in space, $U(t, \vec{x_s})$ and $U(t, \vec{x_g})$ are the Newtonian potentials of Earth at position of the space and ground clock, respectively. c is velocity of light and $\vec{v_s}$ and $\vec{v_g}$ are velocities of the space clock and ground clock relative to Earth, respectively. Term $\frac{U(t,\vec{x_s}) - U(t,\vec{x_g}}{c^2}$ is the frequency shift due to a difference in Earth gravitational potential (effect of other bodies is negligible at this level of measurement). Because of the ISS orbit having a varying gravitational field, the redshift will be modulated by about 10%. Term $\frac{1}{c^2}(\frac{v_s^2}{2} - \frac{v_g^2}{2})$ is the frequency shift due to the second order Doppler effect between two moving clocks. Given the velocity of PHARAO (7 km/s) it amounts to about -3.3×10^{-10}.

Measurement of the gravitational redshift was already performed with an atomic clock in orbit on the Gravity Probe A. In 1976 Smithsonian Astrophysical Observatory and NASA launched a rocket containing a hydrogen maser to a height of 10,000km. During two hours of free fall, measurements from the maser in a time varying gravitational field were compared to a ground clock. The relative accuracy reached was 70×10^{-6}. Using the more precise PHARAO clock with an accuracy objective of 10^{-16} and the MWL, ACES will provide an improved measurement reaching an accuracy of 3×10^{-6} when comparing to a ground clock of the same accuracy and 2×10^{-6} when comparing to a clock of 10^{-17} accuracy.

3.3.1.2 Drift of fine structure constant

In General Relativity physical constants are universal and constant in time. However, several new theories (64) allow for their variation, but cannot agree at which level

(65, 66). ACES will give the validity domain of the general relativity.

Transitional frequency in atoms is related to the three dimensionless constants derived from physical constants: the fine structure constant $\alpha = \frac{e^2}{4\pi\varepsilon_0\hbar c} = 1/137.0359895(61)$ characterizing the strength of the electromagnetic interaction, m_q/Λ_{QCD} and m_e/Λ_{QCD} which depend on quark mass m_q and electron mass m_e and the QCD mass scale Λ_{QCD} (67). A possible drift of the these constants could be determined by comparing hyperfine transitions of atomic clocks using various atoms as a function of time (for example (68)) and would imply a variation of the other two constants.

A change in the transition frequency between two clocks can be attributed to a fundamental constant value change if the value is larger than the accuracy budget of both clocks. However, the relative rate of change between clocks can be calculated by atomic physics if some fundamental constant varies. For a convincing test, multiple clock comparison is necessary.

ACES will provide a possibility to compare microwave clocks operating on hyperfine transitions (cesium: SYRTE (6), NIST (4), NRLM (69), LTF (Bern) (70), PTB (7), NPL (5), NIL (71), INRIM (72), etc, rubidium: SYRTE (6), NPL (73)) and optical clocks operating on electronic transitions (mercury ion: NIST (74), JPL (75), ytterbium: INRIM (76) and NIST (46), ytterbium ion: PTB (77), CSIRO (78), NPL (79) aluminium ion: NIST (80), calcium ion: University of Innsbruck (81), strontium: Tokyo University (82), JILA (83), NIST, SYRTE (84), PTB (85), strontium ion: NRC (86), NPL (87)).

Four different atomic transitions are sufficient to constrain three independent frequency ratios and establish limits on time variation of the three constants. Comparison of more than four atomic clocks will allow for a comprehensive unambiguous identification of variation and improve the confidence of the results. With clocks of 10^{-16} accuracy on both ends, the variation uncertainty will be 10^{-16} after one year of integration time and $3 - 5 \times 10^{-17}$ after three years of integration time. With ground clocks of 10^{-17} accuracy, the constraint resolution would reach 10^{-17} after one year of measurements and 3×10^{-18} after three years.

3.3.1.3 Anisotropy of light

According to Special Relativity, laws of physics are unchanged under Lorentz transformations. Lorentz invariance composes of rotational invariance and boost invari-

ance (changes in the velocity of a reference frame). General Relativity incorporates it through the Equivalence Principle which states that the outcome of an experiment in a freely falling laboratory does not depend on its velocity and location. Due to gravity Lorentz covarience can only be applied locally in an infinitesimally small region of space-time. In case of its violation the laws of physics would be different for a moving observer compared to a stationary one. This is compatible with the recent Kostelecky's Standard Model Extension (SME) (88) which also permits breaking of CPT symmetry.

To test Local Lorentz Invariance (LLI), experiments with rotating cryogenic sapphire oscillators (89), pulsars (90) and other (91, 92) have been performed. ACES will exchange microwave signals in both directions. By measuring the timing with the clocks and obtaining δc as a deviation of speed of light c for one direction and comparing it to the other, LLI can be validated to an accuracy depending on the medium term stability of the ACES signal (therefore the key is the stability of the SHM), medium term stability of the used ground clocks and the ACES MWL instability over one passage of light during an ISS pass.

By including corrections due to path asymmetries and atmospheric delays Δ_m, constant offset correction due to dyssynchrony of the clocks Δ_s and by knowing Θ angle between link and the preferred direction and half the return travel time T, the difference of travel times is:

$$T_{up} - T_{down} = \Delta_s + \Delta_m + 2\frac{\delta c}{c} T cos\Theta \tag{3.3}$$

Expected sensitivity that will be reached for measuring $\delta c/c$ is 6×10^{-11}. This is almost a two order of magnitude improvement over the previous most accurate test performed in 1997 using GPS satellites and ground hydrogen masers.

3.3.2 Geodesic application

Survey grade GNSS equipment (93) which includes post processing (94) ionospheric correction has horizontal and vertical position accuracy of 1 cm and 2 cm, respectively. However, this does not give information on the local gravity potential. Basis for classical geodetic positioning is using the gravity potential difference in respect to the surface of a geoid. Geoid is a flattened irregular representation of Earth whose surface height is determined from mean sea level observations at tide gauge stations. However, as satellite missions GRACE (95) and GOCE (96) show, mean sea level may differ by several meters.

In relativistic geodesy, equipotential surface is where atomic clocks have the same frequency. Therefore, the difference is measured by performing clock to clock comparisons and measuring the frequency shift due to a different Newtonian potential. The relationship between clock frequencies and potentials f_A, b_B, U_A and U_B of the two clocks is:

$$\frac{f_B}{f_A} = 1 + \frac{U_A - U_B}{c^2}. \tag{3.4}$$

With the ACES ground clock to ground clock comparison over intercontinental distances having a frequency resolution in the 10^{-17} range after one week of integration time and the geometrical GNSS system, it will be possible to establish a new global reference frame where geopotential differences can be resolved with an accuracy of 10 cm.

To validate the on board GNSS system and calibrate the MWL, ELT measurements containing ranging information between the on-board receiver and on-ground reference point will be used. Besides establishing a baseline for MWL accuracy, measurements of data propagation in the optical and microwave domain will give valuable atmospheric signal propagation information and possibility of atmospheric mapping functions at three different wavelengths. To determine azimuthal asymmetries tropospheric delays will be mapped at the ascending and descending pass.

GNSS receiver will ensure orbit determination for ACES, but also provide its signal to a wider community allowing for clock comparison over GNSS network. A time stability of 300 ps/day is expected by using only GPS measurements, and this can be

improved to 200 ps/day with some optimization. The GALILEO system will also be available for comparison.

It is expected the MWL and ELT will improve ground clock synchronization with an accuracy better than 100 ps.This will be of importance, for example, for different VLBI arrays observing same distant radio source simultaneously. Important part in data reduction is synchronization of H-masers at each observing station. Currently, clock offsets and drifts are estimated a posteriori by clock behavior models and the results are biased.

3.3.3 International Atomic Time contribution

International Atomic Time (or TAI from Temps atomique international) is a time scale built by the Bureau International des Poids et Mesures (BIPM) and created as a weighted average of over 300 ground atomic clocks over the world (Figure 3.17). With a high accuracy of 10^{-16} and well defined gravitational potential, PHARAO has a possibility to give a significantly weighted contribution during mission duration. TAI relies on ground clock comparisons using GPS satellites and TWSTFT links with 1 day fluctuations on the order of 10^{-15}, while ACES will allow worldwide clock comparison at an unprecedented level of 10^{-17}, further improving on the TAI.

With the development of optical clocks having better performances than their cesium counterparts a redefinition of the second is foreseen in the future. A global clock comparison system provided by ACES will help in this endeavor.

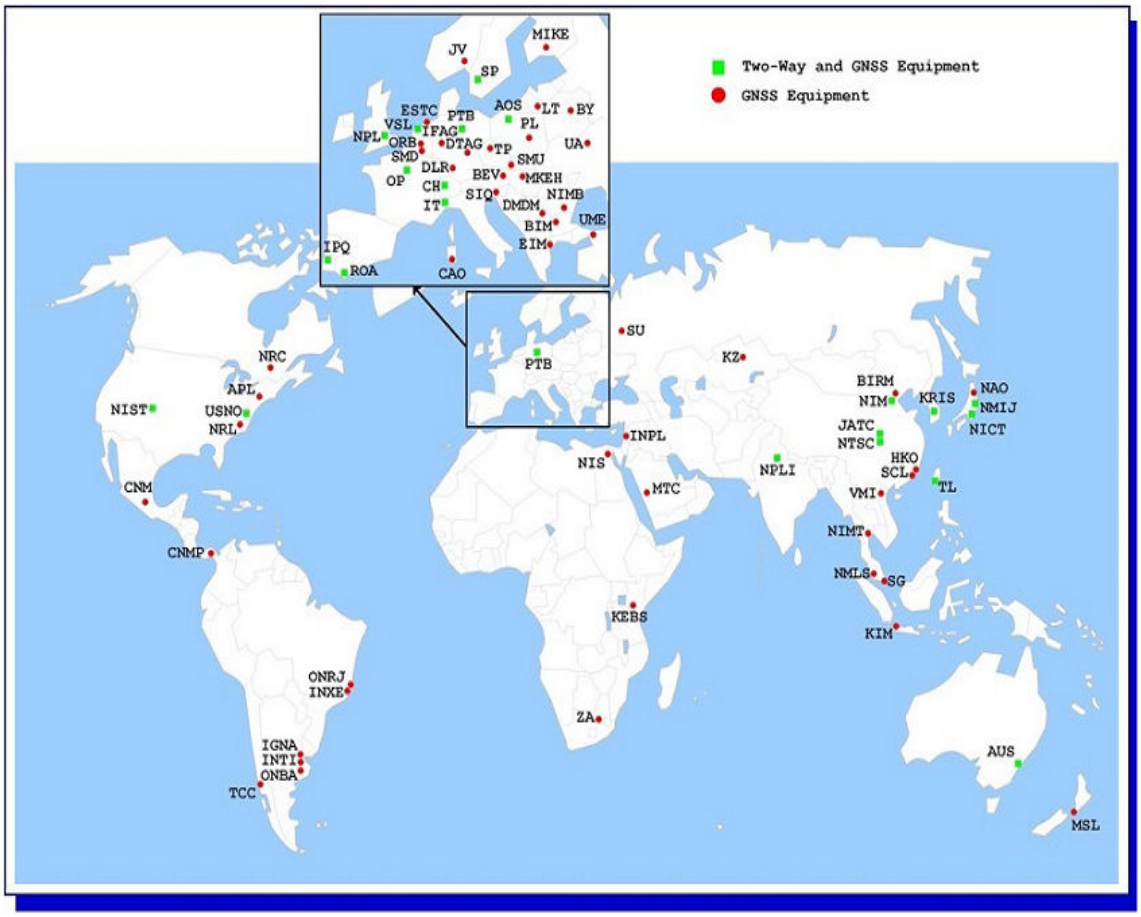

Figure 3.17: Laboratories contributing to TAI (as of April 2013).

4

PHARAO

PHARAO is a primary frequency standard designed for space operation that will perform fundamental physics tests.

The microgravity environment of ISS alows for fine variations of low atomic velocites. At long interaction times most of the systematic effect uncertainties are reduced. On the other hand, due to the thermal expansion, more atoms are lost and the frequency stability is impaired. An atomic velocity giving the best clock accuracy/stability will be found in orbit.

4.1 PHARAO architecture

PHARAO (10, 18, 56, 97) system is composed of five elements: the cesium tube, the laser source, the microwave source, the on-board computer (UGB) and the BEBA electronic unit. The instrument architecture can be seen on Figure 4.1 while a layout is shown on Figure 4.2.

The elements are accommodated inside a volume of 1059 mm $\times$ 336 mm $\times$ 464 mm. Cooling of the baseplate is performed by 4 heat pipes mounted on the wall opposite to where the UGB is installed. Figure 4.3 shows the mass, volume and power dissipation of the PHARAO components.

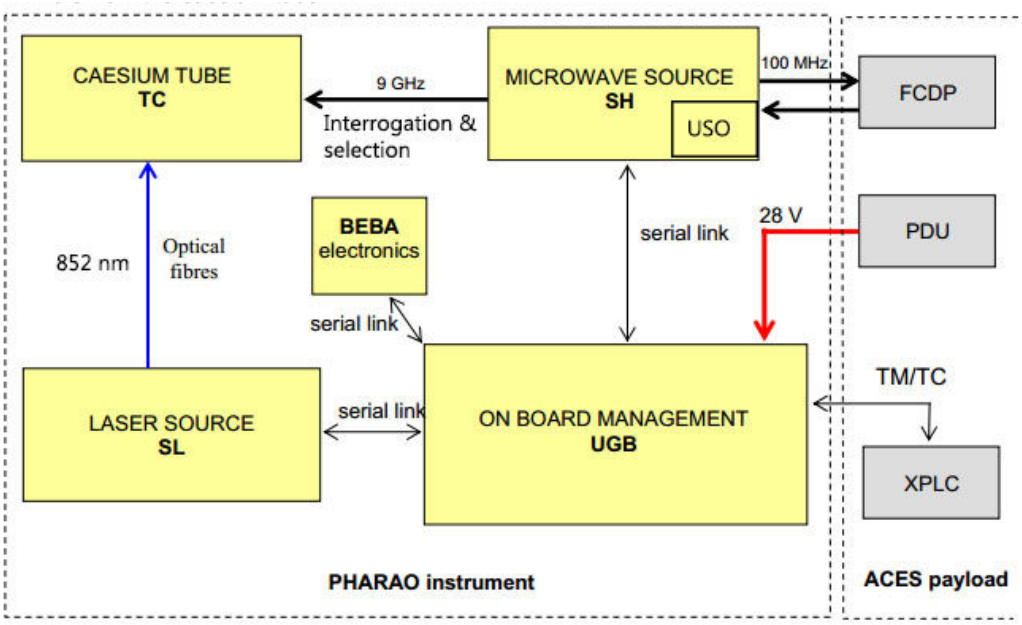

Figure 4.1: System arhitecture of PHARAO

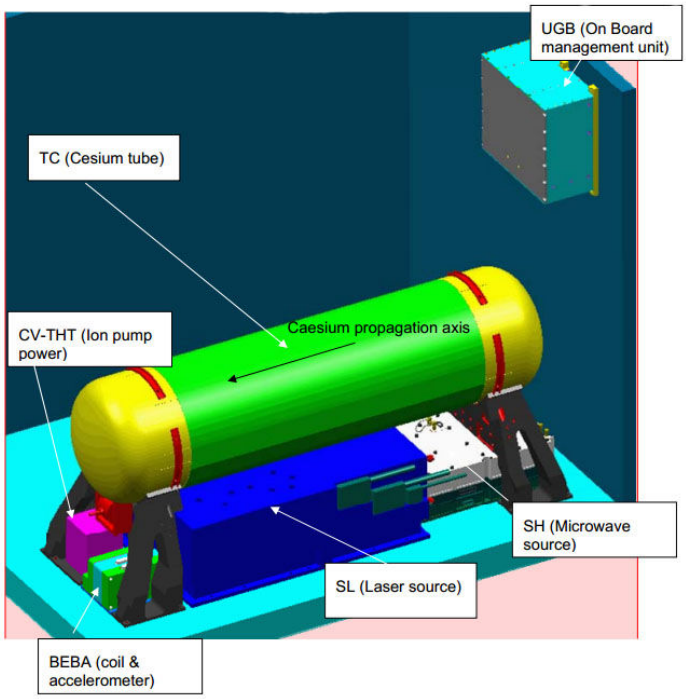

Figure 4.2: Components of PHARAO.

ITEM	MASS (Kg)	SIZE (L x l x h, mm)
Laser source (SL)	21.5	532 x 335 x 198
Caesium tube (TC) + CVTHT	44.8	1059 x 336 x 464
Microwave source (SH)	7	300 x 270 x 117
On board management unit (UGB)	6.3	245 x 240 x 120
BEBA	1.3	134 x 118 x 96
TOTAL (including harness, fixations and margin)	**92**	

ITEM	POWER DISSIPATION Typical (W)	POWER DISSIPATION Maximum (W)
Laser source (SL)	30	47.5
Caesium tube (TC)	5	5.5
Microwave source (SH)	21	26
On board management unit (UGB)	26	31
BEBA	3	4
Total	**85**	**114**

Figure 4.3: Mass, dimensions and power budget of the PHARAO instruments.

4.2 PHARAO development

Three different models of the clock have been constructed: the mechanical and thermal model (STM) to test the environments (vibrations 20g rms, temperature from -40°C to +60°C and +140°C for vacuum outgassing), the engineering model (EM) to test the operation and the performances, and the flight model (FM) which has the improvements deduced from the previous results.

Verification of robustness and evaluation of the temperature accuracy have been simulated and experimentally analyzed with the STM. The tests have demonstrated the robustness, but without sufficient margins. Although the vibration tests on the STM have been successful, the thermal tests have shown a sensitivity of the optical alignment with the temperature.

The engineering model was not submitted to environmental qualifications and more tolerance was given compared to specifications. Among all the optical performances

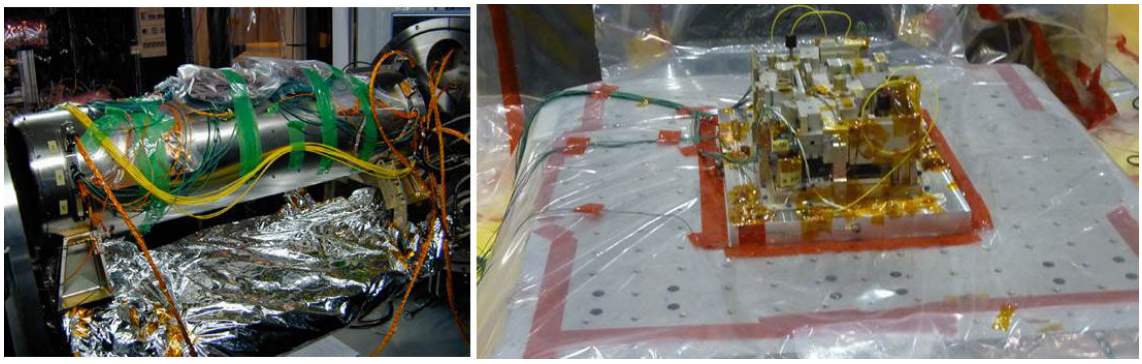

Figure 4.4: STM cesium tube and the laser source vibrational testing.

of the laser source, only two are not in agreement with our requirement: the power of each capture laser beam is low (5mW) and the laser spectra are widened by a too large modulation index used by the frequency servo loops.

The flight model is a full space qualified model which can operate in a temperature range of $+10°C$ to $+33°$C. Its vibration requirement levels are 30 g acceleration at 30 Hz and random vibrations having a RMS acceleration of about 10g.

Based on the experience gathered from the STM and the engineering model, various improvements have been made on the flight model. Mechanical structure and design improvements have been performed for the laser source and the cesium tube. As a result, the power of the laser source was increased to 13.5 mW/beam (a factor of about 3 improvement over the engineering model) and a better optical alignment stability was ensured. Cesium tube has a better robustness and temperature accuracy (70 mK). In order to improve the field homogeneity, magnetic shield design and the assembly process were modified. The material of the shields was changed from Magnifier alloy to Mumetal.

Figure 4.5: Flight model cesium tube with shields during vibrational testing (up) and the vacuum chamber (bottom).

4.3 Microwave source

The microwave source synthesizes two microwave field ultrastable signals of frequency 9 192 631 770 Hz for the two microwave cavities (preparation and interrogation). The microwave source also provides a 100 MHz signal for comparison with the on-board ACES SHM maser via the Frequency Comparator and Distributor Package (FCDP).

The PHARAO microwave source has low phase noise in order not to decrease the clock frequency stability and low phase transient effect (including parasitic spectral

lines). Also, the maximum electromagnetic leakage level has been minimized to a value less than -70 dB. Precautions were made (RF ring filters) to avoid the possibility of the field exiting the interrogation cavity.

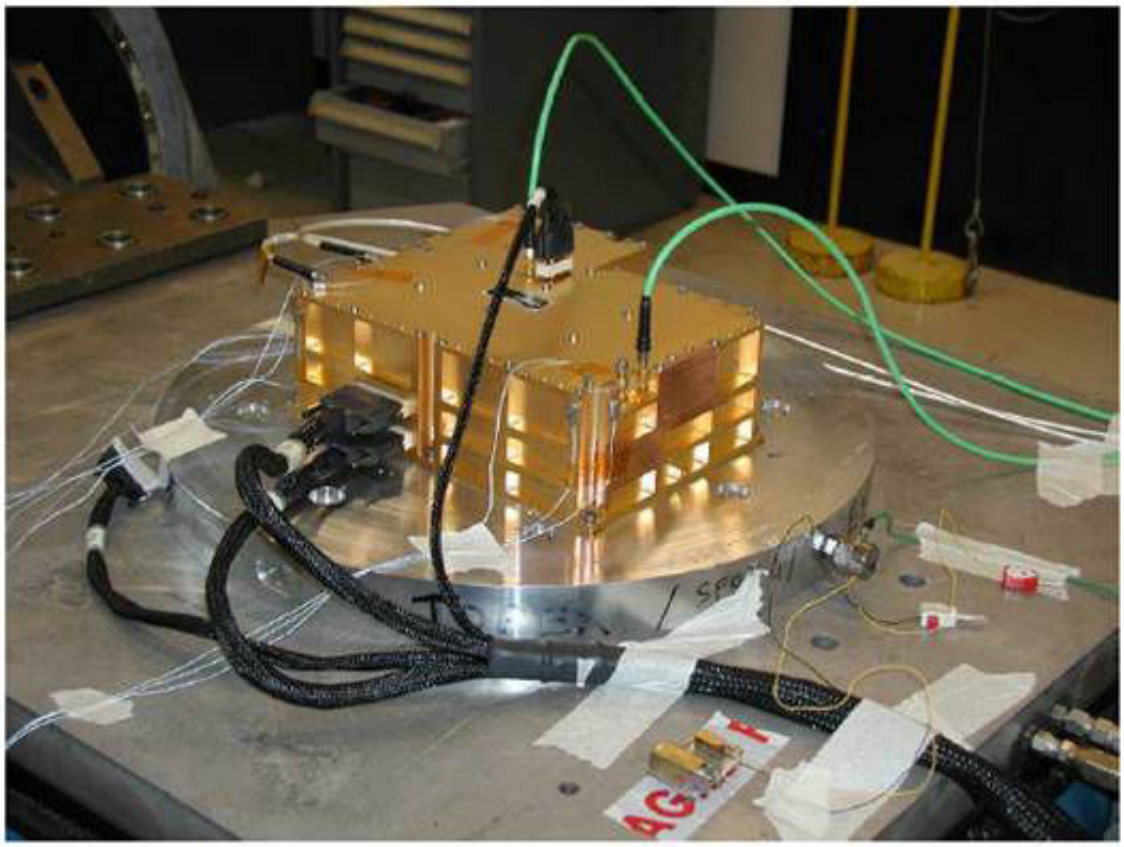

Figure 4.6: The flight model of the microwave source manufactured at THALES.

The microwave source has dimensions 270 mm × 300 mm × 100 mm which is a volume of 8.7 L. The weight is 7 kg and the average power consumption is 24.5 W. It can operate in the temperature range of $10 - 33.5°C$.

Manufacturing of the microwave source was contracted to Thales Airborne Systems and the development to flight model phase lasted 43 months. The spectral noise and purity of the engineering model were compatible with the expected performances. The EM has been tested with the SYRTE FO2 atomic fountain. The frequency stability was determined to be $7.2 \times 10^{-14} \times t^{-1/2}$.

A phase jump with an amplitude of $10\mu rd$ was measured. The is integrated by the maser servo loop and leads to a phase drift of the 9.2 GHz interrogation signal creating

a maximum relative frequency shift of 6×10^{-16} (depending on the loop parameters). Modifications have been made on the microwave synthesis for the flight model and the transient effect was reduced by a factor of 10. A phase transient effect example as measured on the flight model can be seen on Figure 4.7.

The other main difference from the EM is that the quartz oscillator on the FM is less sensitive to microvibrations.

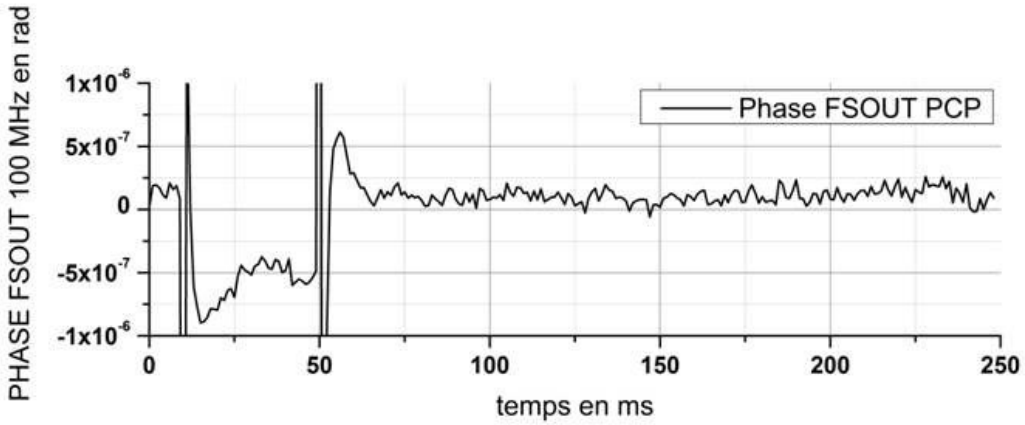

Figure 4.7: Example of a phase transient effect measurement on the flight model of the microwave source. The amplitude of the shift has been reduced by a factor of 10 compared to the engineering model.

4.3.1 Microwave synthesis chain

The initial 5 MHz (more precisely 4.999995 MHz) signal is generated by a quartz oscillator LSA (Low Sensitivity to Acceleration - G sensitivity of $1.76 \times 10^{-10}/g$) USO (Ultra Stable Oscillator) with a very low phase noise of -129 dBc/Hz at 1 Hz. The short term stability is $\sigma_y(\tau = 1s) = 7.7 \times 10^{-14}$ and $\sigma_y(\tau = 10s) = 8.4 \times 10^{-14}$. The USO quartz oscillator of the microwave source has its own regulation at a temperature of $60°C$ in order to decrease noise to the MW output signal. It has dimensions 80 mm $\times$ 130 mm $\times$ 85 mm, average power consumption of 2.2 W at a total weight of 1.2 kg.

The frequency is multiplied by a factor of 77 to phase lock the 385 MHz VCXO oscillator (Voltage Controlled Crystal Oscillator) on this signal. The USO has a low phase noise for frequencies $< 10\ Hz$ and VCXO for frequencies $> 10\ Hz$. The phase lock is performed to provide a low phase noise level at all frequencies.

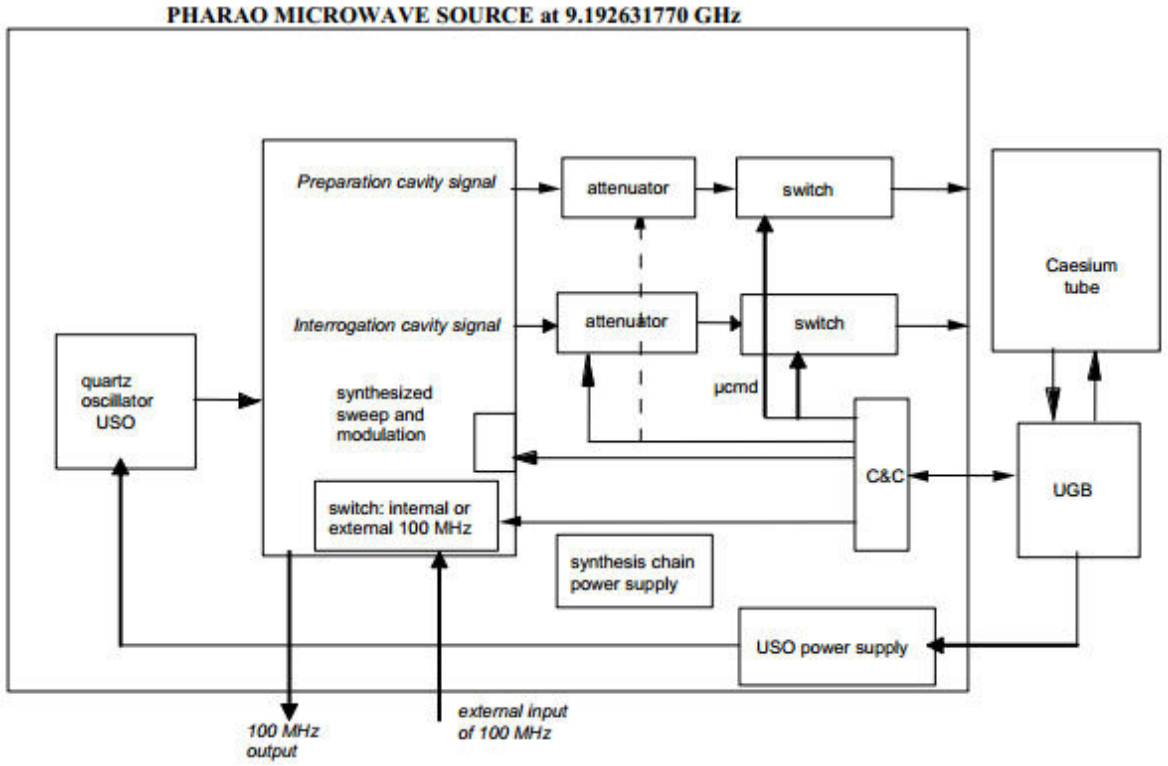

Figure 4.8: Microwave source operation diagram.

The signal frequency is then divided by a factor of 4 to get a frequency of 96 MHz. The multiplication and division of the frequency is done in order to reduce possible harmonics mixing. The signal is mixed with a signal produced by a 48 bit digital synthesizer DDS1 (Direct Digital Synthesizer) to generate a low noise and frequency adjustable 100 MHz signal (fine frequency adjustments by steps of $10^{-7}Hz$). A pseudo random frequency modulation is applied to the DDS1 to decorrelate harmonic lines into white noise. The 100MHz signal is split in two. One part is sent to the FCDP and is used to lock its frequency on the 100 MHz SHM maser signal. The other part is used to synthesize the 9.2 GHz signal (second stage).

In the second stage the 100 MHz signal is split into two (in backup operation this signal is provided by the SHM). One is frequency multiplied by a factor of 85 and again split into two 8.5 GHz separate signals. The other one is frequency multiplied by a factor of 7 and then mixed with a signal from another 48 bit DDS2. This DDS is used to modulate the microwave frequency and lock the signal on the atomic resonance

frequency during the evaluation of performance. The signal is next filtered from additional harmonics using a VCO oscillator (Voltage Controlled Oscillator) to produce two clean 692 MHz signals. They are passed through a 0.02 dB voltage adjustable attenuator with a dynamic range of 60 dB in order to control the microwave power.

Signals of frequency 8.5 GHz and 692 Mhz are mixed thus creating two 9.2 GHz signals intended for the preparation and interrogation phases of clock operation. The two signals pass through an on/off switch with a dynamic range of $80dB$. In nominal operation, only the preparation microwave signal is turned off cyclically, as the signal in the interrogation always stays on (to eliminate the phase transient effect).

Control of the two DDSs frequency, the attenuator values and attenuator switches is performed using 2 programmable integrated circuits FPGA (Field Programmable Gate Array). The DDS1 frequency is corrected periodically every 250 ms to lock the 100 MHz signal on the maser. The modulation and correction of the interrogation signal in the evaluation mode is applied on the DDS2 for every clock operation cycle.

Only DDS2 is used to control the frequency of the two microwave signals. At the beginning of the cycle the UGB (computer) sends two input values FP (preparation frequency) and FI (interrogation frequency). FP is directly applied to the DDS2 and FI is stored in memory. PCP is a micro command that triggers the preparation switch. When the falling edge of the signal is detected by FPGA, it sends FI value to the DDS2.

Two rigid coaxial cables with low thermal phase sensitivity connect the microwave output to the cesium tube cavities.

4.4 Laser source

The laser source includes an optical bench and the dedicated electronics. The laser source are placed in a Duralumin alloy box with dimensions 532 mm × 335 mm × 198 mm. The optical bench (Figure 4.12) has dimensions 400 × 330 mm and is supported by 4 dampers screwed on the laser source base plate. It is thermally regulated to maintain a temperature of $26 \pm 0.2°C$. The orbital thermal fluctuation at the base plate is $\pm 1.5°C$ while the environmental temperature during the mission duration can vary between 10 and 33 $°C$. The regulation is performed using a 10 sec loop based on 5 Peltier coolers and heaters placed around the optical bench. The electronics is placed on the baseplate. The electronic assembly contains 14 boards in order to control

the power supply, digital control board, laser control boards and the radio frequency synthesis board.

The laser source provides 14 laser signals which are combined to 10 laser beams for capture, cooling, launch, selection and detection of the atomic sample. The total mass of the system is 21.5 kg and the electrical consumption is, on average, 30 W.

Critical space qualification requirements are:

- storage temperature between -40 and +40 $\circ C$,
- random vibrations with a RMS acceleration of 12 g,
- vibration levels of 35 g acceleration at 30 Hz,
- air and vacuum operation.

4.4.1 Optical bench layout

The optical bench (the optical assembly diagram is given on Figure 4.11) is dense and has optical component placed on both sides of the bench. The main components are:

- 2 852 nm Extended Cavity Diode Lasers (ECDL) delivering the 2 main frequencies with frequency stabilization units,
- 2 backup Extended Cavity Diode Lasers (ECDL),
- 2 optically injected slave diode lasers (SL) amplifying the laser power,
- 2 backup optically injected slave diode lasers (SL),
- 4 magnetically shielded caesium cells: 2 for frequency stabilization of the ECDLs, 2 to verify that the Slave Lasers are injected,
- 6 photodiodes: to control the laser frequency through fluorescence and absorption in the cesium cells,
- 4 optical isolators (OI): to prevent optical feedback which would induce perturbations on the laser frequency,

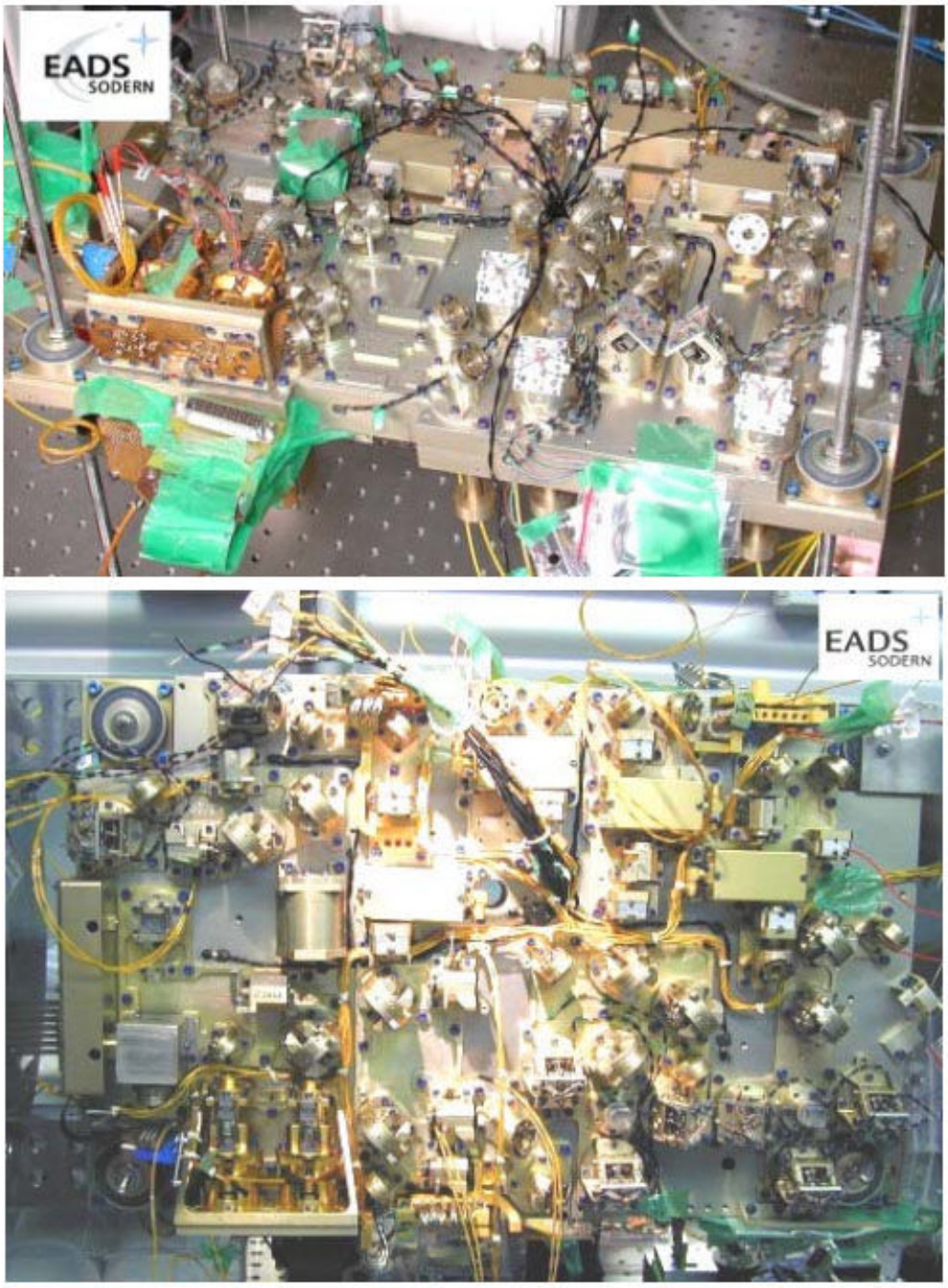

Figure 4.9: Photographs of the flight model laser source optical bench top view (up) and bottom view (down).

- 6 AOMs (acousto-optic modulators): 2 to control laser frequencies and 4 to control the laser powers,
- 7 step by step motors (mechanical shutters - MS) in order to switch the laser power off,
- 4 step by step motors to switch the laser backup,
- 10 polarisation maintained fibers (PM) to deliver all the beams to the different TC zones with the well defined polarization,
- 8 rotating mirror mechanisms to optimize laser beam coupling in the fiber. This allows to balance the power of the 6 capture laser beams.

The laser source optical bench temperature needs to be regulated with a resolution of $0.1°C$ and this is ensured by its own temperature regulation system.

The operation of an AOM is based on Bragg diffraction of light on an internal crystal (or glass) excited by a sound wave. The frequency and power of the exiting light are controlled by the frequency and power of the sound wave. The AOMs have a maximum operation temperature of $40°C$ and this has been taken into consideration in selecting the PHARAO operating temperature range.

14 laser signals are delivered to the cesium tube with the help of 10 fibre optical cables (6 for capture, 2 for selection and 2 for detection). Fiber optical cables provide an output power of 13.5 mW, 2.5 mW and 12 mW for capture, selection and detection $|F = 4\rangle \rightarrow |F = 5\rangle$ transition beams, respectively. Total power of the 4 capture, 1 detection and 1 selection $|F = 3\rangle \rightarrow |F = 4\rangle$ beam is 5 mW, $100\mu W$ and $400\mu W$.

4.4.1.1 ECDL

The laser source is based on two low noise Extended-Cavity Diode Lasers (ECDL) (97) of high spectral purity (100 kHz linewidth) locked on cesium transitions $|F = 3\rangle \rightarrow |F^{'} = 4\rangle$ and $|F = 4\rangle \rightarrow |F^{'} = 5\rangle$ (Figure 2.5). Each ECDL has 2 encapsulated 852 nm Fabry-Perot type AlGaAs laser diodes for air/vacuum operation. These are placed in a hermetic package with an air atmosphere (pressure 1 bar). Laser diode operation in air minimizes the photo dissociative effect due to pollutants (PIF - package induced failure). As shown on Figure 4.10, the ECDL contains a cavity with a laser diode, a

collimating lens (focal length of 2.7 mm), an anamorphic optical system to make the beam circular (2 cylindrical lens of focal length -6.35 mm and 19 mm that circularize the beam into a ray with a 300 nm waist), an interference filter with a spectral selectivity of 80 GHz FWHM and a cats-eye system for the output in order to make the extended cavity less sensitive to mechanical instabilities. The interferometer is tilted to choose the mode which has a frequency corresponding to the cesium line. The output mirror is mounted on a voltage controlled piezo-electric actuator which is used to change the cavity length over a range of $3/2\lambda$ and fine tune the output frequency of ECDL. The maximum power output produced by this ECDL is about 40 mW for a current supply of 100 mA.

There are two ECDLs mounted on the same base. To switch from the nominal to backup in case of failure, a mechanical step by step motor is used which changes the polarization of the beam. In order to allow a good initial beam alignment of the backup ECDL output the beams pass through a diasporametre.

The design of ECDL has been demonstrated at SYRTE, simulated at CNES and the device is manufactured by SODERN.

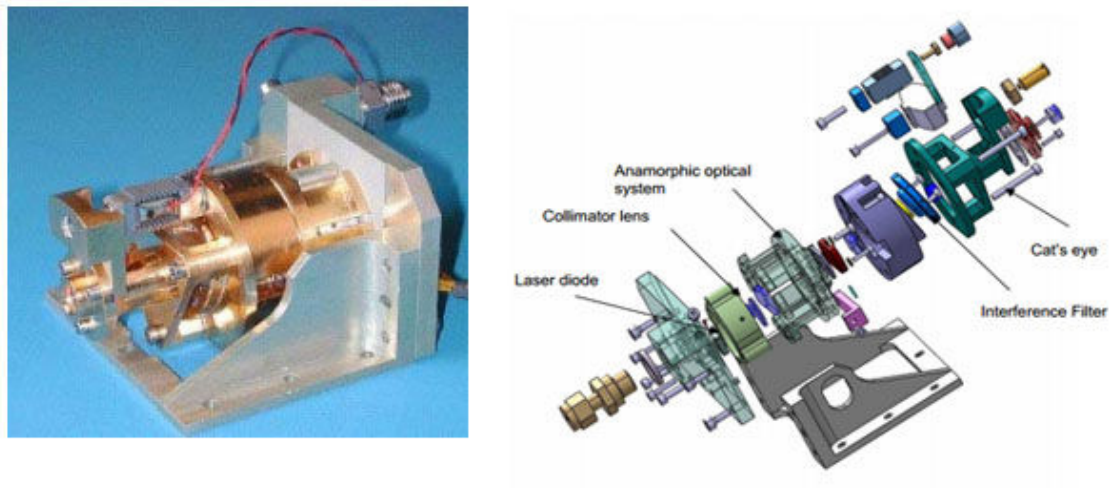

Figure 4.10: Extended cavity laser diode: manufactured by EADS - SODERN

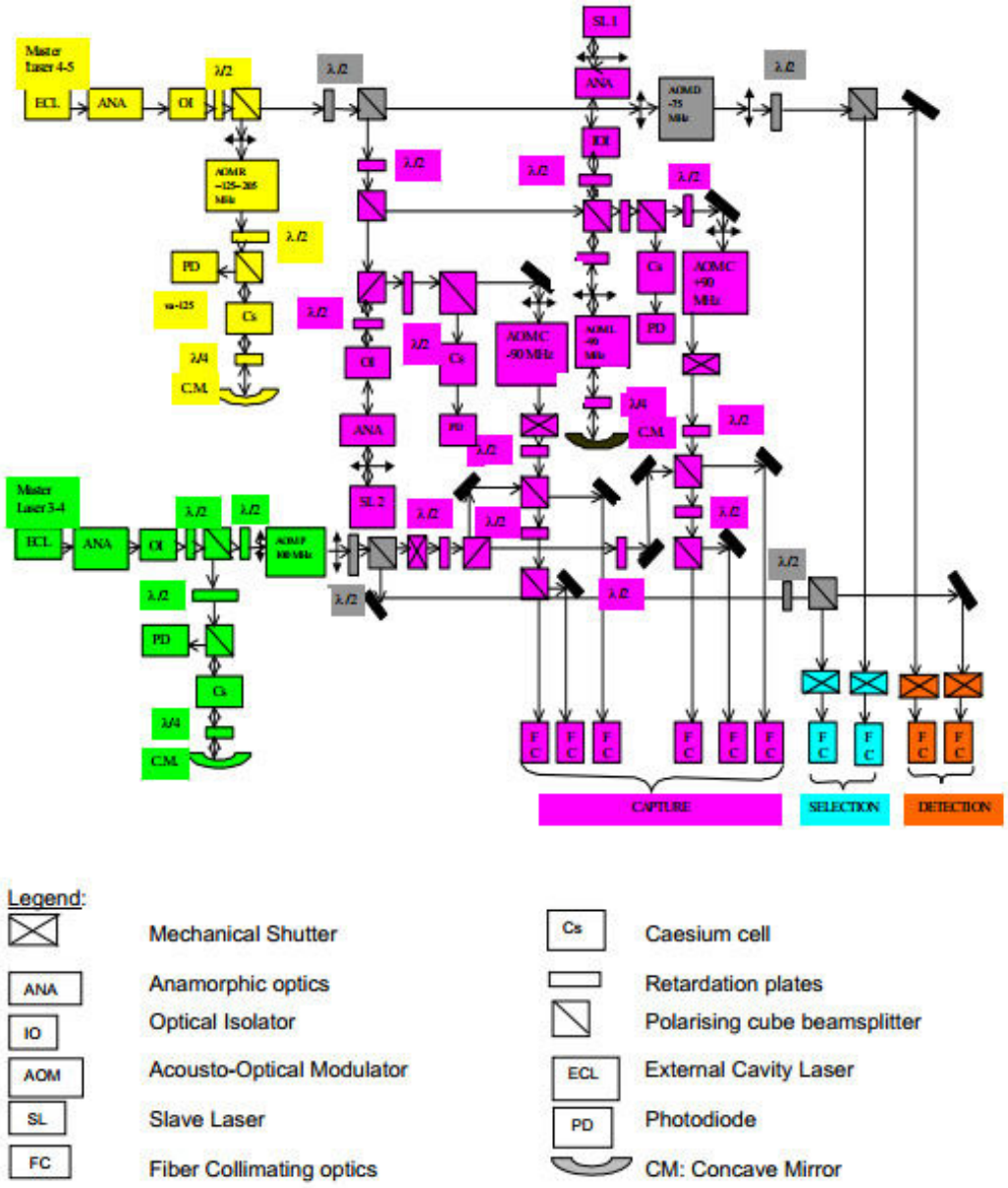

Figure 4.11: Laser source optical assembly diagram.

4.4.1.2 ECDL output

After exiting the cavity, the light in both ECDLs passes through optical isolators used to prevent light reflection back into the laser cavity that would induce perturbations in the laser frequency.

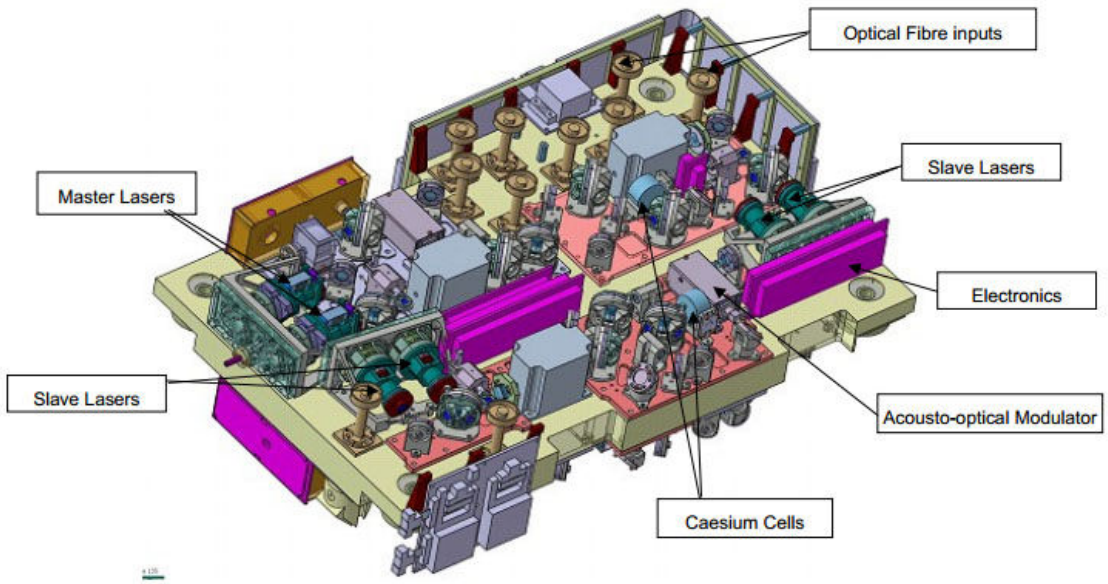

Figure 4.12: CAD view of the laser source optical bench.

The Master laser 4-5 beam passes through AOM-R, two times through a cesium cell (using a mirror) in order to perform saturated absorption spectroscopy and is then reflected to a photodiode. The diode laser current is modulated at 500 KHz (the modulation index is 5) to perform the synchronous detection of the saturated signal and lock the signal. The beam is frequency locked on the cesium crossline (in yellow on Fig. 4.11) of transition $S_{1/2}F = 4 \rightarrow P_{3/2}F = 5$ and $S_{1/2}F = 4 \rightarrow P_{3/2}F = 4$.

AOM-R tunes the laser frequency over a frequency range 140-207 MHz. AOMs are used in order to be able to vary the output frequency very rapidly (0.1-5 ms) and for large values (60 MHz) without delocking it from the cesium transition frequency. This is necessary to accommodate for frequency requirements of different clock operation phases.

The frequency of the laser beam is:

$$\nu_L = \nu_{4-5} - 125MHz + \nu_{AOM-R}, \tag{4.1}$$

where ν_{4-5} - 125 MHz is the frequency of the crossline and ν_{AOM-R} is the frequency of the AOM-R.

The beam is split into two parts (A and B). A part goes to AOM-SD which changes the frequency of ν_L by -75 MHz and is used to control the laser power for selection and detection phase of clock operation. This beam further passes through a mechanical shutter before being split into 2 parts which are sent to piezo controlled mirrors in order to optimize coupling of the beam into fibers (one for selection, other for detection).

Other part of the original beam (B) is split in $B1$ and $B2$. $B1$ injects SL2 (slave laser 2) by using the output polarizing cube of the optical isolator. A backup slave laser can also be used. Part of the slave laser beam passes through a cesium cell to verify the injection phase lock, other part goes to AOM-C (frequency shift -90 MHz) which is used to control laser power. After AOM-C, the beams pass through a mechanical shutter before being split into three and injected into fibres by using the piezo controlled mirrors. These fibers provide the three laser beams needed for capture (first capture triplet).

$B1$ is reflected by a cube followed by a double pass through AOM-L (frequency range 85-90 MHz) used to shift frequency for launching of the atoms (moving molasses technique). The beam next injects SL1 (slave laser 1). One part passes through a cesium cell to verify the phase lock and the other part goes to AOM-C (frequency shift +90 MHz). This is followed by a mechanical shutter, splitting of the beam into three and passage through the piezo controlled mirrors directing the beams into fibres (second capture triplet).

The other ECDL (pumping laser) (in green on Fig. 4.11) is frequency locked on a cesium crossline of frequency ν_{3-4} - 100.7 MHz. The beam next passes through AOMP-P (driven at a frequency of 100.7 MHz) used to change the laser power.

$$\nu_L = \nu_{3-4} - 100.7MHz + \nu_{AOM-P}. \tag{4.2}$$

The beam is next split into C and D. First part passes a mechanical shutter and is next injected into a fibre leading to selection and detection. Part D also passes a

mechanical shutter and is split into $D1$ and $D2$ which are each mixed with the 2 capture beams of each triplet.

The mechanical shutters (OBT) were implemented to allow an efficient light extinction using step by step motors with attenuation better than $-120dB$ and fast response time (2ms). For a photo of the OBT and an AOM see Figure 4.13.

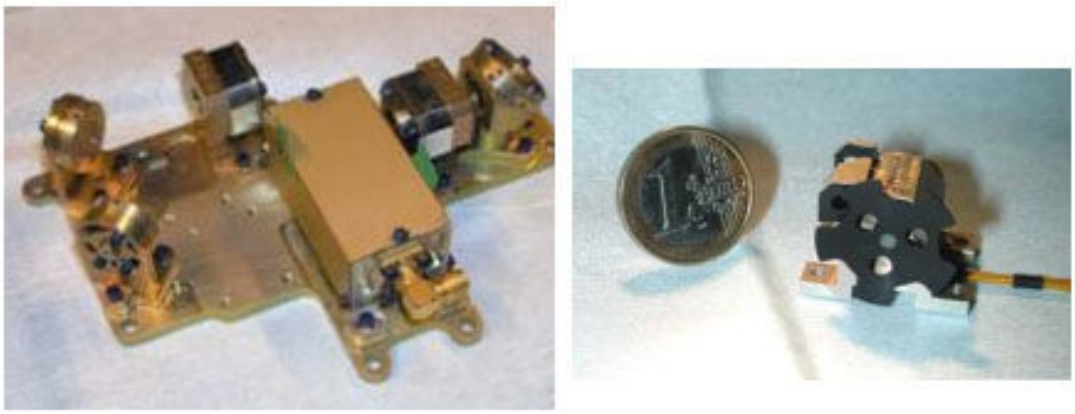

Figure 4.13: AOM (left) and a mechanical shutter (right) of the laser source.

With the FPGA integrated circuit (configured by UGB) all the laser parameters are controlled (optical active components, laser timing during different clock operation phases and laser frequency and power modifications).

4.5 Electronic control system

Main functions of the on-board control management unit UGB are power supply management (provided by the 28V PDU), data handling protocols (with PHARAO and the ACES XPLC computer using serial link), on board timing and synchronization control (using a micro sequencer), TM/TC activities (control of house keeping TM and digital parameters) and generation of microcommands to trigger different events of the clock operation (56).

UGB has a mass of 6.3 kg contained in a volume of 7.3 L. The average power consumption is 26 W. For a photo see Figure 4.14. For the UGB hardware architecture illustration see Figure 4.15.

UGB architecture is based on 5 boards: CPU board, Digital board, Analogue acquisition board, Thermal control board and the DC/DC converter. The CPU board

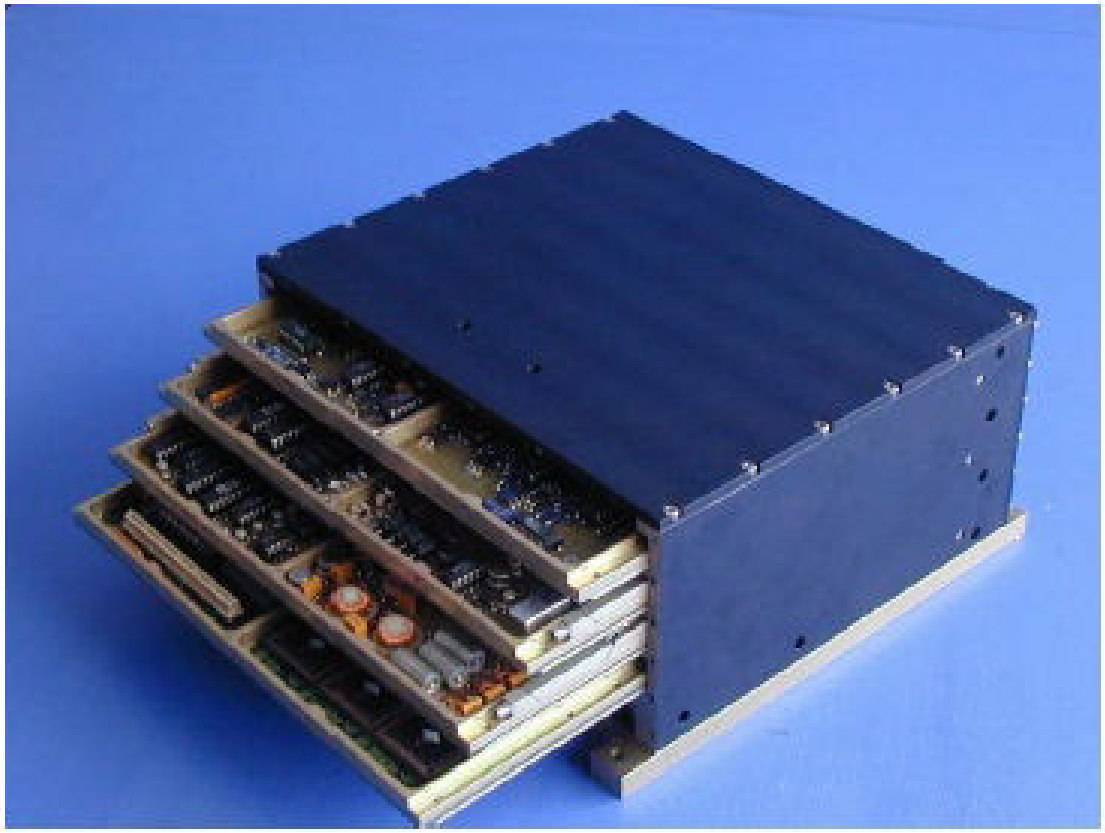

Figure 4.14: Photo of the UGB.

has a RISC 32 bit single chip with a 20 MHz processor and 12 Mb of memory (8Mbytes of local SRAM memory and 4Mbytes of local Flash memory). Digital board has a programmable microsequencer based on a PIC processor (17C756 at 10 MHz), digital data synthesiser (DDS STEL 1173) and digital to analog converter (DAQ) which digitizes signals gathered in clock sub-systems and sends them to the central control unit.

The flight software has about 50 000 lines of code containing around 100 sequences that control different aspects of clock operation.These sequences execute PHARAO performance evaluation procedures, analysis of detected anomalies and different phases of cold atom manipulation during normal clock operation; capture, cooling, selection, preparation, interrogation and detection. During a cycle, the software controls laser intensity, microwave field frequency, thermal regulation, the magnetic shields demagnetisation, the magnetic active attenuation system... Servo loop that locks the central resonance peak during Ramsey interrogation is also performed automatically by the

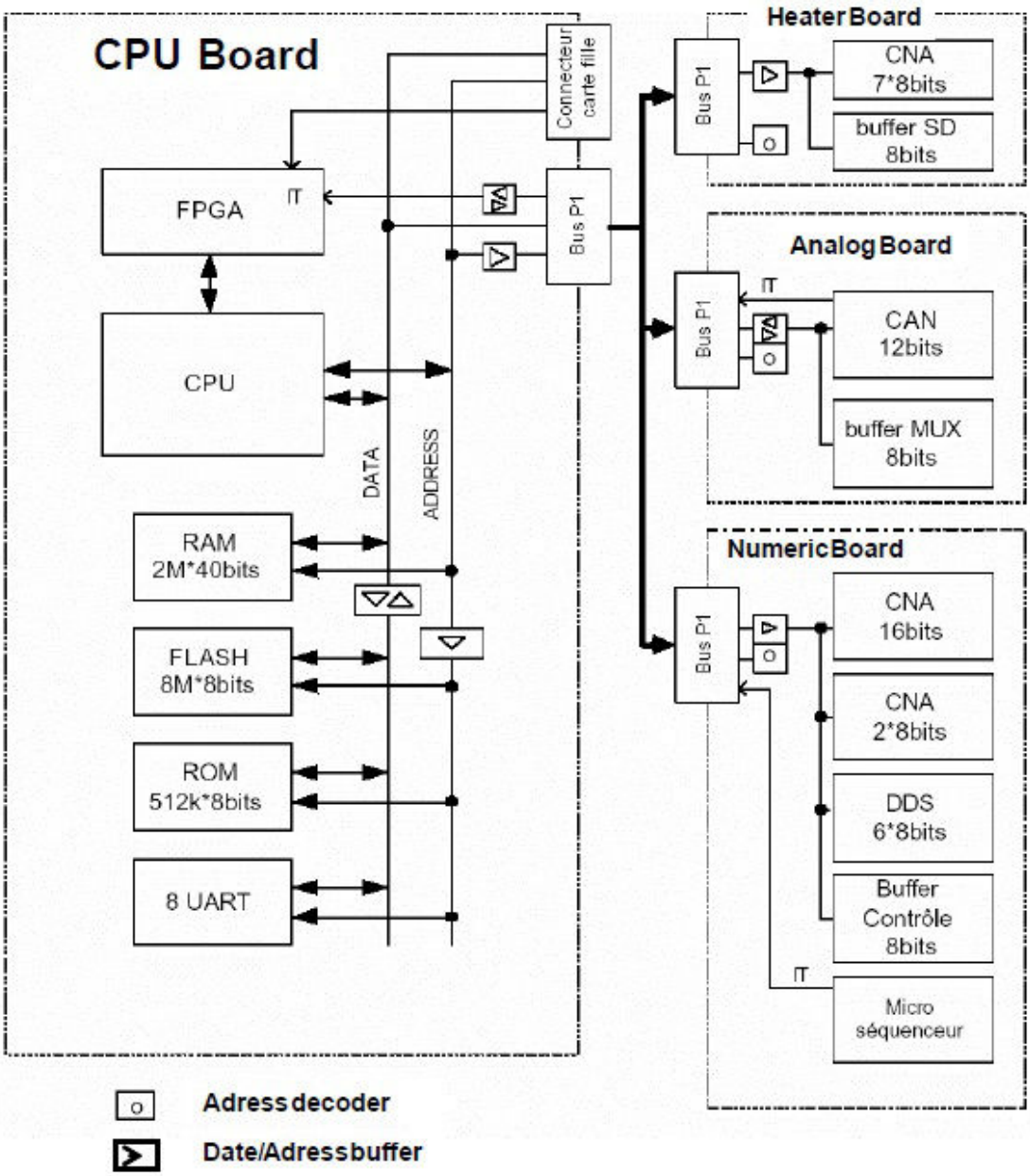

Figure 4.15: Hardware architecture of the UGB.

on-board system.

The BEBA electronic unit controls the magnetic coils and amplifies the analogue signals from the cesium tube. It also has an accelerometer aligned along the cesium tube axis used to measure the vibration level. BEBA has a mass of 1.3 kg and a typical

power consumption of 3 W.

A serial line is used to communicate to XPLC and transfer the data for telecommand and telemetry. Telecommand allows for software and variable modification from the ground station in real time or with a certain delay. Daily transfer rate of telecomand data is estimated to be between 2 and 23 Mb per day, while telemetry download will be between 7 and 87 Mb per day. This is summarized on Figure 4.16. The ground based dedicated console based at CADMOS, CNES in Toulouse collects all the downloaded data creating a database of everything PHARAO related during mission duration. This allows for easy data access available for scientific analysis.

Packet	Size (bytes)	Nb of packets / ACES cycle (10 sec)	Data rate (Mbytes/day, rounded)
Frequency comparison data	6	40	2
ACES Time	18	1	0.2
Telecommands	99	0 to 1	0 to 1
Data load	370	0 to 6	0 to 20
Total TC			**2 to 23 Mbytes / day**
Housekeeping (TM-A)	372	2	6
Science (TM-P)	154	1 to 56	1 to 75
Dump (TM-D)	370	0 to 2	0 to 6
Total TM			**7 to 87 Mbytes / day**

Figure 4.16: Telecommand and telemetry PHARAO data.

4.6 Cesium tube and operation

Manipulation of atoms in PHARAO is performed inside a titanium-made vacuum tube (990 mm x 336 mm x 444 mm). Titanium is used because of the weight/strenght ratio and because its not magnetic. Total weight is 46 kg and the volume is 47 L. The tube consist of 6 separate pieces connected with titanium screws and aluminum gaskets. The vacuum of 2×10^{-8} Pa is maintained inside the vacuum tube by 6 getters and an ion pump which has a pumping speed of 2 L/s. The high vacuum quality ensures a

minimum loss of atoms and a negligible frequency shift (98) value due to collisions with the residual gas. PHARAO operation consists of phases illustrated on Figure 4.17. The layout of PHARAO is given on Figure 4.18.

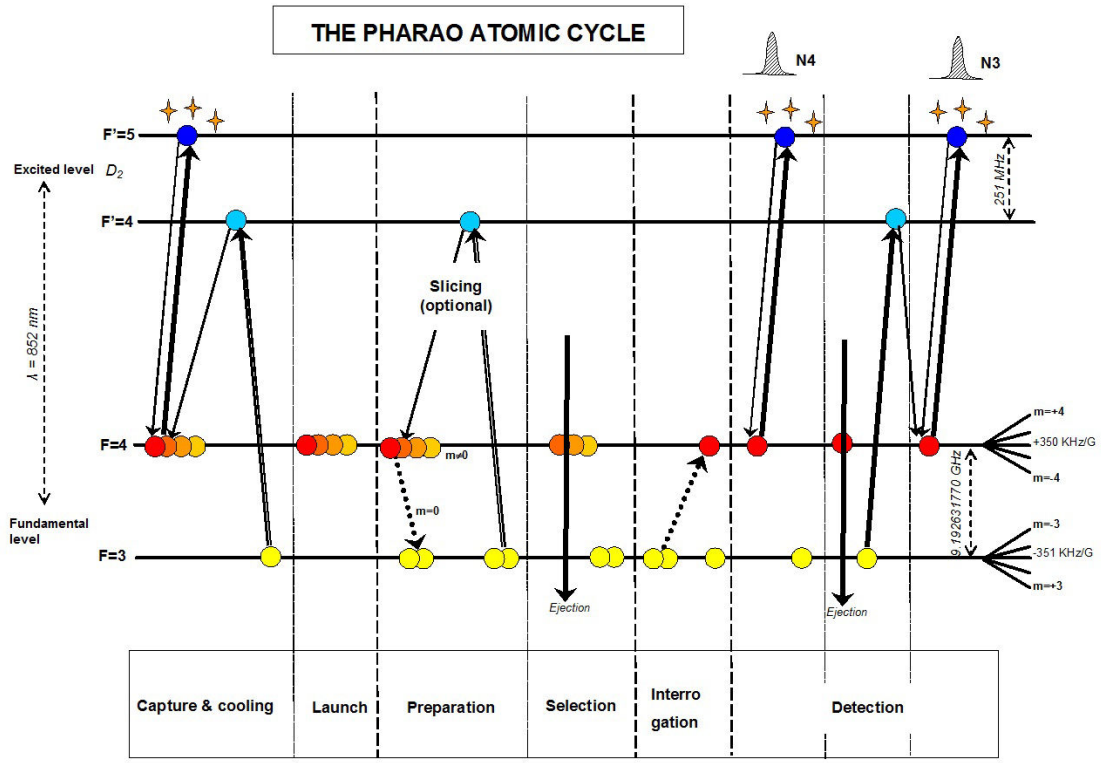

Figure 4.17: PHARAO atomic cycle is composed of capture and cooling, launch, atomic state preparation and selection, atomic cloud interrogation and finally detection of atomic state.

4.6.1 Atom capture

3g of cesium are trapped inside porous titanium by capillarity (cesium condensation temperature is $28.5°C$). From the cesium reservoir the atoms are released towards the capture cavity with a flux of 10^{12} atoms. The atomic flux is modulated by an adjustable valve in order to control the vapor pressure in the capture zone. The cesium pressure there is about 10^{-6} Pa.

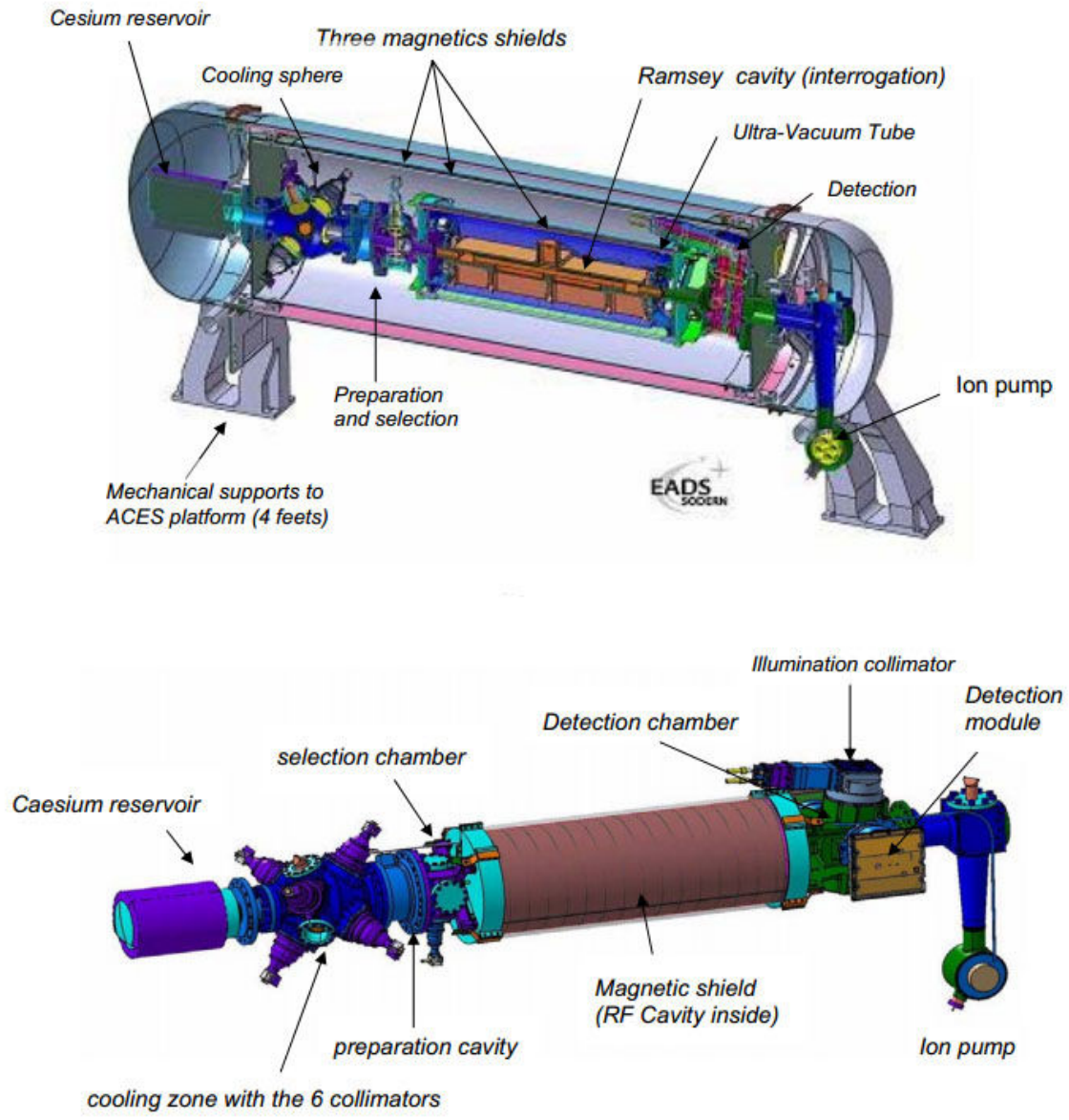

Figure 4.18: Layout of the cesium tube (up) and the vacuum tube (down). The components will be explained in the following sections.

4.6.2 Atom cooling

The atoms are next laser cooled (Doppler, sub-Doppler). The laser beams are positioned on the sides of the polyhedra shaped cavity and intersect at the centre of a polyhedron. The beam diameter is 21 mm. A beamsplitter cube directs the counterpropagating

beams towards a photodiode. This allows for integration of a loop that controls the laser power. After 1 sec the atomic cloud contains about 4×10^8 atoms. The number of atoms is evaluated by fluorescence collected by a photodiode.

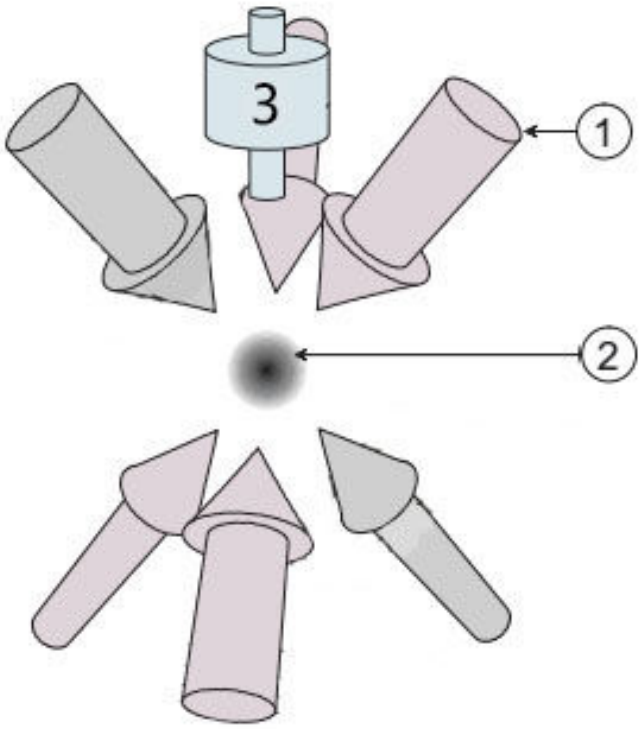

Figure 4.19: Scheme of the laser beam geometry. The atomic cloud (2) is first Doppler cooled using 6 lasers (1). Next, the atoms are launched using the moving molasses technique followed by sub-Doppler cooling. After that, they reach the preparation cavity (3).

From the capture zone, the atoms are launched with an initial velocity between 5 and 500 cm/s. During ground operation the launching velocity is $v = 3.54 cm/s$. The duration of the launch and the following cooling phase is around 0.75 ms and 2.5 ms, respectively.

4.6.3 Preparation and selection

After the cooling phase, the atoms populate the 9 m_f (-4, -3, -2, -1, 0, 1, 2, 3, 4) atomic substates of F= 4 and enter the preparation cavity (31). This is a cylinder made of titanium with a radius of 54 mm and length of 24 mm. The preparation cavity

is connected to the capture zone by a graphite coated aperture which has dimensions $8 \times 9\text{mm}^2$ and length of 34 mm. The graphite prevents cesium vapor migration.The cavity resonates in mode TE_{011} mode with a quality factor of ≈ 500. The microwave signal is fed by a loop inside the cavity that is connected externally by a coaxial cable to the microwave source. The function of this phase is to produce $|F = 3, m_F = 0\rangle$ pure state atoms which will undergo Ramsey transition in the next step. Removal of $m_f \neq 0$ atoms is important as they are not used in clock operation and present a source of noise and induce clock frequency shifts such as cold atom collisions. Therefore, using a microwave π pulse, the atoms make a transition $|F = 4, m_F = 0\rangle \rightarrow |F = 3, m_F = 0\rangle$.

After preparation the only atoms remaining are in the $|F = 3, m_F = 0\rangle$ and $|F = 4, m_F \neq 0\rangle$ state. In order to remove the latter from the cloud, a laser beam (pointing perpendicular to the atom path) tuned to the $|F = 4\rangle \rightarrow |F' = 5\rangle$ transition keeps transferring the atoms to a higher decaying state until enough kinetic energy has been imparted on them that they are pushed out of the cloud (radiation pressure). This is the selection phase.

With another selection laser beam it is possible to cut the cloud longitudinally. This is performed in order to study the velocity distribution of atoms or simply to reduce the length of the cloud. In microgravity environment in case of very low launch velocity due to thermal expansion the cloud is very elongated. Part of the $F = 3$ cloud that is to be removed is pumped by a laser tuned to $F = 3 \rightarrow F = 4$ and then ejected by the other laser beam.

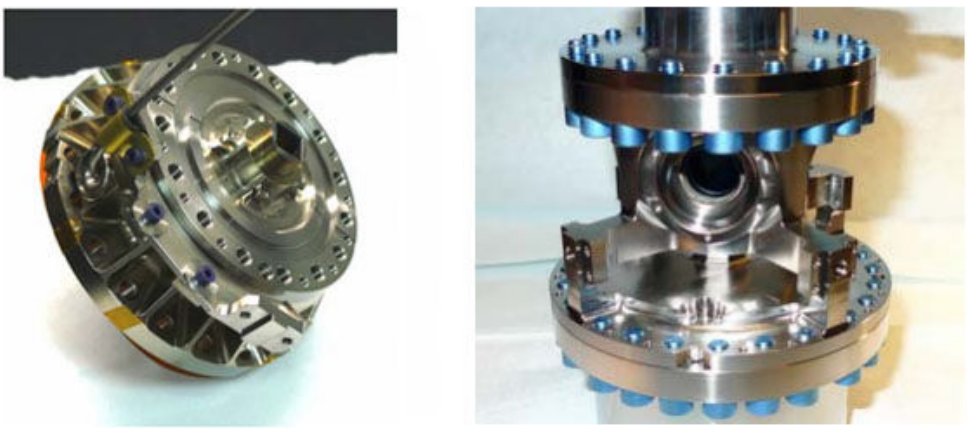

Figure 4.20: The flight model of the preparation (left) and the selection (right) zone.

4.6.4 Interrogation

Next, the atomic sample composed of atoms in the $|F = 3, m_F = 0\rangle$ state enters the interrogation cavity (Figure 4.21). A Ramsey type cavity with two distinct interaction zones was selected for PHARAO (18).

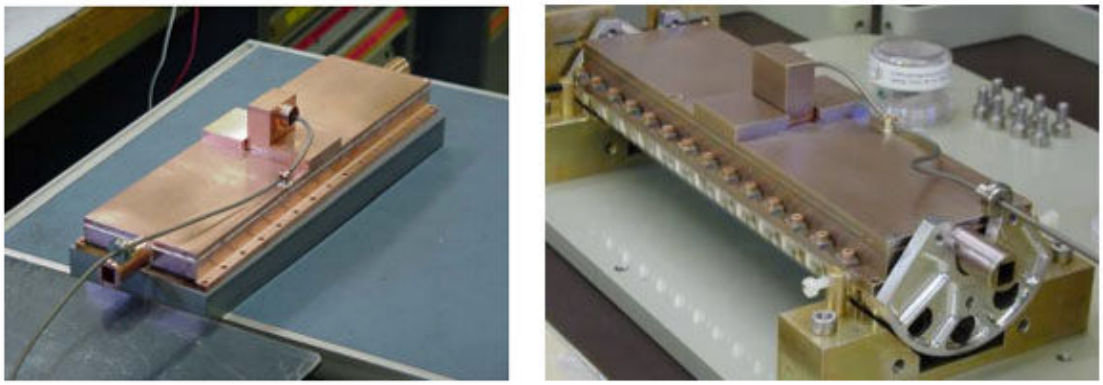

Figure 4.21: PHARAO flight model interrogation cavity and its supporting structure (on the right).

The cavity is 240 mm long (250 mm with walls and 300 mm with apertures) rectangle made of copper (weight 1.5 kg). The dimension of the interrogation cavity has been selected to be resonant on the $|F = 3\rangle \rightarrow |F = 4\rangle$ transition. Quality factor of PHARAO is ≈ 1500.

Figure 4.21 and Figure 4.22 give a photograph of the cavity and a diagram with dimensions, respectively.

The interrogation cavity is supported by an AlSiC made structure which is screwed to the vacuum chamber. The coupling is a rectangular waveguide with a slit mounted on the top of the cover in the middle of the cavity and is connected by a coaxial cable to the microwave field source. Coupling between the cable and the cavity is accomplished by evanescent-wave coupling in the two lateral waveguides. The waveguide has 22 antinodes as seen on Figure 4.23.

The atoms interact with the microwave oscillating field inside the two interaction zones which have a length of 19 mm and are positioned at a distance of 200 mm. Between the two interaction zones, the atoms are in a cutoff waveguide and evolve freely.

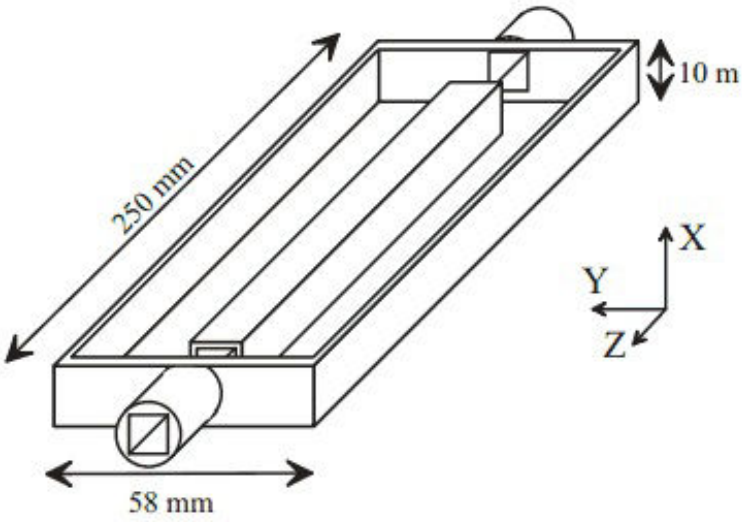

Figure 4.22: PHARAO interrogation cavity with external dimension.

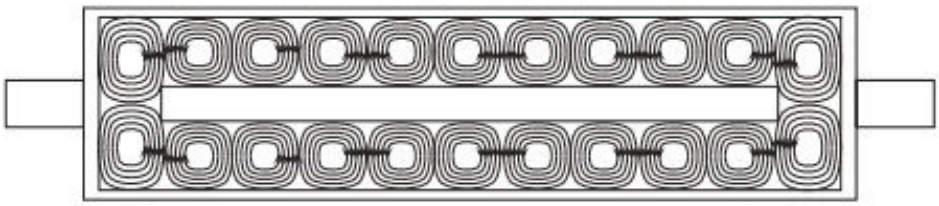

Figure 4.23: Field distribution inside the TE_{013} microwave cavity.

To avoid all microwave field leakage and possible stray light, elongated cylindrical apertures (cut-off) have been added. These cut-offs attenuate the microwave field at the order of 60 dB/cm. Their dimensions are 8×9 mm^2 and length is 3.5 cm. To prevent atomic collisions with the walls, diaphragms of dimensions 7.6×8.6 mm^2 have been placed at the exits of both cut-offs. The total signal of the microwave field cavity leakage have been evaluated to be smaller than $-120dB$.

Due to cavity copper resistivity (dissipation) there exists a phase gradient of the microwave field inside the cavity. This is a transition frequency changing source called the Doppler effect or DCP. For more information see Section 6.4. Simulation performed by IRCOM taking into account the wall conductivity give phase and amplitude field distributions inside the interaction zones (Figure 4.24). Phase gradient on the cavity axis are at the order of 100 μ rad/mm and about 10 μ rad/mm in the transverse

directions.

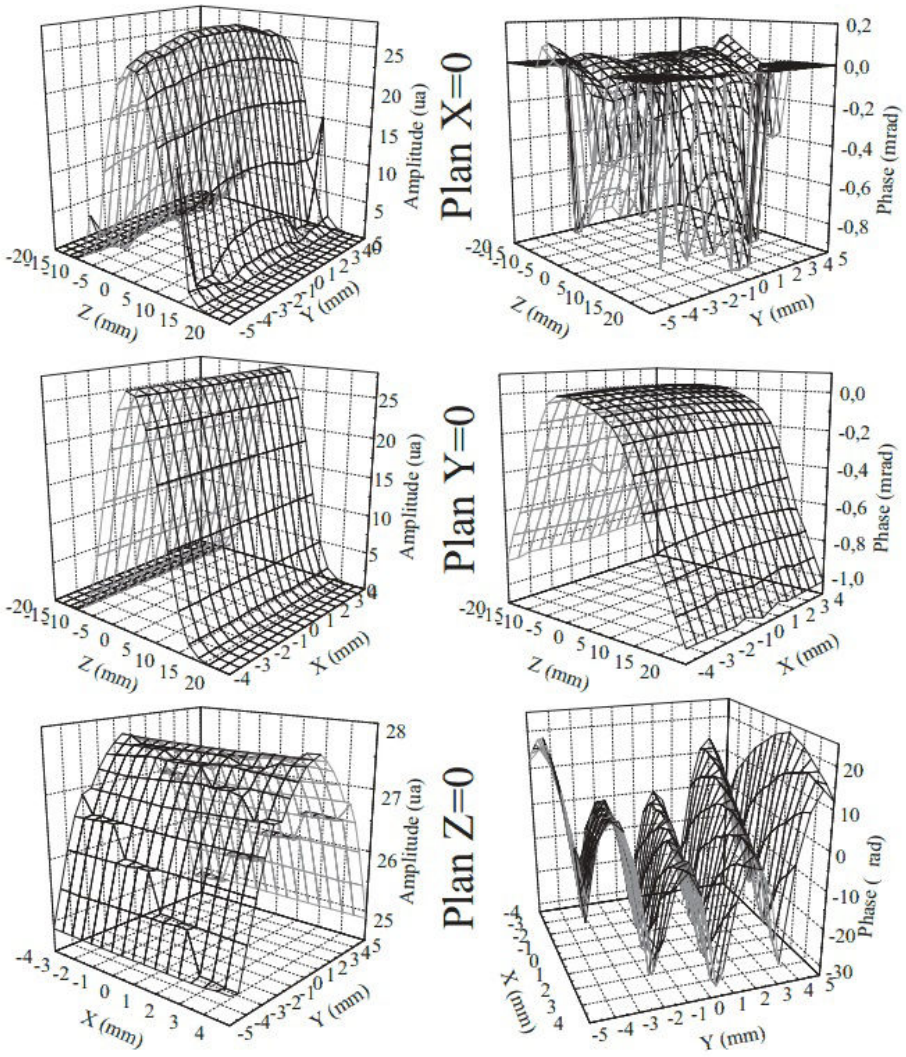

Figure 4.24: Simulations showing the phase and amplitude field distribution inside an interaction zone.

Another frequency shifting effect, that will be analyzed in more detail later (Section 6.2), is concerned with a temperature knowledge along the atom path inside the interaction cavity. This is called the black body effect. Information gathered from the two thermal probes placed outside of the vacuum chamber is fed into a servo loop. In turn, the loop operates two heaters at the ends of the vacuum chamber in order to minimize the temperature gradient.

4.6.5 Detection

After the passage through the interaction cavity the atoms arrive to the detection area in a superposition of internal states. The Master detection laser beam is divided into 4 circularly polarized laser beams which are directed perpendicularly to the atom path and used to invoke transitions inducing fluorescence. The first beam (15×14 mm) is the standing wave used to detect atoms in the F = 4 state. The second beam (15×2 mm) is a traveling beam used to eject the atoms in the F = 4 state. The last beam (14×5 mm) is used to detect the atoms in F = 3.

The power of the first and second beam is $\approx 3mW$, while the third beam has a power at the order of 80 μW. Similarly to the capture cavity, the power of the lasers is managed with a help of photodiodes that are placed near the beam exits and that measure the light intensity. Figure 4.25 illustrates the detection process.

- the process begins by exciting the $|F = 4\rangle$ atoms to the $|F = 5\rangle$ state by a tuned standing wave that the atoms first encounter during their passage. The induced fluorescence of the transition is passed to the window and collected by a photodiode. The florescence signal of N_4 is proportional to the number of atoms in the $|F = 4\rangle$ state.
- these atoms are then pushed away by radiation pressure of a travelling wave.
- the remaining $|F = 3\rangle$ atoms are then pumped to $|F = 4\rangle$ by the other laser beam.
- this is followed by a second standing wave field.The induced florescence is collected by a second photodiode and this signal N_3 is proportional to the number of atoms in the $|F = 3\rangle$ state.

The rectangular detection beam profile is much larger than the interrogation cavity aperture in order to be able to detect all the atoms. Note on Figure 4.26 that the beam has a good homogeneity in the transverse direction.

Efficiency of the collection of the fluorescence light emitted during transitions is about 5.8%. The light is gathered by a combination of lenses, focused towards the photodiode.This is finally converted to an electrical signal by an amplifier with a gain of 0.027 V/nW.

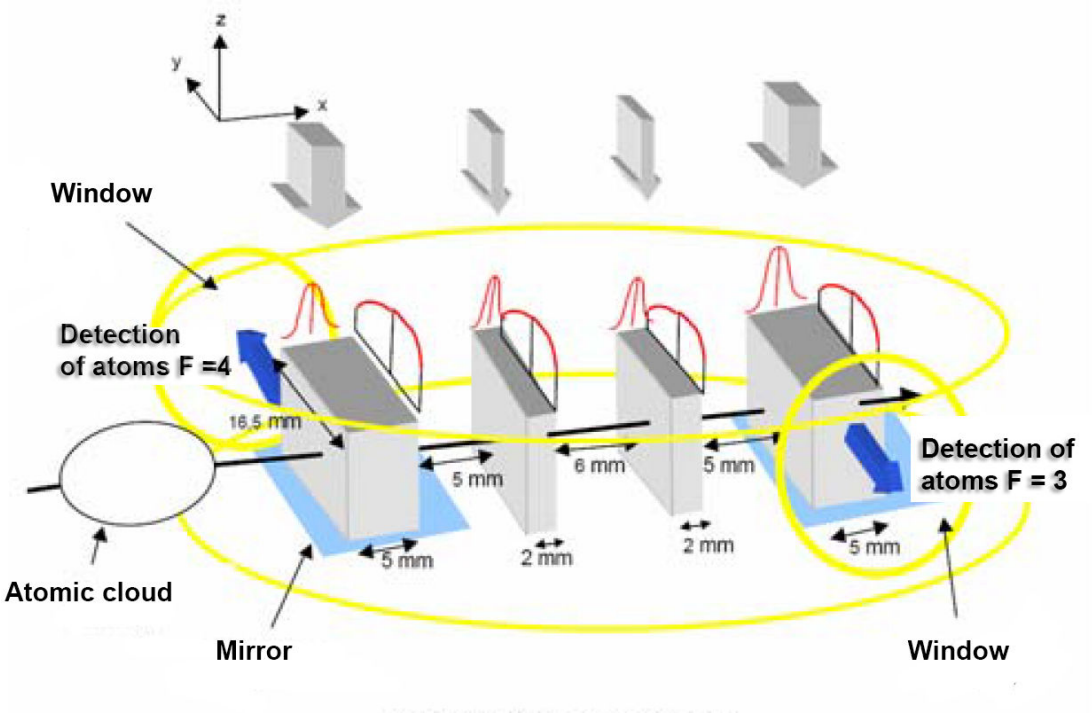

Figure 4.25: Atom state detection zone. First rectangular beam is used to detect F = 4 atoms by exciting the F = 4 → F = 5 transition and measuring the florescence (exiting from the window). Second beam is the pushing beam that ejects the F = 4 atoms from the cloud. Third beam is the F = 3 → F = 4 pumping beam. Fourth beam is another rectangular F = 4 → F = 5 beam. The mirrors under the two rectangular beams are used to create the standing wave.

Figure 4.26: Profile of the rectangular beam. The atomic cloud has the direction of the arrow. The dimensions are in units of *mm*.

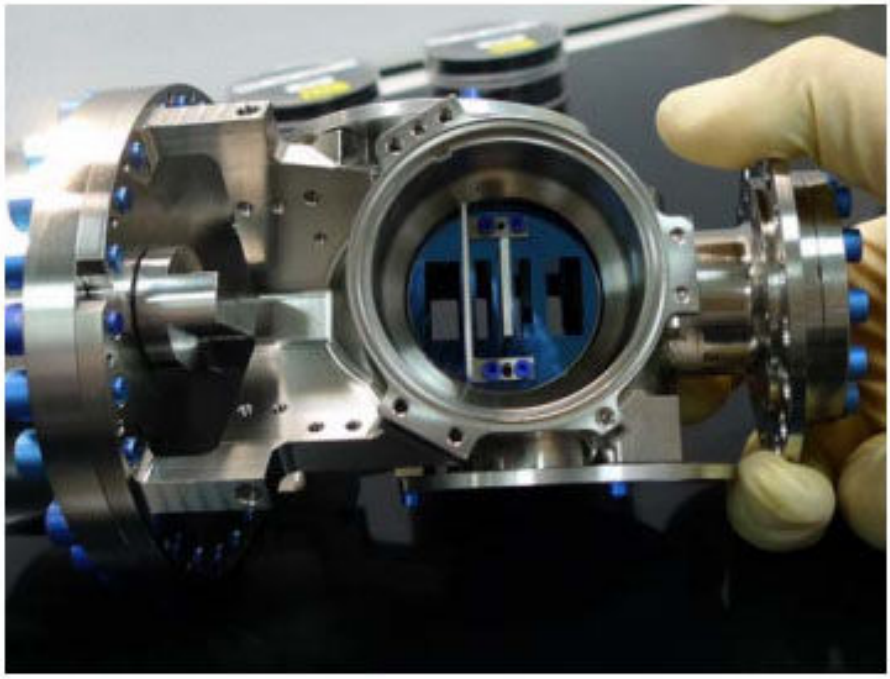

Figure 4.27: PHARAO flight model detection chamber. A dedicated internal baffle (DALP) seen here in blue protects each beam from stray light.

4.6.6 Magnetic shields

The vacuum chamber containing the interaction cavity is encompassed by three cylindrical magnetic shields and magnetic coils. See Figure 4.28.

A large solenoid BP responsible for providing a magnetic field (for Zeeman separation), a wire used for degaussing and the "Zeeman wire" (described in Section 6.1.2.2) are positioned parallel to the interrogation cavity. Smaller coils at the two ends ($BCPC$ and $BCPD$) are used to improve internal magnetic field homogeneity. The solenoids, wires and the cavity are encompassed by the smallest shield $B1$.

Outside of $B1$ are the coils $BSL6$ and $BCSC$ at the capture side of the tube and coils $BSL7$ and $BCPD$ at the detection side of the tube. These coils are used to improve field homogeneity inside the preparation and detection cavity (BS coils) and around the interrogation cavity apertures (BC coils). The shield $B2$ encircles the described componets and also the detection cavity.

The shield $B2$, the cesium reservoir, the magnetometer (DTU) which measures the

magnetic fluctuations and the ion pump (which has its own shielding to protect the rest of the clock from its influence) are enclosed inside the largest $B3$ shield.

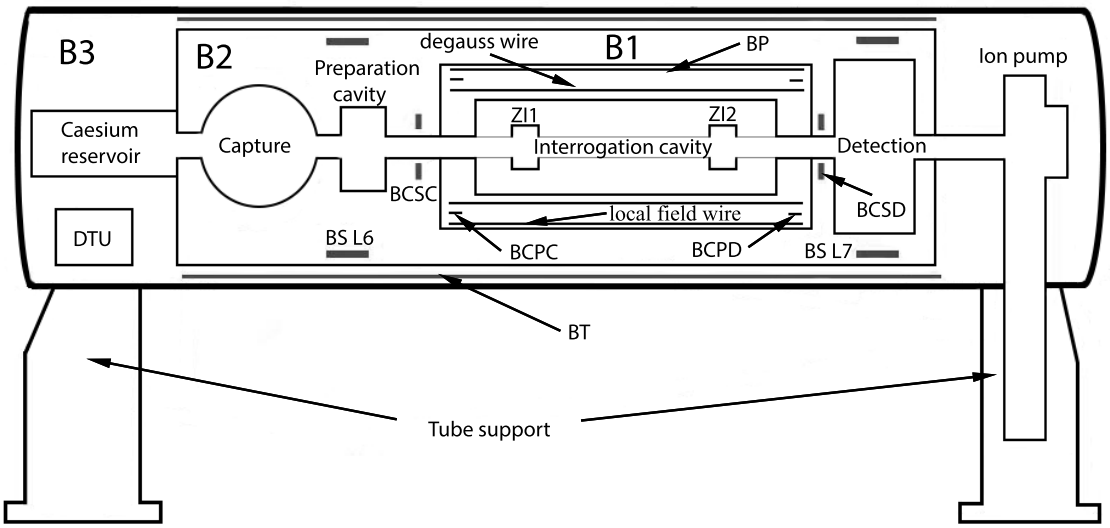

Figure 4.28: Diagram of the PHARAO cesium tube. Labelled are the external shields B1, B2, B3, the DTU magnetometer, ion pump used to maintain vacuum, cesium atoms reservoir, different cavities and coils. From the reservoir cesium atoms are released towards detection passing the capture cavity (where they are cooled), preparation cavity (where F = 3 atoms are selected) and interaction cavity (where the frequency interrogation is performed in the two interaction zones ZI1 and ZI2). In the detection zone, ratio of the two populations is obtained. The three Mumetal shields are used to reduce the magnetic oscillations the atoms experience in flight due to the Earth orbit field. The coils are used to improve and measure field homogeneity, separate magnetic Zeeman levels by providing a static magnetic field and for active compensation (BT).

The validation of the mechanical and thermal clock design lies on full calculation (finite elements) of the mechanical constraints inside the components and on tests of a structural and thermal mock-up (STM) of the clock.

In order to accommodate for strict requirements new technologies have been used for sealing, microwave and electronic isolation, shield and connector manufacturing.

4.6.7 Experimental ground operation

4.6.7.1 Experimental setup

Figure 4.29: Vertically positioned PHARAO cesium tube before being wrapped by a thermal blanket and out into a vacuum chamber.

To control and vary the baseplate temperature in the range $10 - 33°C$ a LAUDA RE320 heating and cooling system was used. The cesium tube was vertically aligned within 1 mrad, but could be tilted to study the performances. The tube was placed inside a vacuum chamber (10^{-6} mbar). The vacuum chamber was surrounded by Helmholtz coils able to provide axial and transverse components of the magnetic field and stimulate the field present in orbit (Figure 4.30).

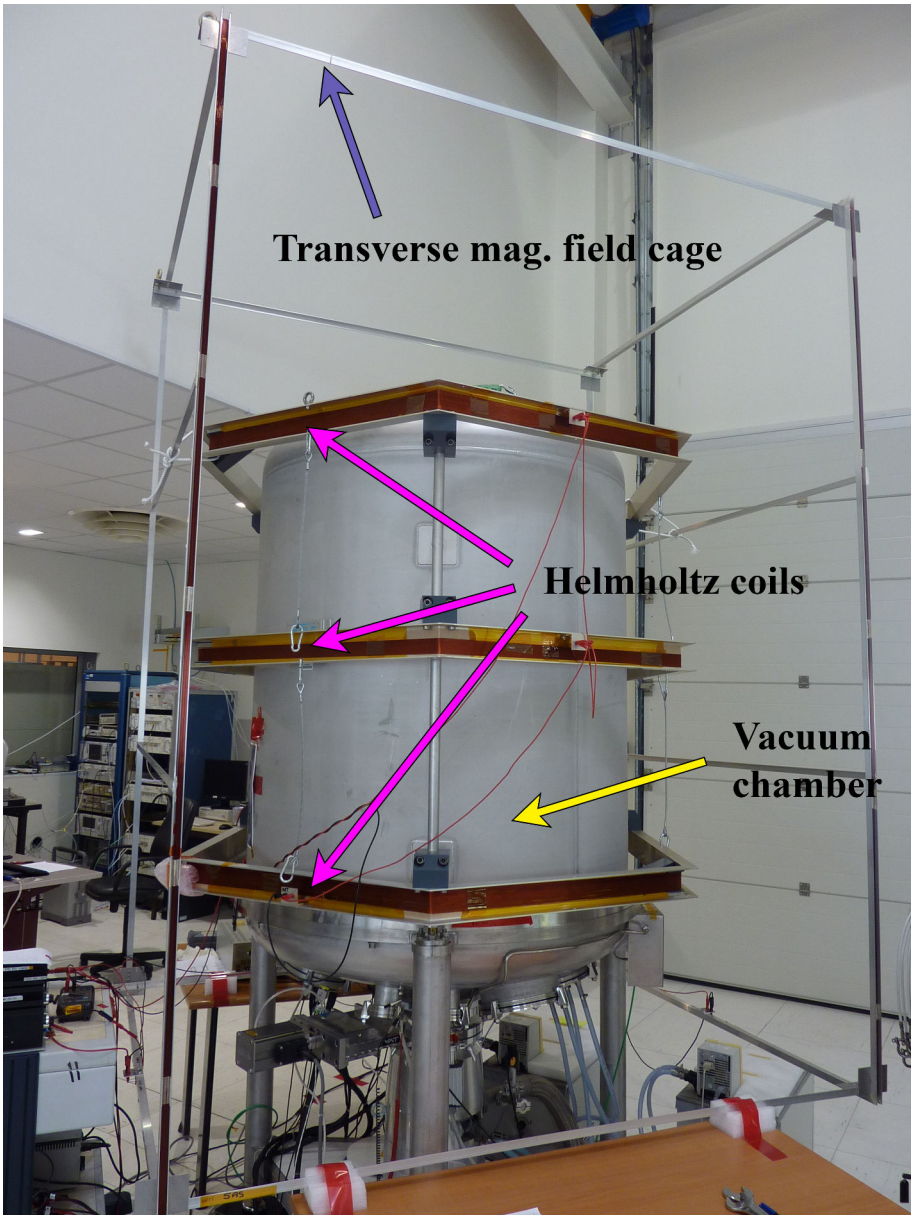

Figure 4.30: Violet arrow shows the cage used to provide the transverse magnetic field, pink arrows represent the Helmholtz coils used to provide the axial field and the yellow arrow shows the vacuum chamber which encircles PHARAO.

Clock frequency stability and accuracy were evaluated. A cryogenic oscillator was used to measure the spectral noise density, to study the phase transient effect and as an external oscillator. Due to low noise the cryogenic oscillator allowed the analysis of the

PHARAO frequency stability. FOM mobile fountain was used to verify the accuracy of PHARAO. To test the short term servo loop of ACES in nominal operation an external H-maser was connected to PHARAO.

Figure 4.31: Ground segment used to send TC, receive TM and examine data with the software package MARIA.

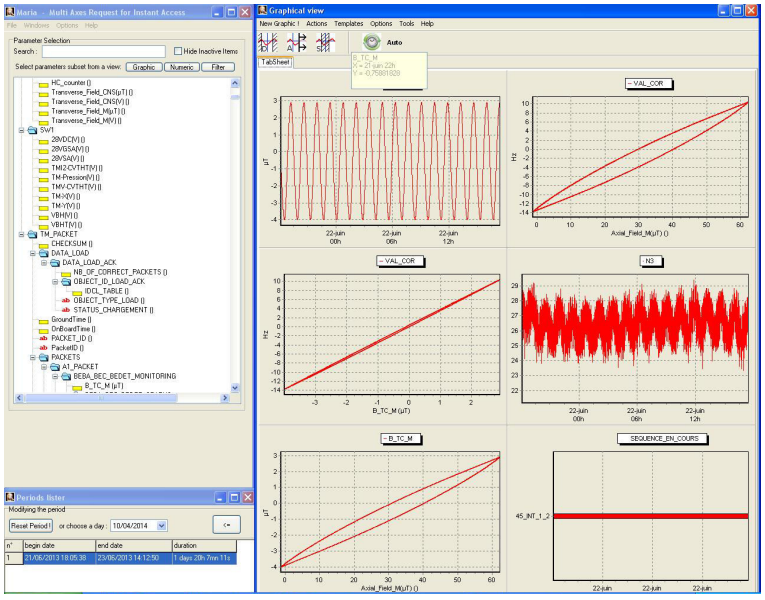

Figure 4.32: MARIA software. Example for an external magnetic field oscillation test.

Ground segment consists of 4 computers: a file server, a server to prepare and

control TC, a database server (which sends TC and receives TM) and the computer used to analyze the data. The latter displays and examines PHARAO parameter evolution with the dedicated computer software MARIA (Multi Axes Request for Instant Access). MARIA allows analysis of data during and after experimentation. The PHARAO data has 11083 software and clock parameters and 1900 TM values. An example of MARIA data analysis is given on Figure 4.32.

4.6.7.2 Initial starting, optimization an results of the clock

Starting up of the clock is performed automatically in the following order:

1. the UGB is turned on (followed by the initialization of the flight software),
2. the microwave source, the laser source and the tube electronics are switched on,
3. thermal regulations of the laser source baseplate, the cesium reservoir, the interrogation cavity and the detection cavity are started,
4. the laser source AOMs and the piezoelectric mirrors turned on,
5. the initialization of 8 rotating mirror mechanisms,
6. the active magnetic compensation system turned on,
7. the degaussing process performed,
8. the magnetic coils turned on,
9. thermal regulation of the diode lasers switched on,
10. the diode lasers initialized (100 mA for ECDLs and 140 mA for slave lasers - maximum is 190 mA),
11. laser source ECDLs search for cesium flourescence,
12. ECDLs mode hop centering,
13. ECDLs locking on the $F = 3 \rightarrow F^{'} = 4$ and $F = 4 \rightarrow F^{'} = 5$ transitions,
14. the slave lasers injection,

15. the opening of the cesium reservoir valve,
16. the measurement of the laser powers inside the cesium tube (with photodiodes),
17. the verification of the AOMs and mechanical shutters operation,
18. the laser beam power optimization (MEF tuning) before fiber insertion performed. The 6 capture MEF are used to balance the 6 capture beams. The remaining two MEFs are used for the selection and detection maximum flux tuning. After rough and fine MEF tuning sequences, the 6 capture beam powers are equal within an error of 1%.
19. the loading of the clock cycle timetable (Figure 4.33),
20. the generic cycle is started.

Capture, preparation, selection, interrogation and detection phase parameters were optimized in order to increase the atom number and the resonance quality.

To have the largest number of cold atoms in the capture zone, the 6 beam laser frequency was modulated while measuring fluorescence. Optimum frequency of the AOM-R was found to be 205 MHz, corresponding to the capture frequency of $F = 4 \rightarrow F^{'} = 5$ - 10 MHz (Figure 4.34).

To have the maximum number of the detected atoms cooling and launch parameters were analyzed from the detection signal and optimized. The 6 relevant parameters are: the launch duration, the cooling duration, the adiabatic shut down duration, the time constant of the adiabatic shut down, the cooling power and the cooling frequency (in microgravity the optimization will be performed for various launch velocities).

The following configurations have been tested:

- the cooling duration from 0.5 to 2.5 ms (step of 0.2 ms)
- the launch duration from 0.25 to 1.4 ms
- the adiabatic shutdown duration is fixed to 0.4 ms
- the time constant of the adiabatic shutdown from 0.2-0.6 ms
- cooling power scan from 0.5 mW to 6.88 mW

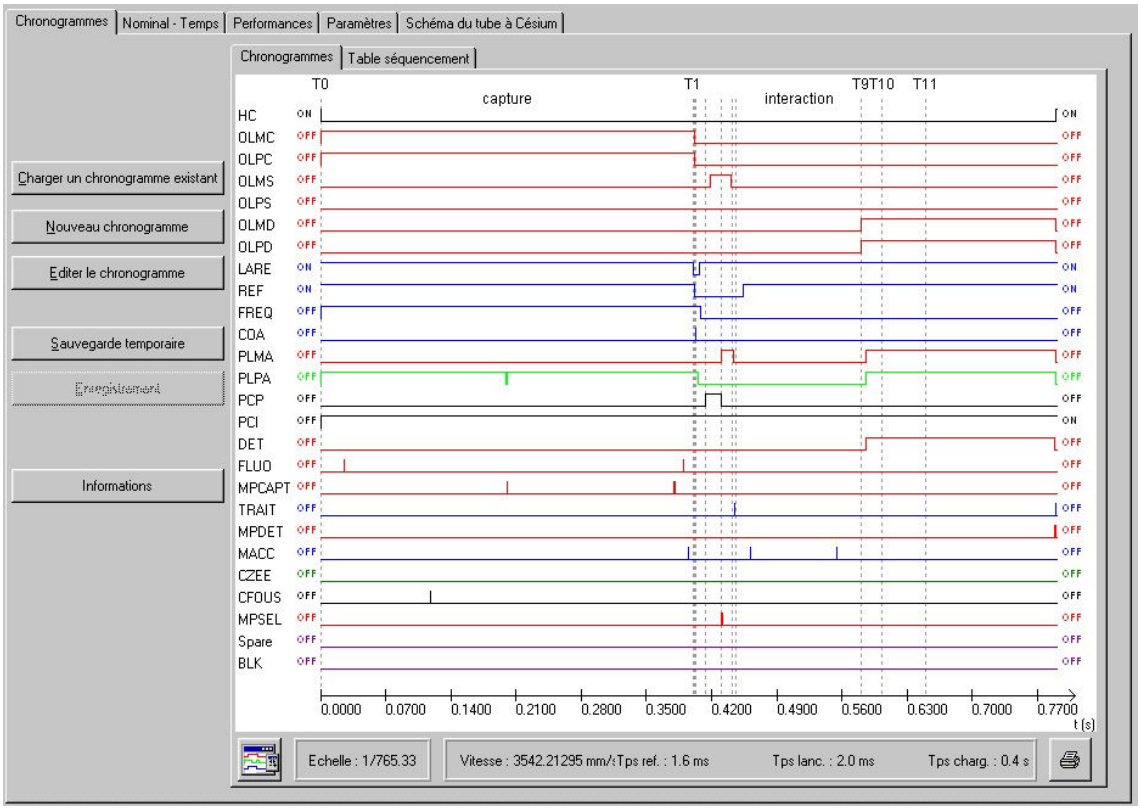

Figure 4.33: An example of the clock cycle timetable. For instance: "HC" drives the mechanical shutters during capture, "LARE" changes the first laser triplet frequency, "PCP" drives the microwave power inside the preparation cavity, "MPCAPT" digitizes the laser power value during capture, "DET" digitizes the two detection signals N3 and N4 value and "TRAIT" process in real time the acquisition data.

The optimal settings for the clock operation were found to be:

- capture frequency of -2Γ (linewidth)
- launch duration of 0.75 ms (launch velocity of 3.54 m/s)
- cooling duration of 2.5 ms
- cooling power of 1.69 mW
- cooling frequency of -13Γ (59.8 MHz)

Figure 4.35 shows the time of flight (TOF) signal obtained in detection. It is the flourescence signal emitted by the cloud of cold atoms during their passage through the

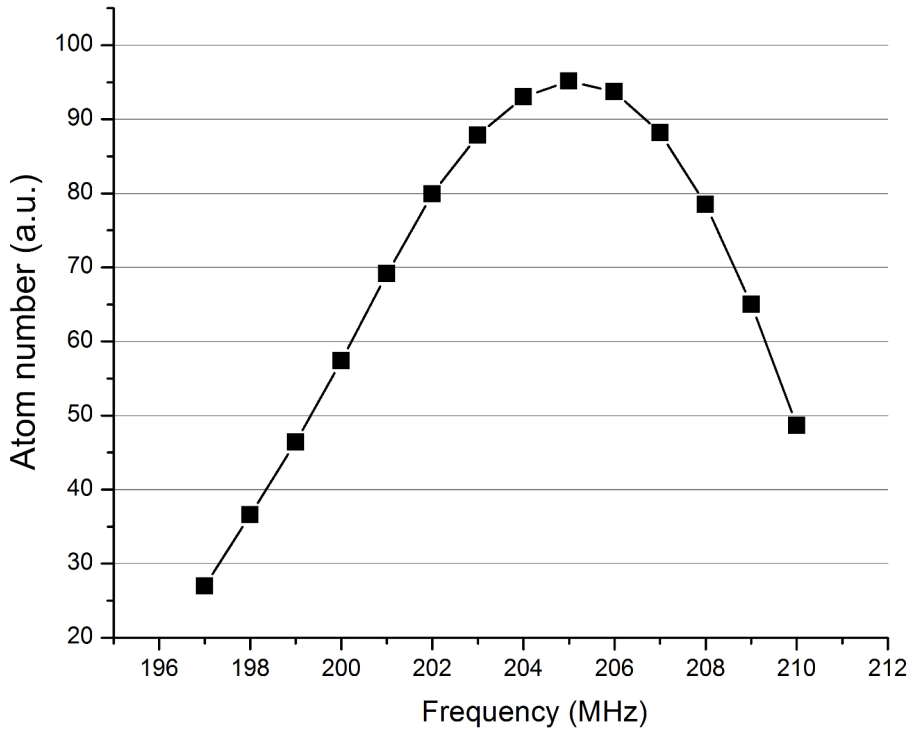

Figure 4.34: Optimization of the number of cold atoms captured. Maximum efficiency for the AOM-R frequency of 205 MHz.

detection zone. This signal is integrated after removing the baseline and the number of atoms are derived. The signal is sampled every $350\mu s$.

Selection pusher laser beam power and frequency were next optimized by scanning the parameters and observing the number of F = 4 detected atoms. The minimum selection power was found to be 1 mW and the optimum frequency 0Γ (minimum number of F = 4 atoms).

The selection slicing procedure was tested. An example is shown on Figure 4.36.

The number of captured atoms on ground is about 4×10^8 and the flourescence and detection signal are saturated. The capture power was therefore decreased from 13 mW to 6 mW per beam and the loading time has been set to 200 ms. The total cycle duration is 0.59 s.

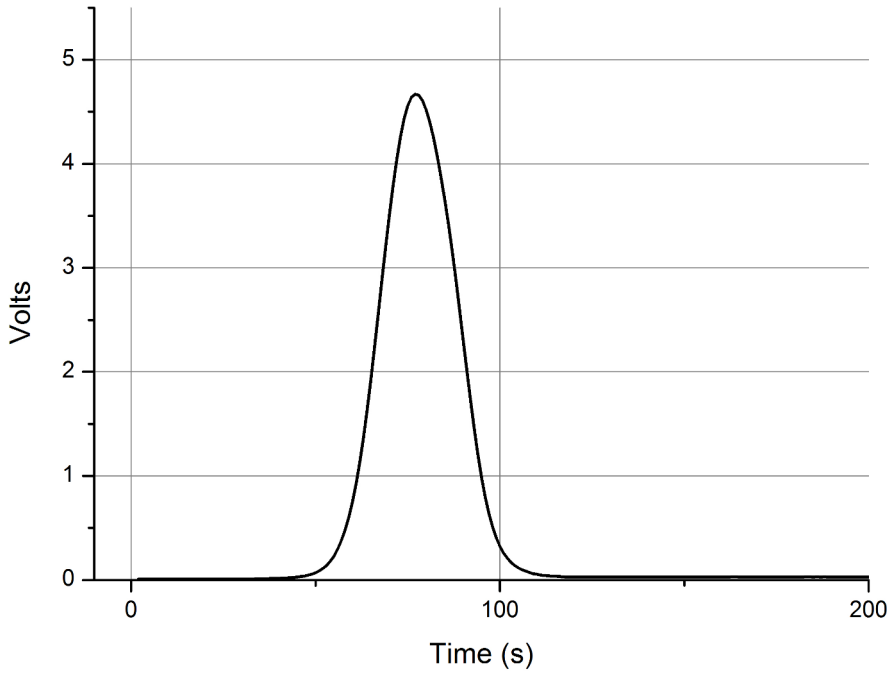

Figure 4.35: Detection zone time of flight signal. A good symmetrical shape.

Preparation phase microwave power was scanned to find the maximum number of atoms in $|F = 3, m_F = 0\rangle$. The Rabi π pulse is -40.4 dBm (Figure 4.37).

The same process was performed for the interrogation power. From the curve on Figure 4.38, the optimum total interrogation power for the Ramsey π pulse is -45 dBm.

Detection lasers parameters were optimized in order to increase the area of the detected time of flight for a launch velocity of 3.56 m/s, to push the atoms in F = 4 and to pump all the atoms to F = 3. The pump laser power needs to be optimized so it does not influence the pushing of the atoms. For the master laser the number of detected F = 4 atoms and for the pump laser the number of detected F= 3 atoms need to be maximized. Optimum pump laser power was determined to be 11.37 μW. Optimum master laser power was determined to be 4 mW and its optimum frequency is +1 MHz (compared to resonance). At larger power some atoms are pumped to the F = 3 level.

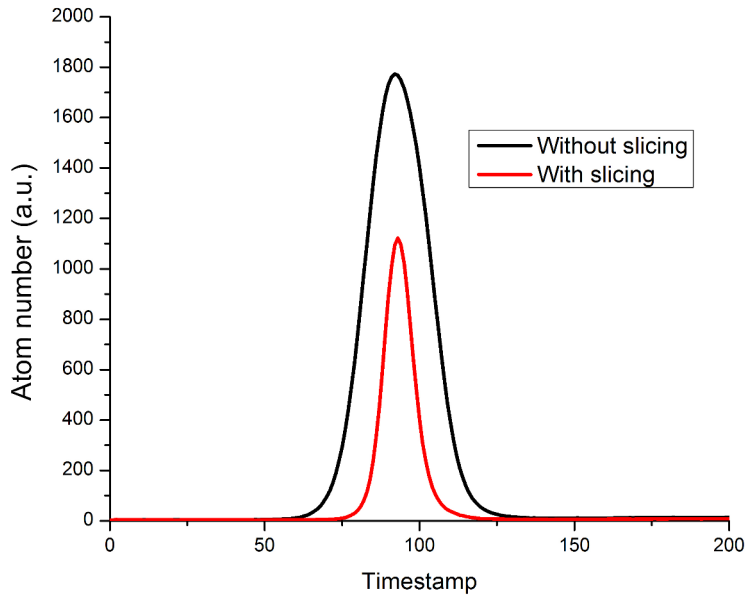

Figure 4.36: Example of the selection slicing. In red TOF with slicing, in black TOF without slicing.

A full frequency scan was performed for the Ramsey interrogation (Figure 4.39). Preparation and selection were deactivated. Large peaks describe cesium $|F = 3, m_F = -3, -2, -1, 0, 1, 2, 3\rangle \rightarrow |F = 4, m_F = -3, -2, -1, 0, 1, 2, 3\rangle$ transitions. Smaller double peaks (red rectangle) are a result of the interrogation cavity microwave field rotation (the field being perpendicular to the applied BP coil magnetic field for a short duration of atom path at the ends of the interrogation cavity). For an illustration see Figure 4.40. Ramsey fringes are clearly seen for all transitions. Finally, with the preparation and selection phases turned on, the Ramsey $m = 0$ interrogation pattern is measured (and shown on Figure 4.41). The central fringe contrast is 89%. This is compliant with the simulations and is due to the interaction zone powers not being balanced (because of gravity deceleration). The transition probability in the first zone is 0.37 and 0.63 in the second zone.

The clock is now ready for operation by locking the microwave signal on the top of the central fringe. To study the performance, the frequency stability and accuracy are examined in the next sections.

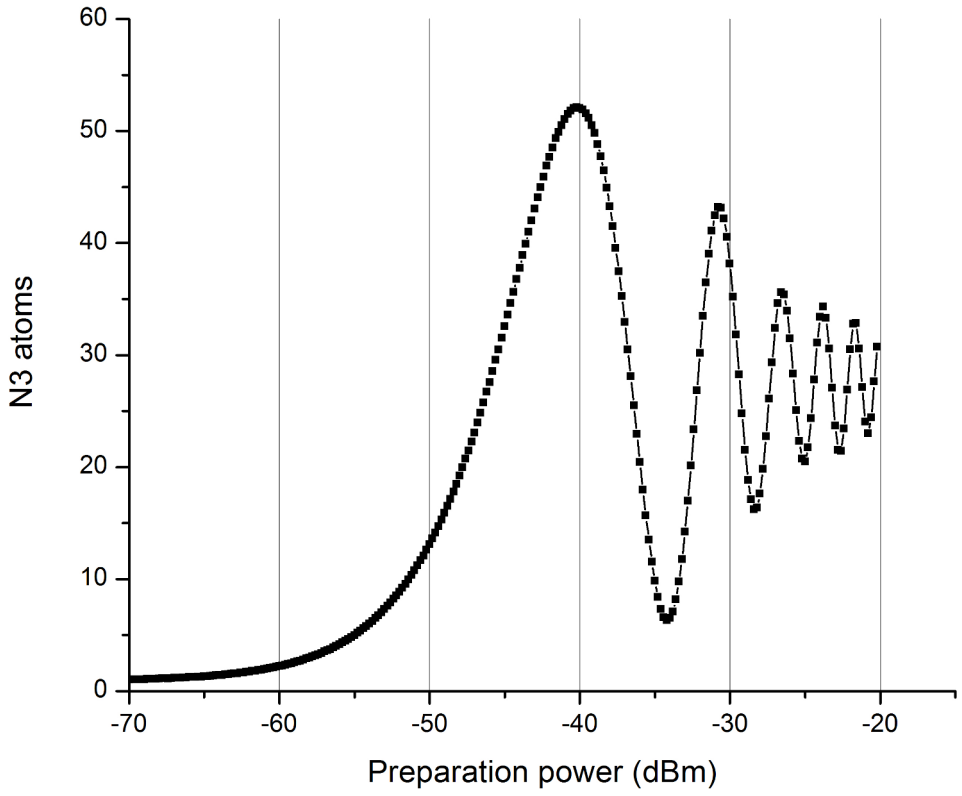

Figure 4.37: Preparation power optimization. Best value was found to be -40.4 dBm for the Rabi π pulse. The dumping is due to the microwave field distribution inside the cavity.

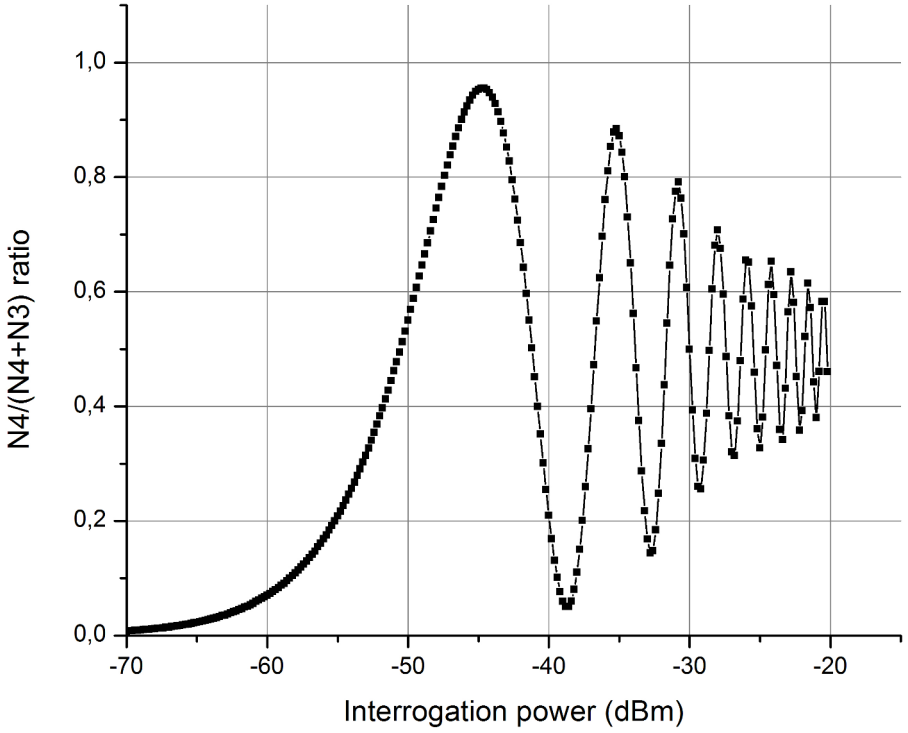

Figure 4.38: Interrogation power optimization. Best value was found to be -45 dBm for the Ramsey $\pi/2$ pulse.

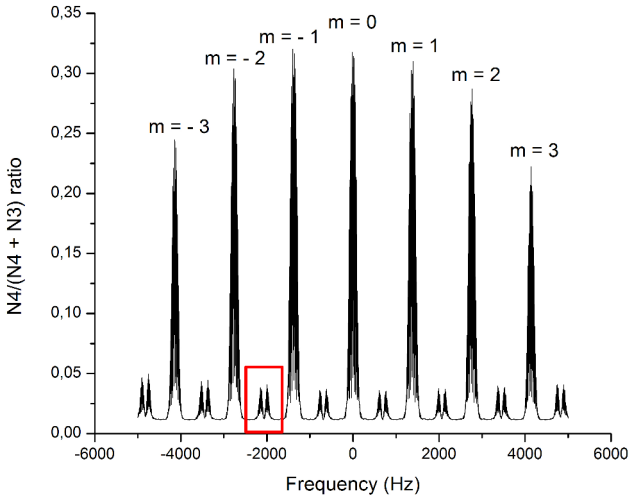

Figure 4.39: Complete frequency scan of Ramsey interrogation without preparation and selection. Resonances of the different cesium hyperfine transitions. Smaller double peaks marked with a red rectangle are explained in the text.

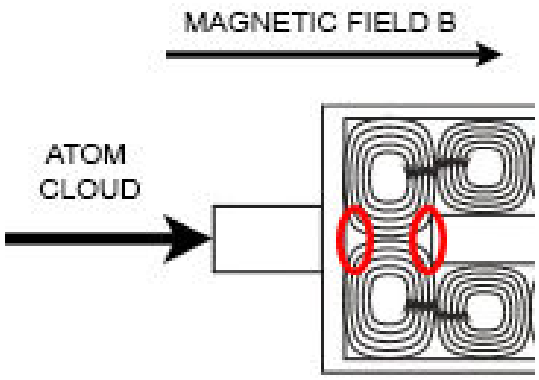

Figure 4.40: Red ellipses show where the magnetic field B is perpendicular to the internal microwave field distribution antinodes causing small double peaks seen on Figure 4.39.

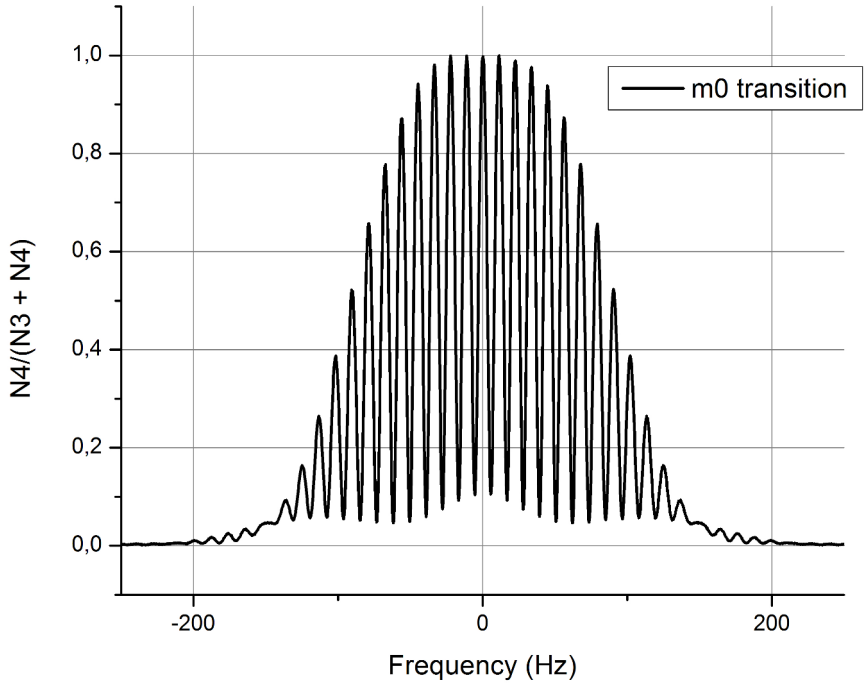

Figure 4.41: Ramsey $m = 0$ interrogation interference pattern. Probability transition as a function of position.

5

PHARAO frequency stability

Short term frequency stability is defined by the noise to signal ratio of the frequency discriminator given by the transition probability P. Long term frequency stability is linked to the frequency accuracy of the clock.

5.1 Sources of noise in PHARAO

The transition probability for Ramsey interrogation for a cold atom clock is given by the following relation:

$$P = \frac{N_4}{N_3 + N_4} = \frac{A}{2}(1 + cos\frac{\pi(\nu - \nu_0)}{\Delta\nu}), \tag{5.1}$$

where N_4 is the detected atom number in level $|F = 4\rangle$, N_3 is the detected atom number in level $|F = 3\rangle$, A is the amplitude of the transition probability ($A \leq 1$), ν is the microwave oscillator frequency, ν_0 is the atomic transition frequency and $\Delta\nu$ is the full width at half maximum (FWHM) of the Ramsey central fringe.

To calculate the effect of fluctuations on clock frequency Equation 5.1 is derived:

$$\delta P = \frac{N_3\delta N_4 - N_4\delta N_3}{(N_3 + N_4)^2} = \frac{A}{2}\frac{\pi}{\Delta\nu}sin\frac{\pi(\nu - \nu_0)}{\Delta\nu}\delta\nu - \frac{A}{2}\frac{\pi(\nu - \nu_0)}{\Delta\nu^2}sin\frac{\pi(\nu - \nu_0)}{\Delta\nu}\delta(\Delta\nu), \tag{5.2}$$

where δP is the fluctuation of transition probability, $\delta\nu$ is the fluctuation of microwave oscillator frequency and $\delta(\Delta\nu)$ is the fluctuation of the FWHM of the Ramsey central fringe due to microvibrations.

Taking into account the frequency modulation ν_m of the oscillator during nominal clock operation:

$$\nu = \nu_0 \pm \nu_m = \nu_0 \pm \frac{\Delta\nu}{2}, \tag{5.3}$$

the sines are equal to 1 in Equation 5.2 and the fluctuation of the clock output frequency is:

$$\delta\nu = \frac{1}{2}\delta(\Delta\nu) + \frac{2\Delta\nu}{A\pi}\frac{N_3\delta N_4 - N_4\delta N_3}{(N_3+N_4)^2}. \tag{5.4}$$

The first term in Equation 5.4 is due to the clock microvibrations.

The second term describes all the noise sources related to the detection of the atoms: fluctuation of number of atoms, noise from determination of N3 and N4 atoms due to quantum projection, photodiode noise, laser noise and microwave noise. These noise sources are not correlated and can be studied separetely. In nominal operation (Equation 5.3 and $N_3 = N_4 = N/2$) the Equation 5.4 becomes:

$$\delta\nu = \frac{1}{2}\delta(\Delta\nu) + \frac{2\Delta\nu}{A\pi}\frac{1}{2}\frac{\delta N_4 - \delta N_3}{N}. \tag{5.5}$$

For the total number of atoms fluctuation (due to capture laser fluctuation) $\delta N_3 = \delta N_4$. Therefore, the second term disappears and this noise contribution is rejected. Other noise contributions will be analyzed next.

5.1.1 Quantum projection

Quantum projection noise (17, 18, 19, 99, 100, 101) originates from the fact the atoms are in a state of superposition after interrogation:

$$|\psi\rangle = \alpha|4\rangle + \beta|3\rangle, \tag{5.6}$$

where the probability to find the system in state $|4\rangle$ is $P = \alpha\alpha^*$ and the probability to find it in $|3\rangle$ is $1 - P$. Therefore, it is a binomial system where $\delta N_3 = -\delta N_4$.

The variance of the second term of Equation 5.5 is:

$$\sigma^2 = (\frac{\Delta\nu}{A\pi})^2(\frac{2\delta N_4}{N})^2 = (\frac{\Delta\nu}{A\pi})^2\frac{4\sigma^2_{N_4}}{N^2}. \tag{5.7}$$

N_4 measurement is binomially distributed and its variance is $N \times P(1-P)$. In nominal operation $P = 1/2$. This contribution is white frequency noise and the Allan deviation is:

$$\sigma_y = \frac{\sigma}{\nu_0}\sqrt{\frac{T_C}{\tau}} = \frac{1}{QA\pi}\frac{1}{\sqrt{N}}\sqrt{\frac{T_C}{\tau}}, \tag{5.8}$$

where $Q = \frac{\nu_0}{\Delta\nu}$ is the quality factor of atomic resonance, T_c is the clock cycle duration and τ is the total integration time.

Quantum projection noise defines the ultimate frequency stability of this kind of clock.

5.1.2 Detection system noise

The number of atoms in the two states $|4\rangle$ and $|3\rangle$ are measured by the fluorescence induced by laser beams.

The noise due to the photodiodes photon $\rightarrow$ electron conversion, the pre-amplifier current $\rightarrow$ voltage conversion and the voltage amplifier transform to noise in the time of flight signal and this transforms to the noise in the number of detected atoms (17, 18, 19, 101). The noise of photodetection is dominated by the photodiode.

The time of flight signal given by the amplifier is filtered and integrated for the two channels:

$$A_i = \int_{-\infty}^{+\infty} h(t)V_i dt, \tag{5.9}$$

where A is the integrated area proportional to the number of detected atoms in each state i, $V(t)$ is the voltage signal and $h(t)$ is the filter response.

Developed variance of the second term of Equation 5.5 is:

$$\sigma^2 = (\frac{\Delta\nu}{A\pi})^2(\frac{\delta N_4 - \delta N_3}{N})^2 = (\frac{\Delta\nu}{A\pi})^2\frac{\sigma_{N_4}^2 + \sigma_{N_3}^2 - 2 < \delta N_3 \delta N_4 >}{N^2}. \tag{5.10}$$

Two different photodiodes are used for detection of N3 and N4 atoms. Since photodiode noise is not correlated the correlation coefficient in Equation 5.10 is $< \delta_{N_3}\delta_{N_4} >= 0$. Equation 5.10 and the left side of Equation 5.8 give the Allan deviation contribution (white noise):

$$\sigma_y(\tau) = \frac{1}{QA\pi} \times \frac{\sqrt{2}\sigma_{\delta N}}{N} \times \sqrt{\frac{T_C}{\tau}}. \tag{5.11}$$

5.1.3 Detection laser noise

The spontaneous emission rate depends on the laser frequency offset δ (Γ is the the spontaneous decay rate) and laser intensity I:

$$\gamma(t) = \frac{\Gamma}{2}\frac{s(t)}{1+s(t)}, \tag{5.12}$$

where $s(t)$ is the detection laser beam saturation:

$$s(t) = \frac{I(t)/I_S}{1+4\delta^2/\Gamma^2}. \tag{5.13}$$

In the worst case where $s(t) << 1$ and $\delta = \Gamma/2$ the spontaneous emission rate fluctuation (spectral density $S_{\delta\gamma}(f)$) (17, 18, 19, 101) is given by:

$$S_{\delta\gamma}(f) = (\frac{2\omega_{laser}}{\Gamma})^2 S_y(f) + S_{\delta I/I}(f), \tag{5.14}$$

where ω_{laser} is the laser frequency, $S_{\delta I/I}(f)$ is the relative intensity noise spectral density and $S_y(f)$ is the relative frequency power spectral frequency density.

Spontaneous emission rate fluctuations invoke time of flight integrated area fluctuations for the two states. The integrated areas are proportional to the number of atoms. A TOF signal has a Gaussian distribution:

$$f(t) = \frac{1}{\sqrt{2\pi}w} exp(-\frac{t^2}{2w^2}), \tag{5.15}$$

where w is the width of the Gaussian distribution depending on the initial width w_x at launch, launch velocity v_0 and the width of the velocity distribution w_v. The TOF signal width is then at time t_{flight}:

$$w = \frac{1}{v_0}\sqrt{w_x^2 + (w_v t_{flight})^2}. \tag{5.16}$$

The atomic cloud is modelized with the parameters $w_x = 5.52 \times 10^{-3}m$ and $w_v = 8 \times 10^{-3}m$.

The atoms pass through the two detection channels at two different times separated by Δt. Time of flight integrated area fluctuations are related to the number of atoms fluctuations for the two states:

$$\delta N_3 = N_3 \times \int_{-\infty}^{+\infty} \delta_\gamma(t) f(t) dt \tag{5.17}$$

$$\delta N_4 = N_4 \times \int_{-\infty}^{+\infty} \delta_\gamma(t) f(t - \Delta t) dt, \tag{5.18}$$

where $\delta_\gamma(t)$ is the spontaneous emission rate fluctuation.

The frequency fluctuation from Equation 5.5 is:

$$\delta\nu = \frac{1}{2}\int_{-\infty}^{+\infty} \delta_\gamma[f(t) - f(t - \Delta t)] dt. \tag{5.19}$$

Laser noise is converted to clock transition frequency fluctuation by a linear filter impulse response:

$$h(t) = \frac{1}{2} \times (f(t) - f(t - \Delta t)). \tag{5.20}$$

The frequency response $H(f)$ is obtained by doing a Fourier transform on $h(t)$:

$$H(f) = \frac{1}{2}(1 - e^{-2i\pi f \Delta t}) \times e^{-2\pi^2 f^2 w^2}. \tag{5.21}$$

Standard deviation of the frequency fluctuation is then:

$$\sigma^2 = \int_0^{+\infty} S_{\delta\gamma}(f)|H(f)|^2 df. \tag{5.22}$$

From the left side of the Equation 5.8, the Allan deviation contribution is:

$$\sigma_y(\tau) = \frac{1}{AQ\pi} \times \gamma_{laser} \times \sqrt{\frac{T_C}{\tau}}, \tag{5.23}$$

where $\gamma_{laser} = \sigma_{\delta\nu}$ and is independent on the number of detected atoms N.

5.1.4 Local oscillator noise - Dick effect

Since the microwave signal is measured during the interaction time t_0 with a period T_C a stroboscopic effect is present which samples the noise at all frequencies multiple of $1/T_C$. This translates to a degradation of the total transition probability of atoms and in turn short term clock stability. The effect is called the Dick effect (102, 103, 104).

Allan deviation contribution is:

$$\sigma_y = (\sum_1^{+\infty} \frac{g_n^2}{g_0^2} S_y^{LO}(nf_c))^{\frac{1}{2}} \sqrt{\frac{1}{\tau}} = \gamma_{LO}, \tag{5.24}$$

where the sum describes the sampling for every cycle, $g_n = \frac{1}{T_C}\int_0^{T_C} g(t)e^{i2\pi n f_c t}dt$ is the Fourier transform of the sensitivity function at frequencies $1/T_C$, g_0 is the normalization coefficient, S_y^{LO} is the relative frequency noise spectral density.

For an explanation of the sensitivity function, its effect on the Ramsey transition probability and the calculation of the frequency displacement see Appendix 10.

The relative frequency noise was derived from frequency phase noise measurement $S_\phi(t)$ with the following relation:

$$S_y(f) = \frac{f^2}{\nu_0^2} S_\phi(t) = S_{-1}f^{-1} + S_0 f^0 + S_1 f + S_2 f^2, \tag{5.25}$$

where f is the Fourier frequency, ν_0 is the oscillator frequency at which the noise is measured and S_{-1}, S_0, S_1 and S_2 are the coefficient describing the frequency noise density spectra. Generally, the most dominant contributions for the Dick effect is the flicker frequency noise given by S_{-1}.

5.1.5 Micro-vibration effect

As introduced in Section 3.1.1, ISS operations and crew activity cause micro-vibrations. The level of activity on the station in terms of induced micro-vibrations is divided into 1 (calm), 2 (perturbed - normal crew activity) and 3 (very perturbed - sport activity). The ISS average activity level distribution:

$$\begin{aligned} \alpha_1 &= 33\% \\ \alpha_2 &= 58\% \\ \alpha_3 &= 9\%, \end{aligned} \tag{5.26}$$

Simulations were performed to obtain the noise spectrum of the ISS at the position of PHARAO. However, the calculations have very low confidence. The spectrum has to be determined by direct orbit measurement with a PHARAO accelerometer placed inside BEBA.

Transverse vibrations lead to a loss of atoms due to the displacement of cavity walls in relation to the atom cloud. This contribution can be neglected.

Longitudinal vibrations influence the time of flight of the atoms by fluctuation δz of the flight length z and consequently the FWHM of the measured resonance.

To have an order of magnitude on this effect an approximate calculation is performed.

The first term in Equation 5.5 $\frac{1}{2}\Delta\nu$ describes the microvibration effect on the frequency fluctuation.

The average resonance width is inversely proportional to the average interrogation time:

$$\Delta\nu = \frac{1}{2t_0} = \frac{v}{2L}, \tag{5.27}$$

where v is the atom velocity.

The frequency fluctuation is then:

$$\delta\nu = \frac{\delta v}{4L}, \tag{5.28}$$

For L = 0.219 m :

$$\delta\nu \approx \delta v, \tag{5.29}$$

To have a clock stability better than 10^{-13} the atomic velocity fluctuation has to be much lower than 1 mm/s.

In term of spectral density the relation between clock frequency and acceleration are given by the following equation:

$$S_y(f) = \frac{1}{(4L)^2}\frac{1}{\nu_0^2} \times S_v = \frac{1}{(4L)^2}\frac{1}{\nu_0^2}\frac{S_{acceleration}}{f^2}, \tag{5.30}$$

where S_v and $S_{acceleration}$ (obtained by the on board accelerometer) are the spectral densities of the velocity and acceleration fluctuations. The relative spectral density related to tube microvibrations is then:

$$S_y^{tube} = 10^{-20} \times \frac{S_{acceleration}}{f^2}. \tag{5.31}$$

The effect of micro-vibration on oscillator stability was taken into account when selecting the PHARAO OUS oscillator. The selected quartz crystal has a vibration effect on relative frequency described by vib.coeff $= 1.73 \times 10^{-10}/g$. The relative spectral density is given by:

$$S_y^{quartz} = \text{vib.coeff}^2 \times S_{acceleration} = 3 \times 10^{-22} S_{acceleration}. \tag{5.32}$$

Clearly, the main microvibration noise contribution is due to the cesium tube acceleration.

A full calculation has to take into account the sampling effect of the microvibration fluctuations evaluated by the sensitivity function. This calculation is similar to the calculation of the microwave noise contribution.

5.2 Experimental results and discussion

The noise contributions affecting the signal stability and explained in the previous sections are decorrelated and their variances can be decomposed and calculated independently. Allan deviation is a quadratic sum of the main individual contributions: (101):

$$\sigma_y(\tau) = \frac{1}{A\pi Q}\left(\frac{1}{N} + \frac{2\sigma_{\delta N}^2}{N^2} + \gamma_{laser}^2 + \gamma_{LO}^2\right)^{1/2}\sqrt{\frac{T_c}{\tau}}, \tag{5.33}$$

where the 5 terms in the parenthesis are the quantum projection noise, detection system noise for the two channels, noise due to power and frequency fluctuation of the laser and local oscillator noise, respectively.

The quantum projection noise is inversely proportional to the square root of the number of detected atoms and the detection system noise is inversely proportional to the number of atoms. As will be shown later, the clock frequency shift is increased with a larger number of atoms due to cold collision. Optimization of clock performance depends on a balance between the quantum projection noise and cold collision.

The Ramsey m = 0 resonance pattern produced by PHARAO is given on Figure 5.1. The central fringe has a width of 5.6 Hz and a contrast of 0.9. The contrast value is because of the unsymmetrical Ramsey interrogation resulting from deceleration by gravity.

After locking on the central fringe the PHARAO stability has been evaluated (on ground without the microvibration effects) at $3.3 \times 10^{-13} \times t^{-1/2}$. The stability curve of PHARAO referenced to a hydrogen maser can be seen on Figure 5.2. For time $\tau < 10sec$ the transient effect of the lock on the atomic resonance is present. For long duration $\tau > 10000sec$ the instability of the hydrogen maser influences the measurement. During these measurement the 100 MHz PHARAO signal is phase locked on the hydrogen maser. Stability of PHARAO is given for time $10sec < \tau < 10000sec$.

To evaluate the individual noise contributions PHARAO was operated in nominal mode with the internal oscillator (microwave source from Section 4.3) and in backup mode with the external cryogenic oscillator (no Dick effect).

Measurements were performed for a varying number of detected atoms. The number of atoms were varied by changing the microwave field power in the preparation cavity. The stability level as a function of the atom number is shown on the Figure 5.3. By performing a fit on the cryogenic oscillator stability curve the Allan deviation contributions from the laser noise (coefficient P1), quantum projection noise (coefficient P2) and detection system noise (coefficient P3 is the asymptotic value independent on the number of atoms) are $7 \pm 2 \times 10^{-14}$, $1.89 \pm 0.09 \times 10^{-12}$ and $4.9 \pm 0.5 \times 10^{-14}$, respectively.

The coefficients from Figure 5.3 are given for the total number of atoms detected in V×ms. The real number of atoms is proportional to the measurement with the

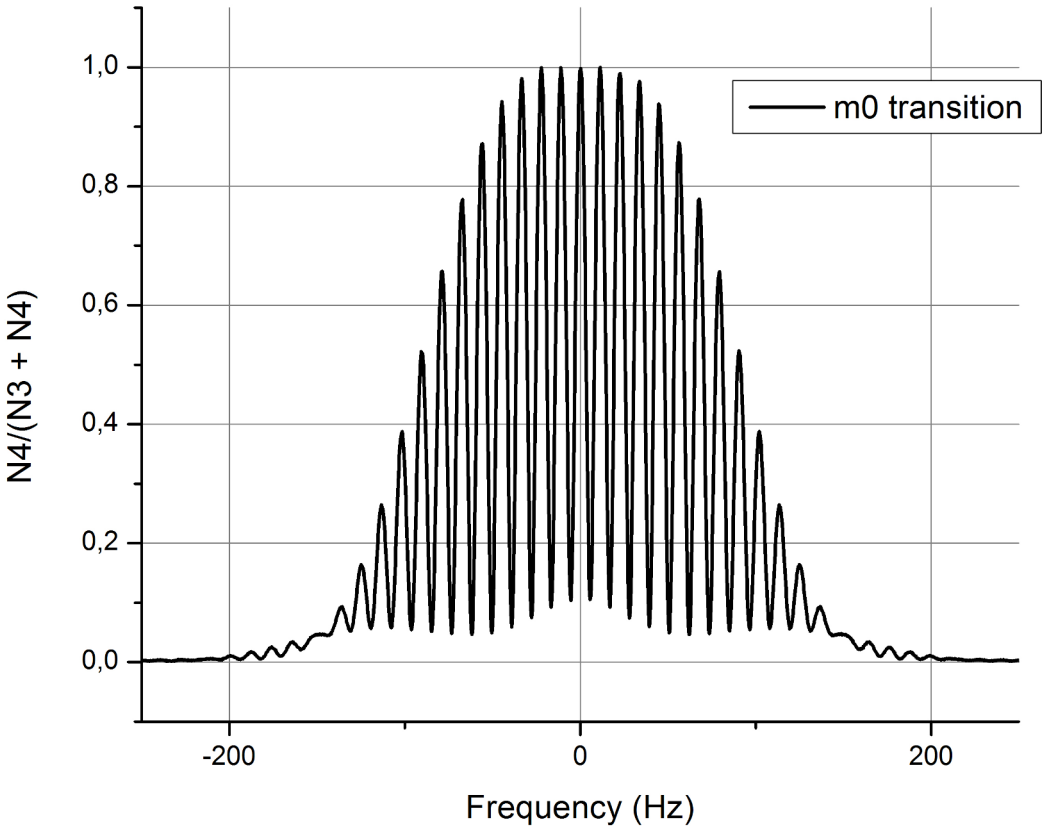

Figure 5.1: Ramsey m = 0 interference pattern.

coefficient k:

$$N(V \times ms) = k \times N. \tag{5.34}$$

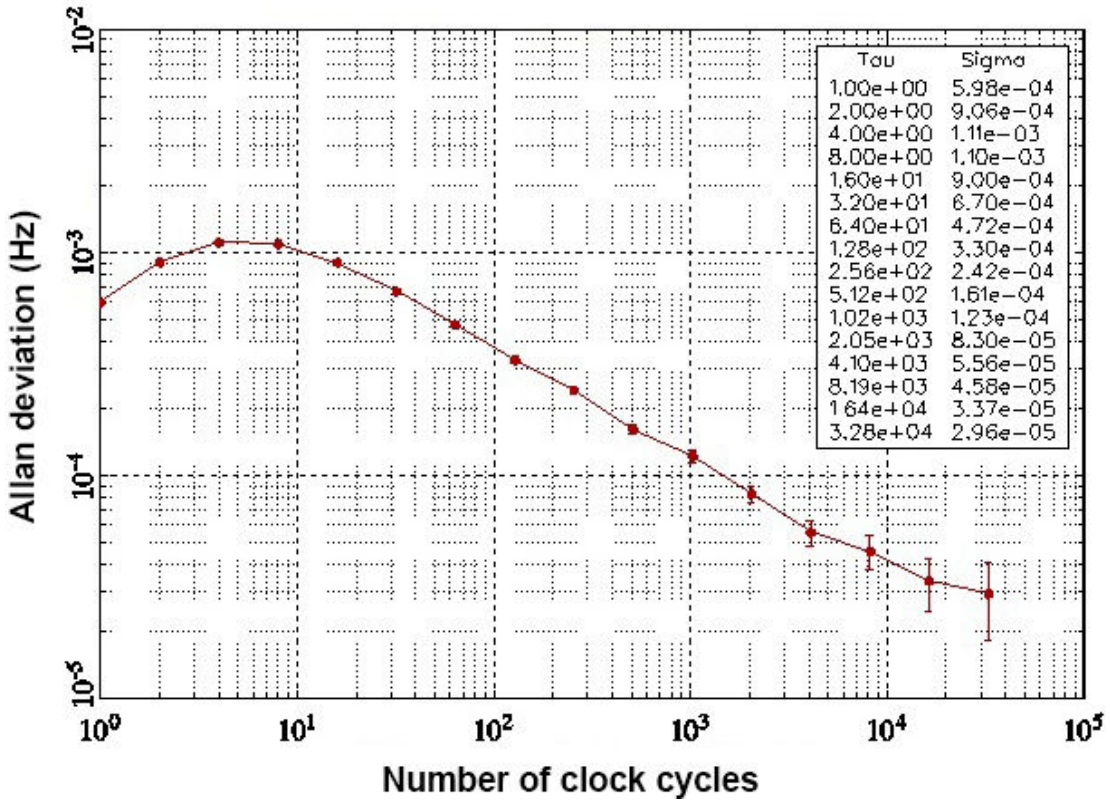

Figure 5.2: On ground PHARAO frequency stability as a function of number of clock cycles (0.59s per cycle).

To determine this coefficient, the value of the quantum projection noise is used because its value is more significant than the other two. The quantum projection noise coefficient P2 is compared with the quantum projection noise term in Equation 5.33. The proportionality coefficient is deduced from the following expression:

$$\frac{P2}{\sqrt{k \times N}} = \frac{1}{A\pi Q}\frac{1}{\sqrt{N}}. \tag{5.35}$$

where $A = 0.9$ and Q is the resonance quality deduced from Figure 5.1. Finally, the coefficient value is $k = 7.687 \times 10^{-5}$. Following from that, the maximum number of detected atoms on Figure 5.3 is 5.0×10^6 (385 V×ms). For this number of atoms the capture laser power was increased to 12 mW just below the saturation signal.

For that number of atoms the Allan deviation of quantum projection is 1.2×10^{-13} after 1 sec. By using the coefficient k and comparing P3 with Equation 5.33 the

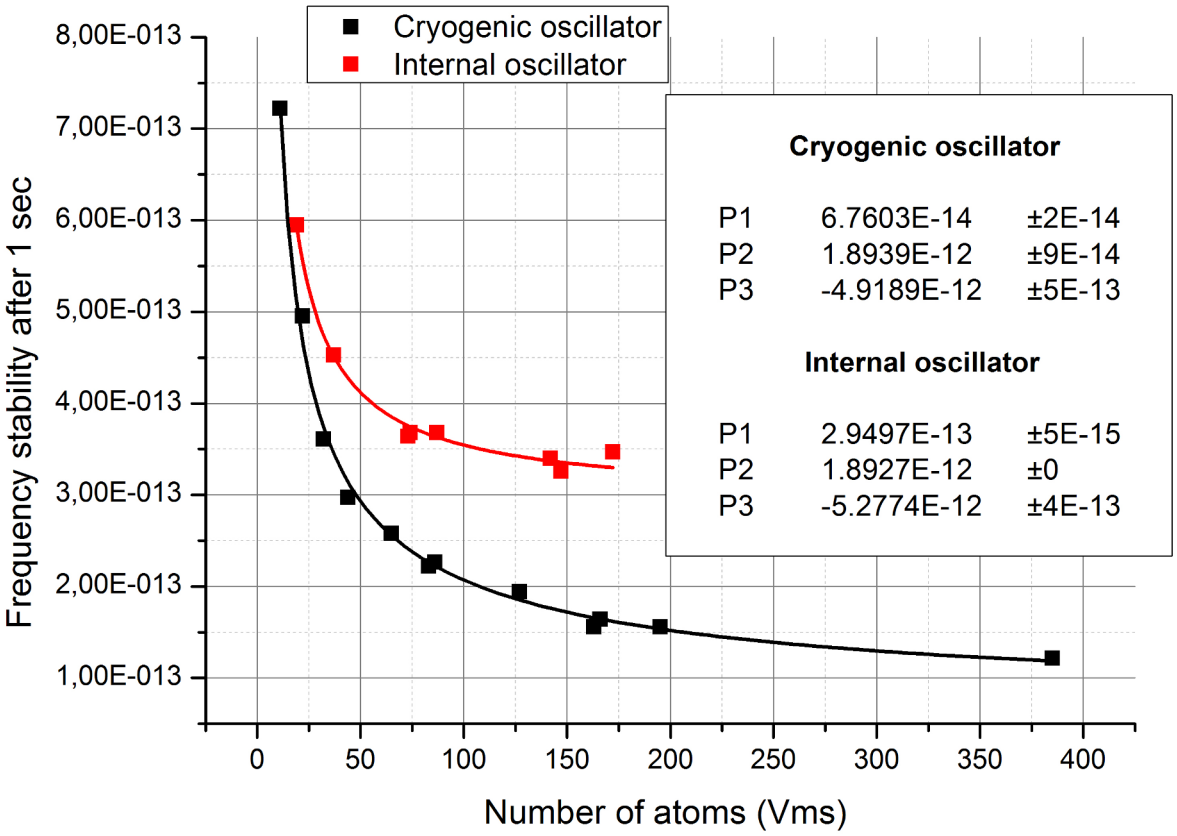

Figure 5.3: Frequency stability after 1 sec (Allan deviation) as a function of the number of atoms (in V×ms) for the internal (in red) and cryogenic (in black) oscillator. In the inset are the fit coefficients. P1 represents the laser noise, P2 represents the quantum projection noise and P3 represents the detection system noise.

detection noise is $\sigma_{\delta N} = 295.698$. This number represents about 300 atoms.

Figure 5.4 shows the measured spectral noise density of the two photodiodes. The noise can be decomposed into flicker noise (level 0.8 $\mu V/\sqrt{Hz}$), white noise (level 4 $\mu V/\sqrt{Hz}$) and f-noise (level 0.03 $\mu V/\sqrt{Hz}$).

Table 5.1 shows the detection noise $\sigma_{\delta N}$ as a function of atomic velocity deduced from previous spectral noise densities.

Detection signal digitization also needs to be taken into account when examining the detection system noise. The sampling is performed with 11 bits for a range between

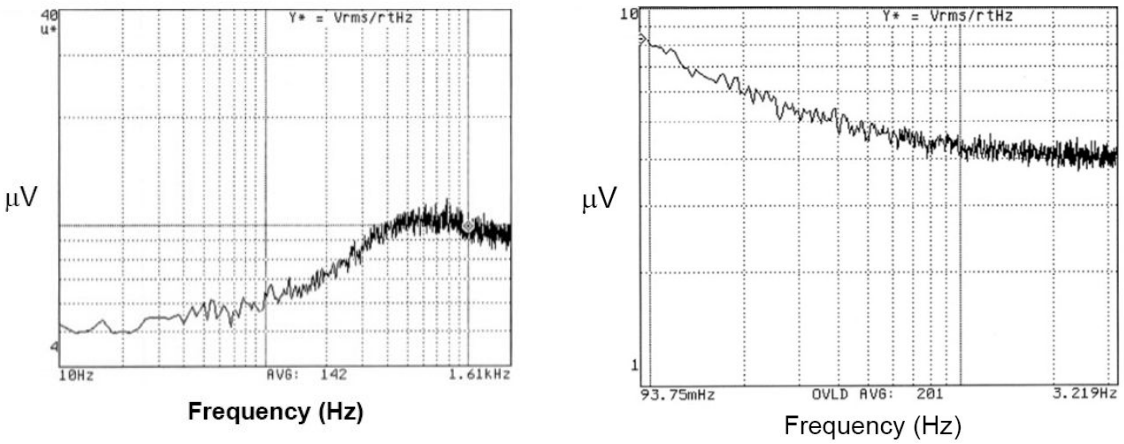

Figure 5.4: Left: spectral noise density of the photodiodes (low frequency). Right: spectral noise density of the photodiodes (high frequency).

Velocity (cm/s)	$\sigma_{\delta N}$
5	115
10	63
20	30
> 30	20

Table 5.1: Number of atoms variance due to photodiode noise (detection system noise) as a function of atomic velocity. Does not take into account the digitization noise significant on ground.

0-5 V. The LSB is q = 2.5 mV. The related acquisition noise is then $\frac{q^2}{12}$. To calculate the number of atoms 340 samples are used (half for the time of flight peak and half for the baseline). Consequently, the digitization noise is $340 \times \frac{q^2}{12} = 1.77 \times 10^{-4} V^2$. The RMS is $\sqrt{1.77 \times 10^{-4} V^2} \approx 13mV$. From the TOF signal and the number of atoms, 1 atom contributes 56 mV. Consequently, $\sigma_{\delta N} = 232.14$. This is multiplied by $\sqrt{2}$ to obtain the total noise contribution for the two channels and amounts to $\sigma_{\delta N} = 328.3$ The number of samples have not been minimized during the measurement. In microgravity a larger gain will be used and the sample number optimized to reach the noise level given Table 5.1 and make the effect negligible.

As the laser noise coefficient P1 does not depend on the number of atoms the value

remains the same and the Allan deviation for detection laser noise is $7 \pm 2 \times 10^{-14}$ after 1 sec.

Detection laser noise contribution is evaluated to a similar value of 7.64×10^{-14} using the laser frequency and intensity fluctuations spectrum. The PHARAO laser source spectral densities $S_{\delta I/I}(f)$ and $S_y(f)$ have been measured and can be seen on Figures 5.5 and 5.6.

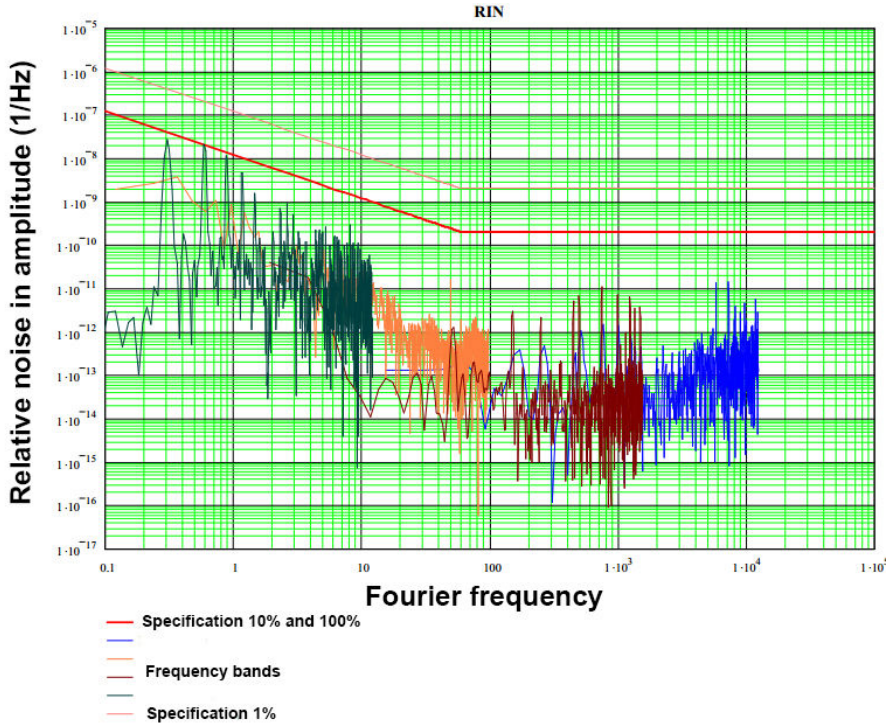

Figure 5.5: Relative noise in amplitude (1/Hz) as a function of Fourier frequency. The red lines are specifications as a function of power and different colors are different frequency bands measurement.

The atomic cloud is modelized with the parameters $w_x = 5.52 \times 10^{-3} m$ and $w_v = 8 \times 10^{-3} m$. For 7 different launching velocities detection laser noise effect on clock stability after 1 sec of integration was calculated as seen on Figure 5.7.

The last noise contribution, the microwave phase noise is deduced from the P1 coefficient. The P1 coefficient of the internal oscillator stability fit contains both the detection laser noise and the oscillator noise. By comparing it to the cryogenic oscillator

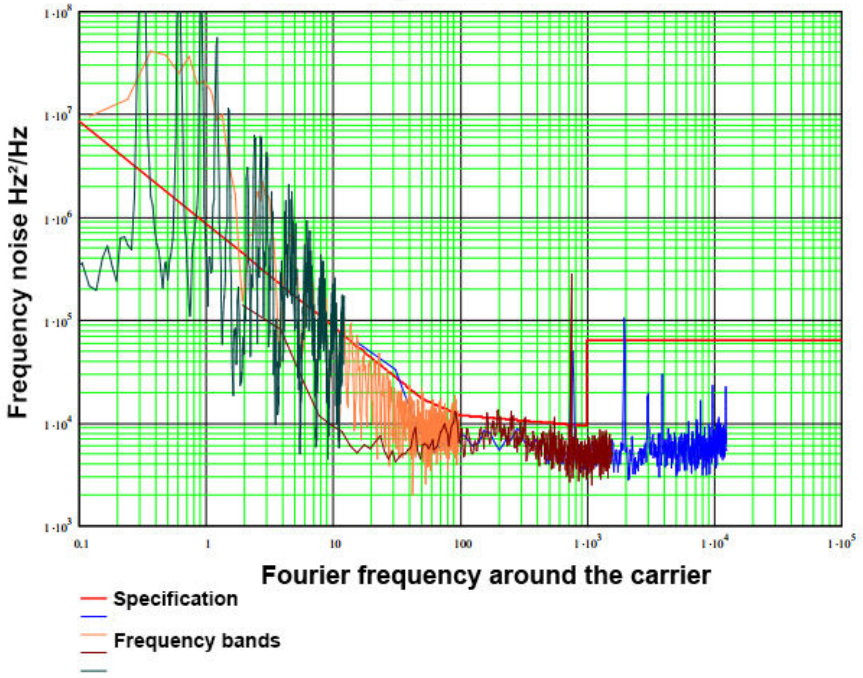

Figure 5.6: Frequency noise (Hz^2/Hz) as a function of Fourier frequency around the carrier. The red line is the specification and different colors represent different frequency band measurements.

P1 coefficient, the local oscillator noise contribution can be derived:

$$\sqrt{\sigma^2} = P1^2_{internal} - P1^2_{cryo} = 2.87 \times 10^{-13} \tag{5.36}$$

The phase noise $S_\phi(t)$ of the microwave source has been measured by a comparison with the cryogenic oscillator. The phase noise of the cryogenic oscillator is at least 10 times smaller than the microwave source and has no contribution in the measurement. The noise of the microwave source is mainly defined by the quartz oscillator noise. The setup used to evaluate the Dick effect is shown on Figure 5.8.

The phase noise spectrum for the local oscillator is shown on Figure 5.9. Multiplication by the factor $\frac{f^2}{\nu_0^2}$ gives the frequency noise spectrum $S_y(f)$.

From Figure 5.9 and Equation 5.24 the stability contribution of 2.3×10^{-13} was calculated. The result is somewhat smaller than 2.87×10^{-13} as deduced from the P1 coefficients. This is probably because of additional phase noise contributions from the experimental setup used to lock PHARAO on the H-maser (long cable sensitive

	v(m/s)	sigma @ 1s
Microgravity	0,15	$3{,}70 \times 10^{-16}$
	0,20	$7{,}38 \times 10^{-16}$
	0,30	$1{,}92 \times 10^{-15}$
	0,60	$8{,}58 \times 10^{-15}$
	1,00	$1{,}92 \times 10^{-14}$
	3,00	$6{,}37 \times 10^{-14}$
Gravity	3,54	$7{,}64 \times 10^{-14}$

Figure 5.7: Detection laser noise effect on clock stability after 1 sec as a function of launch velocity. The noise was calculated with the gravity deceleration for velocity 3.54 m/s and this result can be compared to the one obtained experimentally.

to vibrations, EMC isolation of the phase comparator, ...). The setup has not been verified yet.

PHARAO orbit stability performance has been evaluated by simulation based on the previous results. Figure 5.10 shows the number of detected atoms (10^7 atoms are launched) as a function of the launch velocity in microgravity. Smaller number of atoms with slower velocities implies larger atomic cloud thermal expansion leading to larger atom loss.

Figure 5.11, Figure 5.12 and Figure 5.13 show the simulated Ramsey interrogation patterns for different launch velocities.

Table 5.2 gives the simulated Allan deviation for the quantum projection, detection noise and laser noise followed by the Allan deviation of local oscillator noise and total Allan deviation as a function of the launch velocity. The limiting stability factor for low velocities (lower than 100 mm/s) is the photodiode noise as shown on Table 5.1. Stability does not change significantly for launch velocities 100-1000 mm/s and remains in the 1×10^{-13} range after 1 sec. Constant stability will allow for the study of the systematic effects such a cold collision to be performed in orbit.

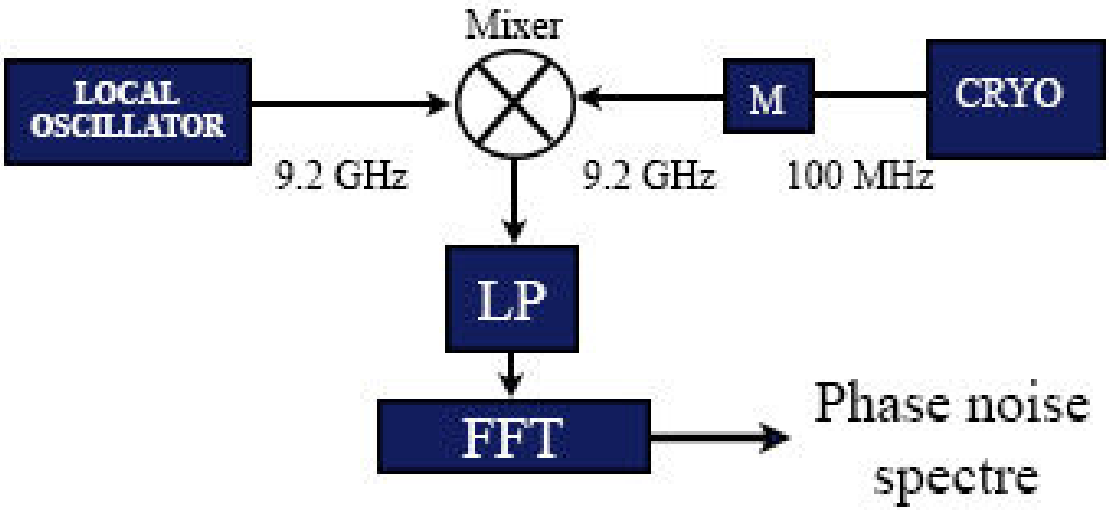

Figure 5.8: Setup for measuring the oscillator phase noise. Local oscillator signal is mixed with the cryogenic oscillator signal (which is transformed by a multiplicator (M) from 100 MHz to 9.2 MHz). Cryogenic oscillator phase noise is low and is used as a reference. The mixer outputs the two signal sum and difference. The sum is filtered by a low pass filter and the difference is fast Fourier transformed (FFT) to produce a frequency spectrum.

Launch velocity (mm/s)	Duration of cycle (s)	Number of atoms	Quantum projection noise	Detection noise	Laser noise	Dick effect	Expected stability in space
50	11,4	8230	1,932E-13	3,46367E-13	1E-16	1,3E-13	4,17372E-13
100	5,7	30480	1,267E-13	6,46413E-14	2E-16	1,09E-13	1,79176E-13
200	2,85	116710	9,211E-14	1,14384E-14	7,38E-16	9,88E-14	1,35559E-13
300	1,9	253300	7,567E-14	4,25252E-15	1,92E-15	9,62E-14	1,22483E-13
400	1,425	426960	6,975E-14	3,01923E-15	3E-15	9,7E-14	1,1955E-13
500	1,14	618050	6,555E-14	2,35829E-15	6,5E-15	1E-13	1,19768E-13
600	0,95	820080	6,319E-14	1,97361E-15	8,58E-15	1,05E-13	1,22863E-13
700	0,81429	1,013E6	6,349E-14	1,78353E-15	9E-15	1,1E-13	1,27338E-13
800	0,7125	1,209E6	6,601E-14	1,69733E-15	9,5E-15	1,16E-13	1,33813E-13
900	0,63333	1,388E6	6,414E-14	1,53952E-15	1E-14	1,21E-13	1,37324E-13
1000	0,57	1,56E6	6,571E-14	1,48802E-15	1,92E-14	1,28E-13	1,45164E-13

Table 5.2: Simulation in microgravity. Table shows launch velocity (mm/s), duration of cycle (s), number of atoms, Allan deviation after 1 sec (quantum projection, detection noise, laser noise), Allan deviation after 1 sec of the local oscillator and total Allan deviation after 1 sec.

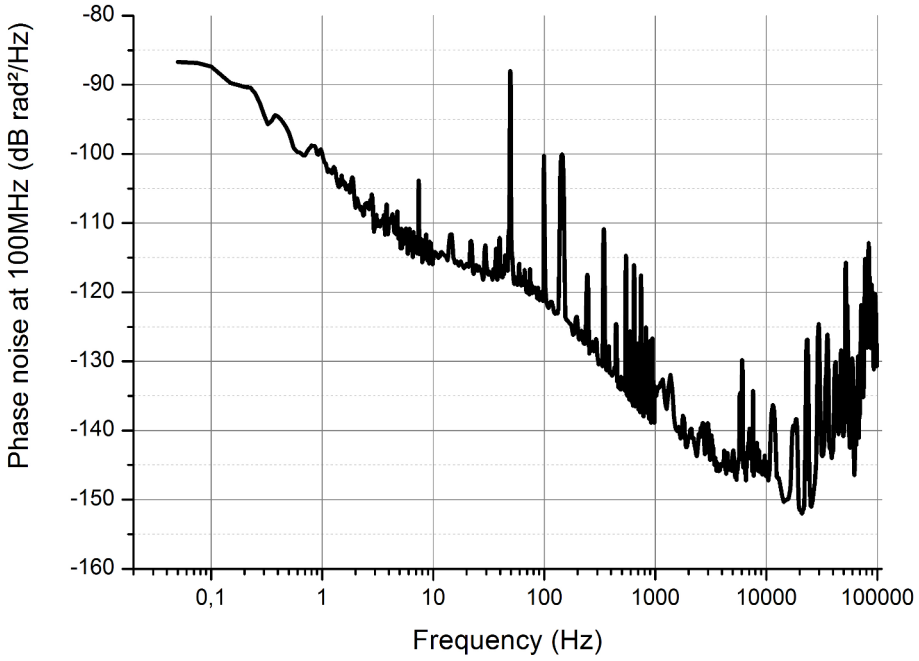

Figure 5.9: FFT phase noise spectrum of the microwave oscillator.

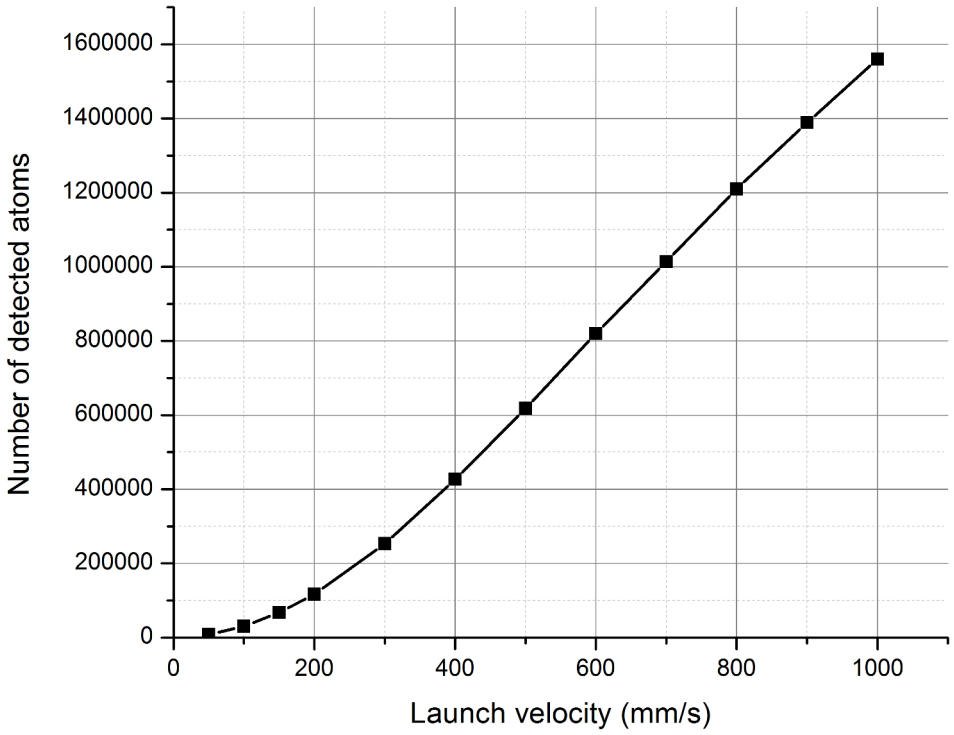

Figure 5.10: Number of detected atoms as function of launch velocity in orbit. Simulation.

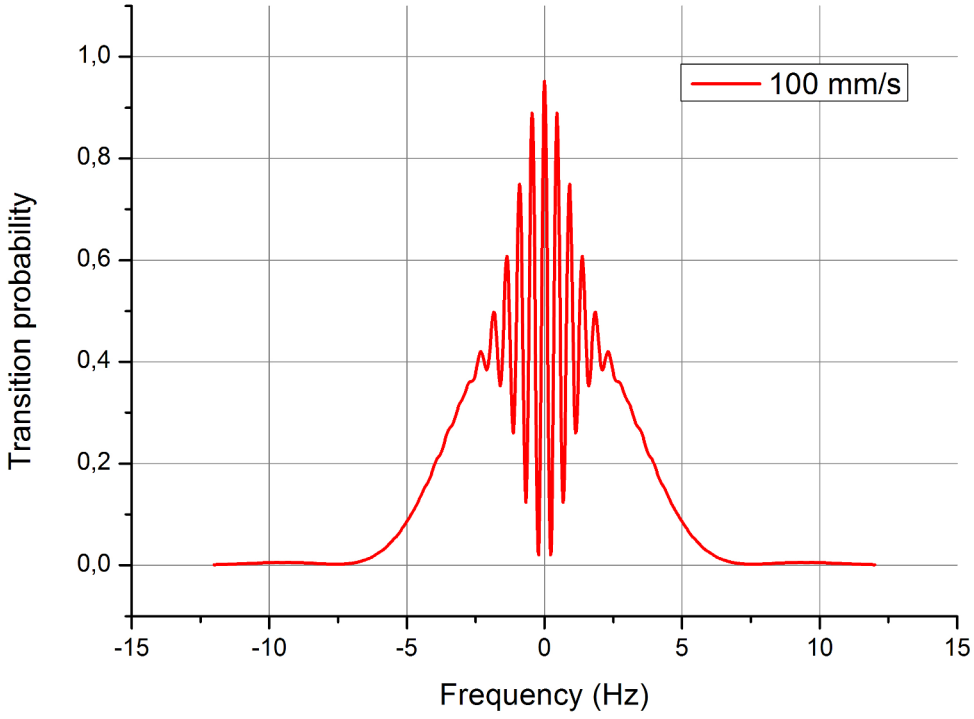

Figure 5.11: Simulated interrogation cavity Ramsey transitions for launch velocity of 100 mm/s.

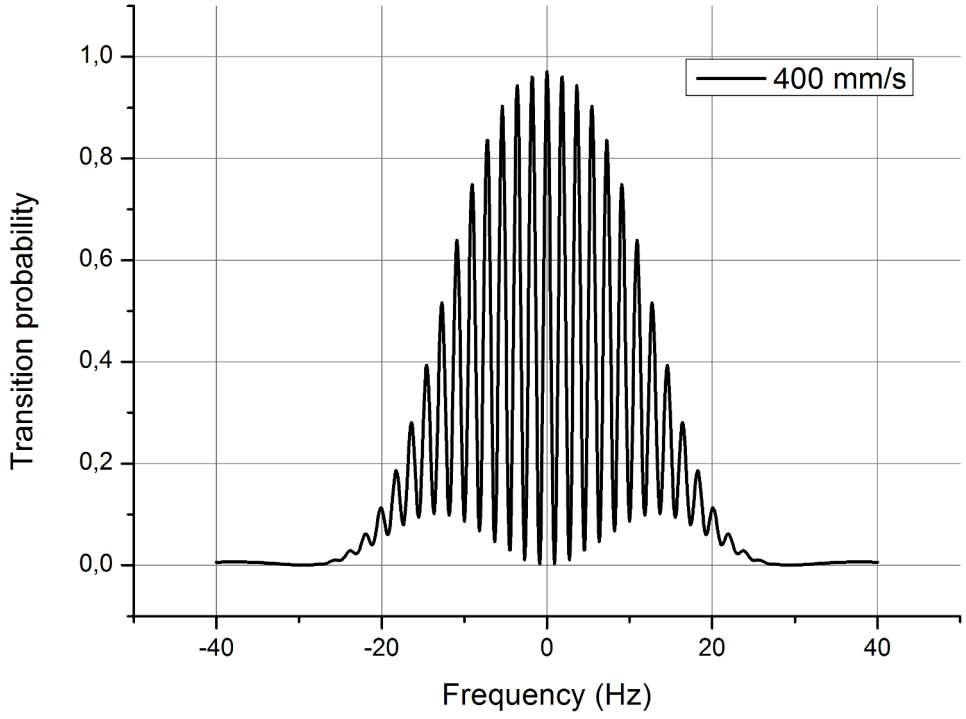

Figure 5.12: Simulated interrogation cavity Ramsey transitions for launch velocity of 400 mm/s.

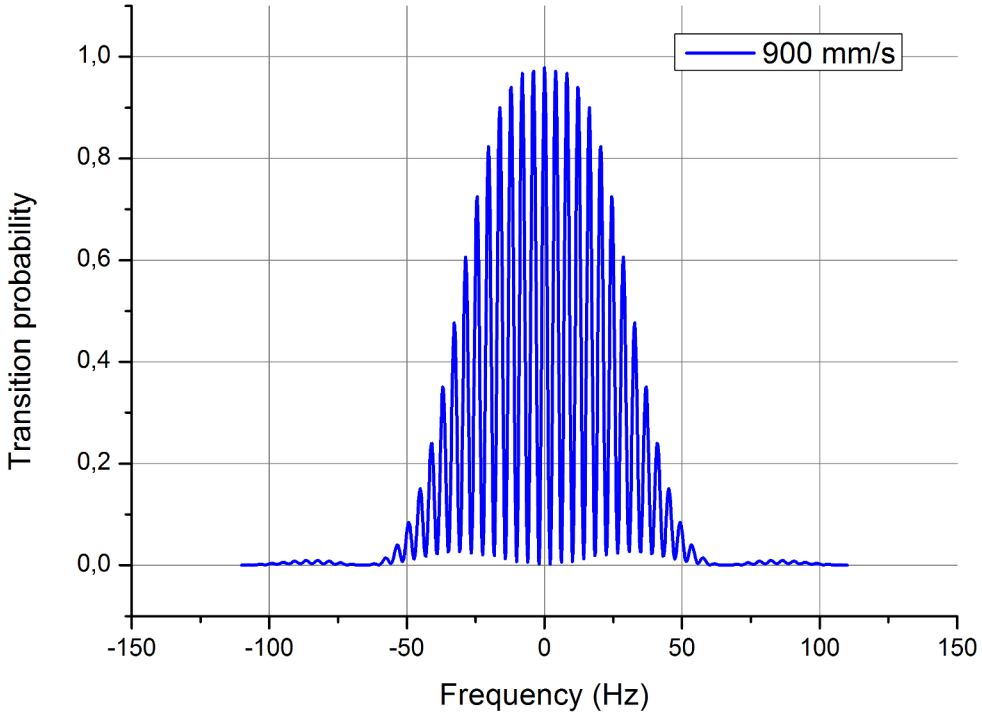

Figure 5.13: Simulated interrogation cavity Ramsey transitions for launch velocity of 900 mm/s.

6

PHARAO frequency accuracy: preliminary evaluation on the FM

The frequency of the hyperfine cesium resonance is given by the definition of the second. Experimentally, the cesium atoms are submitted to many perturbations which shift the hyperfine resonance frequency. Consequently, to correct the frequency delivered by the clock and have a frequency standard all these systematic effects (31) need to be evaluated with the best possible accuracy

In this section the significant systematic effects will be introduced theoretically and experimental results will be presented. As the clock architecture is not optimized to operate on ground (limited frequency stability, limited measurement duration, velocity variation due to gravity) the evaluation is performed at a level of 10^{-15}. With this level we are confident to achieve a frequency accuracy in microgravity in the 10^{-16} range.

Due to clock design and subsystem performances, some of these offsets are negligible. These are offsets due to microwave leaks, due to microwave spectral quality and the electric field. On the other hand, offsets due to black body radiation, magnetic field, atom interactions and the Doppler effect cannot be disregarded.

6.1 Second order Zeeman effect

The most important systematic effect is the interaction of atoms with the magnetic field. A magnetic field is applied to separate the atom energy levels into multiple hyperfine levels and well isolate the resonance of the clock.

6. PHARAO FREQUENCY ACCURACY: PRELIMINARY EVALUATION ON THE FM

Clock operation is based on the $|F = 3, m_F = 0\rangle \rightarrow |F = 4, m_F = 0\rangle$ transition. The frequency dependence (Breit-Rabi formula (31, 105)) with the applied field is quadratic and equal to:

$$\Delta\nu = 4.27453 \times 10^{-2} \times \bar{B^2} \tag{6.1}$$

where $\Delta\nu$ is the frequency shift in Hz, B is the magnetic field in units of μT and $\bar{B^2}$ is the average of the quadratic field in the interrogation cavity.

Field inside the interrogation cavity can be decomposed into the average value $\bar{B_0}$ and the magnetic field inhomogeneity δB:

$$B = \bar{B_0} + \delta B, \tag{6.2}$$

where the average of the inhomogeneity is $\bar{\delta B} = 0$.

The average of the quadratic field from Equation 6.1 is then:

$$\bar{B^2} = \overline{(B_0 + \delta B)^2} = \bar{B_0^2} + \delta\bar{B}^2. \tag{6.3}$$

The maximum frequency uncertainty of the clock frequency ($m = 0$ transition) $d\Delta\nu$ has to be $<< 5 \times 10^{-17} \times \nu_0$ for both the uncertainty on the averaged squared field value $\bar{B_0^2}$ and field spatial inhomogeneity $\delta\bar{B}^2$ contribution.

The maximum uncertainty of $\bar{B_0^2}$ is evaluated by deriving Equation 6.1 over B:

$$d\Delta\nu = 2 \times 4.27453 \times 10^{-2} \times \bar{B_0} \times d\bar{B_0} << 5 \times 10^{-17} \times \nu_0, \tag{6.4}$$

where $d\bar{B_0}$ represents the uncertainty of the averaged magnetic field value. $\bar{B_0}$ is typically 0.1 μT (used to lift the state degeneracy). This leads to a maximum uncertainty of the field:

$$d\bar{B_0} << 5.38 \times 10^{-5}\mu T. \tag{6.5}$$

To evaluate $d\bar{B_0}$, the transition $|F = 3, m_F = 1\rangle \rightarrow |F = 4, m_F = 1\rangle$ is used since it is more sensitive to magnetic fields compared to $|F = 3, m_F = 0\rangle \rightarrow |F = 4, m_F = 0\rangle$ (linear versus quadratic dependency). For a transition between $m_F \neq 0$ and $\Delta m = 0$ states the corresponding frequency shift is (31):

$$\Delta\nu = m_F \times 7008.4 \times \bar{B}. \tag{6.6}$$

From the previous equation and 6.5:

$$d(\Delta\nu) << 7008.4 \times 5.38 \times 10^{-5} = 0.38Hz. \tag{6.7}$$

Therefore, the uncertainty of the frequency of the $m = 1$ transition has to be $<< 0.38Hz$.

On the other hand, the field inhomogeneity $\delta\bar{B}^2$ contribution has to obey (from Equation 6.1):

$$4.27453 \times 10^{-2}\delta\bar{B}^2 << 5 \times 10^{-17} \times \nu_0. \tag{6.8}$$

It follows:

$$\delta\bar{B}^2 << 1.23 \times 10^{-5}(\mu T)^2, \tag{6.9}$$

and finally the RMS value is:

$$RMS = \sqrt{\delta\bar{B}^2} << 3.5 \times 10^{-3}\mu T. \tag{6.10}$$

The magnetic field inhomogeneity in the interrogation cavity needs to be smaller than $3.5 \times 10^{-3}\mu T$.

Note that the field inhomogeneity between the preparation and interrogation cavity is also important. Majorana transitions (106) ($\Delta m = 1$) have to be avoided to keep the atoms in a pure $|F = 3, m_F = 0\rangle$ state before interrogation.

The magnetic field B can also fluctuate. Similarly as for the spatial distribution, the temporal averaged magnetic field fluctuation (for m = 1) needs to be determined with an uncertainty much lower than 0.38 Hz.

6.1.1 Flight model shields characterization with a magnetic probe

6.1.1.1 Shield architecture

In order to reduce internal magnetic field fluctuations and improve field homogeneity several layers of magnetic shields are currently used on ground clocks. The high achievable value of permeability in Permalloy materials such as Mumetal enables the external magnetic flux to more deeply penetrate the material where it is guided around the shielded area and finally evacuated. On board the ISS, the rotation of the clock

around Earth induces large magnetic field fluctuations at the order of $\pm 50 \mu T$ with a period of 5400 s.

Space constraints limit mass and volume and consequently the size and the number of magnetic shields. The magnetic architecture of the clock is a trade-off of all these constraints and numerical models have been used to validate its geometry.

Along the atomic trajectories an axial magnetic field generated by several coils and a solenoid is applied to lift the cesium hyperfine eigen-states degeneracy. The most magnetic field critical part of the clock is the interrogation cavity (24 cm long). For a diagram of the cesium tube see Figure 6.1. The main constraint in all other parts of the cesium tube is to keep the same magnetic field direction and to minimize magnetic field gradients.

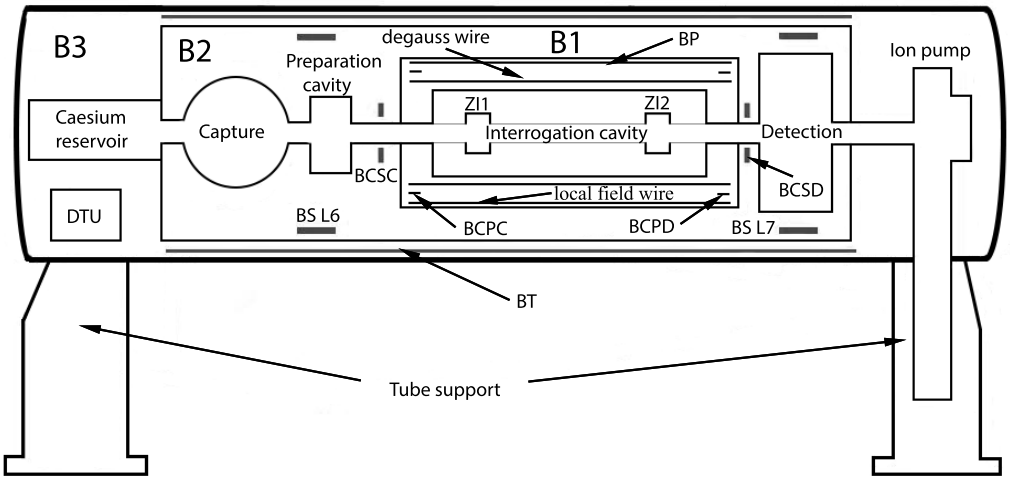

Figure 6.1: Diagram of the PHARAO cesium tube. Labeled are the external shields B1, B2, B3, the DTU magnetometer, ion pump used to maintain vacuum, cesium atoms reservoir, different cavities and coils. From the reservoir cesium atoms are released towards detection passing the capture area (where they are cooled), preparation cavity (where F = 3 atoms are selected) and interaction cavity (where the Ramsey interrogation is performed in the two interaction zones ZI1 and ZI2). In the detection zone, ratio of the two populations is obtained. The three Mumetal shields are used to reduce the magnetic oscillations the atoms experience in flight due to the Earth orbit field. The coils (BP, BS, BCSC, BCSD, BCPC, BCPD) are used to improve field homogeneity, separate magnetic Zeeman levels by providing a static magnetic field and for active compensation (BT).

The clock architecture includes 3 cylindrical Mumetal shields. An introduction to Mumetal spherical shell magnetic shielding is given in (107) or (108).

Thickness, length and diameter of the shields B1, B2 and B3 in mm are (2, 338, 118), (2, 674, 208) and (1.5, 982, 247), respectively. Internal cylinders are closed by an end-cap with a central hole of 21 mm for B1, 24 and 32 mm for B2. Other smaller holes ($\approx$ 5 mm) are used for cable management (coils, optical fibres...). Compared to B2, the shield B1 is off-centre by 60 mm towards the detection side of the clock. The shield B3 has four large lateral holes (70 x 25 mm^2) at both ends where the supports of the vacuum chamber pass through. The shields are fixed to the rest of the cesium tube by non-magnetic materials aluminium and titanium.

Shields have been assembled in a dedicated structure to characterize their performances.

6.1.1.2 Shield characterization experimental setup

Two Helmholtz coils were used to simulate an axial external field around the shields positioned in the centre. The coils diameter is 2 m and is large enough compared to the shield volume to provide a magnetic flux representative of the Earth's magnetic field in orbit along the shield axis. The transverse field effect is less critical as the shield attenuation is at least one order of magnitude larger. Consequently more of the experiments have been made with axial fields.

The coils current is driven by a computer which also digitizes the signal produced by a magnetic probe. The magnetic probe is a fluxgate Mag-01 manufactured by Bartington Instruments. The spatial transfer function of the probe has been characterized; the probe measurement is an average of the magnetic field over a length of 23 mm. We have also evaluated the frequency transfer function. For instance, the probe delay is 0.0314 rad at a frequency of 0.01 Hz. This value is significant for the study of the hysteresis effects in the shields and was removed. The probe is mounted at the end of a rigid rod which can easily be moved along the shields axis to measure the magnetic field at different positions.

In most of the experiments, the external field is modulated with a period of 100 s. Longer periods up to 5400 s (ISS orbit period) were used occasionally to verify that there is no evolution of the shield behavior. With smaller periods of 20-80 s we noticed

some differences due to the probe delay, the excitation response and/or the shields behaviour.

The measurements have been performed by the author on individual shields B3, B2 and B1, shield combinations B1+B2 and B2+B3 and finally on the complete shield configuration B1+B2+B3. Fig. 6.2 summarizes the measurements of the external axial field attenuation as a function of position obtained on the individual shields B1, B2 and B3.

6.1.1.3 The external B3 shield

On the external shield B3 magnetic fields with amplitudes $\pm 61\mu T$, $\pm 15\mu T$, $\pm 1.5\mu T$ and $\pm 0.15\mu T$ have been applied to study the hysteresis phenomena.

The attenuation of B3 is not symmetrical related to the centre of the shield. This is due to the asymmetry of the position of the different apertures. A hysteresis between the internal field and the external field is observed for fields larger than $\pm 1.5\mu T$.

The hysteresis strength is described by a quadratic term and is calculated from the ratio of the maximum width of the loop to its peak to peak value. For the previous external field amplitudes the values are 24%, 8%, 3% and ≈0%, respectively. The evolution of hysteresis shape for a given material depends not only on the applied field, but also on the previous magnetic history of the shield. In our environment with very low frequency evolution, the hysteresis shape no longer evolves after the second period of the applied external field; the hysteresis loop is then closed. In the range of external fields and periods used during the experimentation we did not observe dynamic effects such as accommodation (109). The hysteresis shape is position dependent and that will be of great importance in the development of active compensation. The attenuation increases with the external field amplitude and seems to follow a saturation function (see Figure 6.3). At the shield centre (46 cm) the attenuation is estimated to be 35 for a field amplitude of $31\mu T$.

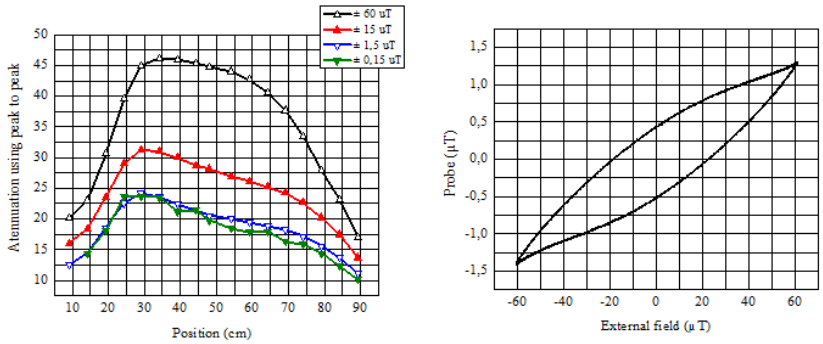

a) B3 shield. Left: attenuation as a function of position and external field amplitude. From top to bottom lines represent amplitudes ±60 μT, ±15 μT, ±1.5 μT and ±0.15 μT. Right: example of the measurement at the center of the shield.

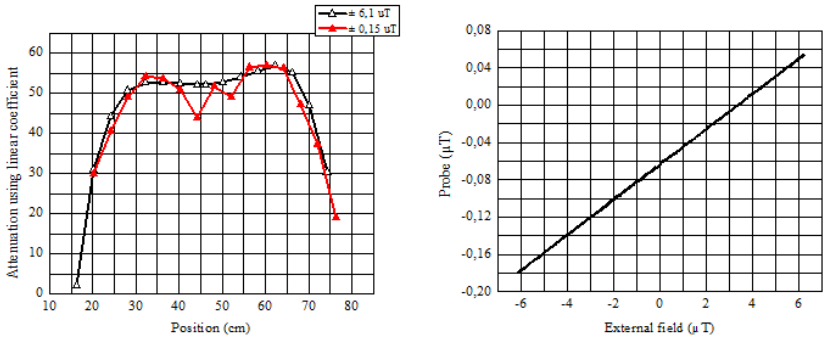

b) B2 shield. Left: attenuation as a function of position and external field amplitude. From top to bottom lines represent amplitudes ±6.1 μT and ±0.15 μT, respectively. Right: example of a the measurement at the center of the shield.

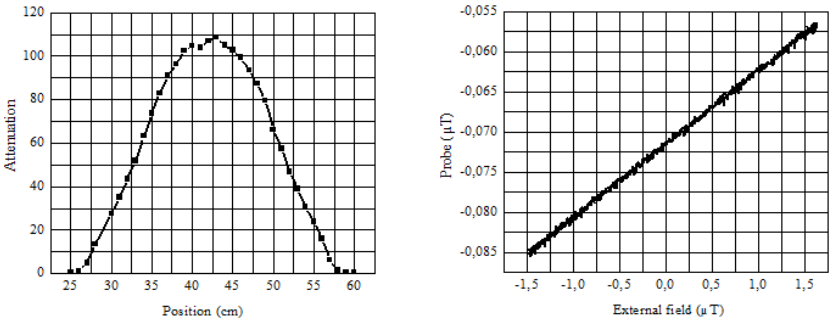

c) B1 shield. Left: attenuation as a function of position for amplitude ±1.5 μT. Right: example of the measurement at the center of the shield.

Figure 6.2: Attenuation results summary and center shield examples for individual shields using an external field period of 100 s and the indicated axial external field amplitudes. The attenuation was deduced from the ratio of the peak to peak value of the external field to the internal field. Exception is the $\pm 1.5 \mu T$ field on B3 and the $\pm 0.15 \mu T$ field on the B2 where due to low signal to noise ratio we used an inverse of the slope of the linear fit. Hysteresis contribution to the total internal field measured on the B3 is around 3% for the external field of $\pm 0.15 \mu T$, 8% for $\pm 15 \mu T$ and 24% for $\pm 60 \mu T$. For the B2, the hysteresis contribution is less than 1% for the larger $\pm 6.1 \mu T$ field. At the current signal to noise ratio the hysteresis cannot be noticed for the weaker fields on B2 and not at all for the shield B1.

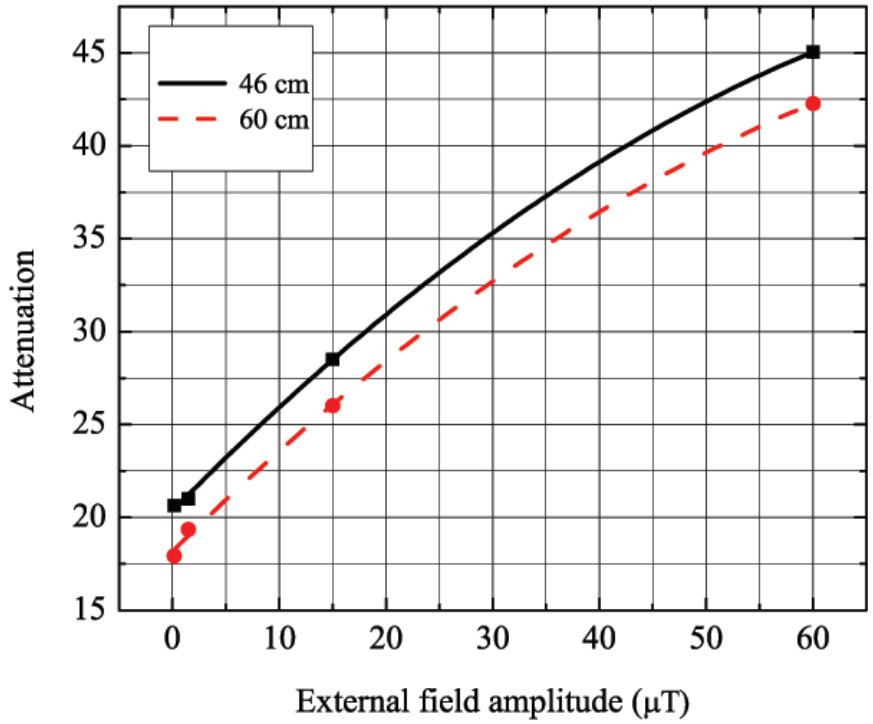

Figure 6.3: Attenuation of the magnetic field as a function of the position and external field amplitudes on the *B3* shield. Full line represents position 60 cm, and the dashed line position 46 cm, in the centre of the shield. For more details see text.

To describe the shield property the relevant parameter is not actually the field amplitude B, but the total magnetic flux intercepted by the cylindrical shield in the axial configuration. The expression for flux is (110):

$$Flux = \frac{BL}{Kt}(1 + \frac{\alpha L}{2R}), \tag{6.11}$$

where R is the shield radius, t is the material thickness, L is the shield length and K and α are parameters that depend on the surface charge distribution and can be determined experimentally.

Considering the dimensions of the shields the magnetic flux is lower for the B1 and B2 shields than the B3 for the same external field amplitude.

The attenuation variation with the field amplitude and the appearance of hysteresis can be explained by the domain theory. Magnetic domains are packages of uniform magnetization separated by layers of finite thickness called domain walls. By default, the magnetization randomly varies from one domain to the next and in the absence of any external field the resulting magnetization on average is 0. Domains exist in magnetic materials because of a complex interplay between energy terms. This relationship is described by the Landau-Lifshitz energy equation. For more detail see (111, 112, 113).

In the presence of an external field (magnetic flux), changes in the domain structure occur in two different ways. Either the magnetization inside the domains is rotated parallel to the field or the domains parallel to the external field grow due to the field pressure their walls experience (111). Conversely to the latter, domains with magnetization in different direction reduce their size and finally disappear with an increasing pressure. Finally, with a very large field only one domain remains (112) and material saturation occurs when this domain, by rotation, becomes aligned with the external field (114). If the field is reversed, this domain decreases size and new domains are nucleated aligned with the new field orientation.

Although Mumetal has a close to zero value of magnetocrystalline anisotropy (energy necessary for changing the magnetization direction) thus favoring magnetization rotation (111), it seems that wall motion is the dominating process (113, 115).

Experiments show high permeability in Mumetal is mostly due to domain wall motion (115). The coupling (exchange energy in the Landau-Lifshitz energy equation) between different domain alinement direction depends on the external field (114) resulting in permeability being a function of magnetic induction inside a material (116). For a more detailed explanation see (113). For extremely low and extremely high values of the field leading to saturation, permeability evolution decreases as can be determined from a virgin magnetization curve of a material (112).

As stated, in the presence of a varying external field, domains can be nucleated and existing domains transform their shape and size and can be annihilated. These processes cause energy dissipation mainly due to eddy currents caused by domain wall mobility and pinning of domain walls on defects and imperfections (112, 113, 114). For example, wall movement accounts for 50% of losses in ferroelectric devices (117). Additionally, some energy is spent against anisotropy of a certain volume in order

to rotate the magnetization in the same volume if the external field magnetization is changed.

These non-linearities are the origin of hysteresis whose area directly corresponds to the amount of energy lost in each magnetization cycle. Dependency of hysteresis size on a periodical external field amplitude is described by the Steinmetz law (112). The fact hysteresis is position dependent can be explained by the geometry of the shields and by the intercepted flux value which evolves along the shield.

6.1.1.4 Individual B2 and B1 shields

As the B2 shield will be positioned inside the B3 shield the maximum external magnetic flux it will experience corresponds to external fields in the $1 - 6\mu T$ range. External oscillating fields with amplitudes $6.1\mu T$ and $0.15\mu T$ (T = 100 s) have been applied. The attenuation keeps the same value for both external field amplitude and no significant hysteresis is observed (less than 1%). The intercepted flux is lower than on the B3 for the same field due to smaller shield dimensions. Consequently it does not cause a significant increase in permeability and consequently energy loss.

The maximum attenuation is about 50 at the centre of the B2 shield. The attenuation profile shape follows the geometrical symmetry of the shield. We notice that the attenuation is slightly lower at the centre of the shield. Possibly, since the length of the shield is relatively long, the intercepted external flux is slightly larger at the centre leading to an increase of the internal field. To a lesser degree this is also seen on the B3.

On the B1 shield we have applied an external oscillating field with amplitude of $\pm 1.5\mu T$ and a period of T = 100 s. As expected, no hysteresis is observed. The attenuation profile is symmetrical related to the shield centre (42 cm from the entrance of the B3 shield on the detection side). The attenuation reaches 110 and it decreases towards the ends of the shield due to the influence of the apertures of the end-caps. The attenuation is about twice the value of the one measured on the B2 since the intercepted magnetic flux is also about two times smaller (given by the diameters ratio).

6.1.1.5 Shield combinations B1+B2, B2+B3 and B1+B2+B3

Shields B1 and B2 were assembled. In the clock geometry, the position of the shield B1 is off-centred by 6 cm towards the detection side. A sinusoidal external field of amplitude

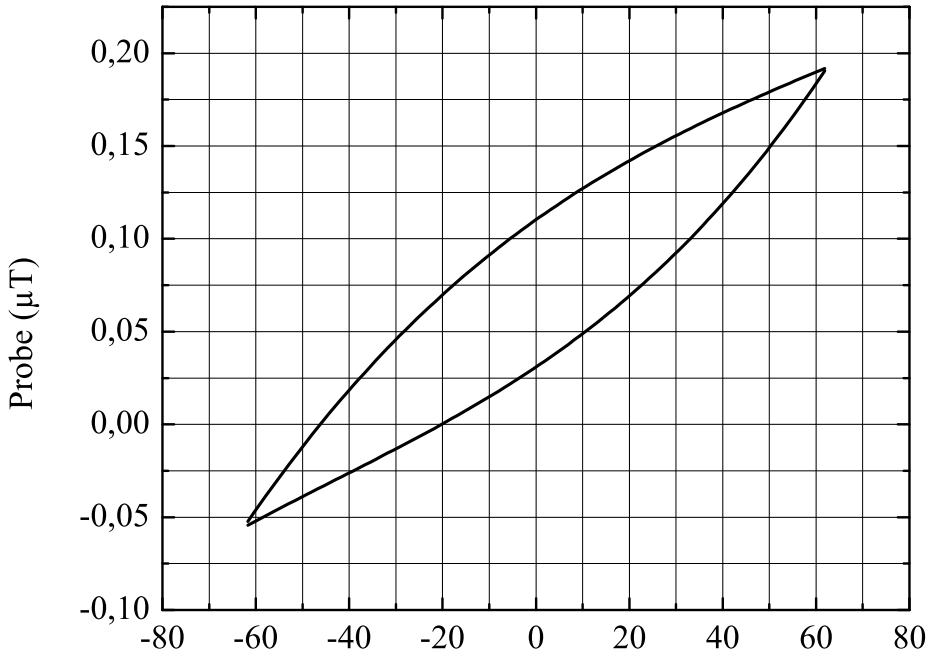

Figure 6.4: Smoothed out hysteresis example (the noise level is around 6%) at the centre of the B2+B3 configuration with a period of 100 s and and external field amplitude of $\pm 61 \mu T$.

$\pm 1.5 \mu T$ was applied. The attenuation is 3300 at the B1 centre and decreases to 1260 and 1250 at the interaction zones (11 cm from the centre). As expected, no hysteresis is present.

Shields B2 and B3 were assembled next. A sinusoidal external field with amplitude of $\pm 61 \mu T$ was applied. An example of a measurement at the centre of the shields can be seen on Figure6.4. A position dependent hysteresis was observed with similar quadratic contribution as on the B3 shield alone. The attenuation profile follows the asymmetry of the shield B3. The attenuation varies between 510 and 600 inside the interrogation zone and is 600 at the position of the preparation cavity.

Finally, all three shields were assembled. A sinusoidal external field of $\pm 31 \mu T$ (representing the amplitude of the axial field the shields will experience in orbit) and a

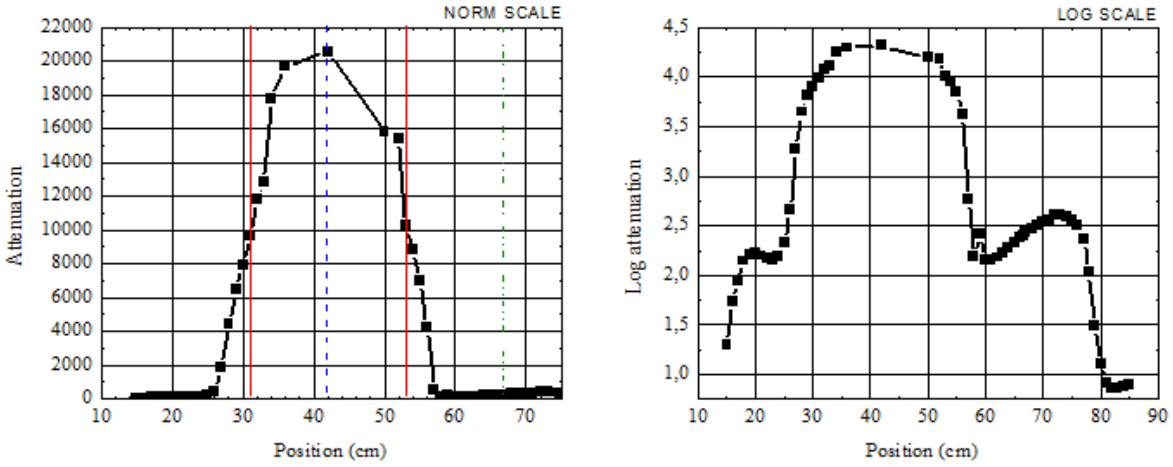

Figure 6.5: Summary of attenuation results as a function of position along the atom path inside all three shields combined in normal scale (left) and log scale (right). Full vertical lines (red) represent the position of the interaction zones, dashed line (blue) is the centre of interaction cavity and the dash-dotted line (green) is the centre of preparation cavity. An external field with amplitude of $\pm 31 \mu T$ was used (representing the field the shield will experience in orbit) and the period was 100 s. An attenuation of 9633 was measured at ZI2, 20550 at the centre, 10275 at ZI1 and 250 inside preparation zone..

period of 100 s were used. The attenuation profile is shown on Figure 6.5. A hysteresis is observed, originating from the B3 shield. The attenuation is 20 550 at the centre and decreases to 10 250 and 9650 at the end of the interrogation zone. The attenuation at the preparation zone position is 250, lower than inside the B2+B3 configuration. This is due to the field lines inside the shield B2 being channelled by the B1 shield which leads to an increase of the flux in this area.

On average, the attenuation in the critical zone inside the interrogation cavity between ZI1 and ZI2 is around 18 000. This attenuation is not sufficient by 1.5 order of magnitude to operate the space clock with full performances. For an orbit field of $\pm 31 \mu T$ the field variation inside is 11.68 Hz which is much larger than the required 0.35 Hz on average. The attenuation will be increased by an active compensation system that will be presented in Section 6.1.3.

The experimental attenuation results were compared to a well-used shielding effectiveness model (118). As this model does not take into account the permeability evolution with the magnetic flux, we initially deduced the permeabilities of individual

shields at experienced external fields. This was performed by using single shield relations for open cylinders (shields B1 and B2) and a closed cylinder (shield B3) and comparing them to the experimental attenuation results. We calculated relative permeability of 13 278, 15 022 and 20 855 for the shields B1, B2 and B3, respectively. At a lower external field of around $\pm 5\mu T$ the calculation of the B3 permeability gives 13 576, similarly as observed on the other shields. This indicates that a value of about 14 000 represents the flat permeability range for Mumetal (at low fields) explaining why we see no variation of attenuation and no hysteresis.

With these permeability values the model gives a central attenuation of 7500 for the B1+B2 combination, 970 for the B2+B3 combination and 35 000 for the three shields. This is the same order of magnitude as the experimental result (larger by a factor of 2). The difference comes from the mentioned permeability variation and the simplified shield geometry the model uses (different apertures, especially in the B3 shield are not taken into account). The permeability values we deduced are far from the manufacturer data (several tens of thousands) since these are given for large oscillating fields at several Hz.

6.1.1.6 Magnetic field homogeneity

The two hyperfine states F = 3 and F = 4 of the cesium atom have 7 and 9 m_f Zeeman sub-levels, respectively. Consequently, 21 hyperfine transitions are available. Among them F = 3, $m_f = 0 \rightleftharpoons$ F = 4, $m_f = 0$ transition is much less sensitive to the magnetic field (by 6 orders of magnitude for a field of 100nT). This transition was chosen as the clock reference frequency.

To lift the quantum states degeneracy a longitudinal magnetic field ($\approx$ 100nT) is applied along the whole atomic trajectory. The field direction is never reversed and the field gradient remains low to avoid frequency mixing between the transitions due to the Majorana transitions (106) (the relevant parameter is V x grad(B), where V is the atom velocity).

The solenoid BP (current dependency $0.883\mu T/mA$) provides a constant magnetic field inside the interrogation cavity. Two solenoids BS L6 and BS L7 (28 mm of length) provide a longitudinal magnetic field around the preparation and the detection (current dependency 164 nT/mA and 150 nT/mA, respectively). Four compensation coils BC (current dependency 100 nT/mA) surround the apertures of the B1 shield end-caps

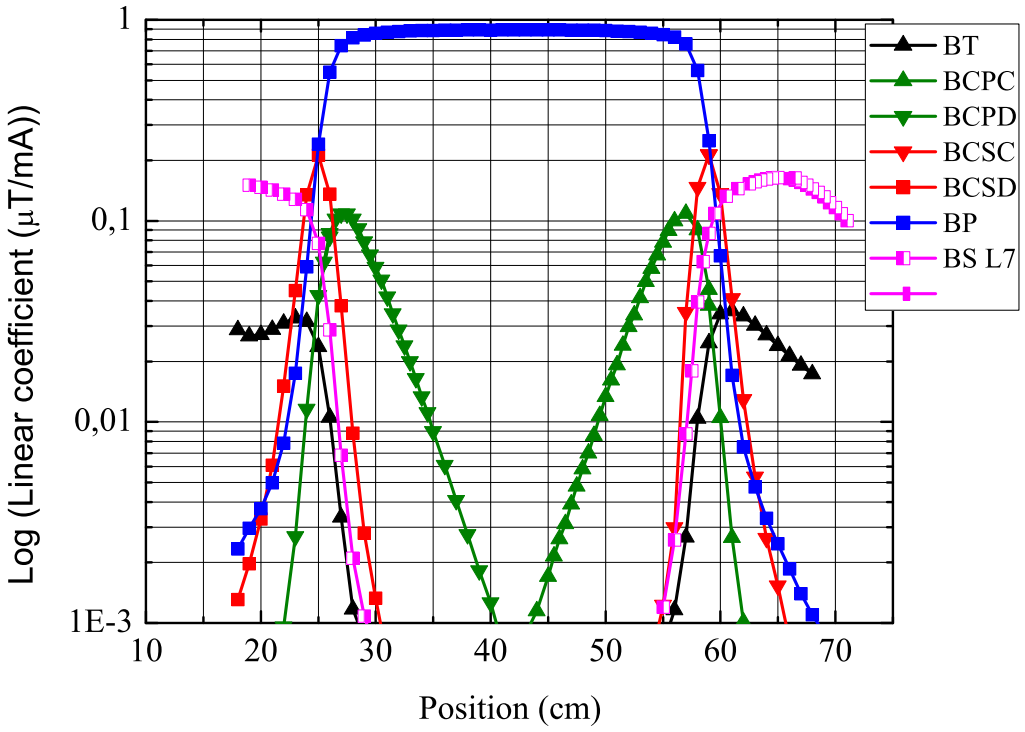

Figure 6.6: Magnetic field radiated by the different coils along the atom path in logarithmic scale.

(inside and outside) to reduce the field inhomogeneity. For the position of all coils see Figure 6.1.

The field radiated by each coil has been mapped by modulating the current at a frequency of 0.01 Hz and by using synchronous measurements to remove static stray fields. The results are shown on Figure 6.6.

The magnetic field inhomogeneity is due to the shield aperture effect, the shields magnetization (environment), the magnet of the ion pump outside the shield B3 (it is shielded and its radiated field is $25\mu T$ at 7 cm) and the Earth field ($\pm 30\mu T$). In order to reduce the residual field, the shields B1 and B2 can be degaussed by means of a damped oscillating current (4 A, 0.1 Hz) circulating in a longitudinal wire passing through both shields. This process can also be performed in space. After degaussing, we obtain the field inhomogeneity of 7 nT shown on the Figure 6.7. By knowing the

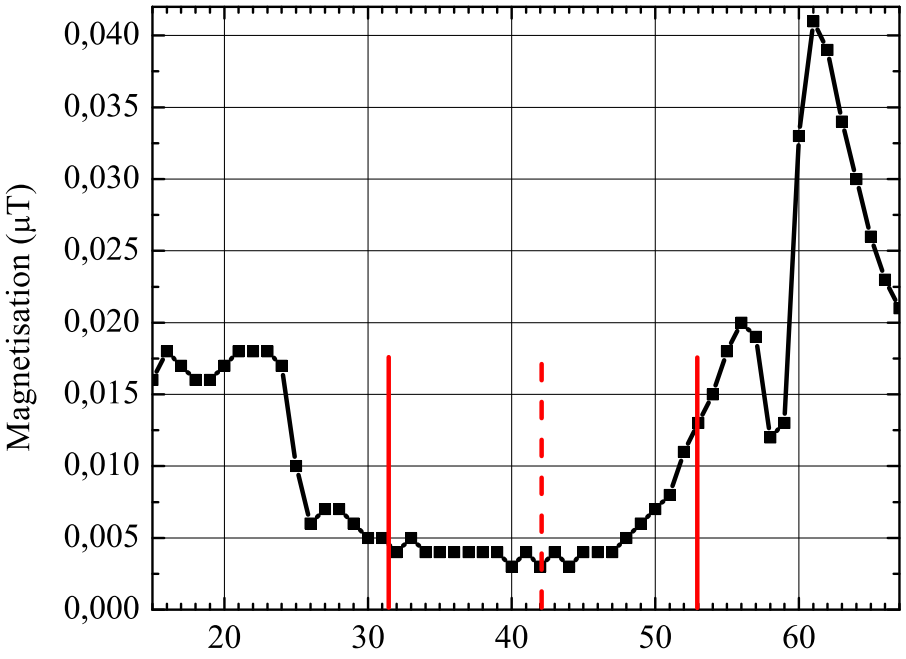

Figure 6.7: Shield inhomogeneity after degaussing by the degauss wire is around 7 nT. From left to right, lines represent zone interaction 2 (full line), center of the interaction cavity (dashed line) and zone interaction 1 (full line).

transfer functions of the coils (Figure 6.6) and simulating the coil effects, BP (0.1 mA), BS L6 (2 mA), BS L7 (2 mA) and BCPC (-0.15 mA), we deduce a static field shown on Figure 6.8. The inhomogeneity in the interaction zone is within 1.6 nT. This value is in agreement with the requirements from Section 6.1, but has to be confirmed by measurement.

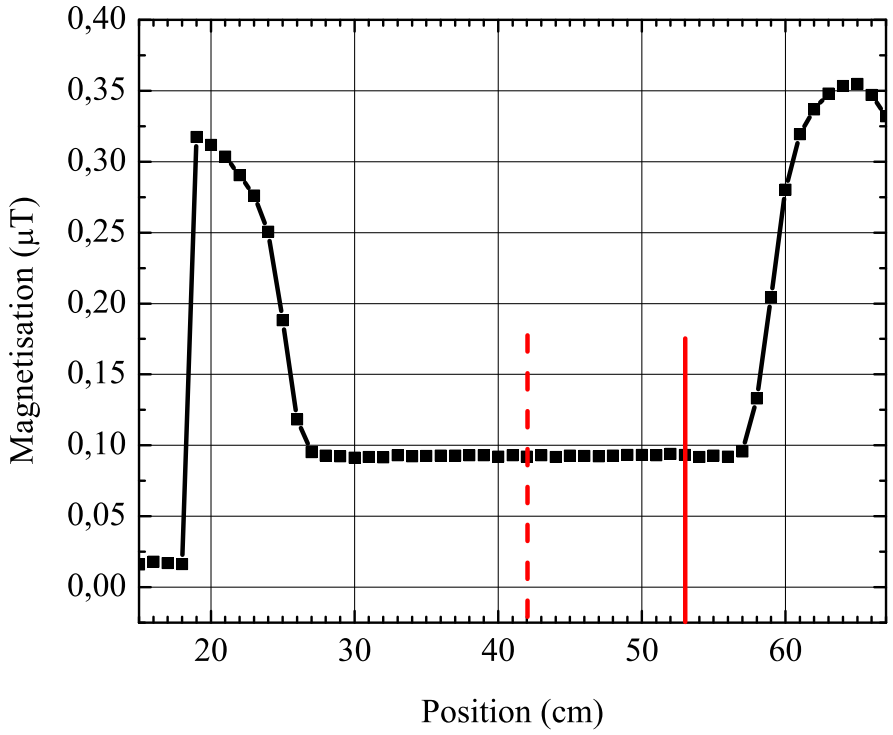

Figure 6.8: Simulated field homogeneity map obtained using coils data and residual field measurements. From left to right, lines represent zone interaction 2 (full line), center of the interaction cavity (dashed line) and zone interaction 1 (full line). Initial values of magnetization at these three points were $0.005\mu T$, $0.003\mu T$ and $0.013\mu T$, respectively. The inhomogeneity is therefore $\Delta = 0.01\mu T$. Simulated final values of magnetization at these three points are $0.091979\mu T$, $0.09199\mu T$ and $0.09337\mu T$, respectively. The inhomogeneity has decreased by a factor of 6 and is now $\Delta = 0.00158\mu T$. To achieve this values we would use the following static field coils with the indicated currents: BP (0.1 mA), BS L6 (2 mA), BS L7 (2 mA) and BCPC (-0.15 mA).

6.1.1.7 Space qualification of the shield

All the previous experiments have been made on the shields alone. During the cesium tube assembly, it is no longer possible to control the magnetism property. The materials we used inside the shields are amagnetic (titanium, aluminium and copper). Furthermore each component and each tool have been measured in a dedicated shielded chamber. Most of the critical components (near the atoms trajectory) have magnetism

in contact with the magnetic probe lower than a few nT.

Mechanical stress can change the shield properties. The critical space qualification requirements are the temperature variations (thermo-elastic behavior): a storage temperature between -40 to $60°C$, and the vibration tests: a RMS acceleration of 8 g. Furthermore, the magnetic field radiated by the vibration equipment, about $100\mu T$, cannot be neglected. The mechanical constraints are first calculated by a full calculation using finite elements. This is verified by the construction of a structural and thermal model (STM) of the clock equipped with magnetic shields and accelerometers and submitted to the environments. Consequently, the parameters used in the calculation can be adjusted to be in agreement with the experimental results. The calculations under the different loading cases (temperature and vibration) always give a level of strengths inside the Mumetal lower than 50 MPa.

Since the elastic limit of Mumetal is 146 MPa (a value which depends on the thermal treatment of the shield), no evolution of the shield behavior is expected. The attenuation and the magnetic field homogeneity have been measured for the STM before the assembly and after the environments (the shields have been removed). No significant deviation has been observed.

6.1.2 Magnetic results of the flight model by using cold atoms

After the qualification tests, the flight model of the cesium tube has been connected to other PHARAO sub-systems (engineering models of the laser source, the microwave source and the computer) to use cold atoms in the cesium tube as a magnetic probe. [1] Attenuation, active compensation and initial homogeneity experiments were performed with this setup. After delivery of the FM subsystems, more complete shield homogeneity experiments were performed with the fully assembled clock.

Three large Helmholtz coils and a surrounding wired cage controlled by a computer were used to radiate the axial and the transverse component of the magnetic field, respectively. The experiment is based on the measurement of the frequency resonance of the cesium transition which is very sensitive to the magnetic field. During clock operation on ground the cesium tube is vertical. The vertical Earth magnetic field contribution is reduced by using the horizontal Helmholtz coils.

[1] This was done because most of the flight model components were still in delivery at the time of testing.

6.1.2.1 Axial and transverse field attenuation

Rabi interrogation was performed at the position of the preparation cavity and both interaction zones and Ramsey was performed inside the interrogation zone. By using the Helmholtz coils, the on-ground external field was compensated and an external sinusoidal field was applied to the cesium tube. The clock is in operation and the microwave frequency is locked on the $|F = 3, m_F = 1\rangle \rightarrow |F = 4, m_F = 1\rangle$ transition (because this transition is more sensitive to the magnetic field).

The internal field is expressed in Hz which represents the offset of the central resonance frequency due to the presence of the magnetic field. The relationship between Hz and μT for the $m_F = 1$ transition is (from Equation 6.6):

$$Field(\mu T) = \frac{Frequency(Hz)}{7008,4} \tag{6.12}$$

For the description of the experimental setup see Section 4.6.7.1. An external axial field of $\pm 31.65 \mu T$ was used. Inside the interaction zones 1 and 2 a Rabi interrogation was performed and attenuations of 11544 and 11259 were measured, respectively.

Ramsey interrogation gives an average attenuation inside the interaction cavity of 18 942 (Figure 6.9).The measured values are very close to the values obtained with a probe.

Transverse field of $\pm 20 \mu T$ was used for interaction zone 1, interaction zone 2 and Ramsey. The measured attenuations were 299 504, 329 033 and 574 459 respectively. However, the transverse field in orbit will reach an amplitude higher than $\pm 20 \mu T$. In order to be able to provide such an external field to the clock shields, the external field coils configuration was modified. As expected, the attenuation is larger with a larger amplitude and it reaches a value of around 4.67×10^6 for an external transverse field of $\pm 35 \mu T$. The measurement is shown on Figure 6.10.

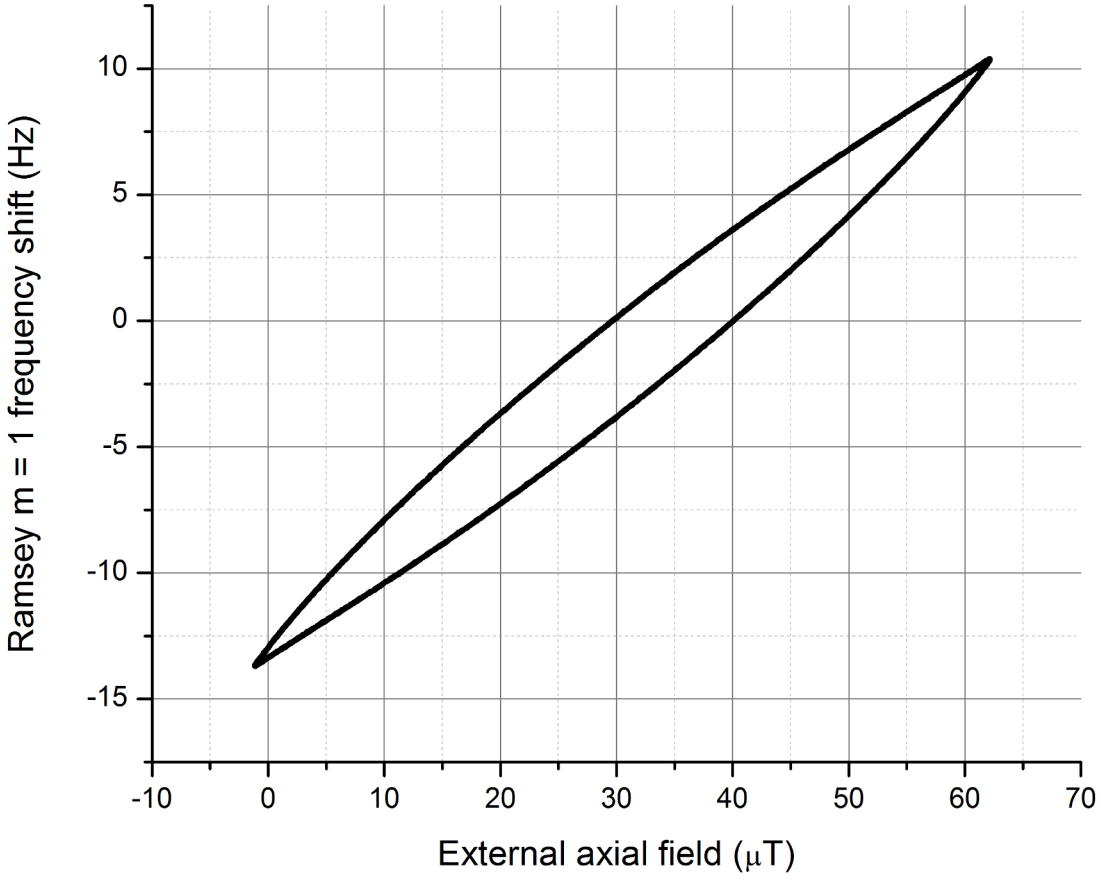

Figure 6.9: The clock frequency shift for Ramsey m = 1 interrogation (Hz) as a function of the externally applied axial sinusoidal magnetic field in μT. Attenuation of 18 942 determined.

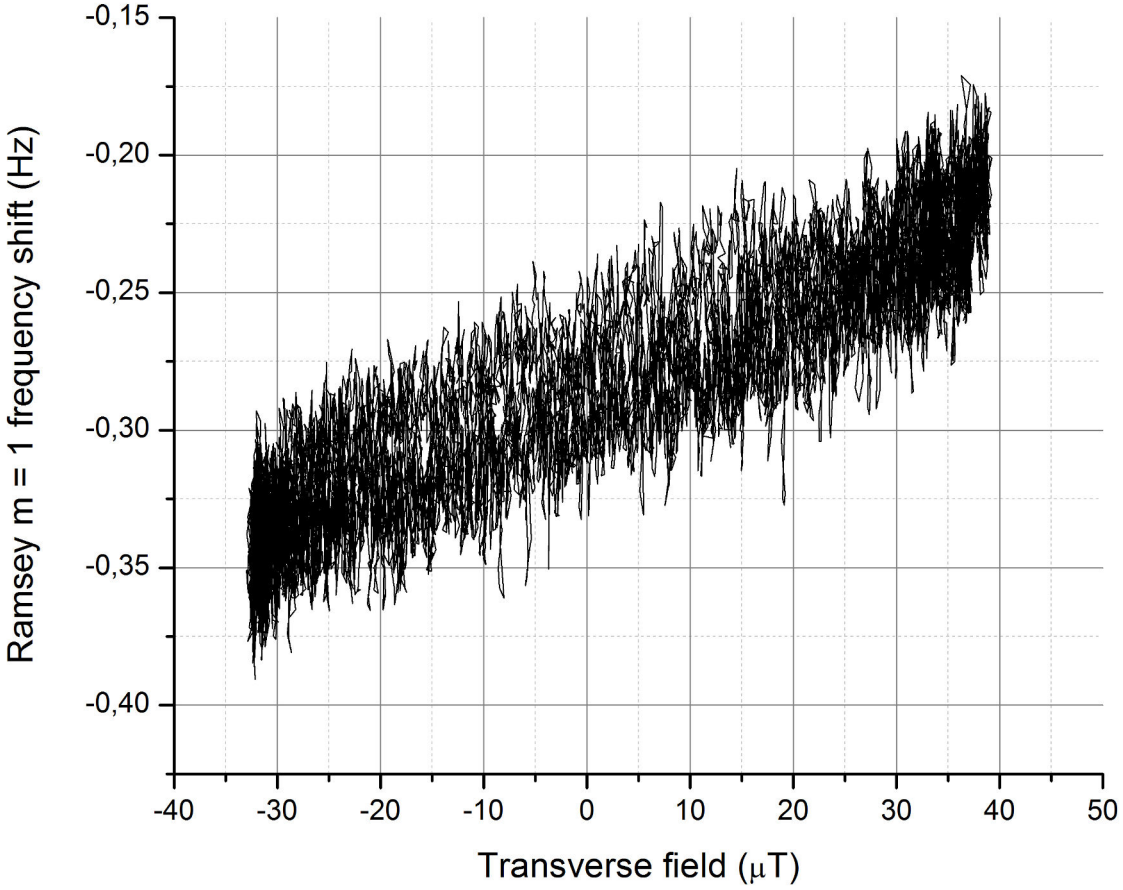

Figure 6.10: The clock frequency shift for Ramsey m = 1 interrogation (Hz) as a function of the externally applied transverse magnetic field in μT. Attenuation of around 4.67×10^6 determined.

6.1.2.2 Magnetic field evaluation

After the optimization process, the coils current values *BP* (0.2 mA), *BCPC* (0.33 mA) and *BCPD* (-0.09 mA) were set. Figure 6.11 and Figure 6.12 show resonances of the Rabi $|F = 3, m_F = 1\rangle \rightarrow |F = 4, m_F = 1\rangle$ interrogations. The frequency resonances at ZI1 and ZI2 are (1380.40±0.015) Hz and (1379.62±0.015) Hz, respectively. A better optimization of internal fields can be obtained, but this level is sufficient for on ground testing.

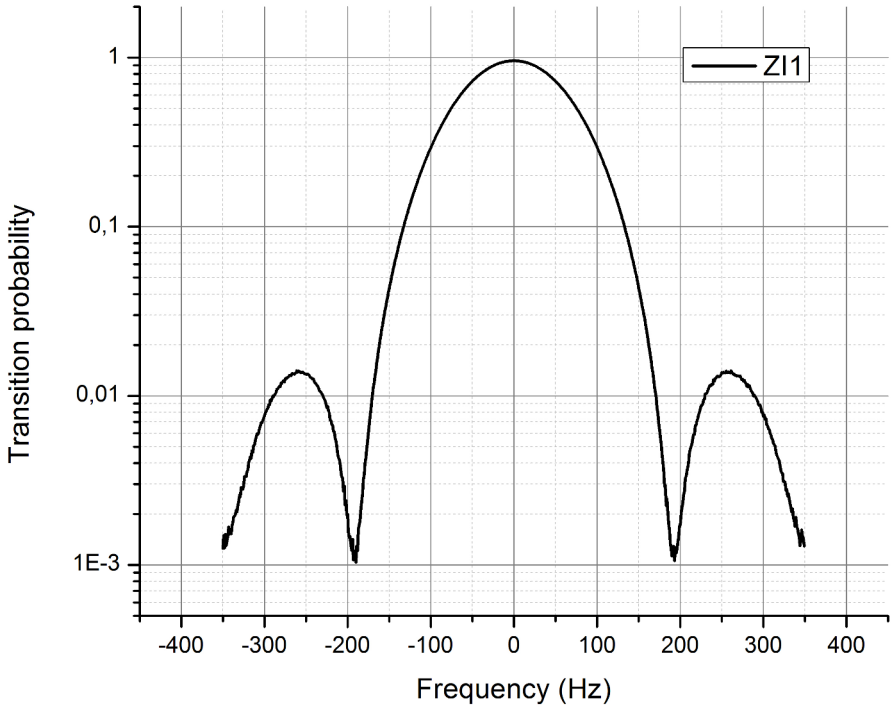

Figure 6.11: Rabi interrogation central fringe at ZI1. Central frequency is (1380.40±0.015) Hz.

Figure 6.13 shows the Ramsey resonance for the $|F = 3, m_F = 1\rangle \rightarrow |F = 4, m_F = 1\rangle$ transition. The value of the mean magnetic field is given by the central fringe of the interference pattern. The frequency of the central fringe is independent of the atomic velocity whereas the frequency and the contrast of other fringes depend on the atomic

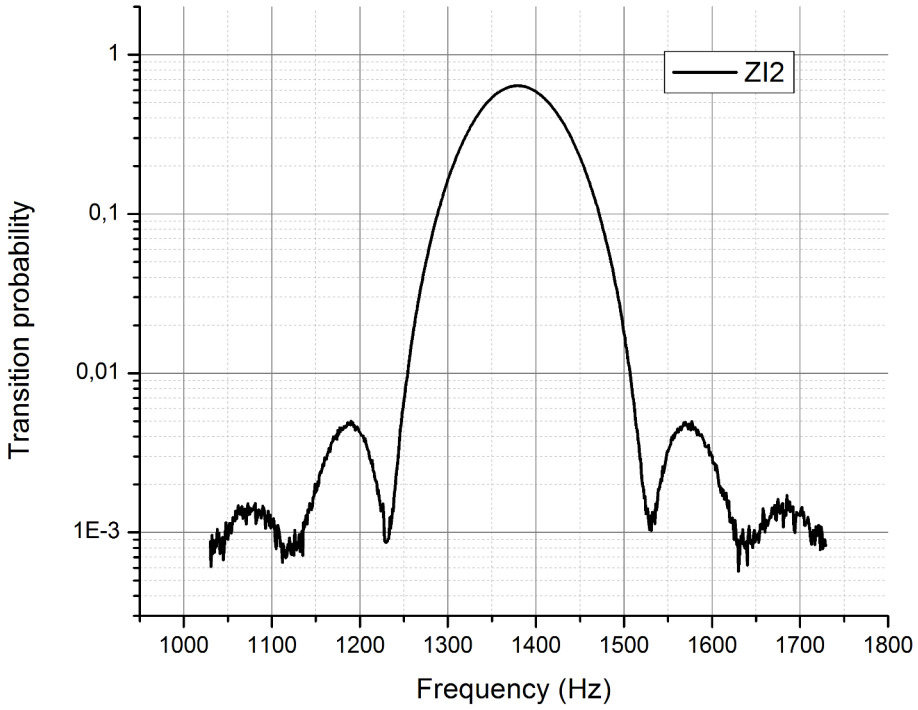

Figure 6.12: Rabi interrogation central fringe at ZI2. Central frequency is (1379.62±0.015 Hz). The transition probability (in log scale) is less than 1 because the power was not optimized for Rabi but for Ramsey.

distribution. The fringe pattern contrast and asymmetry is practically the same as for the $|F = 3, m_F = 0\rangle \rightarrow |F = 4, m_F = 0\rangle$ transition (Figure 5.1). A small difference in the amplitude of the lateral fringes exists due to a slight magnetic field inhomogeneity.

The Ramsey resonance probability values of the m = 0 and m = 1 transitions were subtracted for the three most likely central fringes (the m = 0 transition frequency was adjusted). This is shown on Figure 6.14.

The signal in the red has the smallest amplitude and therefore must correspond to the central $|F = 3, m_F = 1\rangle \rightarrow |F = 4, m_F = 1\rangle$ interrogation pattern fringe. The central fringe contrast amplitude value gives an information on the transverse field homogeneity experienced by the atom cloud.

A contrast degradation of 1% (compared to the m = 0 resonance) is seen on the

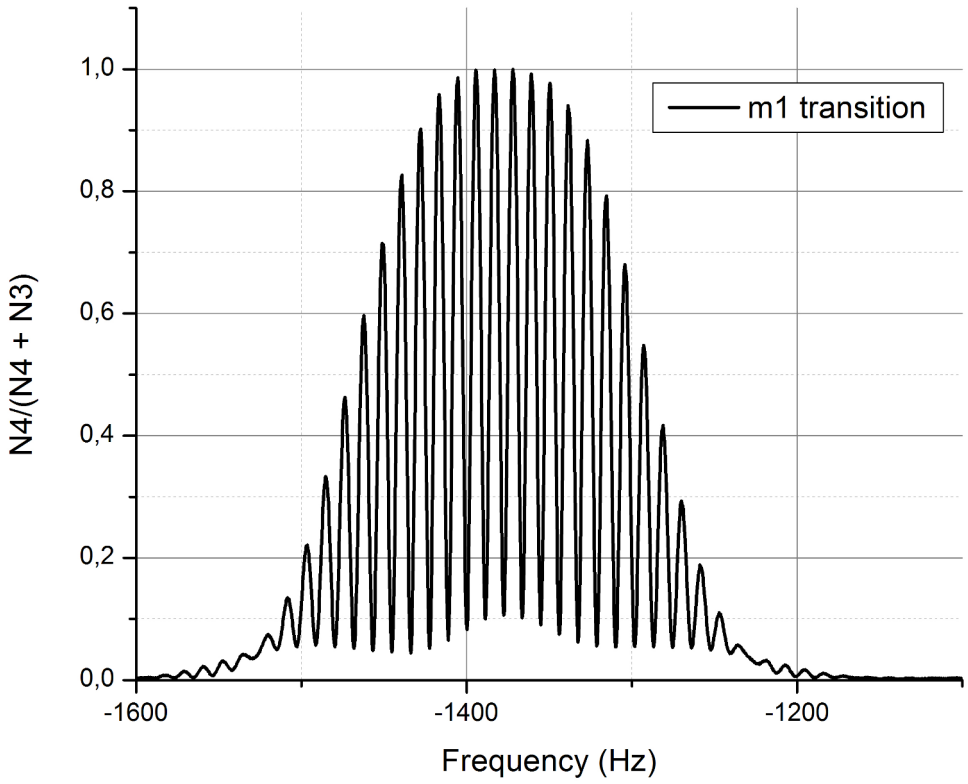

Figure 6.13: Ramsey interrogation for the $|F = 3, m_F = 1\rangle \rightarrow |F = 4, m_F = 1\rangle$ transition.

Figure 6.14. All the atoms are within approximately 0.02 Hz frequency shift (m = 1 transition) in the transverse direction. This corresponds to a magnetic field of 3 pT. The residual asymmetry is due to the small magnetic field difference between the mean field, ZI1 and ZI2.

The m = 1 Ramsey central fringe is very symmetrical and its frequency is (1383.092± 0.007) Hz corresponding to an average field $\bar{B_0} = (0.197348 \pm 0.000001)\mu T$ (from Equation 6.6). This is the average magnetic field inside the interrogation cavity.

The local field seen by the atoms in the interrogation cavity was measured using a procedure called "Zeeman wire". The atoms are prepared in the $|F = 3, m_F = 0\rangle$ state. A microwave field is only pulsed in the ZI2 at the resonance frequency of $|F =$

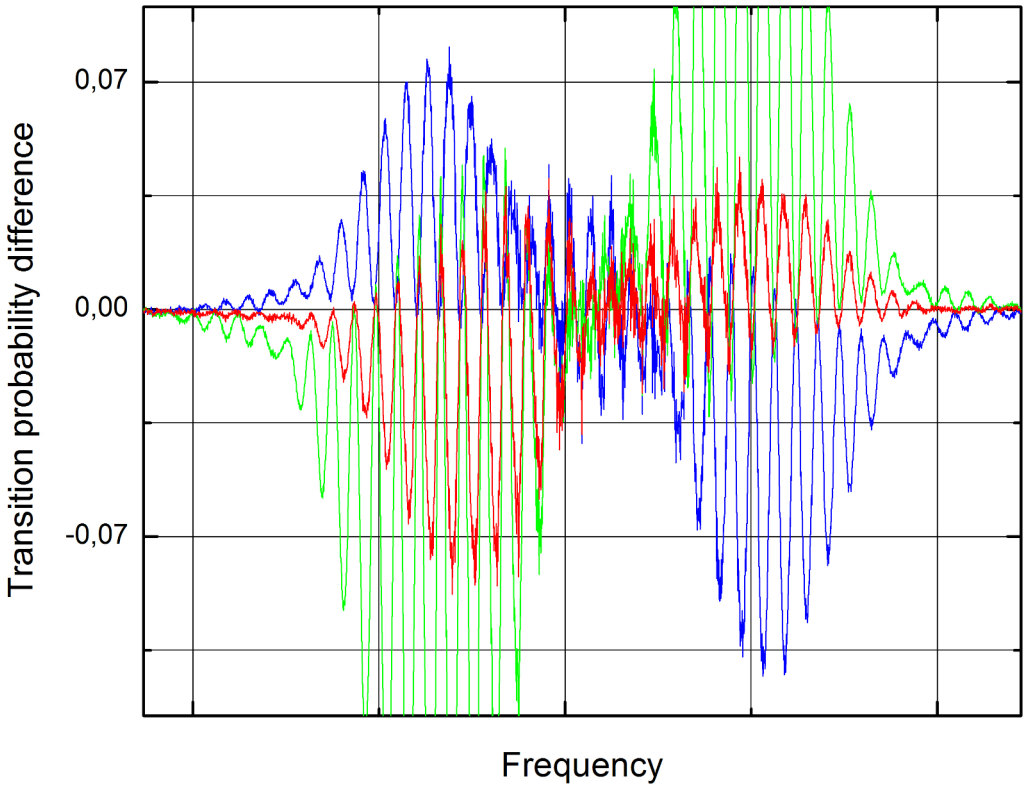

Figure 6.14: Subtracted m = 0 and m = 1 Ramsey interrogation patterns for three different m = 1 potential central fringes. The frequency was shifted for the m = 0 transition in order to be able to do this.

$3, m_F = 0\rangle \rightarrow |F = 4, m_F = 0\rangle$ (Rabi interrogation). A wire ("local field wire" on Figure 6.1) positioned outside of the vacuum chamber parallel to the atom path is used for the procedure. An oscillating current (amplitude of 12 mA) is sent to the wire with a frequency modulated around the $|F = 3, m_F = 0\rangle \rightarrow |F = 3, m_F = 1\rangle$ Zeeman transition. Every cycle the current is pulsed during 10 ms on a different position.

At Zeeman resonance, the number of atoms in $|F = 3, m_F = 0\rangle$ state at ZI2 reaches a minimum value. This translates to a minimum of $|F = 4, m_F = 0\rangle$ atoms in detection and this is how the resonant frequency is found. The frequency value is transformed to

an internal magnetic field value with the relationship (from Equation 6.1):

$$B(\mu T) = \frac{frequency(Hz)}{3509,8}. \tag{6.13}$$

Due to the average cloud size of 21 mm and velocity of 2.5 m/s, the measurement is averaged over 40 mm. The frequency measurements are independent on the amplitude of the current. An offset compensation of the DC current is made before the measurement.

The interrogation cavity field inhomogeneity profile combining the "Zeeman wire" results and the Rabi interrogation inside the two interaction zones ZI1 and ZI2 is given on Figure 6.15. The inhomogeneity is $\delta\bar{B}_0 = 3.7 \times 10^{-3}\mu T$, larger than the maximum ($3.5 \times 10^{-3}\mu T$) deduced previously. A perturbation at the center is visible probably originating from the the interrogation coupling antenna. The measurements has an uncertainty of about 1 Hz equivalent to $1.43 \times^{-4} \mu T$ due to the low SNR and a position uncertainty. When this field is averaged along the cavity, a frequency of 1 Hz smaller than the field measured using the Ramsey m = 1 resonance is found.

Figure 6.16 shows "Zeeman wire" resonances as a function of position inside the interrogation cavity. The amplitude variation (shown with the red curve) is due to the magnetic field attenuation variation originating from the AC shielding effect of the copper cavity. Position of ZI1 is shown. Magnetic field at ZI2 cannot be measured because that is where Rabi interrogation is performed.

The "Zeeman wire" is not very accurate on ground ($\approx 1nT$) due to the low signal to noise ratio at a large atomic velocity. In orbit the BP coil magnetic field will be smaller because the atoms have a lower velocity and a more narrow central fringe can be obtained. The amplitude variation is smaller and the transition probabilities are larger at lower fields because the cavity shielding effect is less efficient.

6.1.2.3 Conclusion to FM shield experiments

The calculated relative Zeeman frequency shift is:

$$\frac{\Delta\nu}{\nu_0} = \frac{1}{\nu_0} 4.27453 \times 10^{-2} \frac{Hz}{\mu T^2} \times (0.197348\mu T)^2 = 1.8109 \times 10^{-13}, \tag{6.14}$$

where ν_0 is the clock resonance frequency.

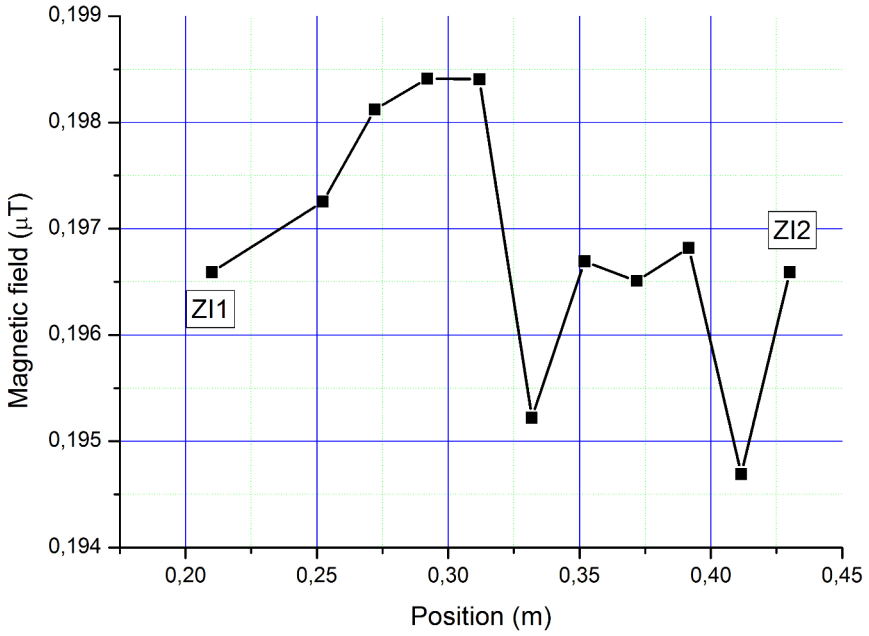

Figure 6.15: Preliminary results. Interrogation cavity homogeneity using "Zeeman wire" and Rabi interrogation (ZI1 and ZI2 values). The inhomogeneity is 3. $\times^{-3}$ μT. Averaging due to pulse duration, cloud size and velocity are taken into account.

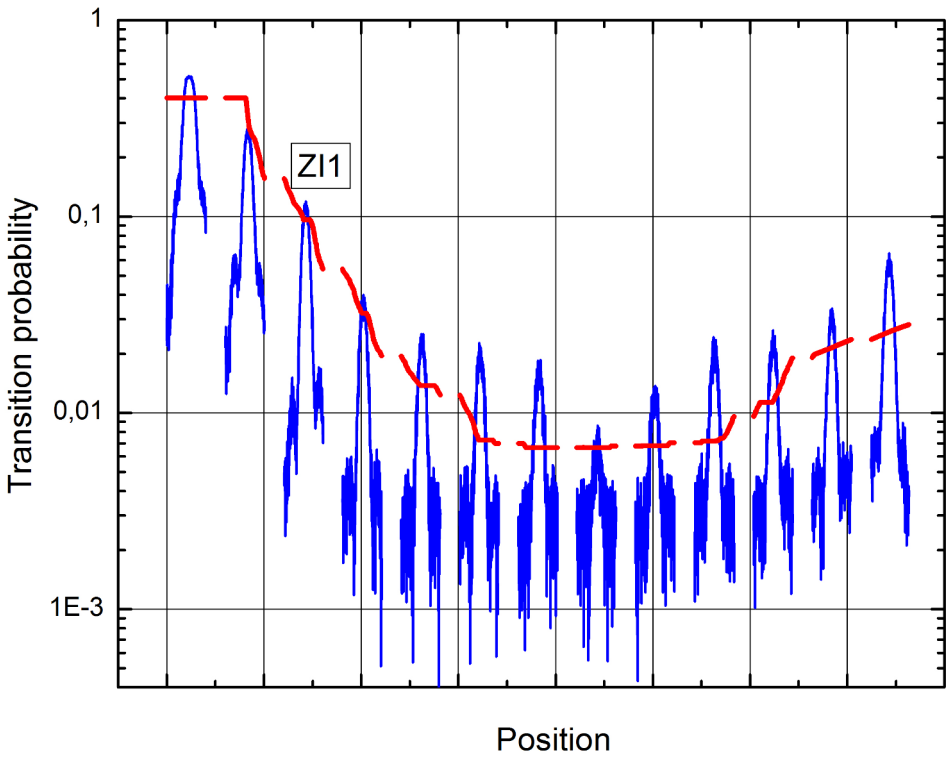

Figure 6.16: Zeeman resonance (F= 4 atom minimum) as a function of interrogation cavity position in log scale. The red curve shows the amplitude variation. Position of ZI1 is shown.

The related frequency uncertainty is (from Equation 6.4 and Equation 6.8):

$$\sigma_{Zeeman} = \frac{1}{\nu_0} 2 \times 4.27453 \times 10^{-2} \times \bar{B}_0 \times d\bar{B}_0 + 4.27453 \times 10^{-2} \times \delta\bar{B}^2 = 7 \times 10^{-17}. \tag{6.15}$$

A linear sum is used because there is a correlation between $d\bar{B}_0$ and $\delta\bar{B}^2$.

The magnetic field homogeneity inside the shield does not show significant evolution before assembly and after qualification.

In the most critical part of the clock, the interrogation cavity, the shields axial attenuation is around 19 000. Attenuations of 11544 and 11259 were deduced at the two interrogation cavity ends. This is not changed after clock qualifications. On average, the attenuation of the interrogation cavity is 1 653 000 for the transverse field amplitude of $40\mu T$.

Unfortunately, the shield attenuation is not sufficient by one order of magnitude to guarantee high clock performances in frequency stability and in frequency accuracy. In order to improve the attenuation an active compensation system that predicts hysteresis behavior inside the shields was developed. The system will be presented next.

6.1.3 Active compensation

We have developed a simple model able to describe and predict hysteresis behaviour inside Mumetal magnetic shields (16), when the shields are submitted to ultra-low frequency (<0.01 Hz) magnetic perturbations with amplitudes lower than $60\mu T$. This predictive model has been implemented in a software to perform an active compensation system. With this compensation the attenuation of longitudinal magnetic fields is increased by two orders of magnitude.

6.1.3.1 Introduction

Improving attenuation inside magnetic shields by adding an active system is widely used for various application domains (116, 119, 120, 121, 122, 123). These systems are based on field cancellation at the position of a magnetic sensor by using a servo-loop acting on the current feeding external coils. However, the response of the magnetic shield is not homogeneous in the shield volume making the efficiency of active attenuation

position dependant. This is even more accentuated when the external field fluctuations are large enough to create a non linear spatially evolving hysteresis phenomena.

The magnetic field fluctuations the clock will experience are in the ultra-low frequency domain (period 90 mn) with amplitude as large as 30μT whereas the average magnetic field inside the clock has to be determined with an accuracy of 20 pT. An attenuation of around 500 000 is required to reach this performance.

Such attenuation can be achieved by a set of magnetic shields. However, due to mass and volume constraints of the space clock the effective shield thickness and layer number (affecting shield attenuation) is limited. Therefore, an active attenuation system has been added. But, due to technical constraints the sensor cannot be placed at the position where the attenuation needs to be maximized. In addition, the external field amplitude is large enough to induce hysteresis. Considering this, it becomes necessary to find a model of the magnetic field hysteresis able to predict the hysteresis behaviour at a distance from the magnetic sensor. The most popular models (124), the Preisach and the Jiles-Atherton model, well describe hysteresis in magnetic materials by taking into account the field history. However, they are not adapted for application in a compensation system. Consequently, we have developed a simple mathematical description. This mathematical model is deduced from extensive experimentation performed on the clock shields. It is the basis of the PHARAO clock active compensation system. The system has been tested by operating the atomic clock in the presence of orbit representative magnetic perturbations.

6.1.3.2 Experiment

The magnetic architecture of the PHARAO clock is shown in Figure 6.1. A fluxgate probe (DTU) measures the magnetic field inside the shield **B3**. It is the sensor of the active compensation. The actuator of the compensation is the long solenoid **BT** wired around the **B2** shield. The most critical part to magnetic perturbations is inside the shield **B1**.

Each shield has been separately tested to determine the linear and non linear contribution. For the applied magnetic fields the measured magnetic hysteresis is due to the shield **B3**. The internal shields are submitted to a much lower magnetic flux and remain in the linear regime (at a few percent). The hysteresis parameters are position dependant inside the shield **B3**. This means that the hysteresis loop characteristics

such as slope, width and shape vary, which results in appearance of hysteresis between any two positions inside the shields. For a comparison of hysteresis between a sinusoidal external field and three positions inside the **B3** shield see Figure 6.17. If the sensor signal is used to cancel the field, the residual in the interrogation cavity is even larger than the original signal.

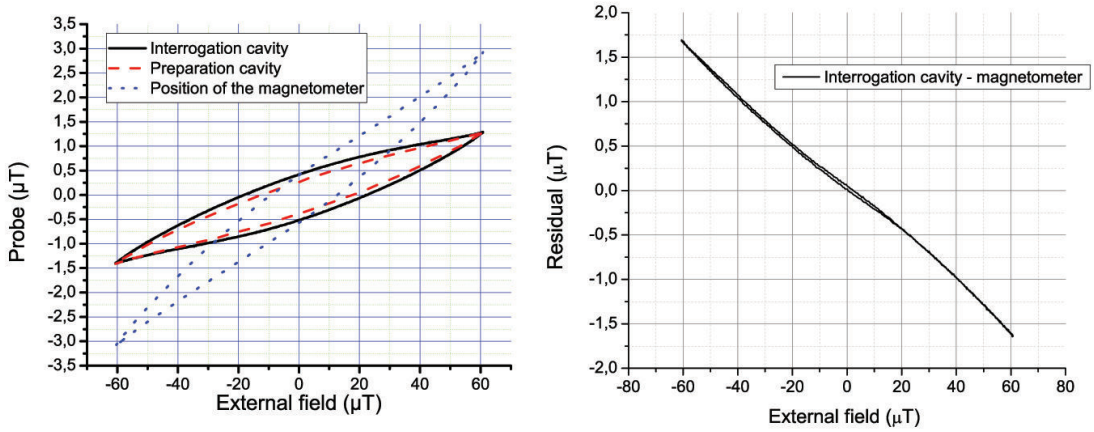

Figure 6.17: Left: hysteresis shape inside the B3 shield alone is position dependant. In black is the hysteresis measured in the center of the shield, in dashed red is the hysteresis measured at the position of the preparation cavity and in dotted blue the one measured at the position of the magnetometer. Right: the residual left when the hysteresis signal from the magnetometer position is substracted from the hysteresis signal at interrogation is larger than the signal.

The hysteresis parameters for a given position depend on the external field amplitude and on shield history. Three model describing postulates have been derived from experiments. It is important to note that the creeping effect (accommodation) (for example (124)) was not observed during testing.

6.1.3.3 Model description

The terminology that will be used such as major loop and minor loop are well known in magnetic modelization theory (for example (125)). Major and minor loop are connected at only one position and the minor loop is always contained inside the major loop. A graphical illustration of a system of hysteresis loops obtained by decreasing the

oscillating external field amplitude (the field trajectory is in the clockwise direction) is shown in Figure 6.18.

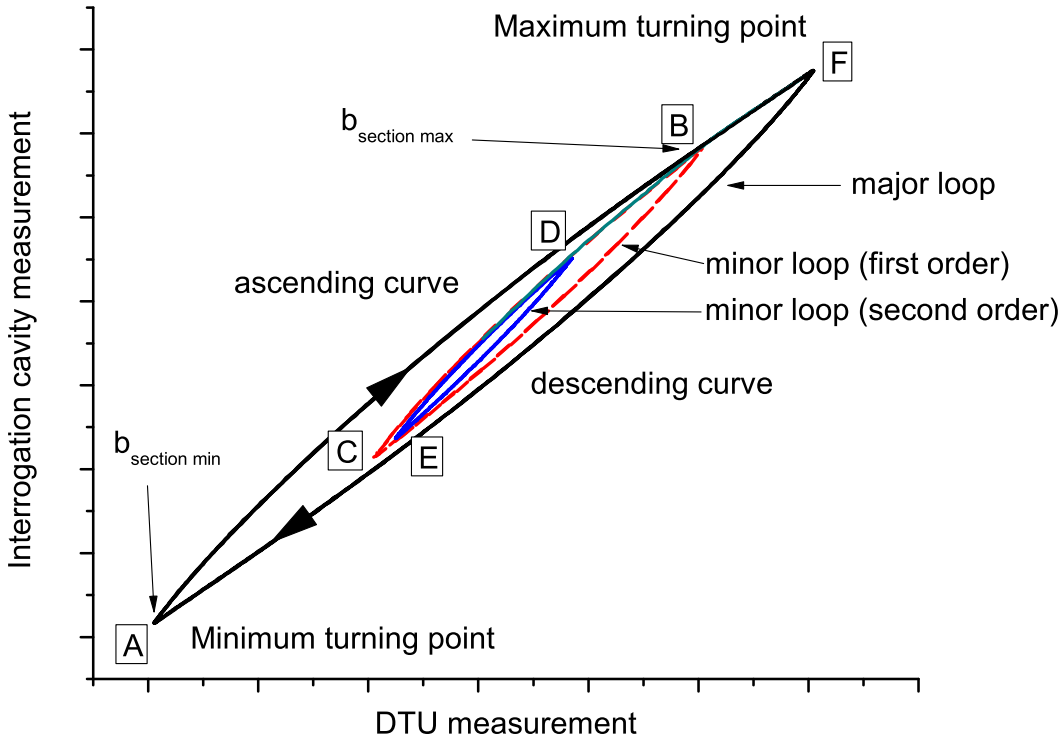

Figure 6.18: Experimental hysteresis measurement. Internal field shown as a clock frequency shift in Hz (Equation 6.22) measured during clock operation as a function of the externally applied field in μT. Illustration of the terms used, field direction and how the minor loops ascending curve switches its trajectory to its major loop trajectory from shield history.

The largest loop in black is the major loop to the loop in red which is the major loop to the loop in blue. If the external field amplitude exceeds the bounds of the major loop (in black) a new major loop is created. Similarly, the smallest loop (in blue) can become a major loop if the external field amplitude reaches smaller bounds.

The turning point is the field value where the magnetic field is reversed creating reversal curves (for example points A and F are turning points of the major loop). That leads to the formation of a loop branch. A branch is the ascending or descending part of a hysteresis loop.

The switching point is the field value where the magnetic field amplitude exceeds the current hysteresis bounds (for example points D and B when the field is increased from C to F) and switches trajectory to its major loop ascending or descending branch.

The hysteresis dynamics model is described by the three postulates:

1. Ascending and descending branch of a closed hysteresis loop are symmetrical with respect to the central point of the hysteresis loop.

2. A turning point on the ascending/descending branch creates a reversal curve. The trajectory of the curve will lead to its major loop minimum/maximum turning point.

3. After a switching point the hysteresis will follow the trajectory of its major loop. The minor loop history is erased.

6.1.3.4 Postulate I

A simple way to check the hysteresis loop central point symmetry is to plot the ascending branch $\mathrm{h}_+(b - b_0)$ as a function of the descending branch $\mathrm{h}_-(b_0 - b)$ where b is the applied magnetic field and b_0 is the central value. This is illustrated with an experimental example on Figure 6.19. The plot is a straight line with the slope 1. The inset on the right shows the residual when the linear part is removed.

In all hysteresis experiments performed for different shield histories, external field amplitudes ($<60\mu$T) and external field offsets (<30 μT) the residual remains within $\pm 1\%$.

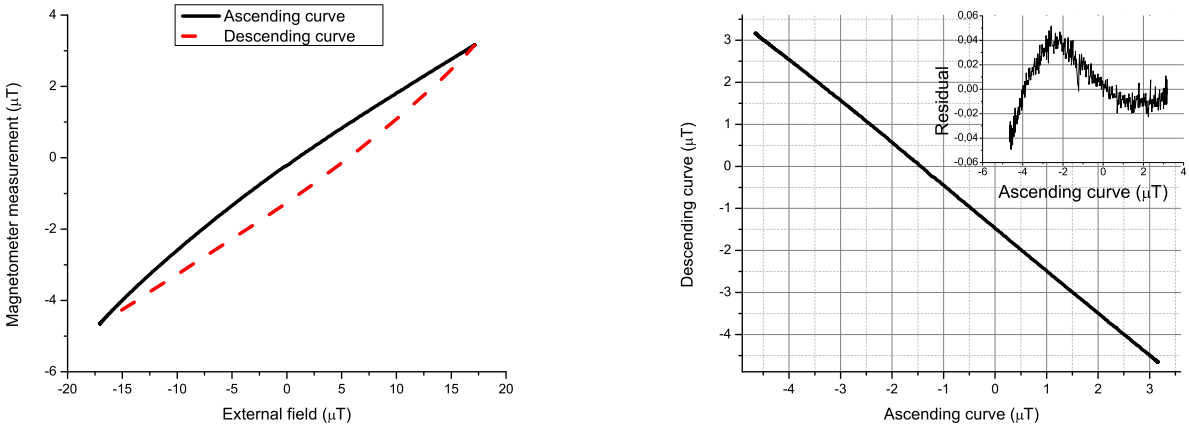

Figure 6.19: Left: Typical closed hysteresis curve from an external field measured internally using a magnetometer. Right: vertical axis Y[i] data of the ascending branch as a function of vertical axis Y[-i] data of the descending branch . In the inset is the residual from the linear fit. The residual is around 1%. This comes from higher harmonics, fit and measurement errors.

Consequently, a closed hysteresis can be described by a third order Rayleigh polynomial:

$$h_{\pm}(b) = \alpha_{0\pm} + \alpha_1(b - b_0) \pm \alpha_2(b - b_0)^2 + \alpha_3(b - b_0)^3, \tag{6.16}$$

where b is the external field, $\pm$ distinguishes the ascending and the descending branch, $\alpha_{0\pm}$ is the corresponding offset, α_1, α_2 and α_3 are the polynomial coefficients, $b_0 = (b_M + bm)/2$ where b_M and b_m are the maximum and minimum turning points of the loop, respectively.

If we look back at Figure 6.18, the first postulate claims that the ascending and descending branches of all three hysteresis loops are symmetrical. The determination of the parameters of one branch of a closed loop is sufficient to predict the parameters of the other branch (ascending or descending). The offset change is obtained at the turning point where the ascending and descending branch are connected.

6.1.3.5 Postulate II

To illustrate the second postulate another experimental example is given in Figure 6.20. Loop 1 and Loop 2 are minor loops to a major loop whose turning points are denoted by 1 and 3 on the figure. Arrows show the clockwise direction of the field. Starting from the minimum turning point 1 of the major loop the field is increased to point 2. Upon reaching point 2 the field is inverted making it a turning point of Loop 1 and making section 1 $\rightarrow$ 2 its ascending branch. The descending branch (section 2 $\rightarrow$ 1) of Loop 1 connects to the minimum turning point of the major loop. Field is then increased to point 3 and inverted to point 4. Another field inversion creates a reversal curve 4 $\rightarrow$ 3 defining the ascending branch of Loop 2 which connects to the major loop turning point.

The descending branches of the two minor loops on Figure 6.18 would also connect to point A if the field was not inverted previously. Therefore, by combining the first two postulates, it can be deduced that section $A \rightarrow B$ and section $B \rightarrow C$ (descending branch of the first order minor loop in dashed red) are symmetrical and can be described by the same set of coefficients (after changing the square coefficient sign and offset). Section $A \rightarrow B$ is part of the major loop ascending branch and can be described with Equation 6.16 by performing an origin transformation (b_0 from Equation 6.16 is zero). The polynomial equation that describes the magnetic field in section $A \rightarrow B$ in the system of $A \rightarrow F$ is:

$$B = \beta_0 + \beta_1(b - b_0^{'}) + \beta_2(b - b_0^{'})^2 + \beta_3(b - b_0^{'})^3, \tag{6.17}$$

where coefficients β have to be determined. $b_0^{'} = \frac{b_{\text{section min}} + b_{\text{section max}}}{2}$ represents the center of the $A \rightarrow B$ section in the centralized coordinates of the major loop. In this case, $b_{\text{section min}}$ and $b_{\text{section max}}$ are points A and point B, respectively.

After comparing Equation 6.17 and Equation 6.16, relationships of the coefficients are deduced:

$$\beta_0 = \alpha_0 + b_0^{'}[\alpha_1 - 3\alpha_3 b_0^{'2} + 2b_0^{'}(\alpha_2 + 3\alpha_3 b_0^{'}] - b_0^{'2}(\alpha_2 + 3\alpha_3 b_0^{'}) + \alpha_3 b_0^{'3} \tag{6.18}$$

$$\beta_1 = \alpha_1 + 2b_0^{'}(\alpha_2 + 3\alpha_3 b_0^{'}) - 3\alpha_3 b_0^{'2} \tag{6.19}$$

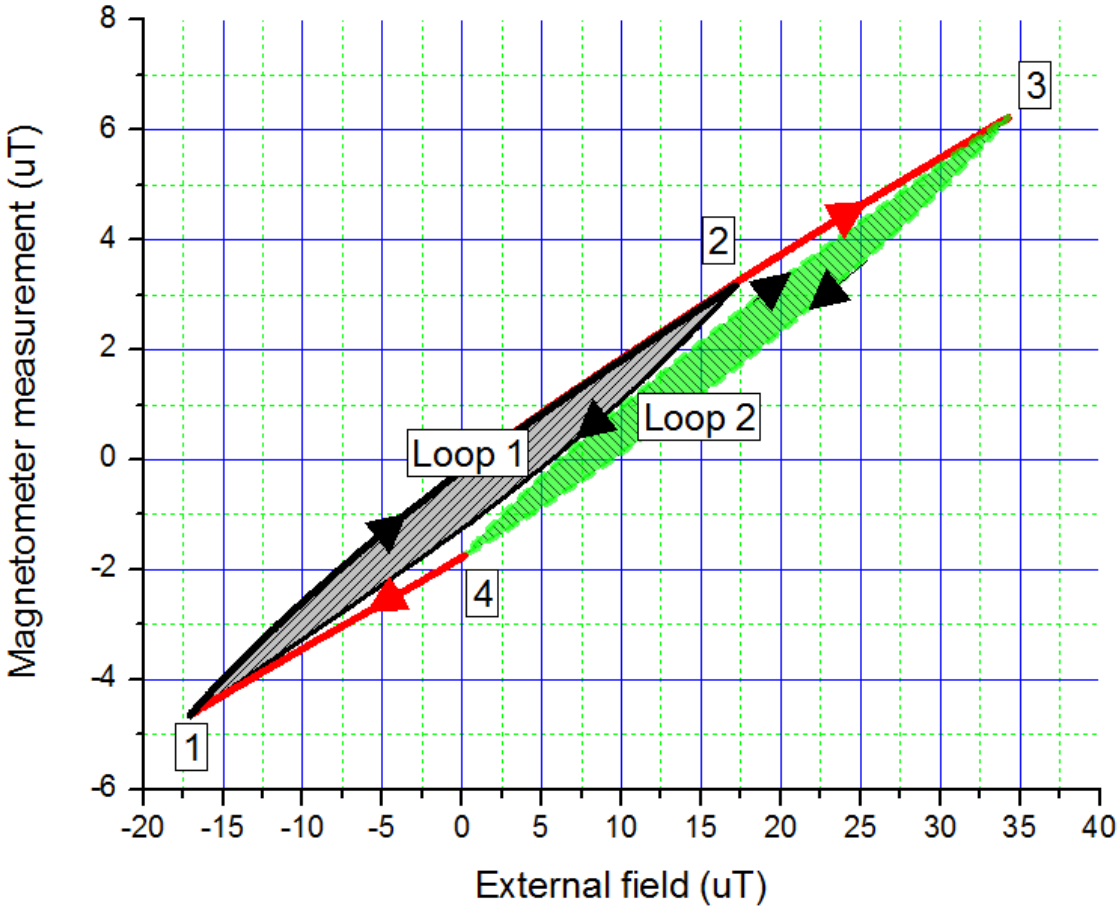

Figure 6.20: Internal field in μT measured with a magnetometer as a function of the externally applied field in μT. Illustration how the minor loop ascending and descending branches always take on the trajectory that will connect them to their major loop turning point (postulate two). See text for more detail.

$$\beta_2 = \alpha_2 + 3\alpha_3 b_0^{'} \tag{6.20}$$

$$\beta_3 = \alpha_3. \tag{6.21}$$

β coefficients describe the first order minor loop branches. By iterating the process, the coefficients describing the second order minor loop (in blue) and its branches can also be calculated.

6.1.3.6 Postulate III

The example on Figure 6.18 is continued. Starting from a point on the major loop, an external field of diminishing amplitude was applied until point E. As we have shown, it is possible to calculate the polynomial coefficients describing these minor loops. However, if the field is now increased above points D and B the trajectory slope is not continuous. The two points become switching points and the trajectory switches between the second order minor loop ascending branch, first order minor loop ascending branch and major loop ascending branch (α coefficient) until reaching point F. After each switching point the smaller hysteresis loop is erased from shield history (the deletion property (125)). If a larger major loop is unknown, the model is not able to describe what happens after point F.

The situation described is analogue to what happens when the field decreases below the minimum turning points of minor loops positioned on the descending branch of the major loop.

6.1.3.7 Active compensation system

The model has been implemented in the software which will control the active compensation system.

The critical region where the largest magnetic attenuation is necessary inside the clock is the interrogation cavity inside the $B1$ shield. The results obtained from the experiments on the flight model shields mockup show that the axial magnetic field attenuation obtained by the $\mathbf{B1 + B2 + B3}$ static shields combination alone is not sufficient to satisfy the mission specifications. In the interrogation cavity an attenuation of 18 800 for the axial component ($\pm 31.65 \mu T$ external field amplitude) and 1 250 000

for the transverse component ($\pm 39 \mu T$ external field amplitude) was measured. For a quasi-sinusoidal external magnetic field experienced in orbit, the fluctuation of the clock frequency would be 1.5×10^{-15} in relative value, a value not compatible with the accuracy objective of 3×10^{-16}.

The active compensation system is a feed-forward system composed of a magnetic sensor and a compensating coil (BT) controlled by a computer. The magnetometer was developed by the Technical University of Denmark (Danmarks Tekniske Universitet or DTU) and is spatially separated from the clock interrogation cavity because of possible electromagnetic disturbances, technical and design issues. It is placed outside of the **B1** and **B2** shields and inside the **B3** shield. For an illustration of the component and shields position see Figure 6.1.

Using the magnetometer measurement and the described model, the field inside the interrogation cavity is calculated (Equation 6.17). This value is expressed using polynomial coefficients in reference to the magnetometer field b. The linear transfer function of the coil BT (3 pT/mA) at the interrogation cavity position has been evaluated. The effect of the BT coil on the magnetometer is also known ($1.3\ \mu T/mA$), and this is removed from the calculation. Next, the coil current is applied and the field is compensated. In order to be able to use the hysteresis shape prediction capabilities of the model, the software can record a maximum of 20 coefficient sets and turning points which is enough for the relatively simple orbital field oscillation.

The DTU magnetometer (due to system restrictions) delivers measurements only every 10 seconds. To improve the results a second order polynomial interpolation is used to calculate additional points which the BT coil receives every 0.1 seconds. The system works with similar efficiency for sinusoidal oscillations longer than 500 seconds because the interpolation loses reliability for a field with a shorter period.

We have determined that the α_3 does not have a significant effect on attenuation in the limit of our application. Therefore, for the sake of simplicity, we will use only α_1 and α_2. This means the α_2 coefficients keeps a constant absolute value (the sign changes), while α_1 will vary.

6.1.3.8 Experimental setup

Three large Helmholtz coils (diameter of 2m) and a surrounding wired cage controlled by a computer radiate the axial and the transverse component of the magnetic field,

respectively. The coils are large enough to provide a well defined magnetic field in direction and amplitude with a field line distribution similar to the one the shields will experience in orbit.

During the tests, the clock operates by using the hyperfine transition which has a linear dependency with the magnetic field (between the Zeeman sub-levels $m_F = 1$). Interrogation cavity field measurements were performed by locking the microwave frequency on the resonance signal.

6.1.3.9 Axial external field pattern and results

In order to test the active attenuation system a special axial external field pattern was devised. This pattern tests if the system correctly calculates the coefficients starting from the measured major loop coefficients. It has multiple centered and not centered minor loops around the zero magnetization value of the magnetometer. The pattern also verifies if the major to minor loop and minor to major loop transitions are correctly performed. See Figure 6.21.

The pattern has a duration of around 15 hours while the individual oscillations have a period of around 90 min. This is similar to what the shields will see in orbit. However, testing with shorter periods down to 500 sec showed no difference in the results.

By looking at the peak to peak of the smoothed out result (in dashed blue) of the attenuated frequency modulation signal (in red) and comparing it to the peak to peak of the non attenuated one (in black), the attenuation value is around 190. The model is able to predict the shield behaviour within 1% of error.

6.1.3.10 Orbital external field testing

The total ISS orbital magnetic field has three main harmonics. The largest one is due to nodal regression (126) where the station is deflected westward every time it crosses the equatorial bulge due to mass attraction. This drift amounts to about 5.04° per Earth orbit and takes 70 days for full revolution. The second harmonic is due to the Earth rotation with a period of about 24h which equals to about 16 orbits of the ISS. The third harmonic is due to the ISS rotation around Earth which is around 91 min. On Figure 6.22 we can only see the second and the third harmonic.

In order to evaluate the effect the magnetic field will have on the PHARAO clock frequency on board the ISS, a quasi-sinusoidal field representing the orbital field was

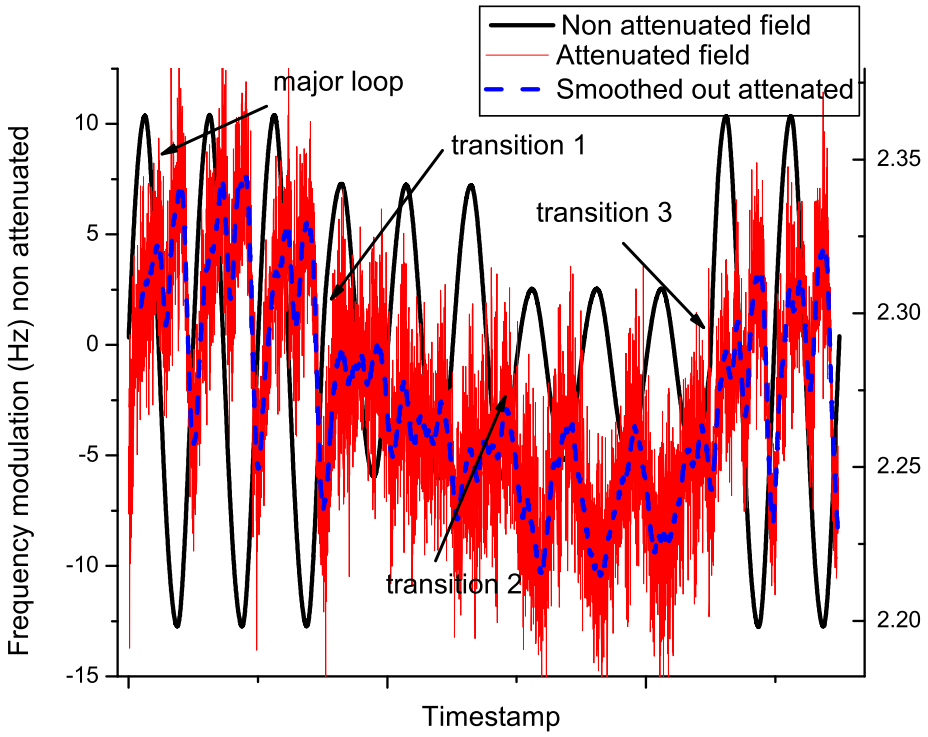

Figure 6.21: Quasi-sinusoidal pattern used to test the active attenuation system. In black (y-scale on the left) is the non attenuated magnetic field measured using Ramsey m = 1 transition and shown in Hz (see Equation 6.22 to transform to μT). In red (y-scale on the right) is the attenuated magnetic field measured using the Ramsey m = 1 transition. The smoothed out (noise averaged) attenuated signal is shown with a dotted line. Transition 1 on the figure represent the transition from the largest major loop to the offseted minor loop where the software needs to calculate new coefficients. Transition 2 on the figure represents the transition from level 2 major loop to the centred level 2 minor loop where the software also needs to calculate new coefficients. Transition 3 represents the transition from the smallest minor loop to the largest major loop where the software needs to use the coefficients from memory. Period of all sinusoidal oscillations is around 90 minutes, with the entire pattern having a duration of around 15h. Taking into account noise, the total attenuation achieved is about 190.

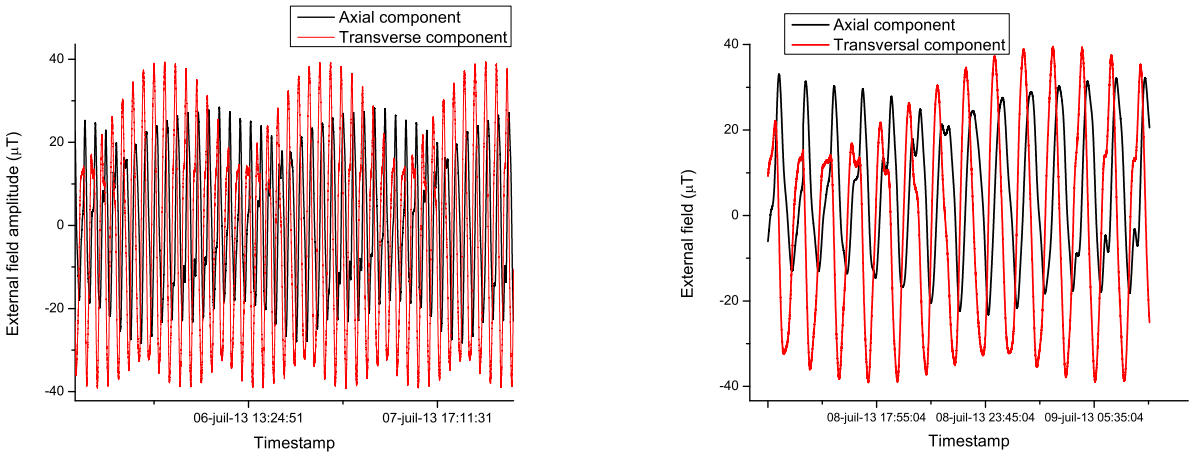

Figure 6.22: Components of the simulated external field in μ T as a function of time during several days (left) and one day (right).

applied. The axial and the transverse component (which can be separated into radial and lateral contributions) were studied separately and then combined. The lateral contribution of the transverse component was not studied as due to its low amplitude ($\pm 5\mu T$) and the large lateral direction shield attenuation it is negligible compared to other components. The total field with the two components can be seen on Figure 6.22. Observe that the two components are in quadrature (phase difference of $\frac{\pi}{2}$).

6.1.3.11 Axial results

The system was tested by applying only the axial component of the orbit field seen on Figure 6.22. Similar period was used as before representing the orbit period of the ISS.

For the experiments using only the axial component of the external field, the external amplitude applied was $\pm 28\mu T$. This results in a frequency modulation of $\approx 22.05 Hz$ peak to peak in the interrogation cavity which is equivalent to an internal magnetic field of about 0.003 μT peak to peak. The relationship is:

$$\text{field}(\mu T) = \frac{\text{frequency shift(Hz)}}{7008,4 Hz/\mu T}). \tag{6.22}$$

Figure 6.23 shows the comparison of the non attenuated and the attenuated hysteresis loop systems between the magnetometer measurement and the clock frequency

modulation. Using the varying linear and fixed absolute value of the square coefficient as before, the orbit field was attenuated by a factor of around 400. This was calculated by comparing the peak to peak of the non attenuated signal in black and the averaged out attenuated signal in thick red.

In orbit it is not possible to control the external field and one needs to determine the coefficients in a reliable and rapid manner using only the orbital field oscillations. For a completely axial field this is not difficult. All the orbital oscillations define a single hysteresis envelope which is their major loop; the branches of the major loop are composed of multiple minor loop branches.

An easy way to study and fit the section of a major loop for an axial external field would be to look at either the descending branch or the ascending branch of the hysteresis loop of lowest or highest turning point value, respectively. One of these sections is centralized and fitted to obtain the α coefficients. Therefore, the maximum necessary time for calibration of the active compensation system in orbit would be half orbit or 12h. For an illustration see Figure 6.24.

Due to the influence of the transverse field component, a less precise method consisting of using coefficients of an average amplitude loop (and not the major loop) will be used on PHARAO. This is because, as will be explained next, the effect of the transverse component cannot be evaluated correctly due to magnetometer restrictions.

6.1.3.12 Degradation of results for the total field and the tracking procedure

With only the transverse component ($\pm 39 \mu T$ external field amplitude) the attenuation inside the interrogation cavity was 1 250 000 compared to 19 000 for the axial component ($\pm 31.65 \mu T$) (15). At the position of the magnetometer the attenuation is 202.5 for the transversal component and 9.4 for the axial.

For the total field, the magnetometer cannot separate the two contributions. This results in the linear coefficient between the magnetic fields measured at the magnetometer and inside the interrogation cavity being about 2.5 times larger for the axial component than the transverse. This factor originates from the difference of the $\frac{\text{axial component attenuation}}{\text{transversal component attenuation}}$ at the magnetometer position and the interrogation cavity. The transverse component is then overcompensated in the interrogation cavity.

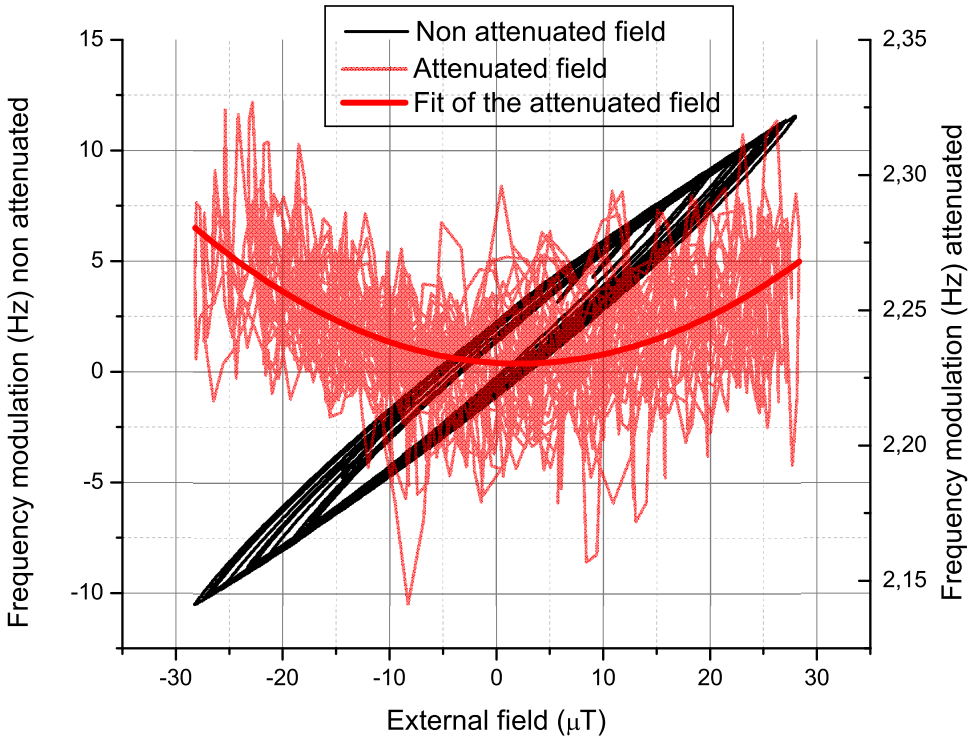

Figure 6.23: Pattern of the simulated orbital field with only the axial component. Ramsey m = 1 interrogation frequency shift (use Equation 6.22 to transform to μT) as a function of the magnetometer measurement. In black is the non attenuated field hysteresis. In the noisy red is the attenuated field. Notice how the hysteresis was rotated (linear coefficient) and flattened (square coefficient) and what remains is the deformation due to higher order contributions. By looking at the peak to peak comparison and ignoring noisy overshoots, the attenuation value is around 400.

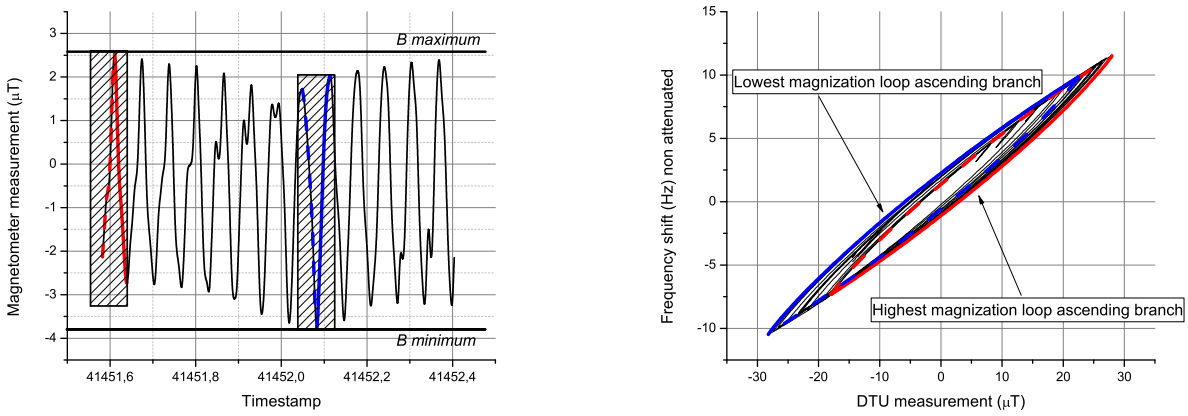

Figure 6.24: The descending and ascending field oscillations inside the axial field envelope of the highest (in full red) and lowest magnetization (in full blue) hysteresis loop, respectively, are part of the imaginary major loop. By measuring, centralizing and fitting these branches it is possible to obtain the coefficients of the major loop. The y-axis shows the internal magnetic field expressed in the Ramsey m = 1 frequency shift.

For the total field experiments the transverse component amplitude was set to $\pm 39 \mu T$, while the axial component amplitude was reduced to $\pm 23.8 \mu T$. This results in a frequency modulation of about $18 Hz$ peak to peak inside the interrogation cavity which is equivalent to 0.0026 μT peak to peak. The value needs to be reduced by at least an order of magnitude with the active compensation system.

Mostly due to mixing of the field components, when using the fixed value linear coefficient the attenuation reaches only 11.

Theoretically, looking at the magnetometer attenuation for the two components the maximum attenuation that can be achieved is 21.5. However, another reason for the degradation of performance compared to the purely axial field is the phase difference between the components. This effect increases the width of the hysteresis between the two positions due to phase quadrature. In order to compensate for the dephasing of the two components which dominates the hysteresis signal for the total field, coefficient α_2 was increased by about 300% compared to the axial field compensation value. Finally, for a varying linear and fixed absolute value of the square coefficient the attenuation is 17.

A comparison of the non attenuated total field (largest system of loops in black),

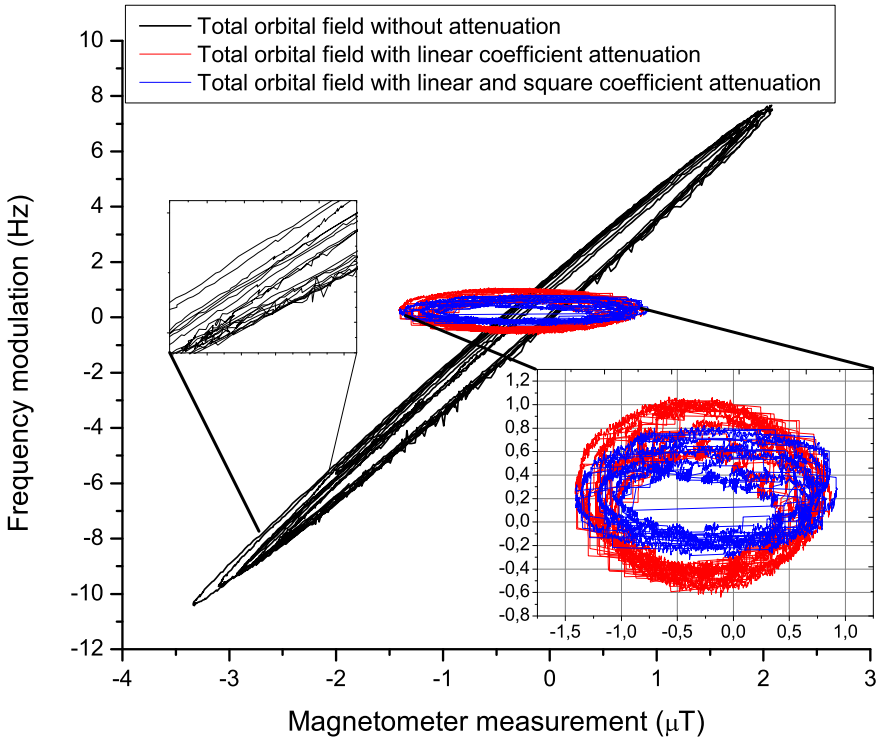

Figure 6.25: Comparison of frequency modulation for the total field (largest system of loops in black) to the attenuated total field using only the linear coefficients (in red) and to the attenuated field using both coefficients (smallest system of loops in blue). To transform Hz to μT use Equation 6.22. The left inset shows the interaction of many loops for an orbital field. The right inset zooms in the two attenuated signals.

linearly attenuated (in blue) and attenuated using both coefficients (smallest system of loops in red) can be seen on Figure 6.25.

It could be possible to change the position and orientation of the probe to decrease the coupling to the transverse field. However, additional frequency dependencies have been measured in correlation with the temperature of the baseplate. The temperature variation influences the electronics that drives currants in the coils (modifying the radiated magnetic fields) and controls the DTU.The contributions to the Zeeman hyperfine frequency have been evaluated: DTU temperature dependency ($0.2Hz/°C$), BP coil dependency ($0.06Hz/°C$) and thermocourant ($0.05Hz/°C$) generated by a tempera-

ture gradient inside the cesium tube. In orbit, the temperature variation will be $\pm 1.5^{\circ}$ with the resulting Zeeman frequency variation of $\pm 0.47 Hz$ which is the same order of magnitude as the magnetic field effect.

Normal clock operation is based on a hyperfine transition between $m_F = 0$ Zeeman sub-levels. To ensure 20 pT clock accuracy (10^{-17} second order Zeeman effect clock uncertainty contribution), every 500 sec for a duration of 10 sec the clock will measure a hyperfine transition more sensitive to the magnetic field (m_F hyperfine transition). Field measurement interval duration depends on the attenuation achieved with magnetic shields and the active compensation system. The internal field will then be interpolated in order to have the knowledge of the internal field within 0.3 Hz at all times.

6.1.3.13 Shield attenuation as a function of external field amplitude and demagnetization

As noticed in (15) and many other papers the shield attenuation has a dependency on the external field amplitude. Shield attenuation is inversely proportional to the hysteresis curve linear slope or factor α_1. On Figure 6.20 the centred hysteresis *Loop*1 and the non centred hysteresis *Loop*2 have the same amplitude $\pm 17 \mu T$. However, when the second loop is centred and compared to the first one it can be seen that their slopes are different (by %10). Therefore, oscillations of the same amplitude do not have to have the same attenuation. This is a result of the material lacking the congruency property. The dependency of attenuation on amplitude is not unique, but depends on previous shield history. By using the model, it is possible to deduce the relationship for a given shield.

In light of this, another possible usage for this model is shield demagnetization. In the limit of our low frequency observation, the findings tell us that demagnetizing a shield in a classical way with a damped sinusoidal external field does not actually erase shield history. Starting from the largest loop the oscillation creates a large number of centred loops of diminishing size which never close on their previous loop turning point (or never reach the switching point) as the field is inverted before they reach it. The final magnetization point depends on the resolution of the demagnetizing wire and on the stopping position on the smallest achieved hysteresis loop. Following a demagnetization process, if we were to increase the field to the amplitude of the starting loop it would

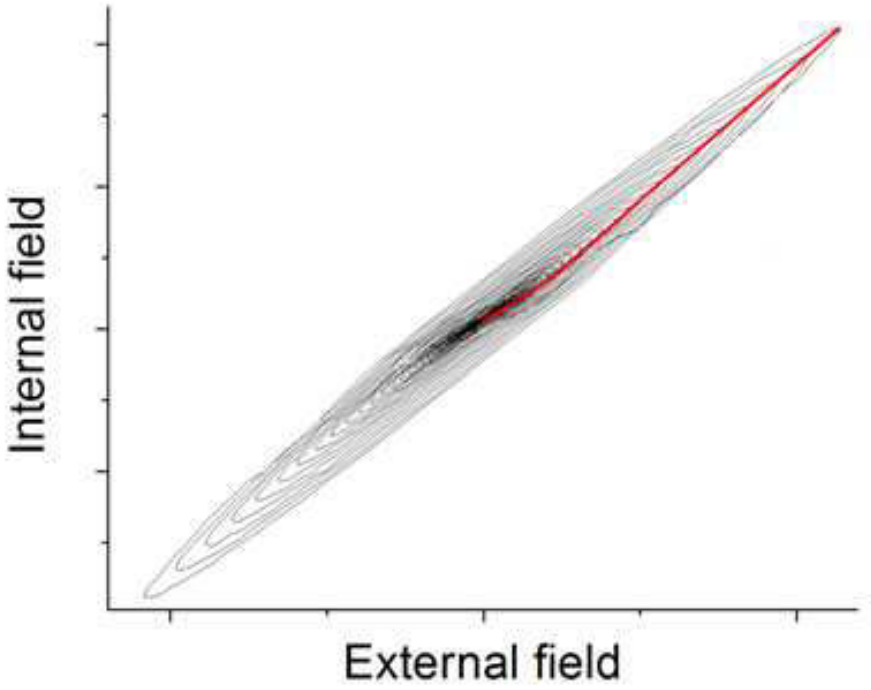

Figure 6.26: How the initial magnetic susceptibility curve is created by following sections of minor curves.

follow the segmented trajectories of different loop sections until the maximum value was reached (see Figure 6.26 for illustration).

As the hysteresis loops created during a demagnetizing process are very condensed due to a relatively low damping factor the magnetizing curve would appear to be continuous and it actually represents the initial magnetic susceptibility curve (112). Therefore, the magnetic susceptibility curve for a given material depends on the parameters of the previous demagnetizing process (125) or, if the shield was subjected to a magnetic field variation after the demagnetizing process (as it mostly is due to the Earth magnetic field), on shield magnetic history created by this variation.

Using the same idea from previous sections, a more efficient and less time consuming demagnetization process can be devised. With an external field source, it is possible to create a magnetization "trajectory" from the initial magnetization value on some

hysteresis loop to a position much closer to the zero magnetization value. For example, on Figure 6.18 the first order solution would be to select point B in such a way that the minor loop descending curve goes to zero magnetization. By ignoring the cube coefficient to simplify and assuming a centralized major loop, Equation 6.16 is translated to the non centralized system to obtain:

$$B = \alpha_0 + \alpha_1(b + b_0) + \alpha_2(b + b_0)^2. \tag{6.23}$$

If the upper equation represents the ascending branch, the descending branch will be the same but for the opposite sign of the square coefficient. By putting $b = b_{\text{section max}}$ (in this example $B = b_{\text{section max}}$), comparing the equations of the two branches and solving for $b_{\text{section max}}$ we obtain the position of B on the ascending curve of the major loop:

$$B = b_{\text{section max}} = \frac{\alpha_0}{2 \times b_{\text{section min}} \times \alpha_2} \tag{6.24}$$

However, the hysteresis may vary as a function of position and the magnetization is not homogeneous inside the shields. That means a demagnetizing trajectory calculated to zero magnetization on one position inside the shields may not finish at zero magnetization on another position. Experimental verification is necessary to validate the procedure and evaluate the significance of the mentioned drawbacks.

6.1.4 Conclusion to Zeeman shift

We have presented the experimental results on the characterization of the magnetic shields used by the PHARAO clock flight model for a low frequency excitation of <0.01 H. These measurements have been performed in two parts: on the shields alone by using a magnetic probe and on the space qualified cesium tube by using cold atoms. The attenuation results were similar. The high amplitude variation induces a hysteresis phenomenon inside the Mumetal shields which creates a dependency of the shield attenuation with the external field amplitude due to a permeability variation above some critical value.

In the most critical part of the clock, the interrogation cavity, the shields axial attenuation is around 19 000. Attenuations of 11544 and 11259 were deduced at the two interrogation cavity ends. This is not changed after clock qualifications. On average,

the attenuation of the interrogation cavity is 1 653 000 for the transverse field amplitude of $40\mu T$.

An active compensation system has been designed to increase the magnetic field attenuation. A model has been developed able to predict minor loop hysteresis behaviour based on major loop parameters and shield history.

Experimental results show that the model works as expected and for a simple axial orbital magnetic field the system yields an attenuation of about 440. We can conclude that our model works well and allows for a significant attenuation of the internal field.

Unfortunately, due to restraints on the PHARAO magnetometer the attenuation is significantly impaired when adding another field component and the attenuation is reduced to 17. Other sources of magnetic perturbation are due to the orbital temperature variation. Normal clock operation is based on a hyperfine transition between $m_F = 0$ Zeeman sub-levels. To ensure 20 pT clock accuracy (10^{-17} second order Zeeman effect clock uncertainty contribution), the magnetic field is measured using the m = 1 transition every 500 sec for a duration of 10 sec. The internal field will then be interpolated in order to have the knowledge of the internal field within 0.3 Hz at all times.

During clock operation the relative Zeeman frequency shift on ground is:

$$\frac{\Delta\nu}{\nu_0} = 1.8109 \pm 0.0007 \times 10^{-13}. \tag{6.25}$$

In orbit, the static magnetic field will be lower than 100 nT. Thanks to a larger velocity range, better magnetic field measurement uncertainty can be expected in (lower than $5{\times}10^{-15}$).

6.2 Black body radiation

6.2.1 Introduction

A body in thermal equilibrium emits electromagnetic radiation according to Planck law. The energy spectral density of the radiation in the frequency interval (ν,ν+$d\nu$) (127) is given by:

$$\rho(\nu) = \frac{h\nu}{e^{h\nu/kT} - 1} \frac{8\pi\nu^2}{c^3} d\nu J/Hz/m^3, \tag{6.26}$$

where h is the Planck constant, k is the Boltzmann constant, c is the speed of light and T is temperature of the body.

On the other hand, the total energy of the black body radiation electric field is proportional to the mean square value of the electric field:

$$\int_0^\infty \rho(\nu) d\nu = \epsilon_0 \langle E^2 \rangle \tag{6.27}$$

By integrating Equation 6.28 over the entire frequency specter, the total energy density or the Stefan-Boltzmann law is obtained. This is compared to Equation 6.27:

$$\int_0^\infty \rho(\nu) d\nu = \frac{8\pi^3}{15} \frac{(kT)^4}{(ch)^3} = \sigma T^4 = \epsilon_0 \langle E^2 \rangle, \tag{6.28}$$

to arrive to:

$$\langle E^2(T) \rangle = (831.9)^2 (\frac{T}{300})^4 (V/m)^2, \tag{6.29}$$

where $\sigma = 7.57 \times 10^{-16} J/m^3 K^4$ is the Stefan-Boltzmann constant.

Radiation of the cavity walls perturbs the energy levels of cesium atoms causing a frequency shift of the clock hyperfine transition by AC Stark effect (128, 129, 130, 131, 132). Calculation and experiments give the relation between the temperature and the frequency shift:

$$\frac{\Delta\nu}{\nu_0} = -1.717 \times 10^{-14} \times (\frac{T}{300})^4 [1 + \epsilon (\frac{T}{300})^2] \tag{6.30}$$

where the factor $-1.717 \pm 003 \times 10^{-14}$ and $\epsilon = 0.013 \pm 0.001$ were obtained experimentally and theoretically. For a much more detailed look into the theory see (133).

By neglecting the T^6 factor and differentiating Equation 6.30 for temperature, the relation between the temperature and frequency uncertainty:

$$\delta(\frac{\Delta\nu}{\nu_0}) = -1.717 \times 10^{-14} \times 4\delta T \times \frac{T^3}{300^4} = 4 \times \frac{\Delta\nu}{\nu_0}\frac{\delta T}{T}, \tag{6.31}$$

A frequency uncertainty $\delta(\frac{\Delta\nu}{\nu_0})$ has to be lower than 5×10^{-17}. Consequently, at $T = 300K$ the temperature uncertainty is lower than 0.22 K.

Inside PHARAO, about 80% of thermal radiation comes from the copper walls of the interrogation cavity. 18% is from the vacuum chamber, while the rest originates from other cesium tube components (whose temperatures is between 20 and $35°C$).

6.2.2 PHARAO thermal architecture, development and temperature uncertainty

The thermal architecture of PHARAO is shown on the Figure 6.27. Beside the other subsystems, the cesium tube is also insulated by MLI to isolate from the thermal radiation of the microwave source, detection source and BEBA.

The vacuum cavity includes the interrogation cavity, the Alu/SiC support and all the other parts which it encompasses. For an explanation of components see Figure 6.28.

The baseplate temperature can vary between 10 to $33,5°C$ on long term (months) and $\pm 1.5°C$ per orbit. To support these variations the cesium tube has 5 independent thermal regulations. The thermal regulation systems are PID (proportional-integral-derivative) loops. The servo loops are driven by UGB at the 10 sec rate. For an illustration see Figure 6.27.

The detection photodiodes and the amplifier AD645 have to be regulated at a temperature inferior than $15°C$ and at $17°C$ (in order to decrease the detection noise), respectively. This regulation is more necessary when the baseplate is at higher temperatures larger then $33°C$. Temperature of the detection zone is controlled by 2 Peltier modules and 2 thermistors.

The temperature of the cesium reservoir is regulated at 0.1 $°C$ in the range of 40 to $60°C$ (to change the cesium pressure). To accomplish this the cesium reservoir uses a heater and a thermistor.

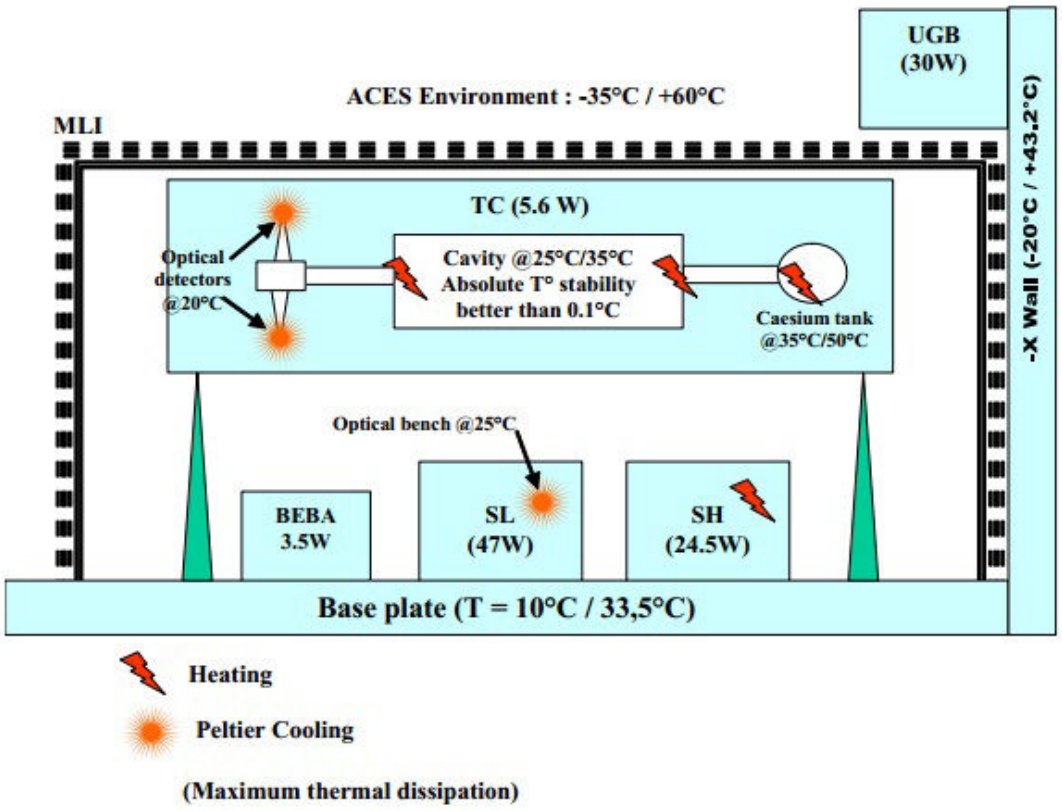

Figure 6.27: Components of the PHARAO thermal control. All the subsystems are isolated by multilayer insulation (MLI).

Thermal regulation of the interrogation cavity is ensured by 2 heaters and 2 thermal probes on each side of the vacuum chamber surrounding the cavity. Each heater is powered by the UGB. In order to reduce the effect on magnetic homogeneity of the interrogation cavity, the heaters are placed outside of the smallest B1 magnetic shield. The heaters are composed of 4 heating bands connected in series with dimensions 30 mm X 13 mm. Total surface per heater is 15.6 cm^2 and maximum power 3.7 W (0.24 W/cm^2). Every heating band is connected to a titan support plate by a two faced tape. In order to limit the radiative heat exchange between the heaters and the magnetic shields, a Sheldal tape of low emissivity was put over each upper side of the heater band. An illustration of the heaters and their position around the X-Wing is given in Figure 6.29.

Experiments and simulations (ESATAN, IDEAS sofware) on the STM and FM were

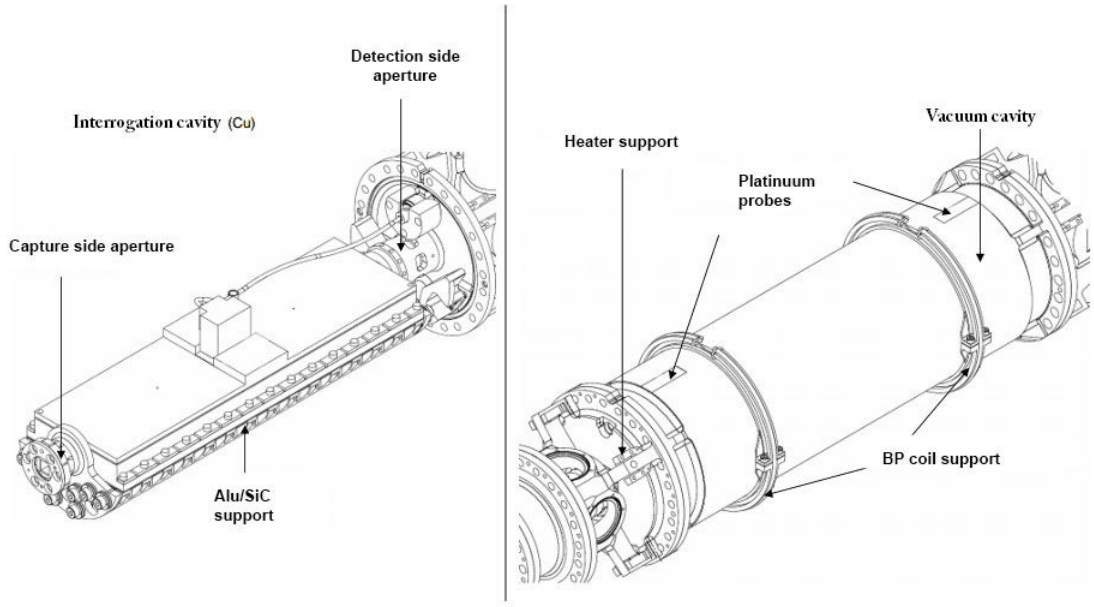

Figure 6.28: The interrogation and the vacuum cavity.

performed. Parameters of the simulations (conductivity, emissivity of the different materials) were adjusted to correspond to the experiment.

6.2.2.1 STM experimental results and modelization

6 platinum thermal probes (accuracy $\pm 0.1°C$) placed around the interrogation cavity, 5 thermistors (accuracy $\pm 0.5°C$) and 40 thermocouples (accuracy $\pm 1°C$) were used to follow the testing temperature and its evolution ($< 0,1°C/h$) at different positions inside the tube. 3 probes are under vacuum; 2 are glued on the cavity and 1 on the cavity support. The other 3 probes are outside of the vacuum; 2 on the sides of the vacuum chamber surrounding the cavity and 1 is at the center. A photo of the probes placed on the interrogation cavity is shown in Figure 6.30.

5 thermistors (accuracy $\pm 0.5°C$) and 40 thermocouples (accuracy $\pm 1°C$) were placed ($< 0,1°C/h$) at different positions inside the tube. 3 thermistors were used for the thermal regulation loops of the cesium reservoir (in combination with a heater) and detection modules (in combination with two Peltier heater coolers).

During the experiments the STM is under vacuum and enveloped under MLI as shown on Figure 6.31.

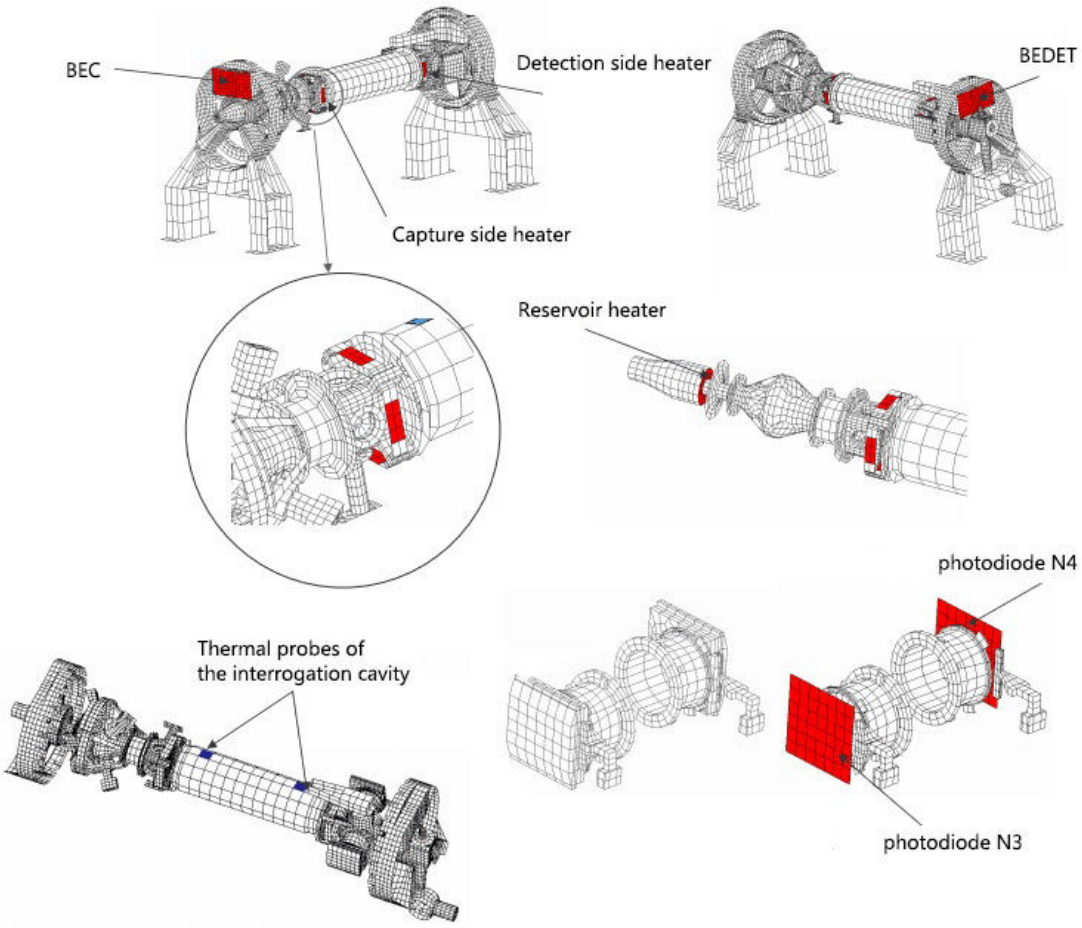

Figure 6.29: Components of the PHARAO thermal control. BEC contains the photodiode amplifiers to measure the laser power during capture. BEDET contains the photodiode amplifiers to measure the laser power in the selection and detection phases. Both devices dissipate heat and this is taken into account.

The cesium reservoir and the interaction zones were regulated at $38 - 55°C$ and $38.5°C$, respectively. Detection modules N3 and N4 temperature was varied $14.5 - 17.5°C \pm 1°C$. In order to test thermal regulation and the resulting internal thermal homogeneity, the tube was submitted to different thermal conditions during one month of testing. The operational range of the TRP temperature is $10 - 31,4°C$. The illustration of the thermal environments to which the tube was submitted are given in Figure 6.32.

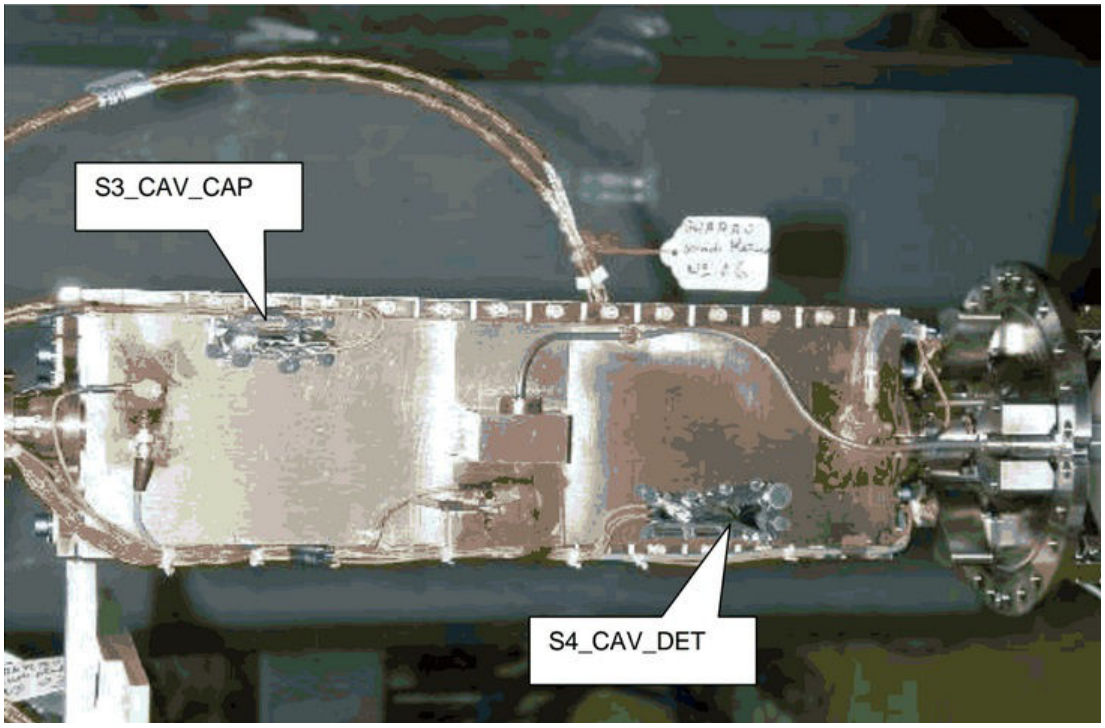

Figure 6.30: Probes positioned on the interrogation cavity for the STM experiments. Photo from above.

Using a finite elements analysis I-DEAS to calculate the temperature of different PHARAO thermalized components with thermal regulation turned on for various operation temperatures of the cesium tube ranging from $0°C$ to $41.4°C$, the temperatures of the reservoir, the detection modules and the interrogation cavity probes were deduced for the improved model based on the STM measurements. A simplified thermal analysis model ESATAN able to describe the heat exchange inside the cesium tube was used to make dynamical calculations in the case of orbital thermal variation.

Due to radiative and conductive thermal exchange other cesium tube parts not inside the vacuum cavity have an influence on its homogeneity. These include the support of the BP coil (which is an aluminium solenoid with an average thickness of 2 mm) and the Mumetal B1 magnetic shield which is connected at each side by 4 attachments positioned on the X-Wings. The heat exchange paths are illustrated in Figure 6.33. The interrogation cavity and the Alu/SiC support are conductively heated by the microwave field cable and radiatively by the vacuum cavity which is cooled by the BP coil and heated by the magnetic shield B1 (which is heated by shields B2 and

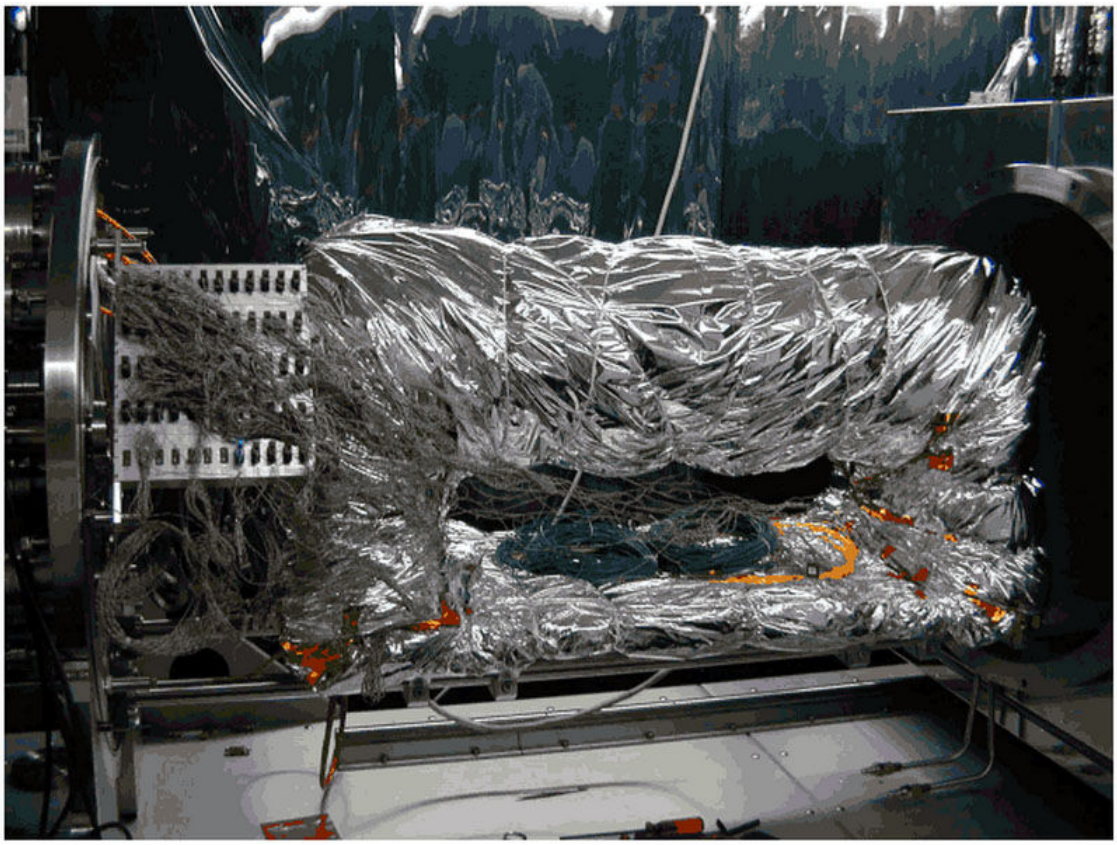

Figure 6.31: STM cesium tube wrapped in a thermal isolation blanket during testing.

B3) and the two ends of the atom path.

ESATAN software was used for calculation of internal temperatures in cases of dynamical hot and cold temperature variations. For the hot case the temperature of the cesium reservoir was $60°C$ and the temperature of TRP was $31.4°C$ with a variation of $-2°C$ and temperature variation slope of $0.2°C$/min. The calculated results for the temperature variation inside the interrogation cavity and the cesium reservoir conform to specifications of $< 0.22°C$ and $< 2°C$ respectively. Similarly, the temperatures conform to requirements for the cold case variation of $40°C$ cesium reservoir and $10°C$ TRP.

Figure 6.34 shows the temperature values at different positions comparison between STM I-DEAS simulations (model) and measurements (exp) for the three most important temperature cases. As the differences are very small, the modelization is validated. For TRP temperature of $10°C$ the interrogation cavity homogeneity is 0.1 K. However,

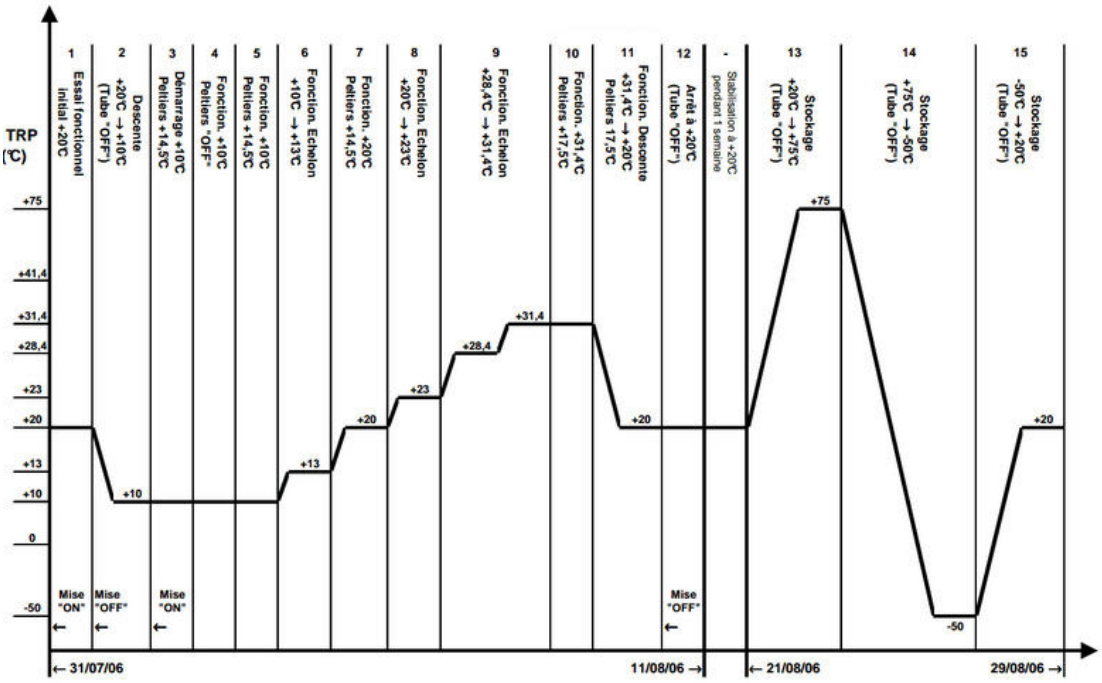

Figure 6.32: STM cesium tube testing bottom of cesium tube support temperature (TRP) sequence.

taking into account the probes used for thermal regulation are glued outside on the vacuum chamber the temperature difference is 0.6 K. The vacuum chamber homogeneity is 1 K. For TRP temperature of $20°C$ the interrogation cavity homogeneity is 0.1 K and the difference with the external probes is 0.5 K. The vacuum chamber homogeneity is 0.7 K. For TRP temperature of $31.4°C$ the interrogation cavity homogeneity is also 0.1 K, while the difference concerning the thermal regulation probes and the vacuum chamber homogeneity are better and are 0.3 K.

For colder TRP temperatures the magnetic shields B1, B2 and B3 had a higher temperature, while the vacuum cavity had a lower temperature than predicted. This can explain the larger temperature gradient inside the interrogation cavity. The reason for the low temperature of the vacuum cavity is probably the coil BP. Due to last minute mechanical design changes the coil was better thermally isolated than it was envisioned by the thermal analysis. This caused the coil to be colder than expected and in turn it cooled the vacuum cavity more than planned which caused inhomogeneity

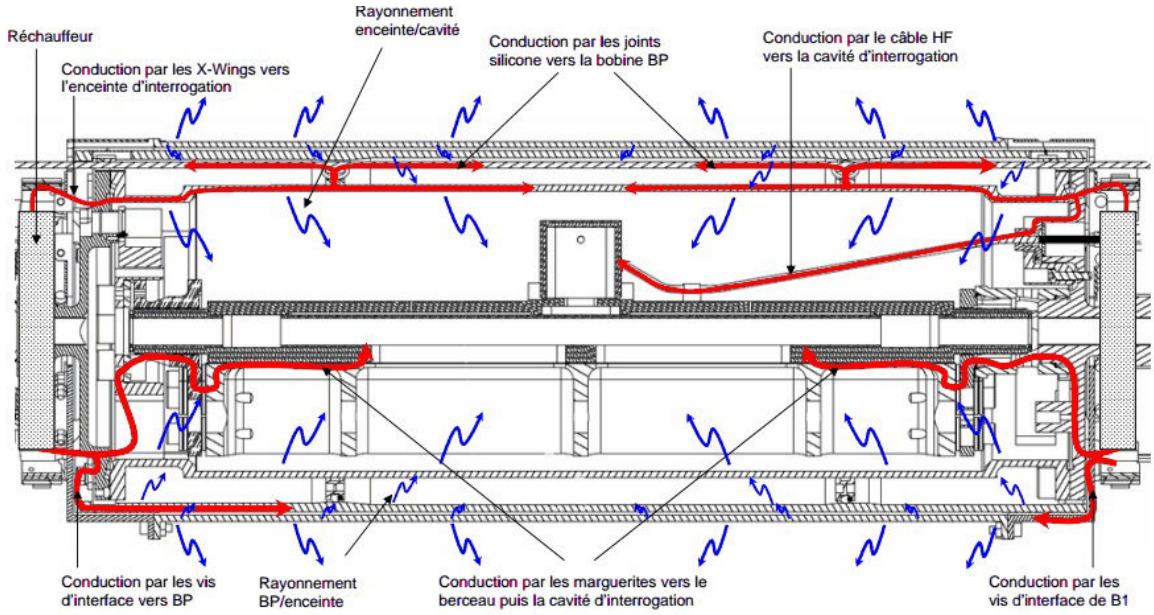

Figure 6.33: Radiative and conductive heat exchange inside paths inside the vacuum cavity.

inside the interrogation cavity.

From software calculations it was concluded that the results could be improved by radiative decoupling between the vacuum cavity and the magnetic shields and by making modifications to the BP coil connection thermal resistance. As was found that the B1 and B2 shields have a large temperature difference (B2 shield had $\approx 10°C$ higher temperature), it was decided to gold coat the shield B1 in order to better isolate it and reduce cooling of the BP coil. The position of the regulation probes and the heaters was also decided to be changed. It was suggested that the temperature to which the Peltiers are regulated is increased from $14.5°C$ to $20°C$ in order to reduce its larger than expected power consumption (by 90% for the hot case).

The software analysis shows that the gold coating of the B1 shield increases the temperature of the vacuum cavity by about $0.6°C$ which improves its homogeneity by 35%. This also decreases the large power consumption of the heaters present in the original STM experiments. By increasing the regulation temperature and better isolating the detection zone, the consumption of the Peltiers decreases by 42%. By reducing its thermal isolation, the temperature of the BP coil increases and therefore

its effect on the cooling of the interrogation cavity significantly decreases for the hot case situation. However, for the cold case the BP was still too cold and would have created an inhomogeneity inside the interrogation cavity.

In conclusion, the simulations showed that the mechanical and design improvements significantly improve homogeneity and it was decided to implement them on the design of the FM.

	Cas essai n°5 (10°C)			Cas essai n°7 (20°C)			Cas essai n°10 (31,4°C)		
	Model	Exp.	Diff.	Model	Exp.	Diff.	Model	Exp.	Diff.
Température (°C)									
TRP1Capture	10.0	10.0	0.0	20.5	20.5	0.0	31.9	31.9	0.0
TRP2 Détection	10.1	10.1	0.0	20.9	20.9	0.0	32.5	32.5	0.0
Cavité 1 ZI capture	38.5	38.5	0.0	38.5	38.5	0.0	38.5	38.5	0.0
Cavité 2 ZI détection	38.5	38.5	0.0	38.5	38.5	0.0	38.5	38.5	0.0
Module N3	14.5	14.5	0.0	14.5	14.5	0.0	17.5	17.5	0.0
Module N4	14.5	14.5	0.0	14.5	14.5	0.0	17.5	17.5	0.0
Réservoir	37.9	38.0	0.1	40.0	40.0	0.0	54.9	55.0	0.1
Cavité interro-coté-cap	37.9	37.9	0.03	38.1	38.1	0.01	38.2	38.3	0.01
Cavité interro-coté-det	37.9	37.9	0.00	38.0	38.0	-0.02	38.2	38.2	-0.02
Berceau milieu	37.9	38.0	0.07	38.0	38.1	0.05	38.2	38.3	0.06
Cavité interro-milieu	37.4	37.5	0.06	37.8	37.8	-0.01	38.3	38.3	-0.03
Réservoir	17.5	18.4	0.9	25.7	26.3	0.6	36.7	37.0	0.29
Collimateur capt. inf.	25.8	25.8	0.0	31.0	30.6	-0.4	38.9	37.4	-1.5
Collimateur capt. sup.	27.1	27.8	0.7	31.6	31.8	0.2	38.5	37.5	-1.0
Collimateur sél. inf.	34.9	35.8	0.9	36.4	36.8	0.4	38.4	38.3	-0.1
Réchauffeur HR1	53.1	72.6	19.5	47.8	60.8	13.0	40.3	43.9	3.6
X-wing sél. sup droit	37.9	39.3	1.4	38.3	39.1	0.8	38.7	38.8	0.1
X-wing dét. sup droit	36.5	35.8	-0.7	37.0	36.5	-0.5	37.6	37.5	-0.1
Détection côté N3	27.8	29.3	1.5	30.8	31.9	1.1	34.7	35.5	0.8
Détection illumination	25.9	27.3	1.4	30.0	30.8	0.8	35.4	35.7	0.3
Détection côté N4	26.2	27.4	1.2	29.7	30.4	0.7	34.3	34.6	0.3
Détection côté croix	17.7	18.2	0.5	26.5	27.2	0.7	36.7	38.1	1.4
Pompe ionique	14.8	15.6	0.8	24.8	25.3	0.5	36.1	36.8	0.7
Roue capture bas	15.0	14.1	-0.9	24.0	23.4	-0.6	34.8	34.2	-0.6
Roue capture interne	14.6	14.4	-0.2	23.7	23.4	-0.3	34.7	34.3	-0.4
Carte BEC	20.8	17.4	-3.4	29.3	26.1	-3.2	41.1	37.0	-4.1
Roue capture haut	16.9	16.2	-0.7	25.3	24.9	-0.4	36.1	35.5	-0.6
Roue détection bas	15.5	15.5	0.0	25.5	26.0	0.5	36.9	38.3	1.4
Roue détection Peltier	15.5	15.8	0.3	26.2	26.4	0.2	38.4	39.2	0.8
Carte BEDET	25.2	19.4	-5.8	34.8	29.1	-5.7	48.0	41.6	-6.4
Roue détection haut	16.7	17.2	0.5	26.3	26.9	0.6	37.4	38.7	1.3
Peltier face chaude	17.0	16.8	-0.2	28.9	28.0	-0.9	42.7	38.9	-3.8
Peltier face froide	10.3	9.2	-1.1	9.4	8.3	-1.2	11.7	17.3	5.6
BP milieu	36.7	36.7	0.0	38.3	37.4	-0.9	38.3	38.4	0.1
B1 côté sélection	31.3	33.9	2.6	34.0	35.7	1.7	37.6	38.1	0.5
B1 milieu	30.6	31.9	1.3	33.6	34.4	0.8	37.5	37.8	0.3
B1 côté détection	30.8	32.1	1.3	33.7	34.4	0.7	37.4	37.7	0.3
B2 côté capture	19.2	20.5	1.3	26.9	27.5	0.6	36.3	36.2	-0.1
B2 milieu	19.5	21.6	2.1	27.3	28.4	1.1	36.5	36.9	0.4
B2 côté détection	18.0	19.0	1.0	26.7	27.5	0.8	36.8	37.9	1.1
Fond B3 côté capture	16.4	16.0	-0.4	24.8	25.4	0.6	35.5	34.9	-0.6
B3 côté capture	16.8	17.4	0.6	25.2	26.8	1.6	35.9	38.2	2.3
B3 milieu	17.0	18.0	1.0	25.6	26.4	0.8	35.7	36.6	0.9
B3 côté détection	16.6	17.0	0.4	26.1	25.4	-0.7	37.0	35.6	-1.4
Fond B3 côté détection	16.0	16.8	0.8	25.7	26.3	0.6	36.8	37.9	1.1

Figure 6.34: Summary of the STM thermal modelization and measurements for the three TRP temperature cases. Most important probes are the two probes on the vacuum chamber ("Cavite 1 Z1 capture" and "Cavite 2 ZI detection"), cavity support probe ("berceau milieu") detection zone probes ("Module N3" and "Module N4", cesium reservoir ("reservoir") and probes under vacuum on the cavity ("Cavite interro-cote-cap", "Cavite interro-cote-det" and "Cavite interro-mileu").

6.2.2.2 FM modelization

For the STM the experimental regulation temperature was kept at $38,5°C$ during all the experiments. To improve the cavity temperature measurement the baseplate-cavity gradient was reduced. Figure 6.35 shows the new specifications for the thermal loop regulation temperature based on the TRP temperature (which reflects the environmental temperature).

TRP temperature	Regulation temperature
10 °C-20 °C	25°C
15 °C-25 °C	30°C
21,4 °C-31,4 °C	35°C

Figure 6.35: Thermal loop regulation temperature determined for different temperature of the TRP.

The STM design improvements described in the previous section have been implemented on the FM. Additional changes performed on the FM include the increase of the cesium tube support height by 20 mm and adding achievements to the detection side heater. The latter was done because it was noticed that the centre of the detection zone was too cold which was a source of inhomogeneity inside the interrogation cavity. For an illustration of these attachments see Figure 6.36. Simulations show that the addition of the attachments improves the interrogation cavity homogeneity by about 30%, from $\pm 0.18°C$ to $\pm 0.13°C$. It also significantly decreases the temperature difference between the regulation temperature and the cavity temperature.

I-DEAS software was initially used to construct a FM thermal model and verify its performances. An overview of different temperatures for 3 different temperature cases is shown on Figure 6.37.

For the three TRP temperature range cases (cold case $10-20°C$, typical case $15-25°C$ and hot case $21.4-31.4/20°C$) the gradient between the external probes and the cavity is 30 mK. This is a significant improvement over the STM. The vacuum chamber has a gradient of 260 mK. However, the vacuum chamber walls have a contribution of only 18%.

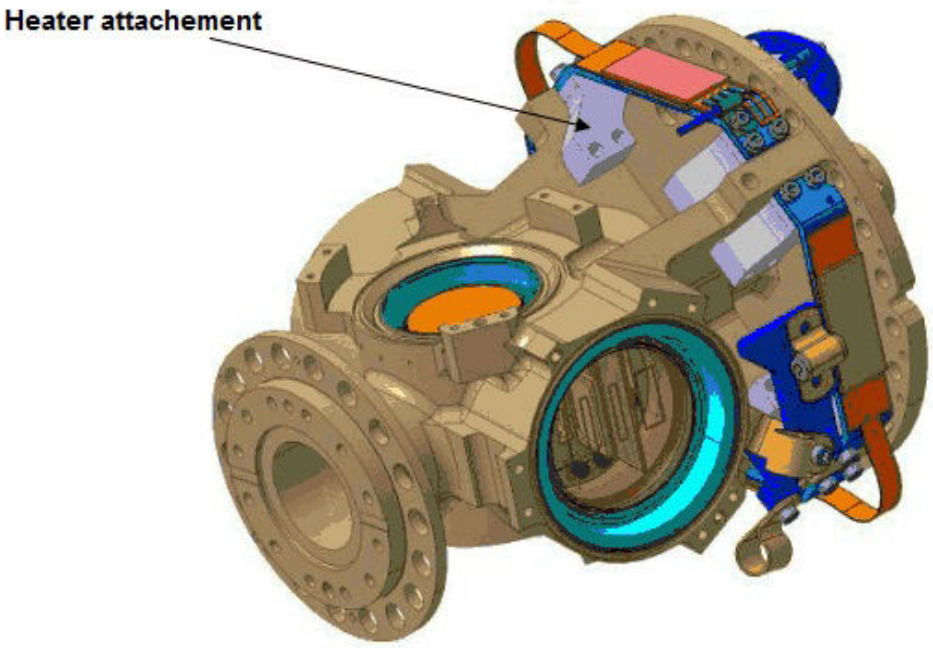

Figure 6.36: Attachments added to the detection side heater in order to increase the temperature of the detection zone.

ESATAN thermal analysis software was used on the FM for thermal modelization of dynamic cases. 48 nodes inside the cesium tube were taken into account for calculation. Thermal conductive coupling along the cesium tube is shown in Figure 6.38. On the other hand, the main radiative heat exchange is between the vacuum cavity and the magnetic shield B2 and at the level of the interrogation cavity.

By taking into account the heat capacity of the nodes and 5 thermal regulation loops, ESATAN is able to simulate the dynamic thermal behavior of the cesium tube. 8 different dynamic cases have been used. These are separated into cold, hot and typical cases for both the starting and perturbation type. The two types have different sequencing; for the starting type the detection thermal regulations is turned on after the stabilization of the main interrogation cavity thermal regulation, while for the perturbation type detection and all of the thermal regulation loops are turned on at the same time followed by 10 hot and 10 cold TRP temperature orbits. The former type has a goal to observe the stabilization time and the effect of turning on of different systems on internal homogeneity, while the latter type is used to study the operation case orbit

Modèle recalé MSTH + Evolution MV + réchauffeurs ZI en position basse	Cas froid plage 10°C/20°C		Cas typique plage 15°C - 25°C		Cas chaud plage 21,4 - 31,4°C	
	Consigne ZI à 25°C	Consigne ZI à 25°C	Consigne ZI à 30°C	Consigne ZI à 30°C	Consigne ZI à 35°C	Consigne ZI à 35°C
Température (°C)						
TRP1Capture	10.0	20.0	15.0	25.0	21.4	31.4
TRP2 Détection	10.0	20.0	15.0	25.0	21.4	31.4
Cavité 1 ZI capture	25.0	25.0	30.0	30.0	35.0	35.0
Cavité 2 ZI détection	25.0	25.0	30.0	30.0	35.0	35.0
Module N3	20.0	20.0	20.0	20.0	20.0	20.0
Module N4	20.0	20.0	20.0	20.0	20.0	20.0
Réservoir	40.0	40.0	40.0	40.0	40.0	40.0
Cavité interro-coté-cap	25.03	24.98	30.03	30.00	35.01	34.97
Cavité interro-coté-det	25.03	24.98	30.03	30.00	35.01	34.97
Berceau milieu	25.03	24.98	30.03	30.00	35.01	34.97
Enceinte interro-milieu	24.76	24.93	29.74	29.93	34.75	34.94
Réservoir	16.8	24.1	20.9	28.3	26.2	33.6
Collimateur capt. inf.	21.3	25.7	25.3	29.8	30.0	34.6
Collimateur capt. sup.	21.3	25.3	25.5	29.5	30.3	34.5
Collimateur sél. inf.	23.5	24.9	28.3	29.7	33.3	34.8
Réchauffeur HR1	29.2	25.6	34.8	31.1	39.7	35.8
X-wing sél. sup droit	24.6	25.0	29.5	30.0	34.5	35.0
X-wing dét. sup droit	25.7	25.2	30.8	30.3	35.8	35.3
Détection côté N3	22.4	24.0	27.0	28.5	31.8	33.5
Détection illumination	20.7	23.6	25.3	28.3	30.4	33.6
Détection côté N4	21.5	23.6	25.9	28.1	30.7	33.1
Détection côté croix	15.1	22.5	20.0	27.6	26.6	34.5
Pompe ionique	13.0	21.7	18.0	26.9	24.7	33.9
Roue capture bas	14.2	22.4	18.7	26.9	24.4	32.7
Roue capture interne	14.0	22.4	18.5	26.9	24.3	32.6
Carte BEC	20.1	27.7	24.3	32.0	30.8	38.4
Roue capture haut	16.1	23.6	20.3	27.9	25.8	33.5
Roue détection bas	13.3	21.9	18.4	27.2	25.3	34.6
Roue détection Peltier	13.1	22.0	18.4	27.6	25.6	35.5
Carte BEDET	22.9	31.2	28.0	36.4	36.8	45.7
Roue détection haut	14.5	22.7	19.5	27.9	26.3	35.1
Peltier face chaude	13.5	22.7	19.2	28.9	27.3	38.2
Peltier face froide	18.7	18.1	17.5	16.8	15.9	15.2
BP milieu	24.6	24.9	29.5	29.9	34.5	34.9
B1 côté sélection	23.1	24.6	28.0	29.5	33.1	34.7
B1 milieu	22.9	24.5	27.7	29.4	32.9	34.6
B1 côté détection	23.1	24.5	27.9	29.5	33.1	34.7
B2 côté capture	16.7	23.4	21.1	27.8	26.7	33.5
B2 milieu	16.6	23.1	21.2	27.8	27.1	33.8
B2 côté détection	15.4	22.7	20.3	27.7	26.6	34.3
Fond B3 côté capture	16.0	23.4	20.1	27.6	25.4	32.9
B3 côté capture	16.0	23.5	20.2	27.7	25.7	33.2
B3 milieu	15.6	22.7	20.0	27.2	25.8	33.1
B3 côté détection	14.5	22.5	19.4	27.6	26.1	34.6
Fond B3 côté détection	13.9	22.1	18.9	27.3	25.5	34.3

Figure 6.37: I-DEAS FM simulation results.

thermal variation effect. Different cases signify different average TRP temperatures: $10°C$ for the cold case, $20.7°C$ for the typical case and $31.4°C$ for the hot case. Variation of the TRP temperature implies different interrogation cavity regulation temperatures: $25°C$, $30°C$ and $35°C$ respectively. For the typical case regulation temperature of both $30°C$ and $35°C$ was used. The reservoir temperature was kept at $40°C$, while the

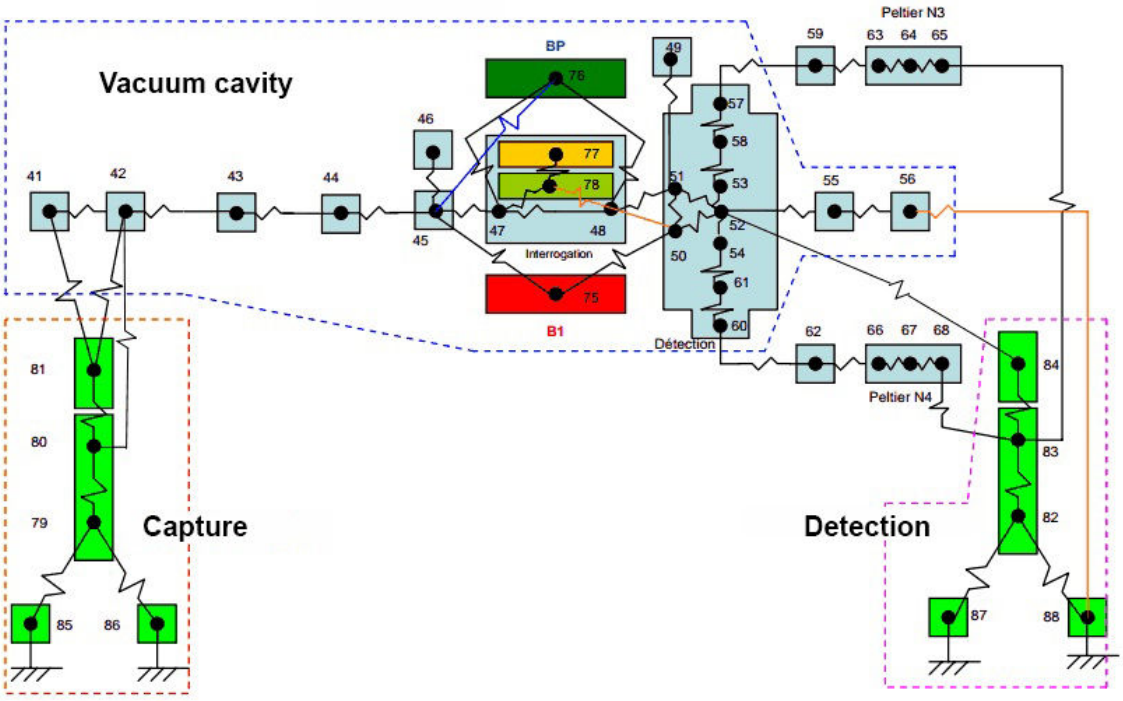

Figure 6.38: Thermal conductive coupling between the nodes of the cesium tube. Node 41 is the cesium reservoir, 44 is the preparation cavity, 45 is the selection cavity, 46 is the heater on the capture side, 47 and 48 are the two probes, 49 is the heater on the detection side, 56 is the ionic pump.

detection zone was kept at $20°C$ for the typical and hot case and $17°C$ for the cold case.

To illustrate the perturbation type cases, variations of the TRP temperature for the hot case is presented on Figure 6.39. Figure 6.40 takes a closer look on a single oscillation shape and slope used.

To study the derivation of the difference of temperature between the vacuum cavity and a interrogation cavity/support the following equation is used:

$$H(t) = [T_{vacuum}(t) - T_{interrogation/support}(t)] - [T_{vacuum}(t_0) - T_{interrogation/support}(t_0)], \tag{6.32}$$

where t_0 is the time of the first oscillation, T_{vacuum} is the temperature of the vacuum cavity and $T_{interrogation/support}$ is the temperature of the interrogation cavity/support combination.

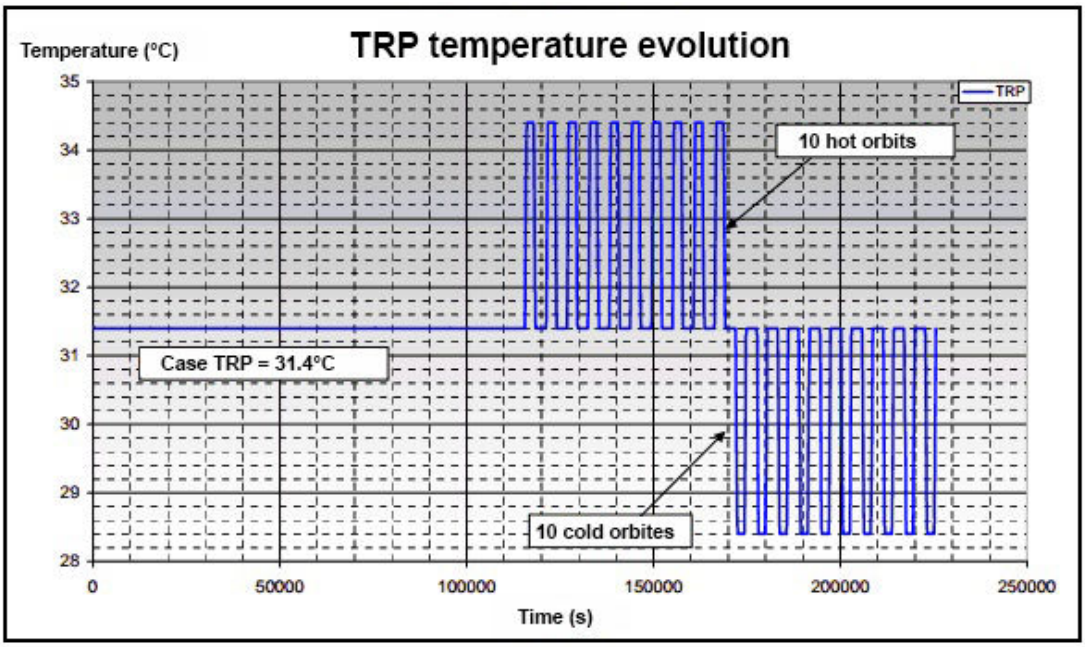

Figure 6.39: Hot perturbation case is composed of 10 orbits of higher temperature and 10 orbits of lower temperature for the TRP average temperature of $31.4°C$. This simulates the orbit hot case thermal variation.

With the derivation function $H(t)$ it is possible to follow the relative evolution of homogeneity during different perturbations. Additionally, if the vacuum cavity homogeneity is ensured and its temperature known, using the derivation value it is possible to deduce the interrogation cavity temperature.

Results of the dynamic calculation show that for the starting case the average time for stabilization after turning on the BEC and BEDET cards is around 250 000 sec, while the stabilization time after turning on the detection modules and regulation loops is around 60 000s.

For the reservoir, the interrogation cavity/support combination and the vacuum cavity the oscillations are +5 mK/ -8 mK, +12 mK/ -14 mK and +5 mK/- 6mK, respectively. The derivation function (Equation 6.32) for the oscillation described in Figure 6.39 varies from +15 mK to -13 mK implying a good homogeneity of the vacuum chamber. This is illustrated on Figure 6.41. From the experiments and the simulations the temperature difference between the probes and the cavity is evaluated at 30 mK.

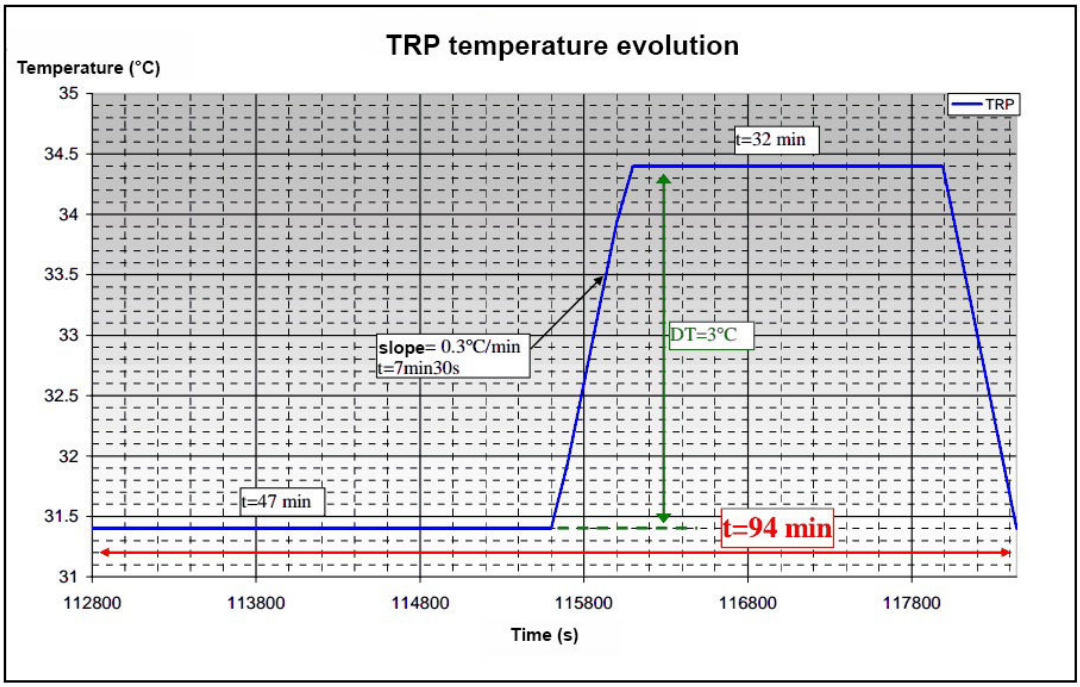

Figure 6.40: Single oscillation has a slope of $0.3°C$, amplitude of $3°C$ and a period of about 90 minutes.

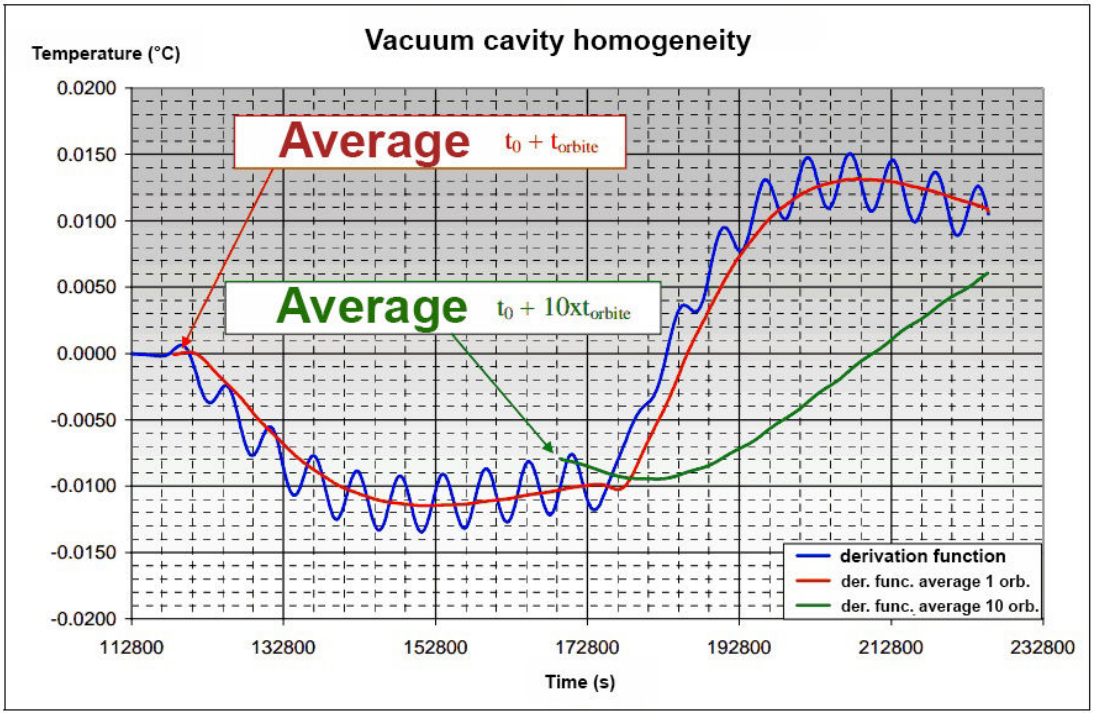

Figure 6.41: Oscillation of the derivation function in blue. The red curve is the average of the derivation function during one orbit and the green curve the average of the derivation function during 10 orbits (Figure 6.39).

6.2.2.3 FM experimental results

The experimental goals were to verify the operation of the thermal regulation loop, evaluate effect of external orbit representative thermal variations on interrogation cavity temperature (with and without thermal regulation), evaluate the interrogation cavity thermal gradient (between the probes and the cavity) and evaluate the effect of the cesium reservoir and detection zone thermal regulation on the interrogation cavity temperature.

Thermal probes 118 Rosemount PT100 were placed around the tube and on the cables as shown on Figure 6.42.

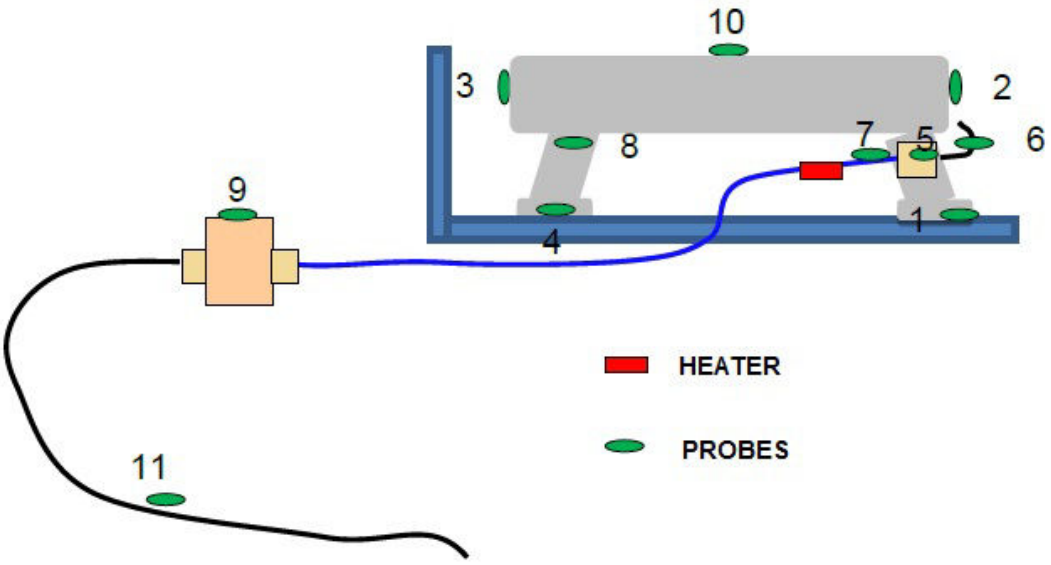

Figure 6.42: Position of the thermal probes and the heater for FM thermal experiments.

The tube was thermally isolated by MLI (Figure 6.43) before being placed into the vacuum chamber.

On the FM there are no thermal probes on the interrogation cavity. The temperature of the cavity was deduced by using a Vector Network Analyzer (VNA) to measure the cavity resonance frequency. The resonant frequency of a resonator is a function of its dimensions and field wavelength.

For copper, the resonant frequency variation is a function of the length of the cavity

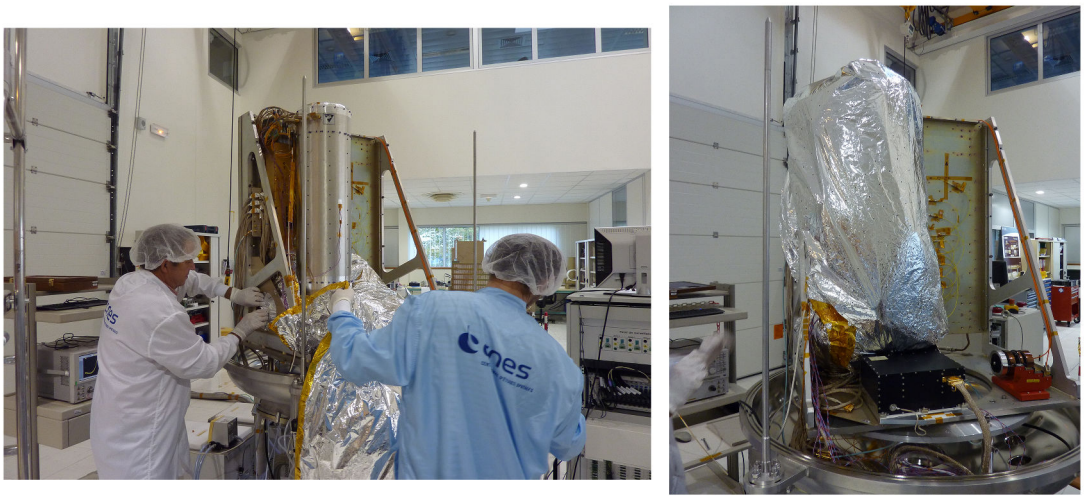

Figure 6.43: Thermal isolation of the cesium tube inside before vacuum.

variation which expands as a function of temperature as:

$$\frac{\delta\nu}{\nu} = \frac{-\delta L}{L} = -1.56 \times 10^{-5} \frac{1}{^\circ C}. \tag{6.33}$$

Therefore, at 9.2 GHz the frequency resonance sensitivity of $155.8 kHz/^\circ C$ is expected.

By thermalizing the system at different temperatures and measuring the frequency, the frequency-temperature relation of the cavity was obtained. The degree of the cavity thermalization was evaluated by the evolution of the resonance peak frequency. The thermalization time was from a few hours to a day depending on the external conditions.

For every temperature the resonance peak frequency, resonance peak amplitude and the resonance peak FWHM were tracked for a duration of a few hours. The measurements were carried out every few seconds and a Lorentzian fit was automatically performed on the resonance peak. A typical measurement can be seen on Figure 6.44.

The noise of the frequency measurement was estimated at $\pm 2 kHz$ after a few hours of measurement at a constant temperature (Figure 6.45). This corresponds to around $\pm 7 mK$ in the cavity temperature calculation noise and the Allan deviation remains below 2 mK.

The effect of the external cable used for VNA frequency measurements was evaluated. A dependency of the frequency on the external cable temperature (probe 11 from

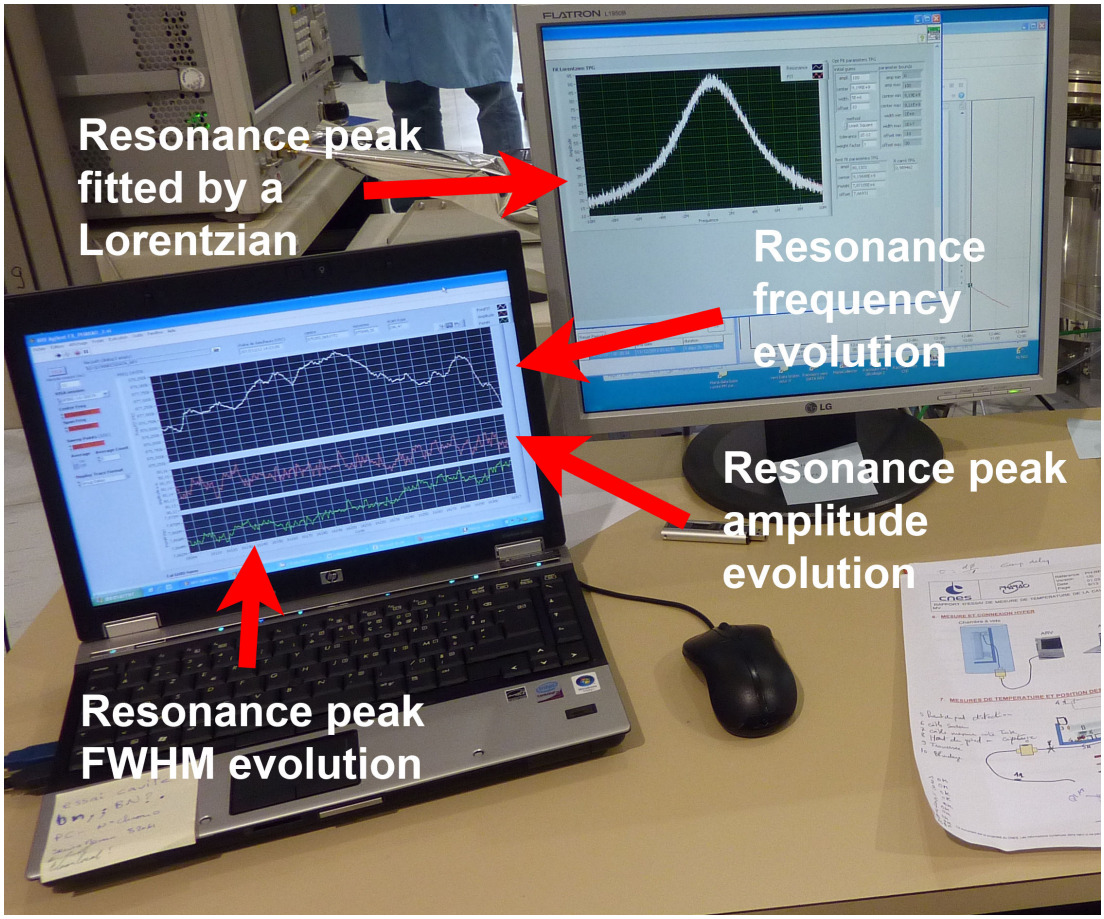

Figure 6.44: An example of the resonance frequency peak measurement. External cable was used to connect the cavity to the VNA. The peaks were fitted by a Lorentzian giving information on the central frequency, amplitude and FWHM. Values were tracked in time.

Figure 6.42) was measured (4 kHz/$^{\circ}C$). An example can be seen on Figure 6.46.

In this experiment the temperature of the cable is synchronously measured and its effect removed when deriving the cavity frequency-temperature relation. The corrected smoothed out signal from the same example is shown on Figure 6.47.

Frequency measurement is also sensitive to internal cable temperature. Using a heater the cable was heated resulting in a frequency shift corresponding to a temperature shift of $5mK$ for every $^{\circ}C$ of cable temperature. Contrary to the external cable case, this is probably due to the heat transfer from the interior cable to the interrogation cavity. The comparison of the internal cable temperature oscillation seen by the two probes and the cavity frequency oscillation is seen on Figure 6.48.

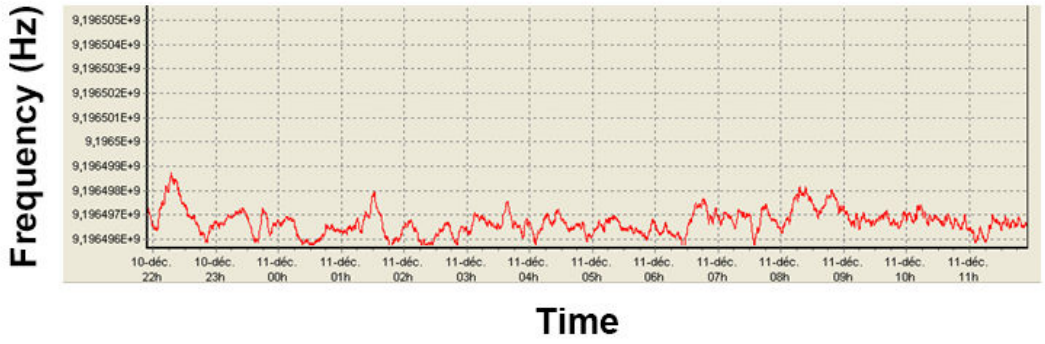

Figure 6.45: Noise of the VNA resonance frequency measurement time evolution.

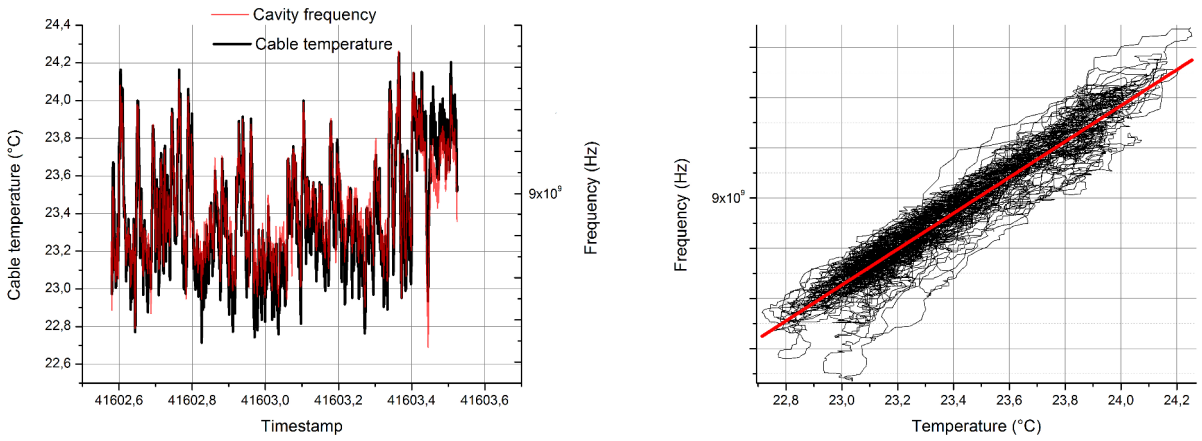

Figure 6.46: Left: comparison of the probe temperature signal and VNA frequency signal. Right: The two signals are correlated showing a strong influence of cable temperature on interrogation cavity frequency

If the interrogation cavity thermal regulation is turned off, the cavity temperature will stabilize around the temperature of the TRP. Capture side probe will give on average a 300 mK higher temperature than the detection side probe. This does not imply a cavity gradient of such magnitude as the capture side probe is better coupled to the cavity. The reservoir and the DDF (detection photodiode) thermal regulation will to a good degree compensate for the thermal orbital variations arriving from the tube support. For a TRP oscillation of $1°C$ the interrogation cavity temperature will

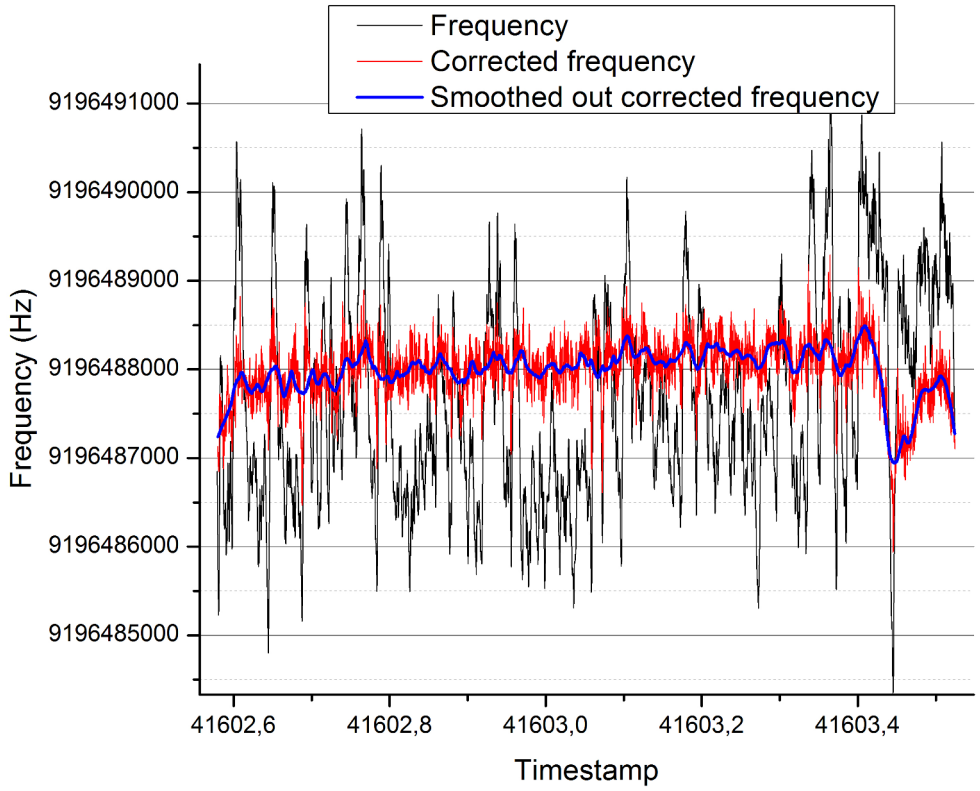

Figure 6.47: Resonance frequency example for a temperature plateau of $\approx 21°C$. In black is the VNA measurement, in red is the measurement corrected for the effect of the external cable and in blue is the smoothed out corrected frequency.

vary $\pm 10mK$, while for a TRP oscillation of $3°C$ the cavity temperature will vary $60mK$. For an illustration of the temperature distribution inside the cesium tube for the two TRP temperature cases see Figure 6.49. The figure shows how the DDF and cesium reservoir termal regulations compensate external perturbation. Note that the operation temperature of the probes is $19.1 - 40.4°C$ and if the TRP temperature is outside of these values the interrogation cavity probes cannot deliver temperature. Results show how the reservoir and DDF regulations reduce the effect of the TRP temperature fluctuation seen by the cavity.

All the frequency resonance measurements as a function of the temperatures are shown on the Figure 6.51. The measurements were performed for the following 6 cavity

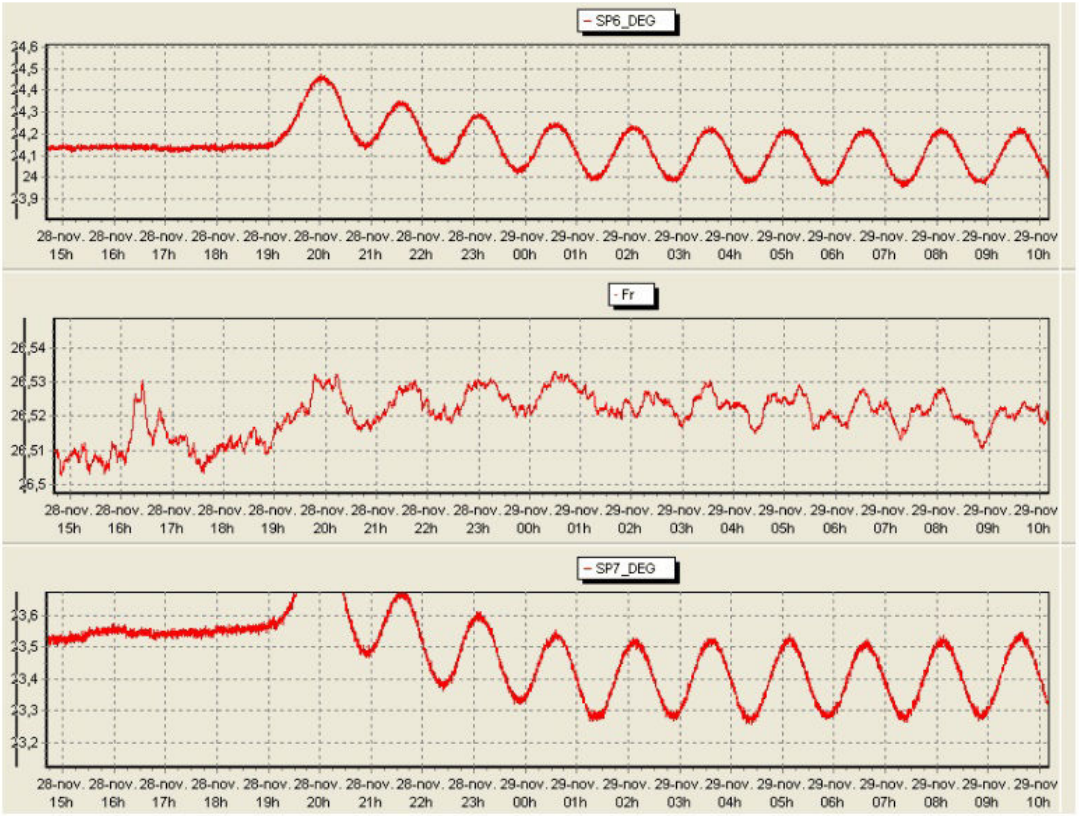

Figure 6.48: Heating of the cable as seen by probe 6 (top) and probe 7 (bottom) and its effect on the cavity resonance frequency (middle).

temperatures: $21°C$, $26.5°C$, $27°C$, $29°C$, $31°C$ and $35°C$. The TRP temperature was varied between $17°C$ and $30°C$. A linear fit was performed on the different temperature points to obtain a transfer relation: $-155.8kHz/°C$. This relation enables a direct calculation between the cavity resonance frequency and its temperature.

The residual of the linear fit is shown on Figure 6.52. The maximum residual value is 40 mK and the RMS is 30 mK. Therefore, it can be claimed that the temperature difference between the probe and cavity remains within 30 mK on average. This value is the temperature uncertainty between the thermal regulation probes and the cavity.

Figure 6.53 gives a list of all measurements with the average capture and detection side probe values (and their peak to peak fluctuations), average VNA frequency value, conversion to temperature, fit error and interval date.

As seen on Figure 6.53, thermal orbital variations were applied at 4 different tem-

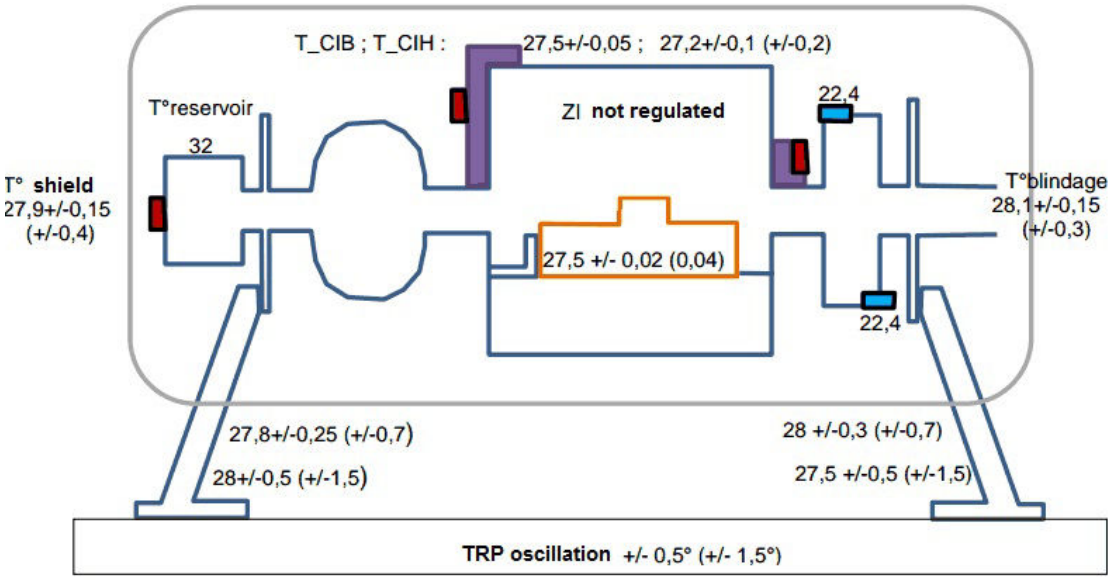

Figure 6.49: Illustration of the temperature distribution at different parts of the cesium tube for the two TRP thermal oscillations.

peratures to verify the performances of the thermal regulation. The perturbations are representative of the ones at position of the ISS and were simulated by a sinusoid with a $1.3°C$ peak to peak amplitude and a period of 90 min (orbital period).

For a stabilized temperature of $23°C$ at TRP, orbital variations are filtered by the interrogation cavity thermal regulation (but also cesium reservoir and DDF thermal regulations) and have an internal amplitude of 10 mK, as measured by the VNA.

Another example is given on Figure 6.54 for TRP stabilized temperature of $28°C$. The external probe temperature variation is 10 mK peak to peak and the interrogation cavity temperature variation is 20 mK, which is still well below specifications. Taking into account the probe and the cavity temperature variation the worst case gradient is 30 mK (which is inside the residual of the frequency temperature relation).

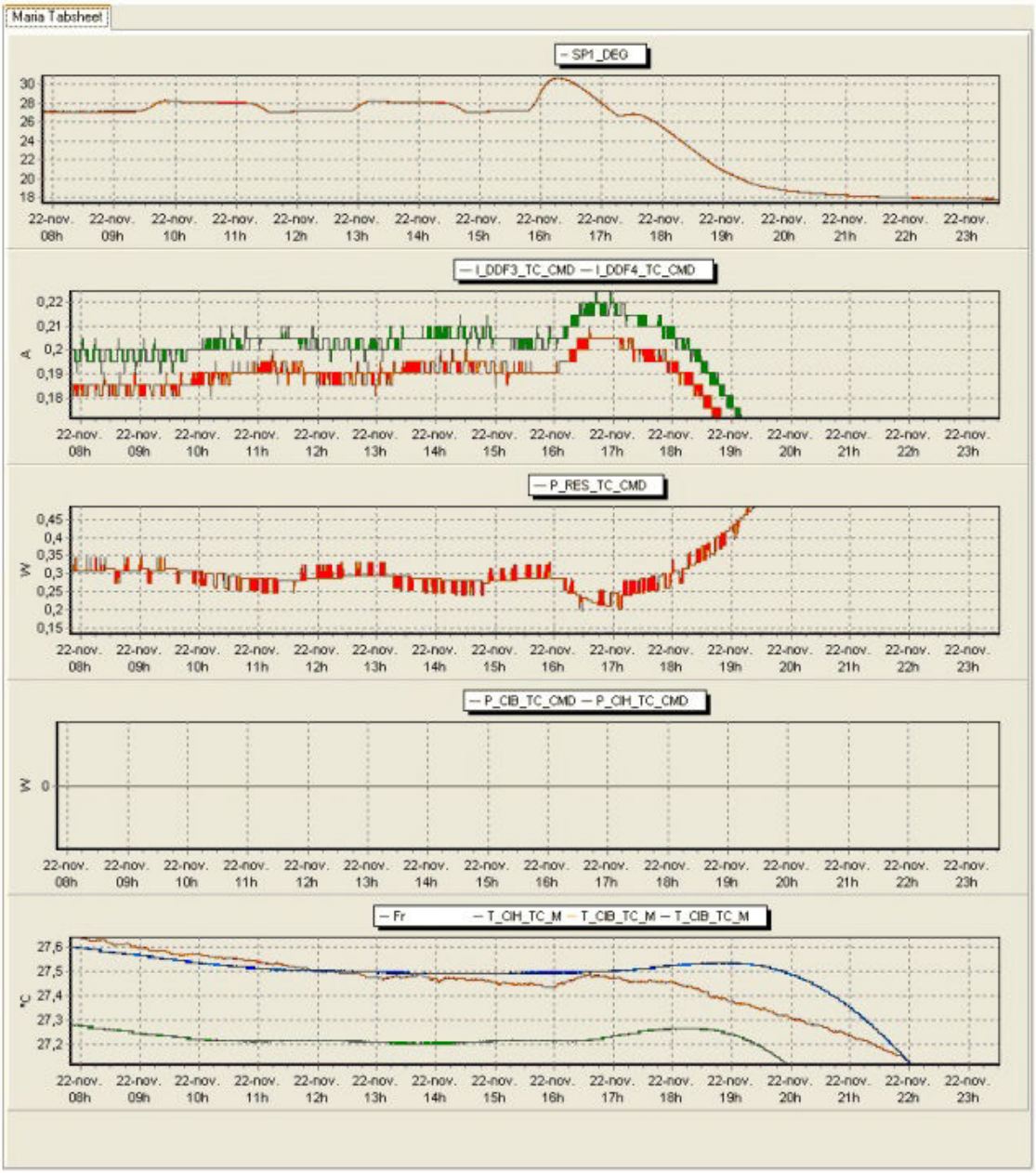

Figure 6.50: Starting from the top: TRP temperature oscillation (probe 1), DDF thermal regulation current, cesium reservoir thermal regulation power, interrogation cavity thermal regulation power (2 heaters), cavity frequency and the temperature of the two probes. DDF and cesium reservoir thermal regulation (as seen by their current and power oscillation respectively) compensate the TRP thermal oscillation of $1°C$. The interrogation cavity regulation is turned off (as seen by the zero power of the two heaters). The resonance frequency and the temperature of the two cavity probes stabilize and the external field oscillation is around $10mK$.

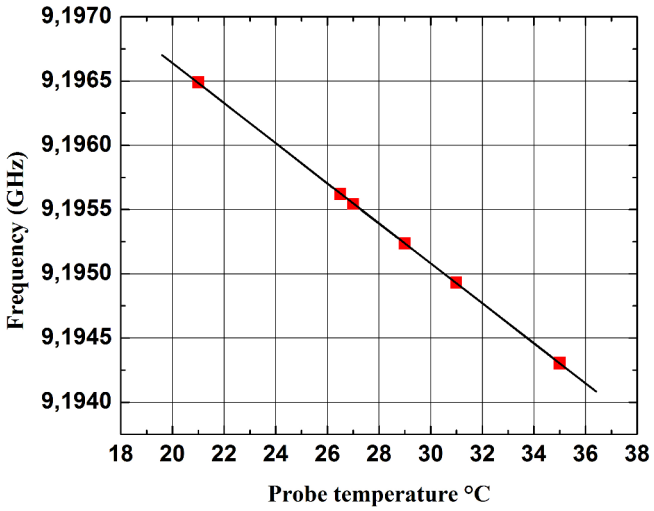

Figure 6.51: Frequency-temperature linear fit of the cavity.

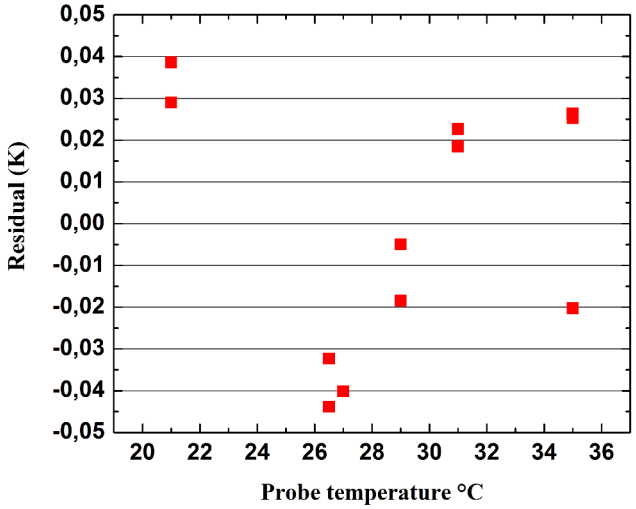

Figure 6.52: Residual from the linear fit is below 40 mK. Its RMS is 30 mK.

	Plateaus	T_CIB	T_CIH	fluctuation mK	Frequency	Cavity average T (°C)	Frequency error	T calculated	Temperature error	Measurement interval	
1	palier 29°	29,009	29,003	6	9,195223	29,006	0,5	29,073	-0,067	21/11/13 6:00	21/11/13 12:00
3	palier 21°	21,004	21,009	12	9,196488	21,0065	0,5	20,977	0,029	24/11/13 12:00	25/11/13 12:00
5	palier 26.5°	26,504	26,506	6	9,1956213	26,505	0,5	26,524	-0,019	28/11/13 10:00	28/11/13 15:00
7	palier 27°	27,005	27,029	6	9,195542	27,017	2	27,032	-0,015	2/12/13 0:00	2/12/13 6:00
8	palier 29°	29,003	29,009	6	9,1952361	29,006	0,2	28,989	0,017	3/12/13 8:00	3/12/13 11:00
10	palier 31°	30,997	30,998	6	9,194929	30,9975	0,5	30,955	0,043	4/12/13 19:00	5/12/13 2:00
12	palier 35°	35,002	35	6	9,1942988	35,001	0,4	34,988	0,013	6/12/13 3:00	6/12/13 9:00
2	cavité non régulée	27,495	27	60	9,195474	27,2475	8	27,467	-0,219	22/11/13 12:00	23/11/13 18:00
4	palier 21° + Orbites	21,004	21,009	6	9,1964895	21,0065	1	20,968	0,039	25/11/13 19:00	26/11/13 15:00
6	palier 26.5° + Orbites	26,504	26,506	12	9,1956195	26,505	1	26,536	-0,031	28/11/13 19:00	29/11/13 10:00
9	palier 29° + Orbites	29,003	29,009	6	9,195234	29,006	0,2	29,003	0,003	3/12/13 12:00	4/12/13 3:00
14	palier 35°+ Orbites	35,002	35	15	9,1943059	35,001	20	34,943	0,058	6/12/13 21:00	7/12/13 6:00
11	palier 31° PPE 24 -> 22	30,998	30,997	6	9,1949295	30,9975	0,5	30,952	0,046	5/12/13 2:00	5/12/13 11:00
13	palier 35°PPE 28 -> 25	34,996	34,993	6	9,194307	34,9945	5	34,936	0,059	6/12/13 9:00	6/12/13 16:00

Figure 6.53: List of temperature plateaus without orbital variation, with orbital variation and thermal regulation, with orbital variation and without thermal regulation. Information of the average capture and detection side probe values (and their peak to peak fluctuations), average VNA frequency value, conversion to temperature, fit error and measurement interval.

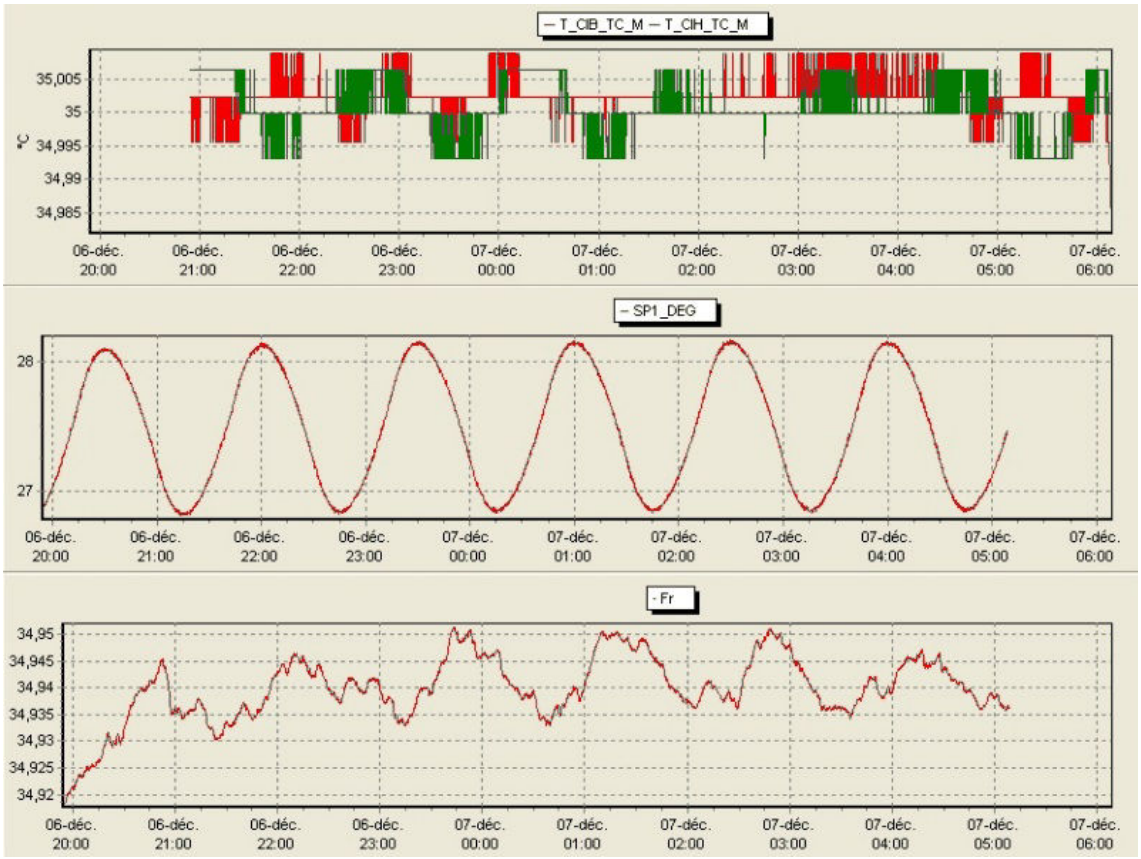

Figure 6.54: Orbital variation at $28°C$ TRP. From top: temperatures of the capture (T CIB TC M) and detection (T CIH TC M) side probes (10 mK peak to peak), TRP temperature variation, interrogation cavity temperature variation as obtained from VNA resonance frequency and converted with the frequency-temperature relation (20 mK peak to peak variation).

Limitation of the thermal loop as a function of the external thermal oscillation slope was studied. This is useful, for example, when changing the regulation temperature. The interrogation cavity thermal regulation loop is based on the idea that the interrogation cavity probes follow the temperature inside the cavity. If the regulation temperature is suddenly increased, $\approx 10h$ is necessary for the probes to stabilize on the new temperature and $\approx 20h$ for the cavity interior. This is due to different thermal inertia of the probe and the cavity (because of thermal resistivity, coupling to TRP, etc...). Similarly, for a more rapid thermal oscillation a larger gradient will be created between the two. The limiting value was found in the form of the maximum external oscillation slope during a half orbit period of 45 min. Only the rising part of the heating sinusoid was observed as this is where the loop heaters are applied while for the other 45 min the temperature changes more slowly allowing better thermalization.

The procedure was to increase the two heaters power and observe the gradient between the probes and the cavity (obtained from the cavity resonance value) (Figure 6.55) when the regulation is off.

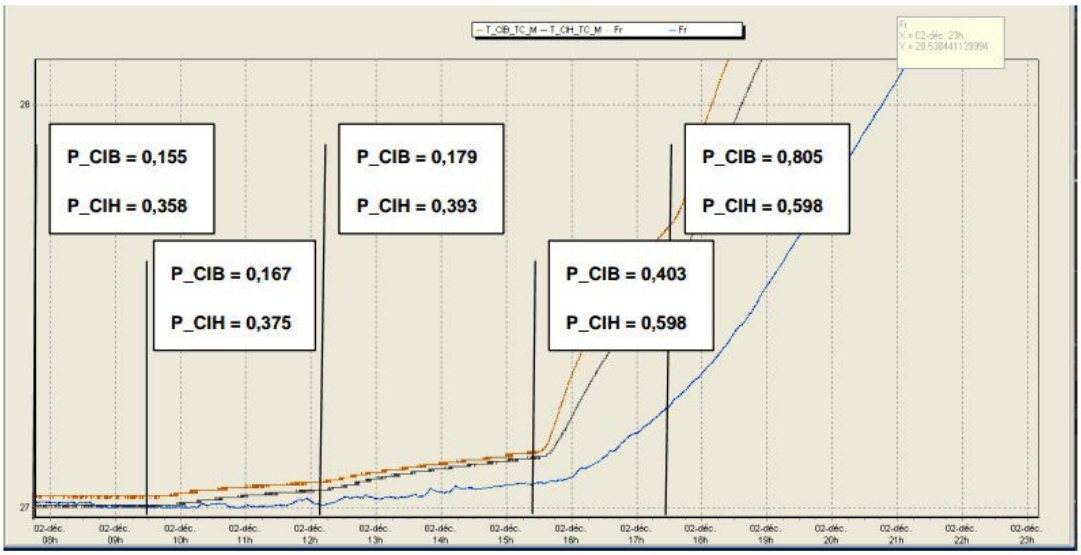

Figure 6.55: Temperature value of the two probes compared to the cavity temperature obtained from resonance frequency. The maximum capture and detection side heater power after which the gradient is too large is P CIB = 0.18 W and P CIH = 0.4 W, respectively.

The heater power values were transformed to oscillation slope values in units of $mK/45min$. For a slope value of 25 mK/45min slope a gradient of 100 mK between

the probes and cavity is created during the rising part of the orbital oscillation. For the oscillation of $\pm 1.5°C$ on the TRP the gradient is the point circled in red on Figure 6.56.

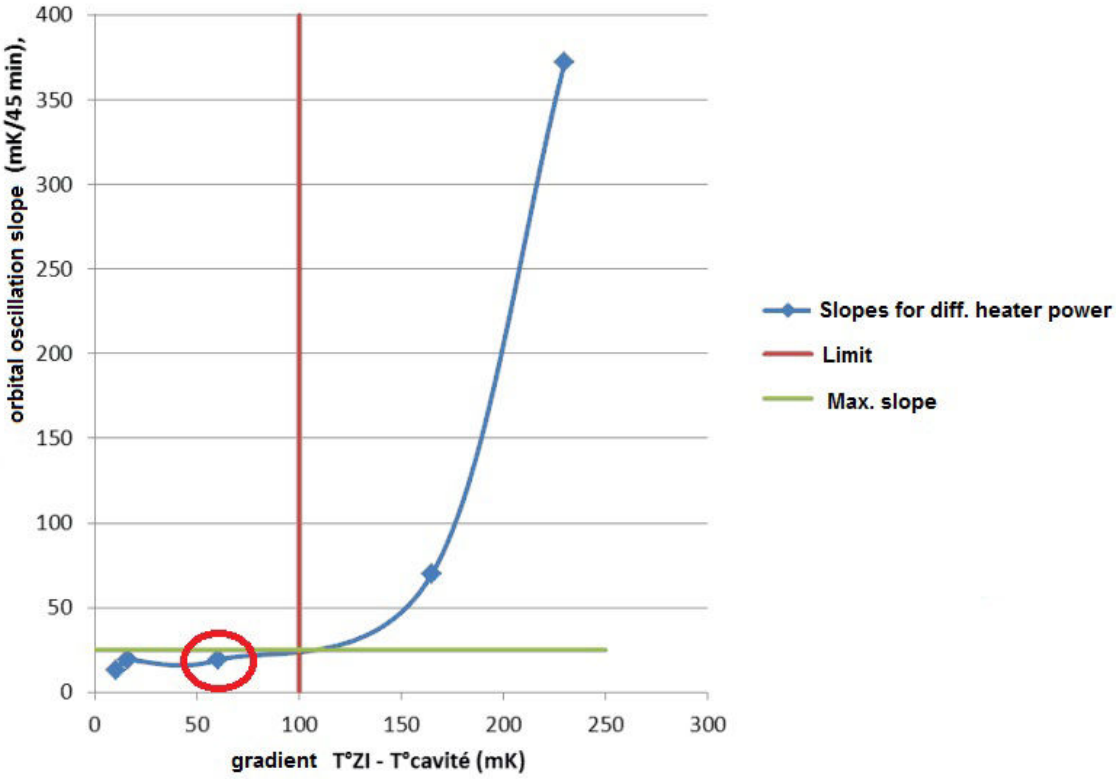

Figure 6.56: Value of the created probe-cavity gradient created for different oscillation slopes. Red vertical line is the 100 mK gradient and the corresponding oscillation slope of 25 mK/45 min. The point circled in red is for the $\pm 1.5°C$ TRP oscillation measured with the thermal regulation off.

From measurements and simulations it can be concluded that the cavity probe gradient remains below 30 mK when the thermal regulation is turned on. In the next section the accuracy budget of the probes is evaluated and the total temperature uncertainty given.

6.2.2.4 Measurement uncertainties

The probes used for the interrogation cavity thermal regulation are positioned on two sides of the vacuum cavity relatively close to the corresponding heaters. The reason

why the probes are not directly on the interrogation cavity is to avoid stray EM and MW fields inside the sensitive volume. Photograph of one of the EM probes glued on the vacuum cavity can be seen on Figure 6.57.

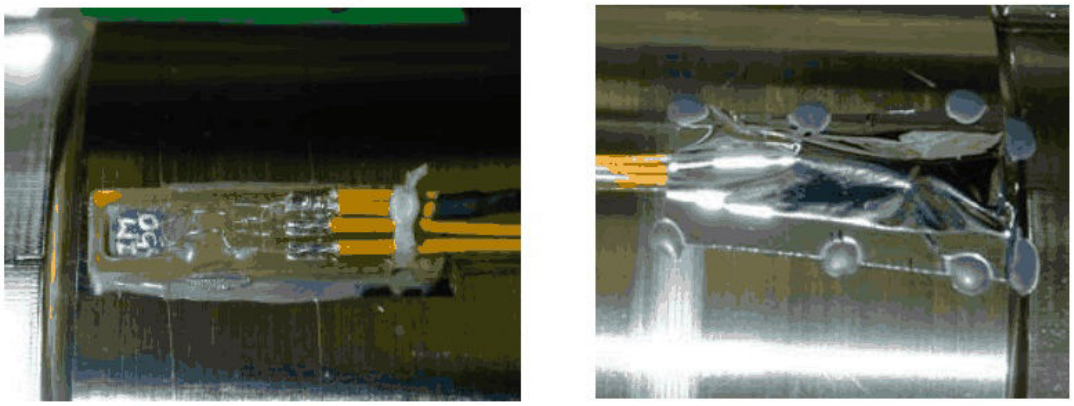

Figure 6.57: Interrogation cavity probe. The Sheldal tape seen on the right decreases the thermal exchange with the environment.

Figure 6.58 illustrates the measurement chain. The circuit is composed of the voltage reference (LT1021BMH-5), a Wheatstone circuit with the resistance reference, the probes which measures resistance, the primary and the secondary amplifier and an analogue to digital converter. The calibration needs to be performed not only for the probes themselves, but also for the supporting electronics package. For each block initial precision, thermal perturbation influence, aging and radiation effects were studied. If the effects were correlated a linear summation was used. Otherwise, the contributions were summed quadratically. Aging was calculated for entire mission duration, temperature variation for a range of $\pm 17°C$ and radiation for a cumulative dose of 0.8 krad.

A 3 wire configuration was used to measure the probe resistance. The probe measurement scheme is given on Figure 6.59 with the uncertainty contributions that will be explained next.

The probes used for thermal regulation are the 118MM Rosemount PT500 flight model which has an operational temperature range $20-40°C$ and should be stable for a total of 76 months of mission duration (30 months on ground, 10 months storage and 36 month orbit). Calibration was performed at LNE (Laboratoire national de mtrologie et d'essais) by submerging them in a thermalized bath whose temperature is determined

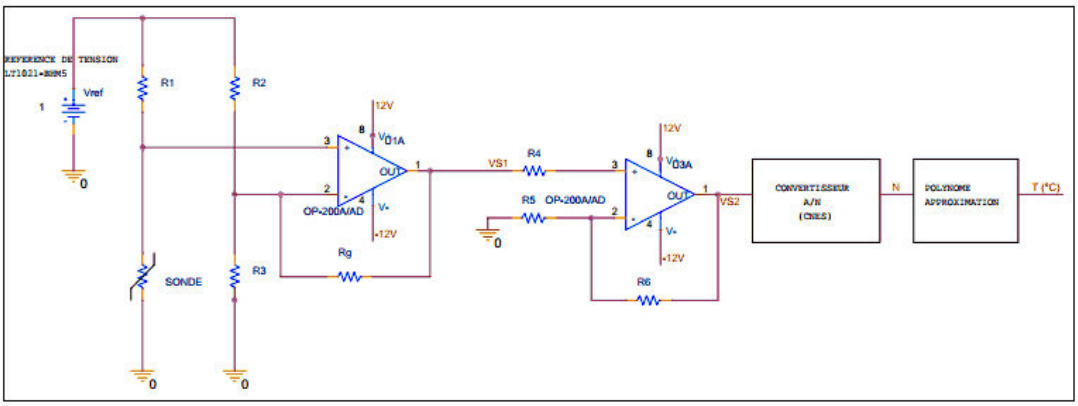

Figure 6.58: Temperature measuring circuit composed of the voltage reference, temperature probes, primary amplifier, secondary amplifier, analogue voltage to digital data converter and the transfer polynome.

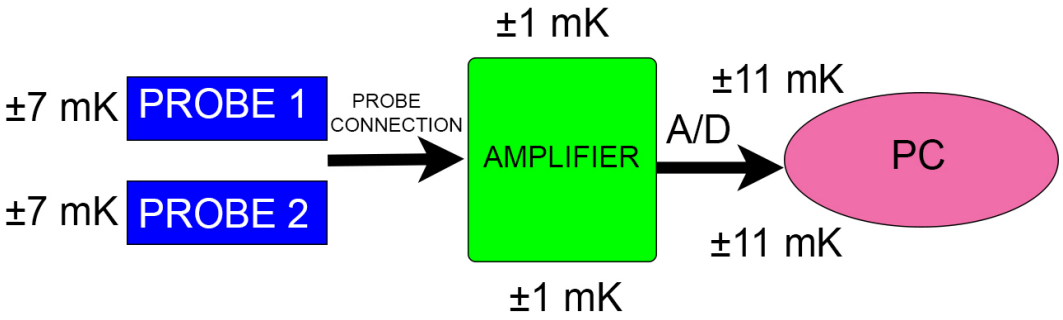

Figure 6.59: Probe measurement scheme composed of the two probes, connection wires, amplifier and the A/D conversio with the uncertainty contributions.

by a reference probe. Probe accuracy depends on measurement repeatability, sensor aging, thermalized bath temperature precision, probe connection (quality of connection to the tube, length of cables and connection resistance) and probe self heating. Thermal treatment has been performed on the probes and aging can be considered negligible for PT500.

Self-heating is due to the current flowing through the probe generating heat that raises the temperature. Difference between the average probe resistance for 1 mA and the value extrapolated to 0 mA (using measurements at $\sqrt{2}mA$) gives the self-heating error estimated at $\leq 5mK$ for our range of operation (Figure 6.60). The manufacturer

gives a self-heating value of $46mW/°C$ for a probe submerged into oil. For $1mA$ of probe current, the dissipated power is $P = I^2 \times R = 0.001^2 \times 550\Omega = 0.055mW$ which should be equivalent to a self heating value of 12 mK. However, as Figure 6.60 shows, the resistance difference between $1mA$ and $0mA$ is on average 0.054Ω which corresponds to an actual value of 27 mK. During operation, a current of $0.8mA$ is sent to the probe equivalent to power dissipation of $0.0352mW$. For a probe in Stycast, self heating is lower by a factor of 2 compared to oil. The power is less than $0.0176mW$. Comparing the power dissipation in oil and the measured self heating with the power dissipation in Stycast, the calculated self heating is $8.6mK$. This value needs to be deducted from $27mK$ to correct the probe calibration at $1mA$. Therefore, probe measurement temperature needs to be corrected by $-18mK$.

Total individual probe calibration error was determined at $\sigma = 8mK$ (including the self heating uncertainty). Every temperature was measured 2 times (second measurement after 15 second) to include the repeatability error (Figure 6.60).

Number of measure-ments	Probe immersion depth (mm)	Average temperature (°C)	Average probe resistance for 1 mA (Ω)	Average resistance extrapolated to 0 mA (Ω)	Resistance difference (Ω)	Probe uncertainty (°C)
2	150	-0,003	499,9484	499,9200	-0,0457	0,005
2	150	38,012	574,6570	574,6025	0,7931	0,008
2	150	-0,002	499,9570	499,9319	-0,0391	0,005
2	150	35,049	568,8740	568,8158	0,7387	0,008
2	150	31,966	562,8461	562,7954	0,6747	0,008
2	150	30,003	559,0079	558,9507	0,6361	0,008
2	150	28,059	555,1986	555,1407	0,5934	0,008
2	150	27,049	553,2219	553,1689	0,5743	0,008
2	150	25,024	549,2614	549,2106	0,5406	0,008
2	150	23,075	545,4314	545,3754	0,4941	0,008
2	150	-0,002	499,9562	499,9318	-0,0390	0,005

Figure 6.60: Evaluation of the uncertainty of one of the probes.

Probe connection resistivity is much smaller than the wire resistivity. Figure 6.61 shows the influence of wire resistance on the temperature error with a sensitivity of $0.4\%/°C$. An error of 3 mK was determined due to the wiring (green wire 24) for

the total temperature range. As our temperature range is $\approx 24 - 34°C$ the error is estimated at 1 mK.

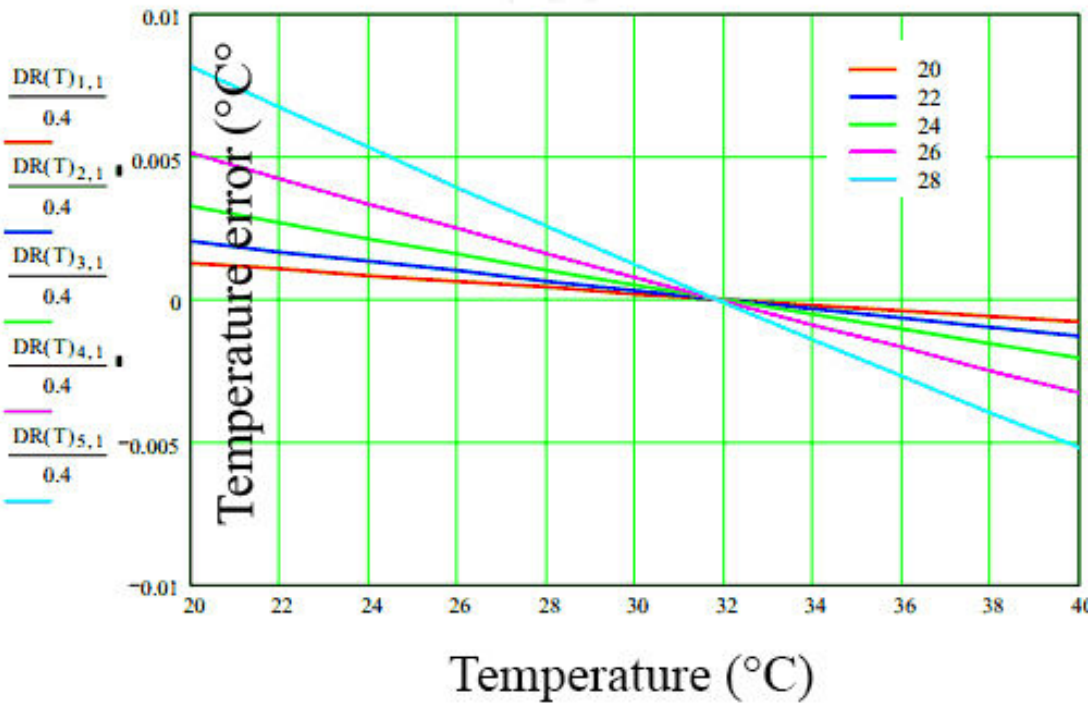

Figure 6.61: Wire resistance effect on temperature error as a function of wire diameter. Figure courtesy of SODERN.

With an initial uncertainty of 1%, LT1021BMH-5 was the most precise 5V space qualified voltage reference at the time of experiments. Thermal variation, aging effect and radiation effect were evaluated at $3ppm/°C$, 18 ppm and $11\mu V/krad$, respectively.

The analogue voltage to digital data conversion to UGB error is estimated at $\sigma = 11mK$.

Amplifier model OP200AZ is used as the primary and the secondary amplifier. Figure 6.62 gives the characteristics of the amplifier. The primary amplifier amplifies and converts the probe resistance to a voltage output with a range of $\pm 2.5V$ (corresponding to the probe temperature range of $20 - 40°C$).

A linear relation between the input resistance and the output voltage for the primary amplifier is shown on Figure 6.63. The polynomial (3rd order) transformation (R - V) error is evaluated at $\sigma = 1mK$. Primary amplifier was connected to the voltage

Parameter	Initial uncertainty	Thermal effect	Aging effect	Radiation effect
Offset voltage	75 µV	0.5µV/°C	1.2µV/an	10µV/krad
Polarization current	2 nA	7 pA/°C	0	150 pA/krad
Offset current	1 nA	0.4 pA/°C	0	150 pA /krad

Figure 6.62: OP200AZ perfomance given by manufacturer.

reference and two resistors (RNC90Z) to test performances inside a circuit. Calibration allows for removal of the initial uncertainty value depending mostly on the amplifier voltage offset and the two resistors. Thermal stability depends mostly on the stability of the voltage reference and influence of the amplifier voltage offset. The montage aging effect is mostly due to the resistance and the radiation effect mostly affects the voltage offset stability (but is negligible compared to aging).

Figure 6.64 shows the different effects on the voltage output as a function of probe temperature. The blue dashed line is the linear sum (to evaluate the worst case) of the effect of aging, radiation (8 krad) and temperature ($17°C$). These are estimated at 6 mV, 2.5 mV and 3.5 mV, respectively. Their quadratic sum is 7.4 mV which, taking into account the primary amplifier gain of $3.85 - 4.17°C/V$), is equivalent to $\approx 30mK$ (end of mission).

Primary amplifier output is next sent to the secondary amplifier which is used to adjust the output dynamic range to $\pm 8V$ (gain of $\approx 3V/V$). Main source of uncertainty (2 mK) of the secondary amplifier are the initial amplifier uncertainty and aging. However, this can be neglected as its negligible compared to the primary amplifier uncertainty.

Repeatability error of the two connected amplifiers was evaluated at $\sigma = 1mK$. Thermal sensitivity was determined to be 5.8 mK when varying the temperature between $17°C$ and $45°C$ (Figure 6.65).

Two 3rd order polynomials are used to describe and calibrate the probe and amplifier package transformations. Figure 6.66 describes the V(R) relation between the amplifier package input resistance and its voltage output. The relation error is evaluated at $\leq 1mK$.

By connecting the temperature probe, applying the V(R) relation and varying the

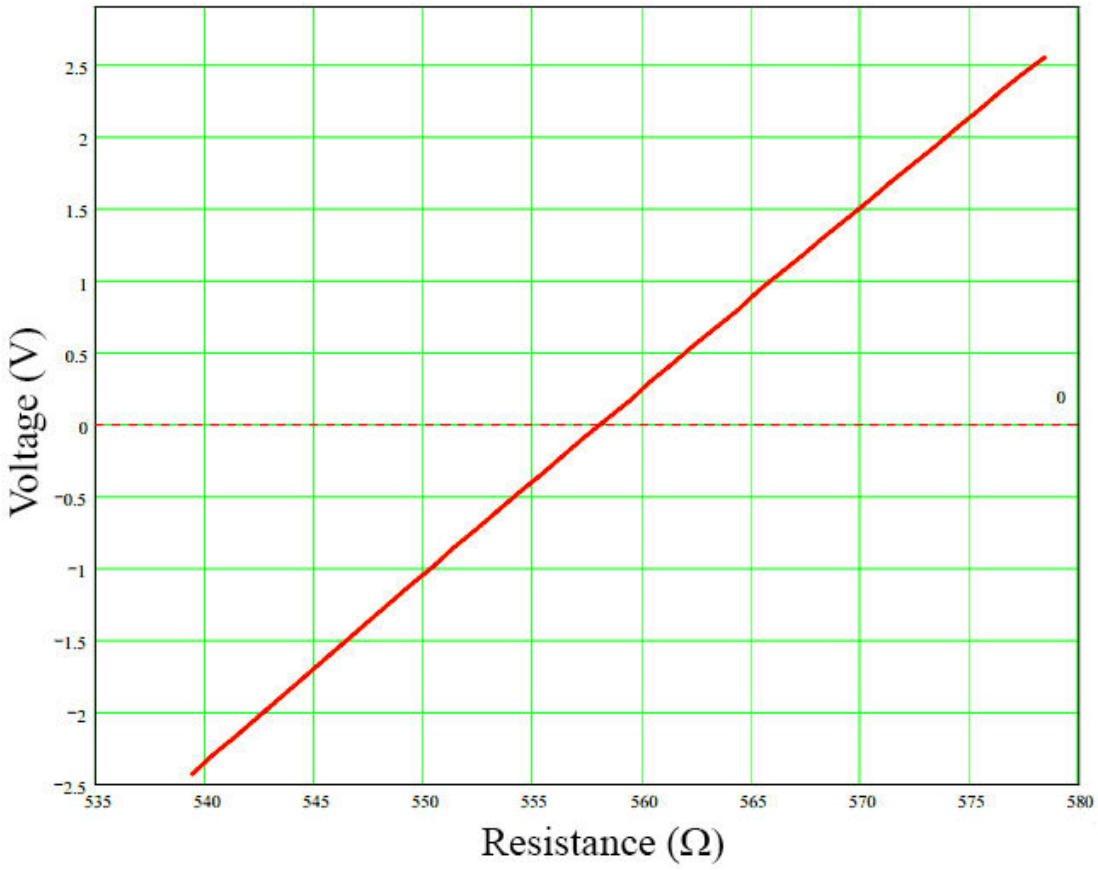

Figure 6.63: Amplifier package linear relation between the input resistance and output voltage. Figure courtesy of SODERN.

temperature the T(V) probe calibration polynomial is obtained with an uncertainty evaluated also at 1 mK (Figure 6.67). The errors are linearly summed to 2 mK. However, after evaluating the data points, they are inside the temperature probe 7 mK uncertainty and can be neglected. For explanation see Figure 6.68.

Temperature measurement error was summed linearly (worst case where it is assumed the contributions are independant) and quadratically (where it is assumed the contributions are dependant) for one probe and for a set of two probes. Uncertainties due to the probe calibration ($\sigma = 8mK$), wire resistance ($\sigma = 1mK$), amplifier package repeatability ($\sigma = 1mK$), A/D conversion ($\sigma = 11mK$) and primary amplifier aging, radiation and thermal effect ($\sigma = 0$ to $\sigma = 30mK$) were taken into account.

Start of life and end of life conditions were calculated without the primary amplifier

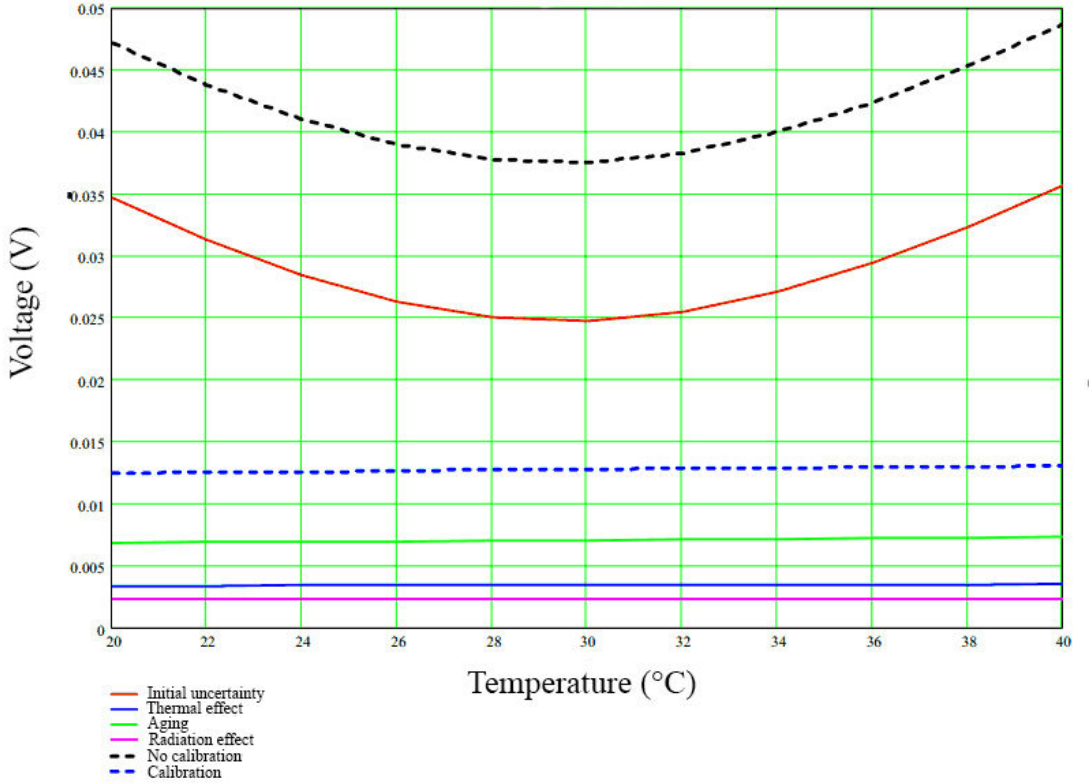

Figure 6.64: Primary amplifier error budget in output voltage as function of probe temperature. Figure courtesy of SODERN.

aging, temperature and radiation effects and with the primary amplifier aging effects, respectively. The resulting quadratic sum range of uncertainties for a single probe is $\sigma = 13$ to $33mK$.

For the two probes separate uncertainty contributions were added quadratically, while the primary amplifier uncertainty was considered to be the same for the two channels. The uncertainties are summarized on Table 6.1. Start of life quadratic sum is $\sigma = 18mK$, while end of life quadratic sum is $\sigma = 48mK$.

Total uncertainty of the absolute temperature determination is a combination of the temperature measurement uncertainty and the temperature difference between the probe and the interrogation cavity. As it was shown in Section 6.2.2.3 this value is on average $30mK$. Therefore, as illustrated on Table 6.2, the uncertainties quadratic sum range is $35 - 57mK$.

Note also that values given by the probes need to be corrected by $-18mK$ because

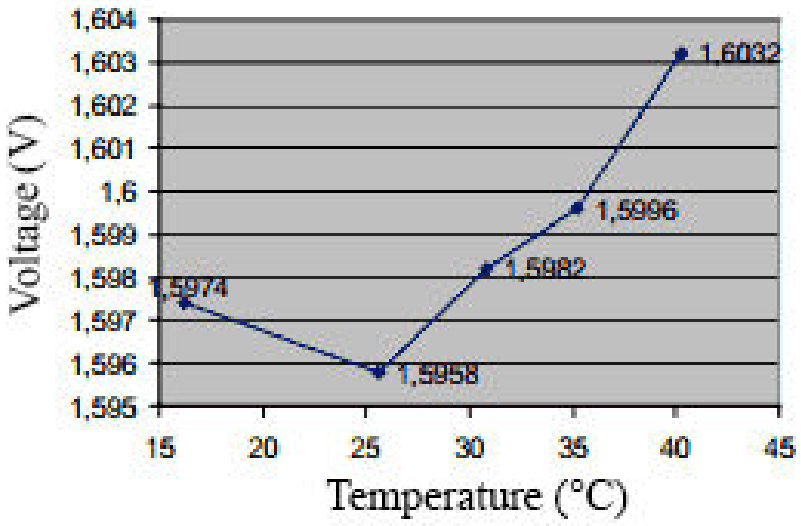

Figure 6.65: Thermal pertrubation effect on amplifier output.

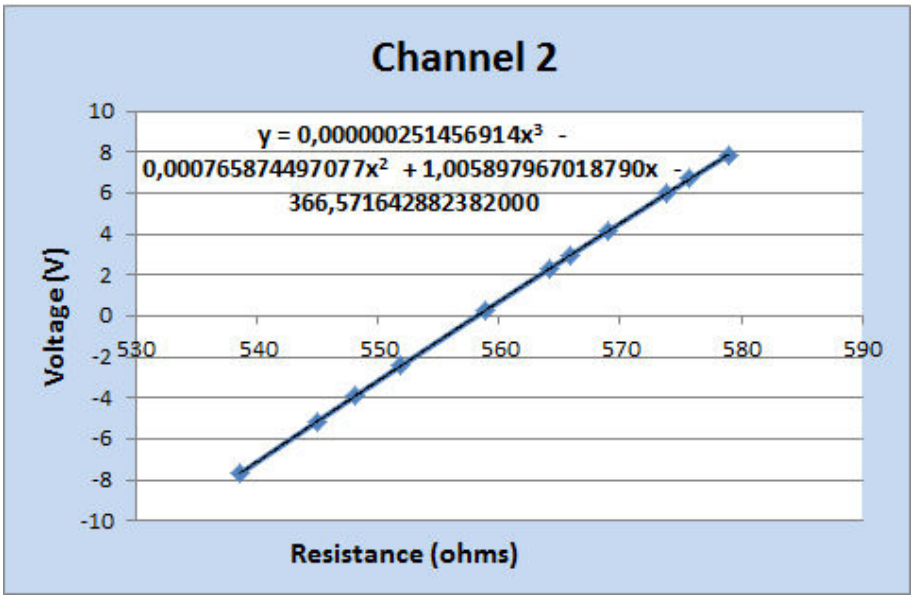

Figure 6.66: Relation between the amplifier package resistance input and voltage output.

of self heating.

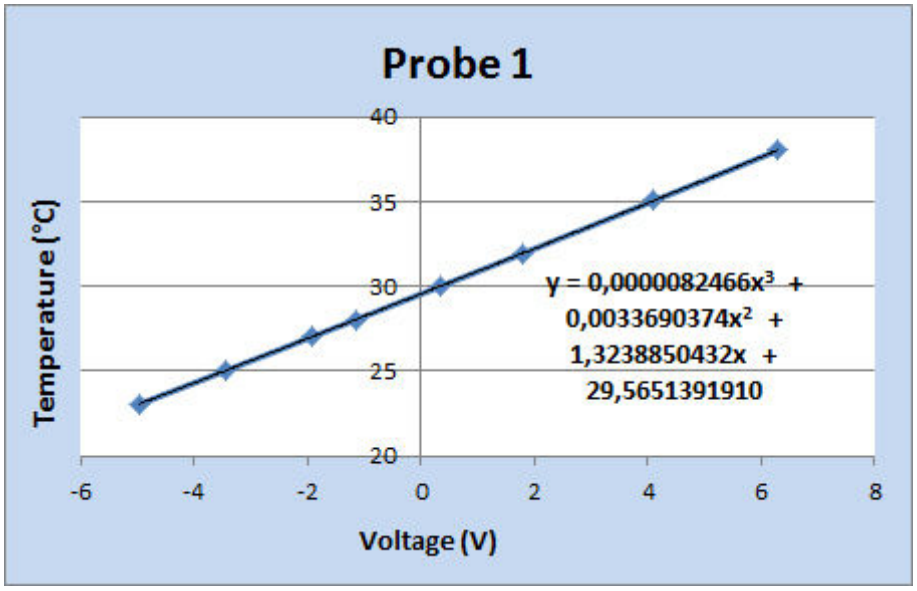

Figure 6.67: Relation between the amplifier package voltage output and final temperature calculated for one of the temperature probes.

6.2.3 Conclusion to black body

A thermal analysis performed on the STM (PHARAO cesium tube model representative of the engineering model) using 45 thermal sensors was performed in order to be able to modelize the thermal distribution. The measurements show an existence of a temperature gradient of a few 100 mK between the cavities and the 2 temperature sensors that will be used for temperature determination in orbit. The variability of this gradient results in the uncertainty of temperature in Equation 6.30 which results in the increase of frequency shift uncertainty.

On the PHARAO engineering model the frequency shift was determined to be -1.63×10^{-14} with an uncertainty of 2.2×10^{-16}. However, the engineering model was not optimized thermally and the measurements were performed with a non calibrated probe.

Numerous improvements have been made on the PHARAO flight model to reduce the intra interrogation cavity temperature gradient and improve the interaction cavity temperature determination. This includes modifications in the thermal servo loop, thermal resistance and emissivity of the cavity walls. The thermal servo loop is composed of two heaters at each side and the aforementioned thermal sensors.

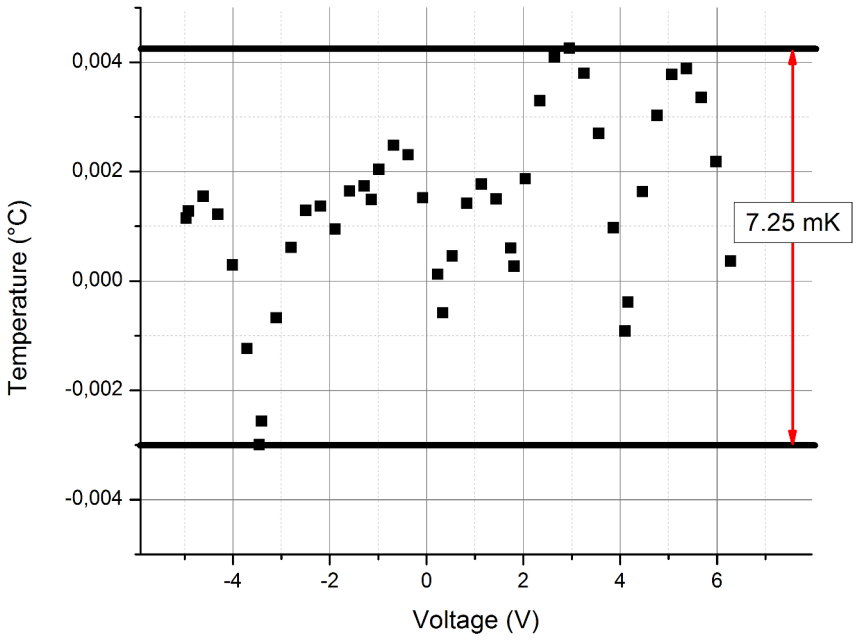

Figure 6.68: Final transformation polynomial data points (temperature as a function of amplifier voltage). We know the probe measurement uncertainty is $\sigma = 7mK$. When adding the $\pm 2mK$ V(R) and T(V) error, the data points ($\pm 4.625mK$) are well within the probe uncertainty and can be ignored.

Equation 6.30 can be simplified to:

$$\frac{\Delta\nu}{\nu_0} = -1.717(3) \times 10^{-14} \times (\frac{T}{300})^4. \tag{6.34}$$

For a thermal regulation temperature of $25°C$, global error in the absolute temperature knowledge of 35-57 mK (start of life - end of life) (Figure 6.2) and the uncertainty of the coefficient in Equation 6.34 of 3×10^{-17}, the FM frequency shift is -1.675×10^{-14} with an uncertainty of 3×10^{-17} to 3.2×10^{-17}.

The effect of the radiation emitted by other parts of the tube through the apertures (1% contribution) also needs to be taken into account. A Monte Carlo simulation may be performed in the future.

For one probe error (mK)		For two probes error (mK)
probe calibration error	8	
wire resistance	1	
amplifier repetability	1	
primary amplifier	0 to 30	
A/D conversion	11	
QUADRATIC SUM	13 to 33	18 to 48

Table 6.1: Temperature measurement error budget.

Global error	Start of life	End of life
Temperature meas. error (mK)	18	48
Probe/cavity uncertainty (mK)	30	30
QUADRATIC SUM (mK)	35	57

Table 6.2: Global error in the absolute temperature knowledge.

6.3 Cold collision

6.3.1 Introduction

The use of ultracold atoms leads to a frequency shift due to low velocity atomic collisions (134, 135). This is because at such low temperatures de Broglie wavelength becomes comparable to the range of the interaction potential which results in quantum behaviour (36).

The frequency shift depends on atomic density $\bar{n}$ in a linear fashion:

$$\frac{\delta\nu}{\nu_0} \approx -2 \times 10^{-21}\bar{n} \tag{6.35}$$

By extrapolating to zero density, the atomic clock can be corrected for this shift. However, atomic density cannot be measured directly in an atomic clock. What we measure is the detected number of atoms N.

A relationship between density and number of atoms is not necessarily linear; same number of atoms can create different spatial distributions. By applying a π preparation cavity pulse an atomic sample with maximum density n and atom number N is produced. Due to the field distribution all the atoms in the preparation cavity do not see the same microwave field amplitude, but all the atoms see the same frequency. By modifying the preparation cavity pulse frequency, as devised by Kurt Gibble, it is possible to have atomic samples with $\frac{n}{x}$ density and $\frac{N}{x}$ number of atoms.

In order to correct for the frequency shift, the differential method is used. It consists of alternating low density and high density atomic samples (with modifying the relative energy) for which the density and number of atoms ratio has the same value (implying frequency shift - number of atoms linearity defined by the constant k). This is illustrated on Figure 6.69. Different densities are selected by using a frequency offset in the preparation cavity and a slight adjustment in the preparation power.

Two frequency measurements are taken at high density (ν_H) and low density (ν_L):

$$\nu_H = k \times N_H + \nu_0 \tag{6.36}$$

$$\nu_L = k \times N_L + \nu_0. \tag{6.37}$$

The clock frequency without the cold collision frequency shift is ν_0:

$$\nu_0 = \nu_H - k \times N_H = \nu_L - k \times N_L, \tag{6.38}$$

and the corresponding shifts for the two densities are $\Delta\nu_H$ and $\Delta\nu_L$. Therefore, the corrected frequencies are:

$$\nu_H^{corr} = \nu_L^{corr} = \nu_0. \tag{6.39}$$

From Equation 6.38 and Equation 6.39, the high density corrected frequency is:

$$\nu_H^{corr} = \nu_H - \Delta\nu_H = \nu_H - \frac{x(\nu_L - \nu_H)}{1 - x}, \tag{6.40}$$

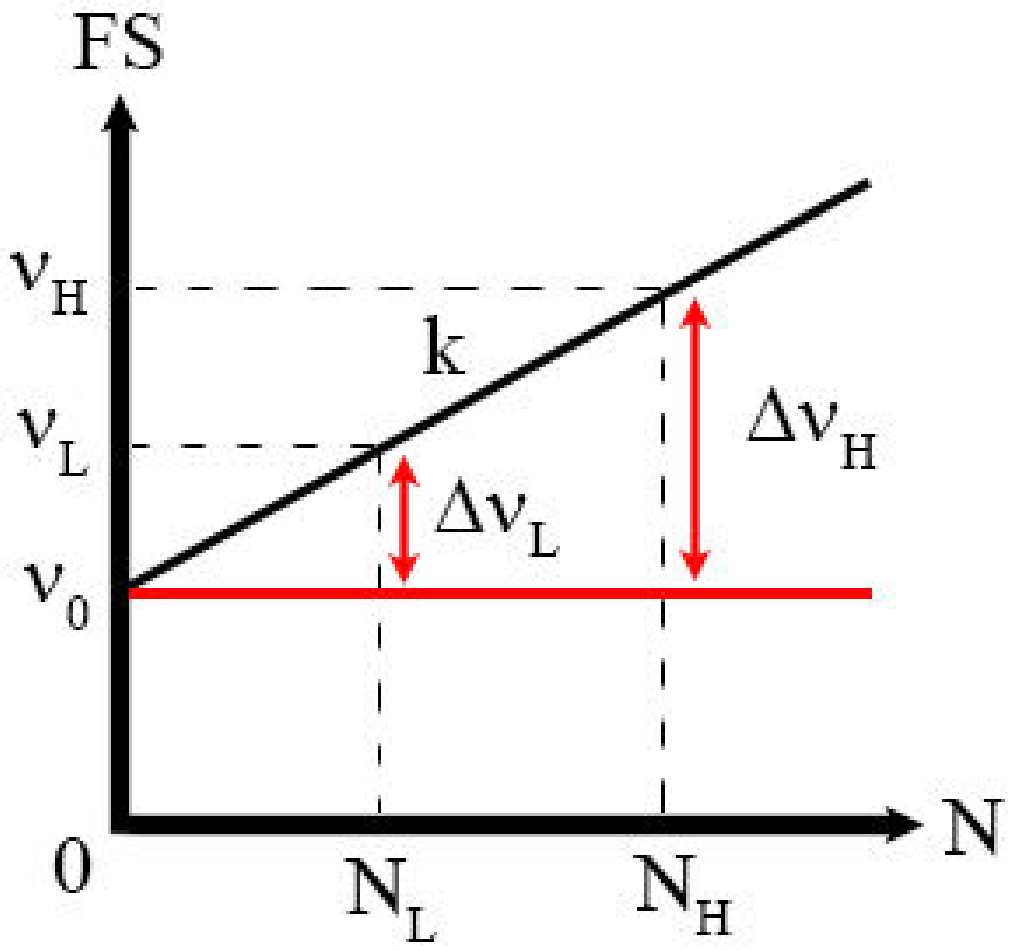

Figure 6.69: Frequency shift (FS) as a function of detected number of atoms (N). Measurements are taken at high density and low density with the frequency shifts ν_H and ν_L, respectively. Number of atoms ratio is the same as atomic density ratio: $\frac{N_H}{N_L} = \frac{n_H}{n_L}$ implying a linearity between the frequency shift and these two values of the number of atoms. With these conditions, it is possible to calculate the frequency shifts $\Delta\nu_H$ and $\Delta\nu_L$ simply by measuring two frequencies ν_H and ν_L, as explained in the text.

where x was defined earlier as $\frac{N_H}{N_L} = \frac{n_H}{n_L} = x$.

The previous analysis in only true when the velocity and position distribution of the cold atoms does not change. It is practically true when the launch velocity is kept constant. If the launch velocity changes a different value of the coefficient k due to the change of the cold collision energy.

The thesis of Yvan Sortais (19) gives a detailed description of the cold collision frequency shift. In the following sections a simulation calculation of the PHARAO frequency shift with the coefficients used in (134, 135) is given.

6.3.2 Collision frequency simulation

To simulate the collision a Gaussian distribution has been used for the captured atoms. The detected time of flight of atoms has a similar distribution as the laser beam intensity distribution at 1D. For each atom the function generates an array of 3 random numbers, x, y and z which are Gaussian distributed and have a standard deviation of $\sigma_0 = 5.25$ mm.

For each atom we check that x, y and z are within the total laser beam size. This parameter is equal to the windows radius of the cesium tube and is 13 mm. After that the coordinates are rotated to come in the new frame with the axis X along the launch direction (111), Y along the feeding waveguide of the Ramsey cavity and Z in the plane of the Ramsey cavity. We transform the new coordinates X, Y and Z in integer data to index a 3D array which is incremented for each new atom. The array is stored when the total number of atoms is reached. Consequently each array element represents the number of atoms in a volume of $1mm^3$.

Figure 6.70 shows the used atomic distribution which follows the laser beams intensity Gaussian distribution.

The atomic velocity has a Gaussian distribution with the standard deviation of σ_v = 8 mm/s. The atomic velocities and positions are not correlated in optical molasses. Based on these distribution values the atomic trajectory is calculated as a function of time and the atomic cloud thermal expansion is derived.

After launch the atoms pass through the apertures of the selection and interrogation cavity which reduce the number of atoms by $\approx 60 - 70\%$ and cut the cloud dimensions in the y and z direction to a final value of $3.95 \times 4.45mm$ inside the interrogation cavity. Thermal expansion of the cloud affects atomic cloud density which is calculated as a

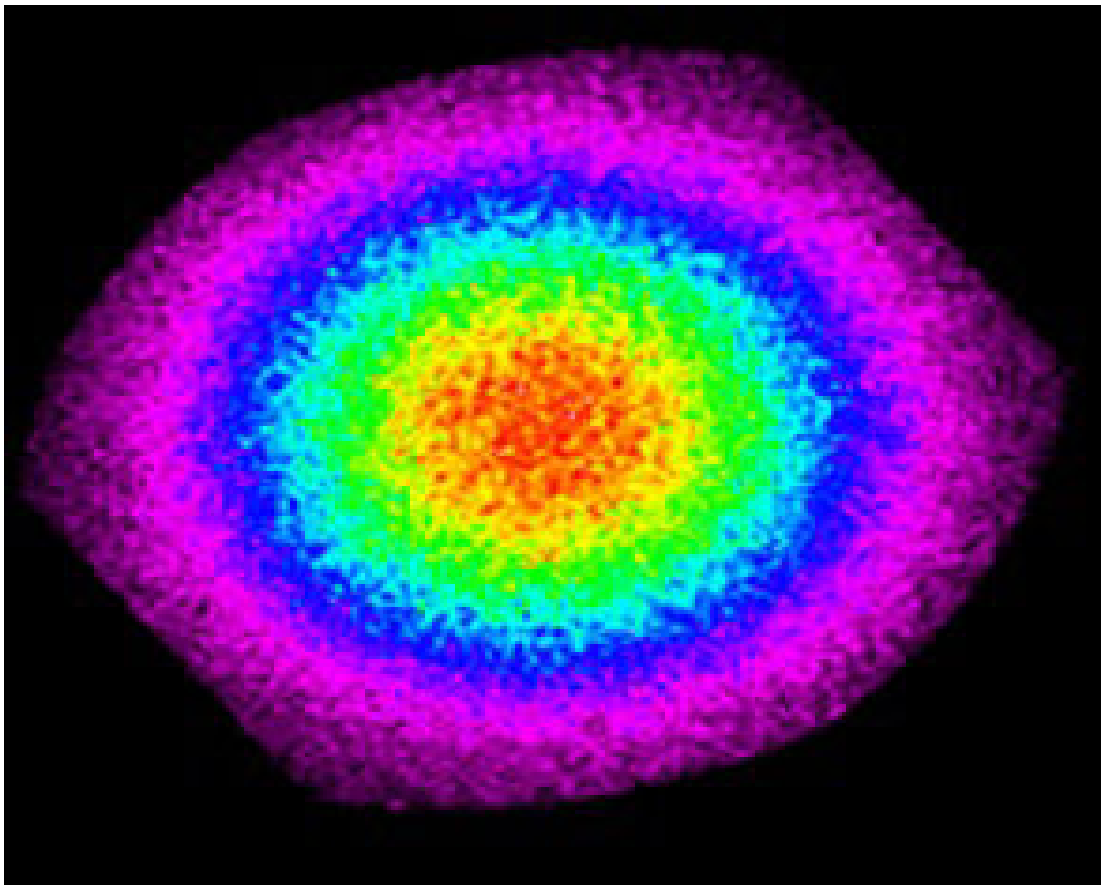

Figure 6.70: Simulation of the initial atomic distribution as defined by the capture laser beam photon distribution.

function of times and taken into account when evaluating the frequency shift. Atomic collisions relevant to the frequency shift occur between the two interaction zones (190.1 mm and 410.1 mm).

An average energy of a gaseous particle for a given temperature is $kT/2$ and this is equal to its average kinetic energy:

$$\frac{3}{2}kT = \frac{mv^2}{2}, \tag{6.41}$$

where $k = 1.380603 \times 10^{-23} \frac{m^2 kg}{s^2 K}$ is the Boltzmann's constant.

In the simulation the atomic cloud was divided into $1mm^3$ cells and the average density is:

$$\bar{n} = \frac{\sum n^2}{\sum N} \tag{6.42}$$

and the average velocity:

$$\bar{V^2} = \frac{\sum V_x^2 + \sum V_y^2 + \sum V_z^2}{N}. \tag{6.43}$$

for each cell was calculated.

Taking into account only the small relative velocity atoms from the bottom of the velocity distribution (whose velocity is not correlated) and using Equation 6.41 collisional energy E_{coll} per cell in units of μK is calculated. The theoretical collision rate coefficients as a function of collisional energy were calculated by Eite Tiesinga (135) and are given on Figure 6.71.

Using Equation 3. from (134), the collisional frequency shift was calculated.

$$\delta\nu(Hz) = \frac{\langle \lambda(E_{coll}) n(t) \rangle}{2\pi}, \tag{6.44}$$

Simulation results on ground for 2.7×10^6 detected atoms and launch velocity of 3.54 m/s give the frequency shift of -1.1×10^{-14}. Experimentally for the same velocity, EM PHARAO frequency shift was -5.3×10^{-15} with an uncertainty of 1×10^{-15} for 1.2×10^6 detected atoms. Taking into account the $\frac{2.7}{1.2} = 2.25$ number of atoms factor, the simulated frequency shift for the same number of atoms would be $\approx -4.9 \times 10^{-15}$ which is comparable to the experimental result.

The results of the simulated cold collision shift as a function of launch velocity (for 10^7 initial atoms) in microgravity are shown on the Figure 6.72.

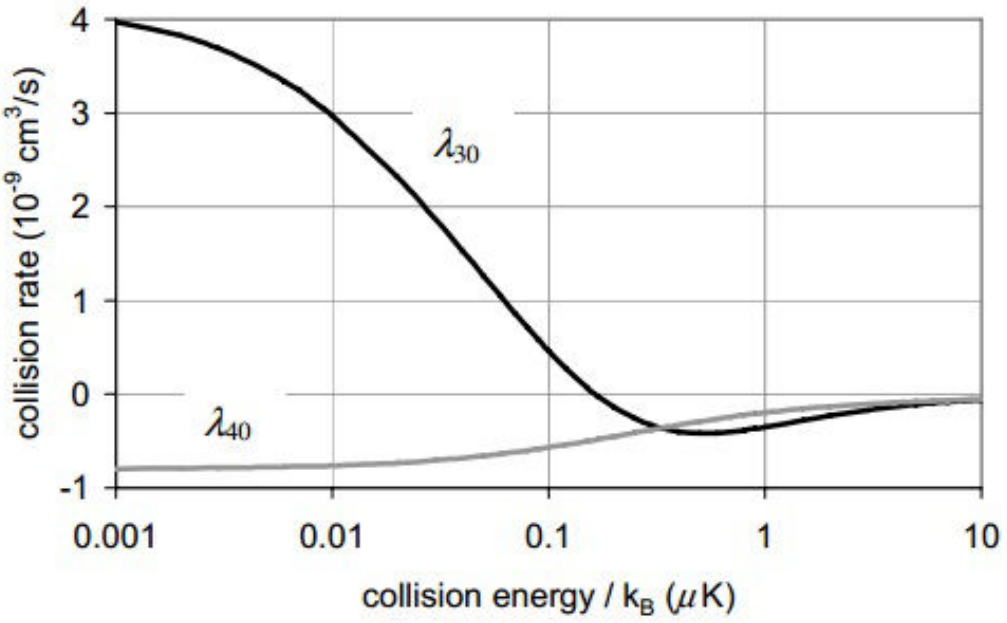

Figure 6.71: Theoretical collision rate coefficients (states $\mid 3,0\rangle$ and $\mid 4,0\rangle$) as a function of collision energy for cesium atoms.

As can be seen, for a launch velocity of about $150mm/s$, the frequency shift vanishes. In microgravity it would be possible to measure the collisional frequency shift at different velocities and to compare with the simulation. Therefore, a frequency correction to normal clock operation based on low launch velocity results could be applied (see Table 5.2).

With the variation of velocity the phase gradient effect is also changed as will be explained in the next section.

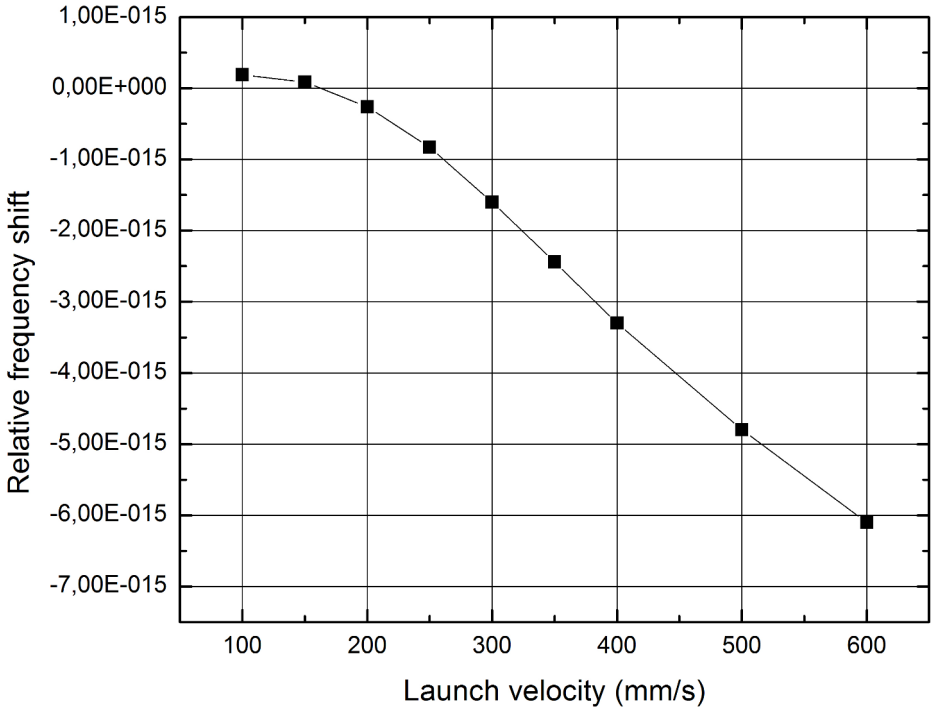

Figure 6.72: PHARAO simulated frequency shift as a function of atom launch velocity

6.4 Doppler effect (DCP)

As the interrogation cavity walls do not have infinite conductivity, energy losses occur in the waveguide wall. This creates a small travelling wave component e^{ikz} which is added to the existing microwave source standing wave. A MW field phase gradient is thus formed which causes a clock frequency shift as a function of the atom velocity. In that way the shift is equivalent to a Doppler shift (136). A spatial phase variation can be decomposed:

$$\frac{d\phi}{dz} = \frac{d\phi}{dt}\frac{dt}{dz} = \frac{\omega}{V_L} \tag{6.45}$$

where $\omega = \frac{d\phi}{dt} = 2\pi\Delta\nu$ is the transition frequency shift and $V_L = \frac{dz}{dt} = \frac{L}{T}$ is the atomic velocity. Therefore, the frequency shift due to the phase gradient can be written as a function of the interaction time T:

$$\Delta\nu = \frac{\phi_1 - \phi_2}{L} \times \frac{L}{2\pi T} = \frac{\phi_1 - \phi_2}{2\pi T}. \tag{6.46}$$

The frequency shift can be separated into 2 contributions: shift due to the phase distribution inside interaction zones seen by the atoms and the shift due the constant phase difference between the two interaction zones. Both effects depend on the cavity manufacturing and microwave field feeding of the zones. As both contributions have a time of flight dependency, it will be possible to evaluate them in orbit by changing the launching velocity.

For a single atom passing through the interaction cavity, the phase variations cause a transition probability perturbation. Using the sensitivity function from Section 10.1 and Equation 10.1 it can be written:

$$\delta P = \int_{z_1}^{z_2} g_1(z)\frac{d\phi_1}{dz}v(z)dz + \int_{z_3}^{z_4} g_3(z)\frac{d\phi_2}{dz}v(z)dz + v \times (\phi_2 - \phi_1), \tag{6.47}$$

where the first two terms are contributions from the phase distributions inside the two interaction zones, while the third term $\int_{z_2}^{z_3} g_2(z)\frac{d\phi}{dz}v(z)dz = v \times (\phi_2 - \phi_1)$ is due to the constant phase difference of the microwave field between the two interaction zones. As given on Figure 10.1, $g_3 = const$ and $g_1 = g_3$ in microgravity.

A finite element modelization was used to calculate the cavity phase distribution. Figure 4.24 and Figure 6.73 give a phase and amplitude distribution inside the interaction zones. From Figure 6.73 a phase gradient of $100\mu rad/cm$ can be approximated at the center of the cavity. The sensitivity of the phase gradient distribution with cavity asymmetry due to machining resolution has been calculated to be lower than 10 μrad. New simulation are being performed by the Gibble group, but no new results are available currently.

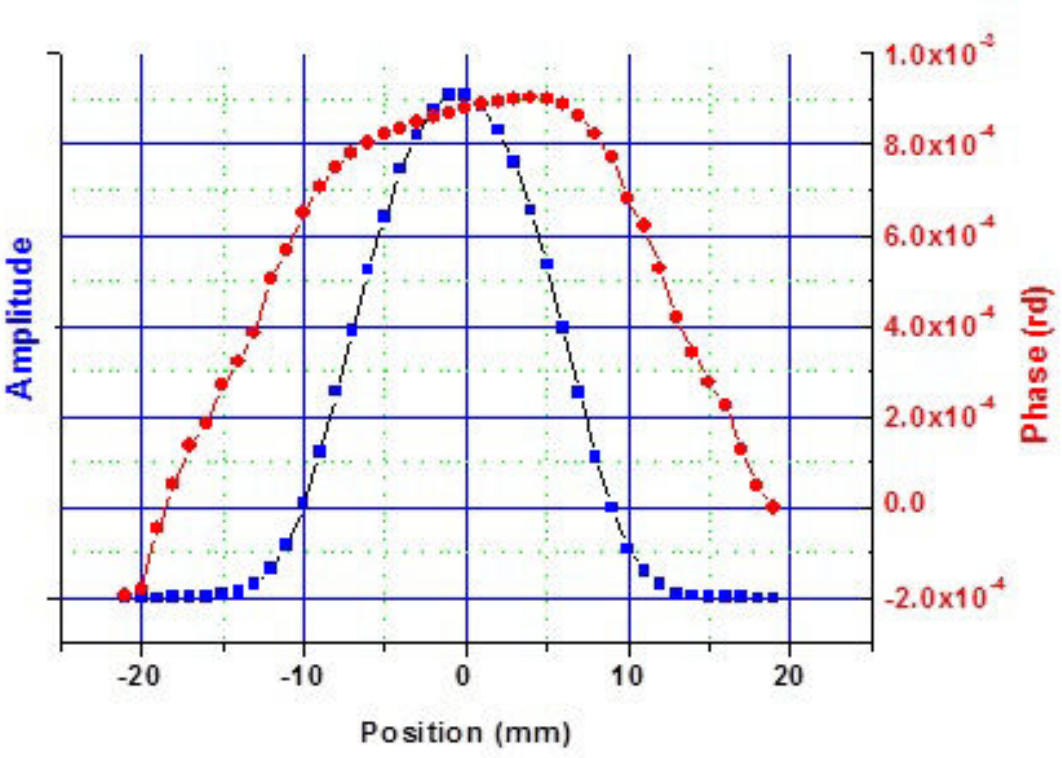

Figure 6.73: 1D interaction zone phase (red) and amplitude (blue) numerical simulation distribution result for a central trajectory. The phase gradient is $\approx 100\mu rad/cm$ at the center.

To examine the phase gradient between the two interaction zones, the PHARAO interrogation cavity was placed inside the FO1 fountain (101). The phase gradient lower than 21 μrad was estimated between the two zones producing an end-to-end frequency shift of $(5 \pm 17) \times 10^{-16}$.

On-ground DCP testing is difficult as the velocity variation due to gravity leads to $g_1 \neq g_3$. A frequency shift for only one active interaction zone was calculated. For Z1

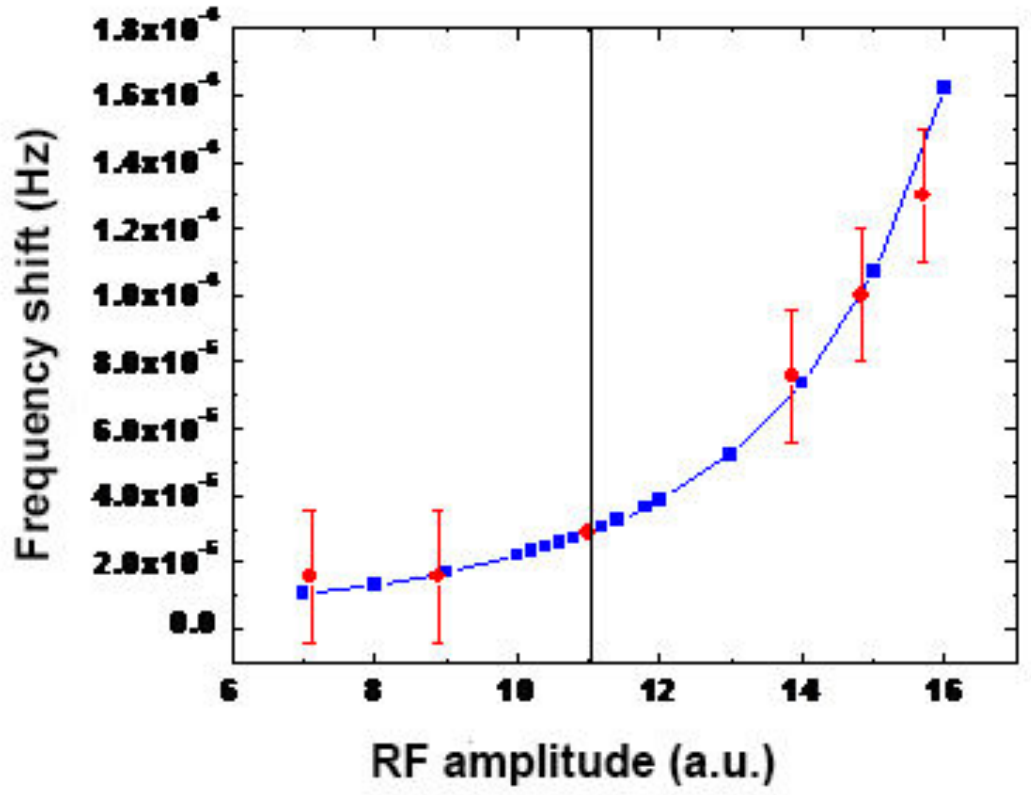

Figure 6.74: Calculation of the frequency shift induced by the microwave phase distribution inside the Ramsey cavity as a function of the RF amplitude. In blue is the calculation and in red the measurements. The black line shows the optimum amplitude.

a frequency shift of $-4.32 \times 10^{-3} Hz$ and for the Z2 a frequency shift of $3.2 \times 10^{-3} Hz$. The frequency difference is only because of the velocity deceleration. In addition, the launch velocity can not be changed significantly. A numerical simulation for an on-ground PHARAO with $\Phi_1 = \Phi_2$ (no phase difference between the two zones) gives a relative frequency shift of 3.3×10^{-15}

The frequency shift results are strongly dependent on the atom transition rate or MW power (Figure 6.74). The measurement have been obtained by the differential method compared to the optimum one.

To verify the simulations, experiments were performed on the PHARAO FM using multiple MW power levels and configurations (interrogation scheme). A frequency shift

of 3.3×10^{-15} was measured with an uncertainty of 10^{-15}.

The clock was tilted by $\pm 25 mrad$ around two axes. For each tilt the PHARAO frequency was compared to the FOM frequency. Preliminary results do not show a frequency shift larger than 2×10^{-15}.

In microgravity numerical simulation results for the PHARAO atomic cloud (with a launch velocity of 400mm/s) give a relative frequency shift contribution of 3×10^{-17} when assuming an identical phase distribution inside the two interaction zones ($\frac{d\phi_1}{dz} = \frac{d\phi_2}{dz}$) and no phase difference between the two zones ($\phi_1 = \phi_2$). Therefore, the shift results from thermal expansions. The effect is studied by changing the atomic velocity from 200 mm/s to 2000 mm/s. For each velocity the cold collision effect is also simulated.

6.5 Conclusion to systematic effects

The mobile fountain FOM has been corrected for all systematic effects. The frequency difference between PHARAO and FOM has been measured at the level of 1.597 $\times 10^{-13}$. PHARAO systematic effects have been evaluated using FOM. Table 6.3 gives an overview of the most important systematic effects of PHARAO on ground and the uncertainties related to their evaluation. Note that the uncertainty of the black body effect is larger than evaluated in Section 6.2.2.4 because the thermal regulation was turned off.

After removing the Zeeman shift, the black body shift, the DCP and the cold collision shift from the PHARAO-FOM difference the remaining value is -1.1 $\times 10^{-15}$. This is within the quadratic sum of all uncertainties as seen on Table 6.3.

Preliminary results on the PHARAO systematic effects have been presented in this thesis. Accuracy is expected to be better in orbit than on ground. Because of the possibility to vary lower atomic launch velocities the uncertainties will be better evaluated. Due to the larger interrogation times, the resolution of the central resonance fringe determination will be better.

Systematic effect	Relative frequency shift	Relative frequency shift uncertainty
Second order Zeeman	1.8109×10^{-13}	7×10^{-17}
Cold collision	-6×10^{-15}	2×10^{-15}
Doppler effect	3.3×10^{-15}	5×10^{-16}
Black body	-1.76×10^{-14}	1×10^{-16}
TOTAL	1.61×10^{-13}	2.07×10^{-15}

Table 6.3: Overview of most important PHARAO systematic effects frequency shifts and their uncertainties as derived from the comparison to FOM.

7

Conclusion

Work performed on the on ground PHARAO characterization and optimization is presented in this thesis.

I have started my thesis in the beginning of 2011 during the manufacturing phase of the PHARAO subsystems. My work commenced on the characterization of flight model magnetic shields and field coils. The experiments took place in a cleanroom at SODERN (Limeil-Brvannes) during 6 months. SODERN is a company that was responsible for the construction of the cesium tube and the laser source of PHARAO. The results were analyzed and the work is presented in this document. In summary, the shield attenuation was measured and the research on the hysteresis shield behavior performed in order to be able to asses the Zeeman shift effect.

This research led me to a creation of a simple hysteresis prediction law and an algorithm that was implemented in the flight model active magnetic field compensation system. Pending subsystem delivery, my work continued on the Monte-Carlo numerical simulation of the thermal evolution of the cold atom cloud inside the cesium tube. The developed software allows for the calculation of the final number of atoms (after aperture cuts) and was used to obtain the first results on the effects of cold atom collisions. With the subsystem delivery I moved to CNES (Toulouse) to continue the experimentation on the assembled clock. The work was concentrated on clock operation in the presence of an external magnetic field simulating the orbital environment. Among other things, the attenuation results were confirmed using cold atoms as probes and the active compensation system was validated. With Christophe Delaroche I worked on the thermal characterization of the cesium tube in order to determine the thermal flux

seen by the atoms and the uncertainty of this evaluation. Finally, I participated in the evaluation of the complete flight model performances. During the thesis, I was involved in the assembly, integration and validation of space instrument. Papers I authored or co-authored during the thesis are: (12, 13, 14, 15, 16).

Transfer of atomic clock technology into space and development of technology useful for cold atom systems development are the main results of the ACES mission. The first primary frequency standard in Earth orbit will allow fundamental physics testing and global clock synchronization previously not available at this level of performance.

The thesis introduced the generalities of atomic clocks and peculiarities related to their operation in a microgravity environment. The ACES mission and its components were presented. PHARAO architecture, operation and components were detailed. Experiments used to establish and improve PHARAO frequency stability and accuracy were described.

Figure 5.1 shows the measured Ramsey m = 0 interrogation pattern, the resonance pattern of the hyperfine transition on which the cesium clock operation is based. The linewidth is 5.6 Hz with the contrast of 0.9 (lower than 1 because of gravity deceleration). Based on ground performance, orbit frequency stability simulation was performed and its results are given on Figure 5.10 and in Table 5.2. A stability at the order of $1 \times 10^{-13} \times t^{-1/2}$ will be achieved in orbit.

A numerical simulation describing the evolution of the atomic cloud inside the cesium tube was developed. The simulation allows for the evaluation of the cold collision and the cavity phase clock frequency shifts. Experiments were performed on these systematic effects as well as on the Zeeman shift and the black body radiation. Section 6 contains the evaluation of all major PHARAO systematic effects. PHARAO was also compared to the mobile fountain FOM which has been corrected for all systematic effects. The resulting overview of the PHARAO frequency shifts and their uncertainties on ground is given in Table 6.3. Because of the longer interaction time in orbit and the possibility to vary low atomic velocities the frequency accuracy of PHARAO will reach the desired 10^{-16} range.

8

Appendix 1

8.1 Ramsey interrogation

Classical, semi-classical and quantum representations can describe the Ramsey (and Rabi) interrogation. The main results obtained from these are used to construct the more intuitive fictitious spin representation.

8.1.1 Classical representation

The Rabi magnetic resonance method is based on an idea that for an atom in a strong magnetic field, a transition from one atomic state to another is possible with adding an additional electromagnetic field having the same frequency as the transition frequency between the two levels (31). By varying the frequency of this smaller field and measuring the probability function, it is possible to deduce the transition frequency with great precision. A case for a particle with 1/2 spin will be presented next.

A magnetic moment of a nucleus m is proportional to the angular momentum N by a proportionality constat called the gyromagnetic ratio γ:

$$m = \gamma N. \tag{8.1}$$

The gyromagnetic ratio for a nucleus is expressed with a nucleus Lande factor $g = -3.82608545$ and the Bohr magneton:

$$\gamma = g\frac{m_B}{\hbar}. \tag{8.2}$$

Placed in a uniform magnetic field that separetes the hyperfine levels, a magnetic moment will precess around its direction with a varying angle of Θ due to the alligning torque τ. This is called the Larmour precession (Figure 8.1). The magnetic moment will not allign completely with the direction of the magnetic field because of the existance of the angular moment which does not have the same direction.

Let us calculate the equations of motion of the magnetic moment when this magnetic field is present. The torque is defined as a time derivative of change of the angular momentum:

$$\tau = \frac{dN}{dt}, \tag{8.3}$$

and is a vector that acts perpendicular to the plane of motion of a magnetic moment:

$$\tau = m \times B_0. \tag{8.4}$$

Following the previous expressions:

$$\frac{dm}{dt} = mx(\gamma B_0). \tag{8.5}$$

If B_0 is in the z-direction $\vec{B_0} = \begin{bmatrix} c0 \\ 0 \\ B_0 \end{bmatrix}$, three differential equations allowing for a description of motion of the magnetic moment can be derived:

$$m_x = Csin(\omega_0 t + \phi) \tag{8.6}$$

$$m_y = Ccos(\omega_0 t + \phi) \tag{8.7}$$

$$m_z = const \tag{8.8}$$

where C is a constant and ω_0 is called the Larmour frequency and represents the angular frequency with which the magnetic moment precesses around the direction of the magnetic field:

$$\omega_0 = -\gamma B_0. \tag{8.9}$$

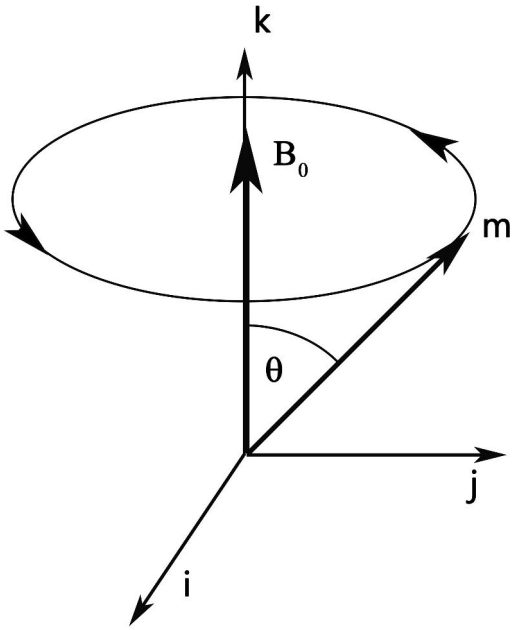

Figure 8.1: A magnetic moment m in a constant magnetic induction B_0.

This frequency actually represents the energy difference between the initial (I) and the final state (F) which are used as a basis for the operation of the clock:

$$\omega_0 = \omega_{at} = \frac{E_F - E_I}{\hbar}. \tag{8.10}$$

If we now want to rotate the magnetic moment (and by that invoke a hyperfine transition) we need to add another magnetic field to the system. Therefore, an alternating magnetic field B_1 of appropriate magnitude and duration positioned in the x-y plane and rotating around the z-axis is now applied with an effort to change the angle between the magnetic moment vector and the k axis.

To achieve this, a new frame of reference Σ' that rotates with angular velocity ω around the k' axis is introduced (Figure 8.2). At $t = 0$ all the axis of the two systems correspond, and, due to rotation, at $t > 0$ only k and k' coincide. Time derivative of any vector A in the laboratory frame is:

$$\frac{dA}{dt} = \frac{\partial A}{\partial t} + \omega \times A, \tag{8.11}$$

where $\frac{\partial A}{\partial t}$ is a time derivative in the rotating system Σ'. With this in mind, a time derivative of the magnetic moment 8.5 can be written in the new system as:

$$\frac{dm}{dt} = \gamma m \times (B_0 + \frac{\omega}{\gamma}). \tag{8.12}$$

In the Σ system the field B_0 is seen as an effective field:

$$B_c = (B_0 + \frac{\omega}{\gamma})\vec{k}. \tag{8.13}$$

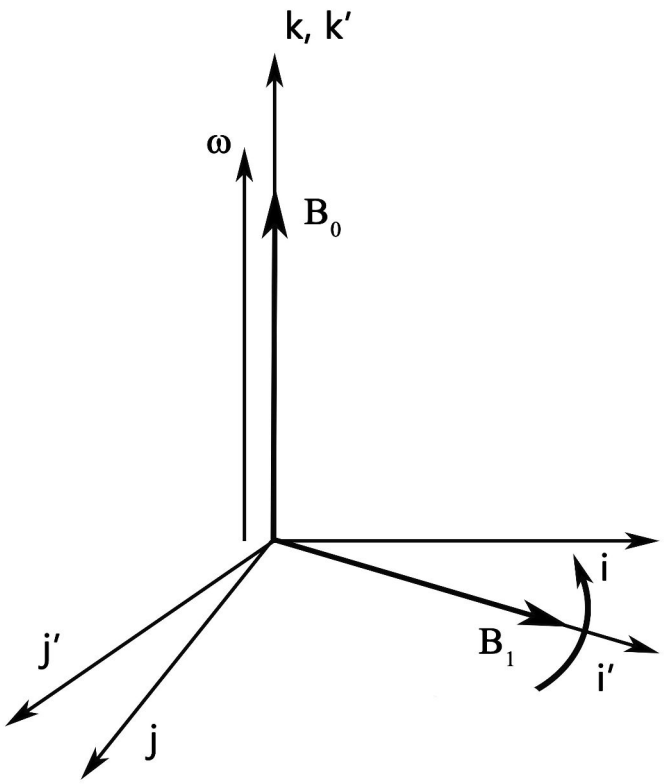

Figure 8.2: Coordinate systems Σ and Σ'.

The angular velocity ω is actually the frequency of the newly added magnetic field B_1 and it is being modulated by the microwave oscillator until the resonance is observed.

On the other hand, the magnitude of the field will determine the angular velocity ω_1 which describes of the precession of the magnetic moment around the axis i':

$$B_1 = -\frac{\omega_1}{\gamma} \tag{8.14}$$

The effective field is now:

$$B_c = (B_0 + \frac{\omega}{\gamma})\vec{k} + B_1\vec{i'}. \tag{8.15}$$

Using 8.35 and 8.14 the amplitude of the effective field is :

$$|B_c| = \frac{\sqrt{(\omega - \omega_0)^2 + \omega_1^2}}{\gamma}. \tag{8.16}$$

The first term in the previous equation describes the field component in the direction of the k axis and is zero if $\omega = \omega_0$. That would be the case of resonance and the magnetic moment would then be directed perpendicular to the i' axis (along the j' axis) and would precess around it with angular velocity ω_1. A pulse (Rabi frequency) π or two times $\frac{\pi}{2}$ for the Rabi or Ramsey method is applied then, respectively. Because it is perpendicular due to the frequency resonance and because the angle between the vector and the k' axis is changed by π, the magnetic moment is now completely reversed and the hyperfine transition is maximal. This change of orientation constitutes a transition between two magnetic states in the classical representation (137).

On the other hand (illustration on Figure 8.3):

- If ω is far from ω_0, the applied field will produce a nutation of the magnetic moment around the effective field with a fast variation of Θ which is, on average, equal to zero.

- If ω is close to ω_0 (but there is no resonance), the magnetic moment vector will precess around the applied field (i' axis) but the first term of 8.16 will not be completely cancelled and the vector will not be perfectly perpendicular to i' axis.

- If there is a frequency resonance $\omega = \omega_0$, but the total applied pulse is not π the magnetic moment vector will still be perpendicular to i' axis. However, the vector will not be completely inversed as there will be an angle $\neq \pi$ between it and the k' axis.

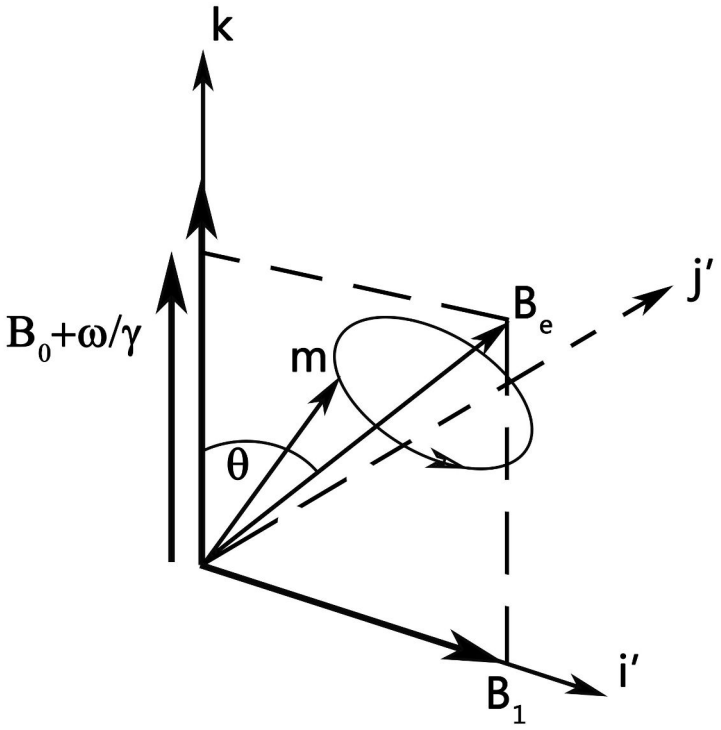

Figure 8.3: Illustration of the motion of the magnetic moment m.

In all these cases, the projection of the magnetic moment vector on the $-k'$ axis will not be m but some percentage of it equal to the transitional probability. This is best described by the following angle equation:

$$sin\Theta = \frac{|\omega_1|}{\gamma|B_e|}. \tag{8.17}$$

So far we have ignored the effect of the intermediate region between the two interaction regions in the Ramsey method. After time τ of the first region the magnetic moment has rotated an angle of $\frac{\pi}{2}$. The field B_1 is now turned off during time T and lenght L of the atom flight. Following the effective field equation, the magnetic moment vector precesses around the always present B_0 field directed along the k' axis with Larmour frequency, as in the beginning. The difference is that now it does this in the $i' - j'$ plane due to the effective field changing too rapidly for the magnetic moment to follow and re-allign(ref rabi). In the quantum picture for a cesium atomic clock, the atoms are

now in a mixed state between the atomic states $|F = 3, m_F = 0\rangle$ and $|F = 4, m_F = 0\rangle$. In the second oscillatory region, a torque due to the new field B_2 appears. As before, in the rotating frame the magnetic moment is now precessing around the oscillating field direction along the i' axis. If the same value of the frequency of the applied field is used (allowing for annulation of the k axis component of the effective field) and the same amplitude and duration (responsible for the angle of rotation) the magnetic moment will be again perpendicular to the i' axis and rotate exactly for an additional angle of $\frac{\pi}{2}$ thus completing the rotation of the vector by a total angle of π (corresponding to the full transition $|F = 3, m_F = 0\rangle \rightarrow |F = 4, m_F = 0\rangle$ of cesium atoms). [1]

If the frequencies $\omega_0 \neq \omega$, a phase difference between the two will accumulate during the free evolution region. For example, if after entering the second interaction zone the phase difference amounts to π, the effect of the second $\frac{\pi}{2}$ pulse will be that the vector of the magnetic moment is rotated back (by precession around the i' axis) to allign with the k' axis as in the beginning. In that way any effect of the field B_1 will be cancelled and no transitional signal will be produced. If the phase difference happens to be an integar multiple of 2π, for an atomic sample with no velocity distribution the effect would be as if there is resonance.

However, in a real sample, atoms have a velocity variation indicating different atoms spend a different amount of time in the intermediate region. This means the accumulated atomic phase shift will also have a variation, and the resonant maximal peak of the atomic samples having an average dephasing of a multiple of 2π will have a lower amplitude (due to a lower number) than in the case of zero-phase resonance $\omega = \omega_0$. Consequently, for zero-phase resonance, there is no dependence on the atomic velocity distribution and the atoms whose precessing angle during free evolution is any multiple of 2π (maintaining perpendicularity as previously described) will create the central maxima of the probability inteference pattern. In both cases (zero-phase resonance and 2π multiple phase resonance), other peaks of the interference pattern will be created by the magnetic moment free evolution when the magnetic moment vector dephases in such a way that when entering the second interaction cavity it is not perpendicular to the i' axis.

[1] Note also that the value of ω frequency inside the first and the second interaction region must be in phase. This means that if there is resonance in the first region, it will be maintained in the second even if there is no applied field in the intermediate region.

In a more complex case of a cesium atom, different m_F states would correspond to different Θ angles between the magnetic moment and the unifrom magnetic field. Consequently, magnetic transitions between them would correspond to angle shifts $\Delta\Theta$. However, the classical representation is not sufficient to qualitatively describe the operation in a cesium frequency standard and for that we will use the semi-classical approach.

8.1.2 Quantum physical interpretation of interference

The interference can be explained by quantum physics (19). Appearance of interference can be explained by the accumulation of phase between waves of the two atomic states used in an atomic clock (Figure 8.4):

$$\Delta\Phi = \Delta k_{at} \times L, \tag{8.18}$$

where L is the lenght of the free evolution region and Δk_{at} is the difference between the wave vector of the initial and transitioned state:

$$\Delta k_{at} = \vec{k_F} - \vec{k_I}. \tag{8.19}$$

Taking into account conservation of energy and momentum laws between the atomic waves of the two states:

$$(\frac{1}{2}mv_I^2 + E_I) + \hbar\omega = (\frac{1}{2}mv_F^2 + E_F) \tag{8.20}$$

$$m\vec{v_F} - m\vec{v_I} = \vec{K}, \tag{8.21}$$

where m is the mass of the atom, E_I and E_F are energy levels of the two states and v_I and v_F are the velocities of the wave packets in the initial state before the photon absorption ($\hbar\omega$) during Ramsey interrogation and the final state after, respectively.

From the previous two equations and 8.10 and by assuming the atoms propagate in the same direction, the total expression for dephasing between the two wave paquets 8.19becomes:

$$\Delta\Phi = \frac{\omega - \omega_{at} - \frac{\hbar K^2}{2m}}{v_f} \times L \tag{8.22}$$

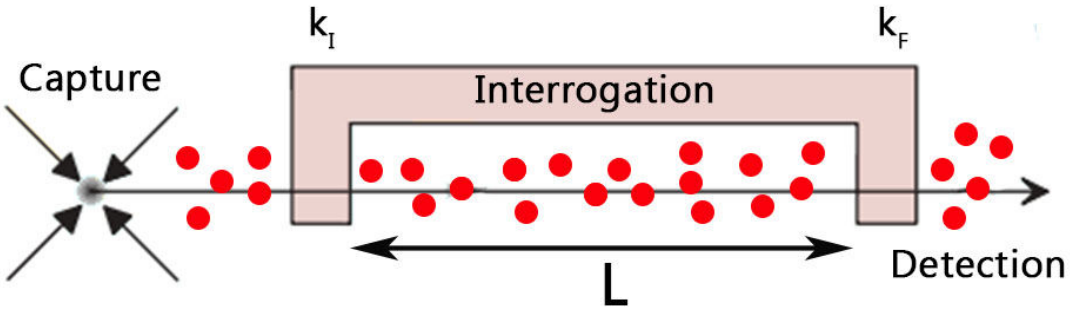

Figure 8.4: Formation of an interference pattern by variation of the initial and final state dephasing.

The dephasing is proportional to the recoil term $\frac{\hbar K^2}{2m}$ and the frequency difference between the applied field and the atomic transition. By varying this difference, as is performed in atomic clocks by modulation of the applied field frequency in order to find the atomic frequency, an interference pattern is formed. The exact expressions for transition probabilities containing this variation will be calculated in the next section.

8.1.3 Semiclassical representation

8.1.3.1 Single oscillatory field - Rabi magnetic resonance method

In the presence of a static magnetic field, due to the Zeeman effect, splitting of the magnetic spectral lines occurs. The ground state of cesium has a rich hyperfine structure containing a total of 16 levels. Inside a cesium atomic clock, the relevant transition is the $|F = 3, m_F = 0\rangle \rightarrow |F = 4, m_F = 0\rangle$. Therefore, the total system can be reduced to a 2 x 2 density matrix (31):

$$\rho = \begin{bmatrix} cc\rho_{3,3} & \rho_{3,4} \\ \rho_{4,3} & \rho_{4,4} \end{bmatrix}. \tag{8.23}$$

A Hamiltonian describing the interaction between the two levels has their energy states as eigenvalues. If ω_0 is the angular frequency of the transition then the energy between the two levels is $E_4 - E_3 = \hbar\omega_0$ and the unpertrubed Hamiltonian is:

$$H_0 = \begin{bmatrix} cc1/2\hbar\omega_0 & 0 \\ 0 & -1/2\hbar\omega_0 \end{bmatrix}. \tag{8.24}$$

8. APPENDIX 1

A microwave magnetic field applied in the z direction inside the interaction zone is described as a petrubation with a Hamiltonian:

$$H_1 = \mu_B(g_J S_z - g_I I_z)B_z(t) \tag{8.25}$$

where S_z is the electron spin angular momentum, I_z is the nuclear angular momentum and μ_B is the Bohr's magneton used to express electron magnetic dipole moment and is equal to $9.2740154 \times 10^{-24} J/T$. $g_J = 2.00254$ and $g_I = -0.000398853$ are the electron spin and nuclear g-factors, respectively. G-factors are the proportionality constants between the magnetic moment of a particle and the Bohr's magneton. In the following calculations g_I will be neglected and g_J approximated as 2.

It is assumed the microwave field inside the interaction zone is a sinusoidal function:

$$B_z(t) = Bcos(\omega t + \phi) \tag{8.26}$$

where B is the amplitude, ω is the angular frequency of the applied field and ϕ is a phase of the microwave field which is equal to zero for the Rabi magnetic resonance method.

The total Hamiltonian describing the Rabi pulsation inside the interaction zone is formed by combining 8.24 and 8.25:

$$H = \frac{\hbar}{2}\begin{bmatrix} cc\omega_0 & be^{-i(\omega t+\phi)} \\ be^{i(\omega t+\phi)} & -\omega_0 \end{bmatrix} + CC \tag{8.27}$$

where b is the microwave field amplitude in units of Bohr's magneton:

$$b = \frac{\mu_B B}{\hbar} \tag{8.28}$$

and actually represents the Rabi angular frequency of the atoms.

The complex conjugate part of the matrix is neglected in the rotating wave approximation. By using the Schrodinger equation

$$\frac{d}{dt}\rho = \frac{1}{i\hbar}[H, \rho] \tag{8.29}$$

on the density matrix to study the evolution of the system, a set of differential equations is produced:

$$\frac{\partial a_1(\Theta)\partial\Theta + \Omega_0 a_2(\Theta}{+} b_2 a_3(\Theta) = 0 \tag{8.30}$$

,

$$-\Omega_0 a_1(\Theta) + \frac{\partial a_0(\Theta)}{\partial \Theta} - b_1 a_3(\Theta) = 0 \tag{8.31}$$

,

$$-b_2 a_1(\Theta) + b_1 a_2(\Theta) + \frac{\partial a_3(\Theta)}{\partial \Theta} = 0 \tag{8.32}$$

,

where b_1 and b_2 are components of the pertrubation term of the hamiltonian and have values:

$$b_1 = bcos\phi \tag{8.33}$$

.

$$b_1 = -bsin\phi. \tag{8.34}$$

Ω_0 is the offset of the microwave field angular frequency from the atomic level angular frequency:

$$\Omega_0 = \omega - \omega_0, \tag{8.35}$$

while $a_1(\Theta)$, $a_2(\Theta)$ and $a_3(\Theta)$ are real numbers and represent fractional population of $|F = 3, m_F = 0\rangle$, fractional population of $|F = 4, m_F = 0\rangle$ and fractional population difference between the two levels at time Θ spent in the interaction zone, respectively:

$$\rho_{3,4} = \frac{1}{2}(a_1(\Theta) + ia_2(\Theta))e^{-i\omega t}\rho_{3,3} - \rho_{4,4} = a_3(\Theta) \tag{8.36}$$

.

Time Θ will depend on the lenght of the interaction zone l and the atomic velocity v:

$$\Theta = \frac{l}{v} \tag{8.37}$$

.

Equations 8.30 can be solved analytically by using the Laplace transform and presented in a matrix form where $a_1(\Theta)$, $a_2(\Theta)$ and $a_3(\Theta)$ are functions of $a_1(0)$, $a_2(0)$ and $a_3(0)$, respectively:

$$\begin{bmatrix} ca_1(\Theta) \\ a_2(\Theta) \\ a_3(\Theta) \end{bmatrix} = R(b_1, b_2, \Omega_0, \Theta) \begin{bmatrix} ca_1(0) \\ a_2(0) \\ a_3(0) \end{bmatrix}, \tag{8.38}$$

and the matrix describing the quantum state evolution is (note that the phase $\phi = 0$ so b_2 must dissapear):

$$R(b_1, 0, \Omega_0, \Theta) = \begin{bmatrix} cos\Omega\Theta + \frac{b_1^2}{\Omega^2}(1 - cos\Omega\Theta) & -\frac{\Omega_0}{\Omega} sin\Omega\Theta & -\frac{b_1\Omega_0}{\Omega^2}(1 - cos\Omega\Theta) \\ \frac{\Omega_0}{\Omega} sin\Omega\Theta & cos\Omega\Theta & \frac{b_1}{\Omega} sin\Omega\Theta \\ -\frac{b_1\Omega_0}{\Omega^2}(1 - cos\Omega\Theta) & -\frac{b_1}{\Omega} sin\Omega\Theta & 1 \end{bmatrix} \tag{8.39}$$

where:

$$\Omega^2 = b^2 + \Omega_0^2 \tag{8.40}$$

.

In the Rabi magnetic resonance method the atoms are often prepared without coherence ($a_1 = a_2 = 0$) in one or the other atomic state before entering the interaction zone. The probability of the transition is then related to the fractional population difference a_3 which can take the value 1 or -1 depending if the atoms are in the state $|F = 3, m_F = 0\rangle$ or $|F = 4, m_F = 0\rangle$, respectively. Using 8.38 and 8.39 the probability of the transition is given by:

$$P(\Theta) = \frac{1}{2}(1 - \frac{a_3(\Theta)}{a_3(0)}) = \frac{b^2}{\Omega^2} sin^2 \frac{1}{2}\Omega\tau \tag{8.41}$$

.

The probability has a maximum at resonance $\Omega_0 = 0$ and for a π pulse:

$$b\tau = \pi \tag{8.42}$$

.

Full width at half maximum of the resonance peak (central frange) is then given when the probablity is maximum as:

$$FWHM = \frac{5.02}{\tau} \tag{8.43}$$

.

8.1.3.2 Double oscillatory field - Ramsey magnetic resonance method

The Ramsey magnetic resonance method is based on two interaction zones of lenght l and flight time τ separated by a relatively long microwave field free space of lenght L and flight time T ¿¿ τ. A static magnetic field is present on the entire atoms path.

The evolution of the atomic quantum state inside an interaction zone is now described by the following matrix that compared to 8.39 has the b_2 factor due to the phase ϕ not necessarily being zero (a phase difference between the interaction zones microwave field is possible):

$$R_i(b_1, b_2, \Omega_0, \Theta) = \tag{8.44}$$
$$\begin{pmatrix} cos\Omega\Theta + \frac{b_1^2}{\Omega^2}(1 - cos\Omega\Theta) & -\frac{\Omega_0}{\Omega} sin\Omega\Theta + \frac{b_1 b_2}{\Omega^2}(1 - cos\Omega\Theta) & -\frac{b_1\Omega_0}{\Omega^2}(1 - cos\Omega\Theta) - \frac{b_2}{\Omega} sin\Omega\Theta \\ \frac{\Omega_0}{\Omega} sin\Omega\Theta + \frac{b_1 b_2}{\Omega^2}(1 - cos\Omega\Theta) & cos\Omega\Theta + \frac{b_2^2}{\Omega^2}(1 - cos\Omega\Theta) & \frac{b_1}{\Omega} sin\Omega\Theta - \frac{b_2\Omega_0}{\Omega^2}(1 - cos\Omega\Theta) \\ -\frac{b_1\Omega_0}{\Omega^2}(1 - cos\Omega\Theta) + \frac{b_2}{\Omega} sin\Omega\Theta & -\frac{b_1}{\Omega} sin\Omega\Theta - \frac{b_2\Omega_0}{\Omega^2}(1 - cos\Omega\Theta) & 1 - \frac{b^2}{\Omega^2}(1 - cos\Omega\Theta) \end{pmatrix}$$

where i denotes the first or the second interaction zone.

The effect of the drift region where the amplitude of the petrbuation $b = 0$ is contained in the matrix:

$$R_i(0, 0, \Omega_0, T) = \begin{bmatrix} cos\Omega_0\Theta & -sin\Omega_0\Theta & 0 \\ sin\Omega_0\Theta & cos\Omega_0\Theta & 0 \\ 0 & 0 & 1 \end{bmatrix}, \tag{8.45}$$

where the time spent in the region depends on its lenght and atomic velocity and is $T = \frac{L}{v}$. Same as for Rabi, before the first interaction the atoms are prepared in one of the initial states and are introduced without coherence: a_3 is either 1 or -1 and $a_1 = a_2 = 0$. After the first $\frac{\pi}{2}$ pulse, a superposition of states is created between the ground and excited state. This depends on both the applied amplitude and frequency offset from resonance. At resonance, the $\frac{\pi}{2}$ pulse will produce equal splitting between the two states. The atoms then enter the drift zone where they evolve freely until entering the second interaction zone where another pulse same as in the first zone is applied. By combining the expression 8.38 with matrices 8.39 (interaction zone) and 8.45 (drift zone), cesium atom quantum state after time $\tau + T + \tau$ can be obtained. From the first term of 8.41 a probability for the transition between $|F = 3, m_F = 0\rangle$ and $|F = 4, m_F = 0\rangle$ can be deduced to be:

$$P(\tau) = \frac{4b^2}{\Omega^2} sin^2 \frac{1}{2}\Omega\tau (cos\frac{1}{2}\Omega\tau cos\frac{1}{2}(\Omega_0 T + \phi) - \frac{\Omega_0}{\Omega} sin\frac{1}{2}\Omega\tau sin\frac{1}{2}(\Omega_0 T + \phi))^2 \tag{8.46}$$

.

The terms with $\Omega\tau$ represent the main excitation corresponding to the resonance, while the terms with $\Omega_0 T$ describe the interference pattern.

For phase $\phi = 0$ between the two regions and at resonance $\Omega_0 = 0$ the maximum probability of transition is for impulse amplitude:

$$b\tau = \frac{\pi}{2} \tag{8.47}$$

.

Full width at half maximum of the central fringe of probability at resonance and optimal amplitude is given by:

$$FWHM \approx \frac{\pi}{T} \tag{8.48}$$

In a near-resonance approximation $\Omega_0 << b$, the expression for the transition probability $|F = 3, m_F = 0\rangle$ and $|F = 4, m_F = 0\rangle$ (Equation 8.46 simplifies to:

$$P(\tau) = \frac{1}{2}(1 + cos(\Omega_0 T + \phi)) \tag{8.49}$$

.

8.1.4 Fictitious spin representation

In order to present the Ramsey interogation more intuitively, we will combine the classical and the semi-classical representation to form a pictorial fictitious spin describtion (19, 31).

It is first necessary to introduce the Pauli matrices:

$$\sigma_1 = \begin{bmatrix} 0 & 1 \\ 1 & 0 \end{bmatrix}, \sigma_2 = \begin{bmatrix} 0 & -i \\ i & 0 \end{bmatrix}, \sigma_3 = \begin{bmatrix} 1 & 0 \\ 0 & -1 \end{bmatrix}. \tag{8.50}$$

Their properties are:

$$\sigma_i^2 = I\sigma_i\sigma j + \sigma j\sigma i = 2\delta_{i,j} I\sigma_i\sigma j = I\delta_{i,j} + i\epsilon_{i,j,k}\sigma k, \tag{8.51}$$

where i,j and k are the Pauli matrix index numbers, i in the last expression is the imaginary unit, δ is the Kronecker delta and ϵ is the permuation symbol.

Together with the identity matrix:

$$I = \begin{bmatrix} 1 & 0 \\ 0 & 1 \end{bmatrix}, \tag{8.52}$$

the Pauli matrices can express full vector space of any complex 2x2 matrix in the form of a linear combination.

Now we can use these matrices to rewrite the density matrix 8.23:

$$\rho = \frac{1}{2}(m_0^f I + \sum_{i=1} m_i^f \sigma_i) \tag{8.53}$$

By using the properties of the Pauli matrices the coefficients m^f can be determined:

$$m_1^f = \rho_{ab} + \rho_{ba}, \tag{8.54}$$

$$m_2^f = i(\rho_{ab} - \rho_{ba}), \tag{8.55}$$

$$m_3^f = \rho_{aa} - \rho_{bb}, \tag{8.56}$$

where m_1^f and m_2^f represent the components of the magnetic moment induced by the pertrubation and m_3^f is the population difference between the two levels.

In the same way as 8.53, the 2x2 total Hamiltonian of the hyperfine interaction between the two states of the atomic clock (8.27) can be expressed by using the Pauli matrices:

$$H = \frac{1}{2}\hbar \sum_{i=1} b_i^f \sigma_i \tag{8.57}$$

where the coefficient b_i^f can be obtained in the same manner as before:

$$b_1^f = bcos(\omega t + \phi) = b_1 cos\omega t + b_2 sin\omega t, \tag{8.58}$$

$$b_2^f = bsin(\omega t + \phi) = b_1 sin\omega t - b_2 cos\omega t, \tag{8.59}$$

$$b_3^f = \omega_0, \tag{8.60}$$

As defined previously in 8.28, 8.33 and 8.34, b is the amplitude of the applied magnetic field corresponding to ω_1 or the Rabi frequency, b_1 and b_2 are components of the petrubation term in the interaction Hamiltonian, ω is the frequency of the RF field and ω_0 is the Larmour angular velocity. Phase ϕ represents the phase between the applied fields B_1 and B_2 in the two interaction regions as defined in the previous chapter and is nominally equal to zero. Finally, components b_1^f and b_2^f represent the x-y

plane (in the used convention) components of the applied field, while b_3^f is the fictitiuos static magnetic induction.

Equations of motion in vectorial form are:

$$\frac{dm^f}{dt} = -m^f x B^f. \tag{8.61}$$

where m^f and B_f have the following components (Figure 8.5):

$$\frac{dm_1^f}{dt} = -(m_2^f B_3^f - m_3^f B_2^f) \tag{8.62}$$

$$\frac{dm_2^f}{dt} = -(m_3^f B_1^f - m_1^f B_3^f) \tag{8.63}$$

$$\frac{dm_3^f}{dt} = -(m_1^f B_2^f - m_2^f B_1^f) \tag{8.64}$$

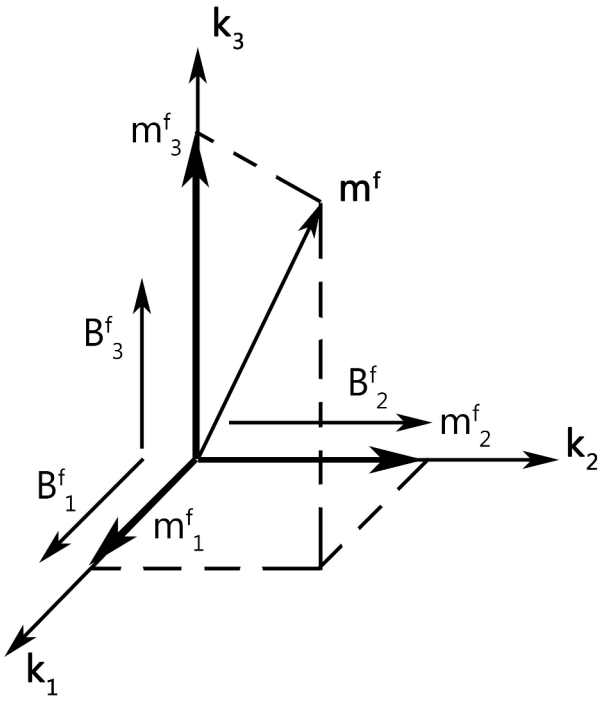

Figure 8.5: Magnetic induction components B^f and fictitiuos spin components m^f.

Equation 8.61 is similar to 8.5. Therefore, using the analogy of the classical representation, this representation describes how components of magnetic induction B^f

(8.58) act on the components of the fictitiuos spin m^f (8.54). From Equation 8.36, Equations 8.54, 8.55 and 8.56 can be rewritten as:

$$m_1^f = a_1 cos\omega t + a_2 sin\omega t, \tag{8.65}$$

$$m_2^f = a_1 sin\omega t - a_2 cos\omega t, \tag{8.66}$$

$$m_3^f = a_3, \tag{8.67}$$

where we recall $a_1(\tau+T+\tau)$ and $a_2(\tau+T+\tau)$ describe the atomic state coherence and $a_3(\tau+T+\tau)$ is the fractional population difference, all of the variable values being measurable physical quantites. Two $\tau's$ represent the time atoms spend in the two interraction regions and T is the time they spend in the intermediate region without the applied field. In the rotating frame (see again Section 8.1.1) at $t = 0$ components of the fictitous magnetic moment are (Figure 8.6):

$$m_1^{;f} = a_1(\tau + T + \tau) \tag{8.68}$$

$$m_2^{;f} = -a_2(\tau + T + \tau) \tag{8.69}$$

$$m_3^{;f} = a_3(\tau + T + \tau), \tag{8.70}$$

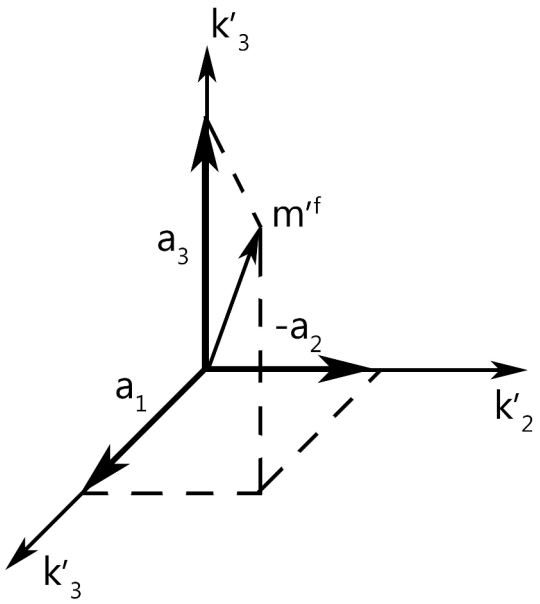

Figure 8.6: Components of the fictitious magnetic moment in the rotating frame.

and components of the fictituous magnetic induction are (Figure 8.7):

$$b_1^{'f} = b_1 = bcos\phi \tag{8.71}$$

$$b_2^{'f} = -b_2 = bsin\phi \tag{8.72}$$

$$b_3^{'f} = -\Omega_0, \tag{8.73}$$

where Ω_0 was defined in 8.35.

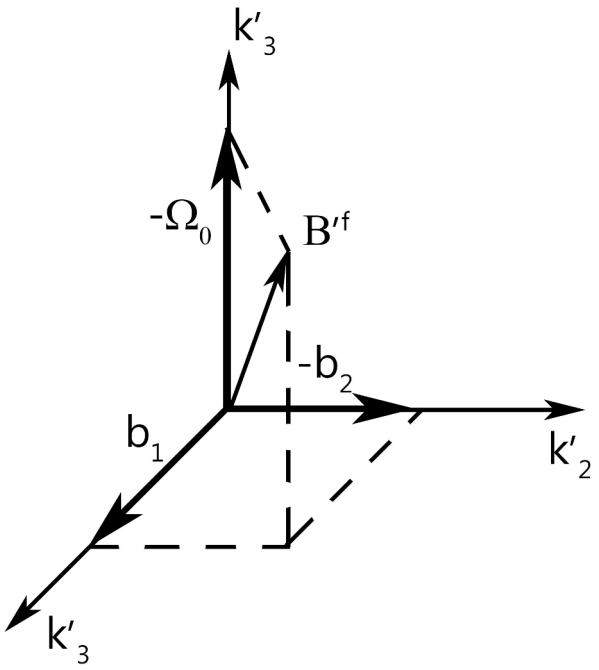

Figure 8.7: Components of the fictitious magnetic induction in the rotating frame.

We can now construct an intuitive pictorial representation of what happens during the Ramsey interrogation in 4 steps:

- Figure 8.8. At the beginning of the process before the atoms enter the first interraction region there is no coherence of atomic states (no state mixing) $a_1 = a_2 = 0$ and all the atoms are in one of the two states $a_3 = 1$ (for example). The fictitius spin vector is directed along the $k'_3 = k_3$ axis.

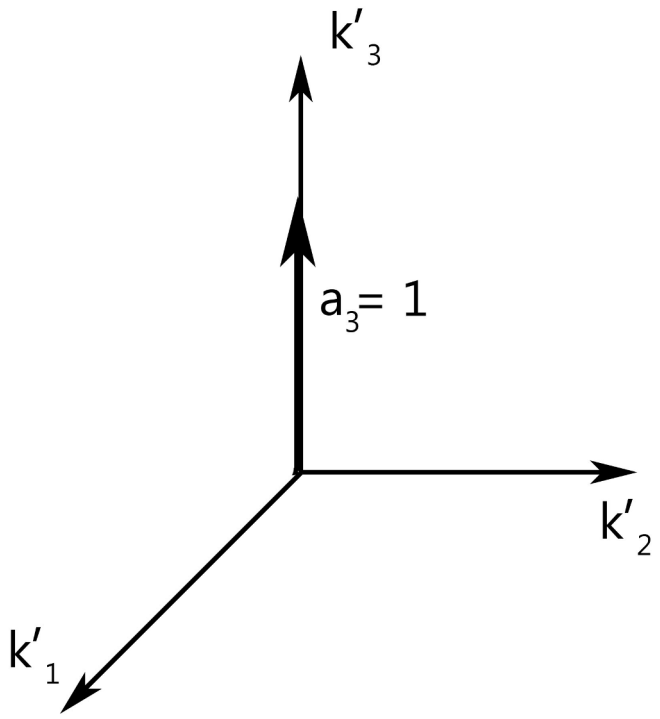

Figure 8.8: Fictitious spin orientation at the beginning. All the atoms are in the same state.

- Figure 8.9. After entering the first interaction region, the applied RF field is turned on and it is directed along the k_1' axis. Because of the torque produced by this field on the fictitius spin, its vector rotates around the k_1' axis by an angle of $b\tau$. The angle is determined by the duration of the RF field application τ and the amplitude b which is actually the Rabi frequency ω_1. If $b\tau = \frac{\pi}{2}$ (8.47), the vector is now in the $k_1' - k_2'$ plane directed along the $-k_2'$ (due to rotation around k_1'). Quantum physically, there is now a perfect mixture of states between the two levels.

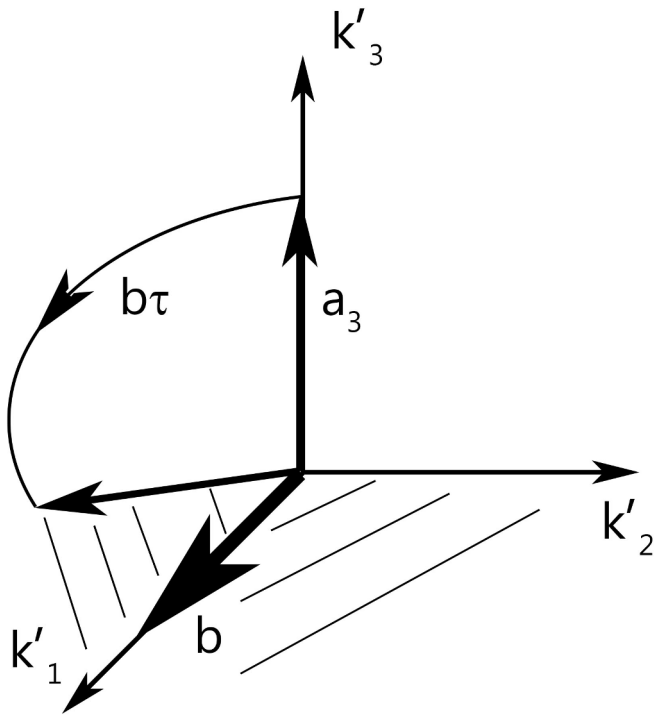

Figure 8.9: Effect of the magnetic field induction directed along k_1' on the fictitious spin orientation.

- Figure 8.10. The atoms exit the first interraction region and enter the free evolution space where there is no RF field anymore. The fictitiuos spin will now precess around the k_3' axis in the $k_1' - k_2'$ plane. The rotation angle it describes before entering the second interraction zone is $-\Omega_0 T$ (T being the time atoms spend in the no field region) due to the fictitious magnetic induction $-\Omega_0$ acting along k_3'.

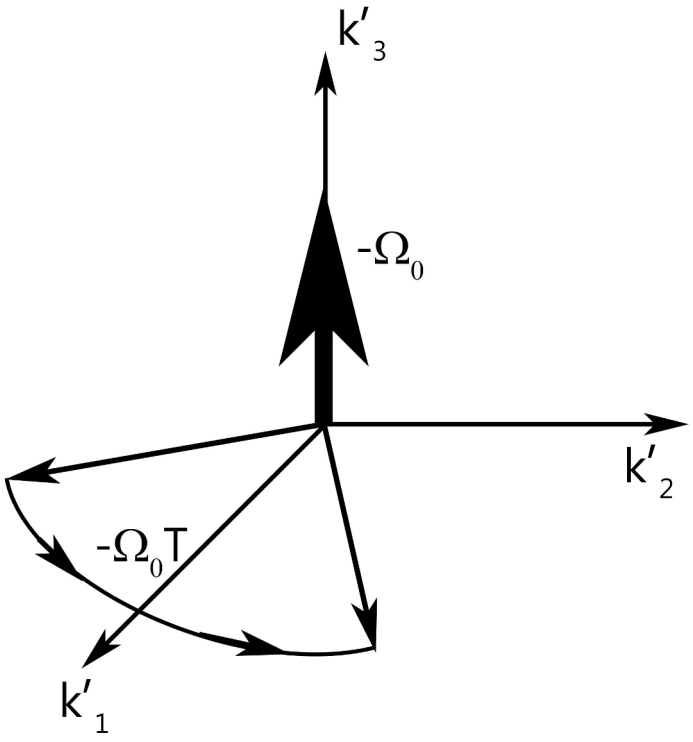

Figure 8.10: Effect of the free evolution region on the fictitious spin orientation.

- Figure 8.11. After entering the second interraction region, the RF field along the k_1' is turned on again and the fictitius spin vector is submitted to another $b\tau$ pulse which rotates it around k_1'. Depending on the angle $-\Omega_0 T$ and assuming again $b\tau = \frac{\pi}{2}$, the atoms will completely or partially transition to the state other than the one they were in at the beginning of Ramsey. If $-\Omega_0 T = 2n\pi$ the transition will be complete and the fictitius spin vector will be directed along the $-k_3'$ axis (in red on the Figure). On the other hand, for other values of $-\Omega_0 T$ there will be an angle between the fictitious spin vector and $-k_3$ and its projection $a_3(\tau + T + \tau)$ will give the information on the transition probability (in blue on the Figure) which will not be maximum ($0 < P < 1$). In an extreme case, if $-\Omega_0 T$ is a multiple of π the RF field will rotate the vector back to the initial state (in green on the Figure) directed upwards ($P = 0$).

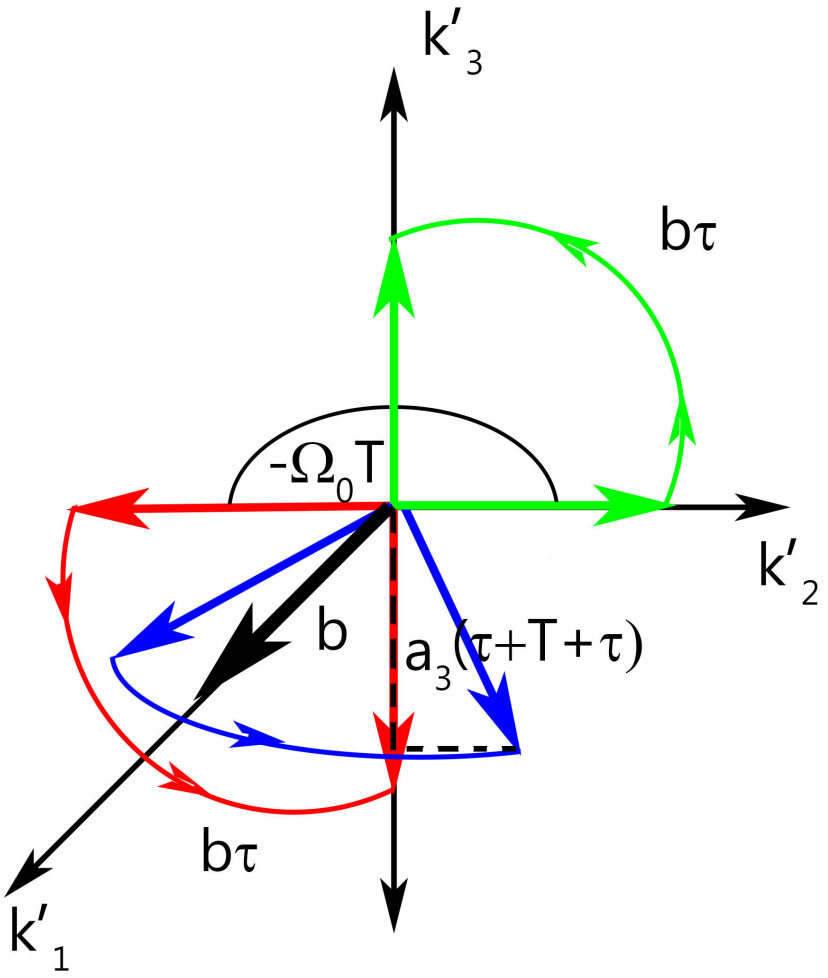

Figure 8.11: The atoms enter the second interaction region. Depending on the amplitude of $b\tau$ and $-\Omega_0 T$ they will make a transition. See text for details.

9

Appendix 2

9.1 Sub-Doppler

If two counter propagating laser beams with the same amplitude ϵ_0, frequency ω and with perpendicular polarisations along the x and y axis ($lin \perp lin$ configuration) are used, an electric field with position dependent ellipticity along the fixed z-axis and the following amplitude is created:

$$\epsilon_z = \epsilon_0 \sqrt{2}(coskz \frac{\epsilon_x + \epsilon y}{\sqrt{2}} - isinkz \frac{\epsilon_y - \epsilon_x}{\sqrt{2}}) \tag{9.1}$$

where ϵ_x and ϵy are polarisations of the two beams in x and y direction, respectively.

For every $\lambda/8$ the polarisation varies between linear, σ_+, linear perpendicular and σ_- polarisation. This pattern is cyclically repeated every $\lambda/2$. Polarisation variation creates a proportional gradient force which is position dependent and produces an equivalent variation of energies and atomic populations along z. Laser tuning and the polarisation variations have been arranged in a way that a propagating atom is always rolling the potential hill.

Starting from the bottom of the dressed state $g_{+1/2}/g_{-1/2}$ level potential where the light is σ_+/σ_- polarized, the atom is mowing towards the potential peak during some finite time because of the deaccelerating gradient force while loosing kinetic energy due to the energy conservation law. As it reaches the peak which is an area of pure σ_-/σ_+ polarisation, it is optically pumped into an energetically higher sub-level e from which it decays to the bottom of the potential well of the state other than the initial one $g_{-1/2}/g_{+1/2}$. As the atom decays, it releases a photon representing the lost kinetic energy. The process is periodically repeated, thus forcing continouus loss of energy and cooling of the atoms.

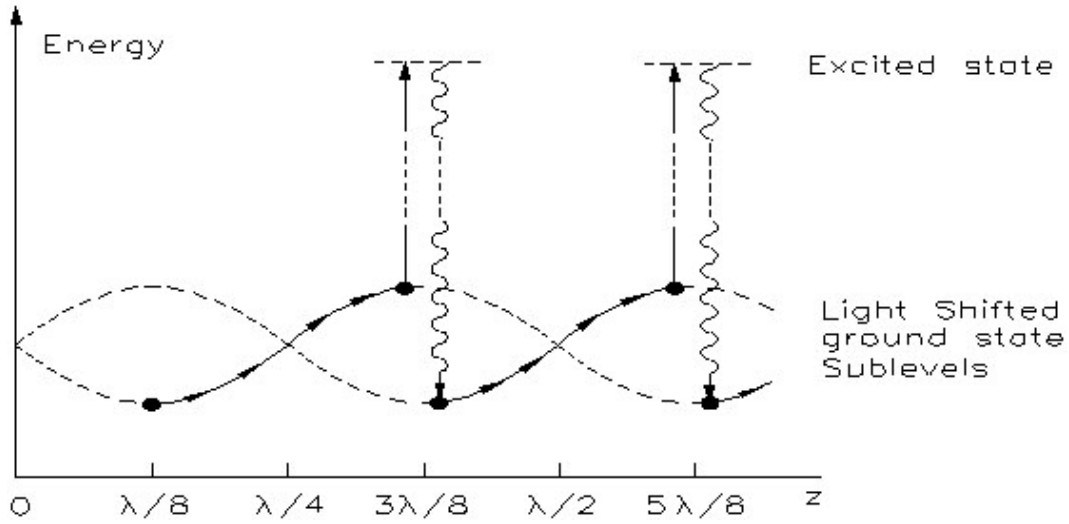

Figure 9.1: Variation of polarization and optical pumping for sub-Doppler cooling.

10

Appendix 3

10.1 Sensitivity function

The sensitivity function can be defined by the following relation (18):

$$\delta P = \frac{1}{2}\int_{T+2\tau} g(t)(\delta\omega_{at}(t) + \frac{d\phi}{dt}(t))dt, \tag{10.1}$$

where $g(t)$ is the sensitivity function defining the perturbation to the transition probability δP. The transition probability depends only on the frequency shift between the atomic frequency and the applied frequency of the local oscillator. The perturbation has a temporal dependency on the frequency of the atomic transition $\delta\omega_{at}(t)$ and the phase of the microwave interrogation field $\frac{d\phi(t)}{\delta\phi(t)}$. The sensitivity function does not take into account effects that can not be described by these two variations. These are neighbouring energy level transitions (Majorana, Rabi, Ramsey transitions), field amplitude perturbations (microwave field leak, cavity phase shift) and parasite microwave field spectral lines. Note that Equation 10.1 is valid for a single atom and that the atomic cloud velocity dispersion also needs to be considered.

Equation 10.1 was obtained from a calculation which takes into account the effect of the perturbation on the initial state atomic wave function $|\psi(0)\rangle$(19):

$$|\psi(t)\rangle = |\psi(t)\rangle_{non_petrubed} + |d\psi(t)\rangle, \tag{10.2}$$

where:

$$|\psi(t)\rangle_{non_petrubed} = U(t)|d\psi(0)\rangle, \tag{10.3}$$

and:

$$d\psi(t)\rangle = iA(t)|psi(0)\rangle. \tag{10.4}$$

$U(t)$ is the atomic state evolution operator and $iA(t)$ represents the perturbation operator.

The transition probability for Ramsey interrogation after time $T + 2\tau$ is now:

$$P = |\langle e|\psi(T + 2\tau)_{non_pertrubed} + d\psi(T + 2\tau)|^2. \tag{10.5}$$

The transition probability expression can be decomposed into three parts describing the effect of the perturbation during the first interaction (dP_1), free time evolution (dP_2 and the second interaction (dP_3):

$$\begin{aligned} dP &= dP_1 + dP_2 + dP_3 \\ &= -\frac{\epsilon}{2}(\int_0^{\tau}[\frac{d(d\phi(t))}{dt} + d\delta\omega_{at}(t)]sin(-R(t))dt - d\phi(\tau)) - \frac{\epsilon}{2}\int_{\tau}^{T+\tau} d\delta(t)dt \\ &\quad - \frac{\epsilon}{2}(d\phi(T+\tau) + \int_{T+\tau}^{T+2\tau}[\frac{d(d\phi(t))}{dt} + d\delta\omega_{at}(t)]cos(-R(t))dt), \end{aligned} \tag{10.6}$$

where $\epsilon = \pm 1$ depending on which side of the Ramsey fringe is interrogated and $R(t)$ is the angle rotation operator. Equation 10.6 leads to Equation 10.1.

Figure 10.1 shows the Ramsey interrogation sensitivity function shape in micro-gravity where there is no velocity variation (18).

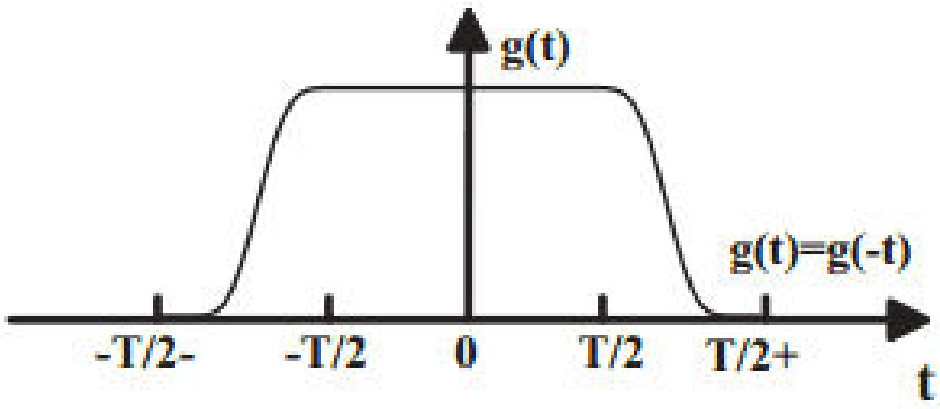

Figure 10.1: Ramsey interrogation sensitivity function shape.

10.2 Clock frequency shift calculation

Clock frequency is deduced by calculating the transition probability of the two half maximums of the central fringe. If the two probabilities are equal, the frequency of the oscillator is the frequency of the hyperfine level resonance. A perturbation shifts the atomic frequency $\delta\omega_{clock}$, which changes the transition probability P at the two sides:

$$P(\delta\omega_{clock} \pm \Delta\omega_m) = P^0(\Delta\omega_m) \pm \delta\omega_{clock}\frac{dP^0}{d\delta}(\Delta\omega_m) + \delta P_{\pm}, \tag{10.7}$$

where $\Delta\omega_m$ is the frequency modulation on the resonance fringe, P^0 is the non-perturbed atom transition probability and $\delta P_{\pm}$ is the probability variation induced by the perturbation. Using Equation 10.1 the frequency displacement is:

$$\delta\omega_{clock} = \frac{1}{T_{eff}}\int_0^{T+2\tau} d\nu_{at}g(t)dt, \tag{10.8}$$

where T_{eff} is the Ramsey interrogation time and gives the normalization relation of the sensitivity function:

$$T_{eff} = \int_{T+2\tau} g(t)dt. \tag{10.9}$$

11

Abstract (in english)

This thesis presents the experimental results obtained during the development and the ground tests of the flight model of the cold atoms space clock PHARAO. PHARAO, the first Primary Frequency Standard (PFS) for space applications, is developed by the French space agency CNES. It is a main instrument of the ESA space mission ACES: Atomic Clock Ensemble in Space with a launch scheduled on 2016. The mission is based on high performances time and frequency comparisons between a payload including PHARAO and ground based clocks to perform tests in fundamental physics. The payload will be installed on an external pallet of the International Space Station. After an introduction on atomic clocks and a summary on the ACES mission, the PHARAO architecture, optimized for microgravity environment, and its operation is described. It is followed by the measurements and the analysis of the frequency stability. On ground the frequency stability is measured at a level of 3.1 10-13 t-1/2. This value is in agreement with the different sources of noise. In space the frequency stability will reach 10-13 t-1/2. Finally the main frequency shifts are analyzed. A detailed study is given on magnetic shield properties, hysteresis and the design of the active magnetic compensation. The objective is to reduce the uncertainty of the second order Zeeman effect within few 10-17. The temperature determination of the atomic environment is also detailed and the goal is to reach an uncertainty on the blackbody frequency shift in the 10-17 range. A preliminary budget on the frequency accuracy of PHARAO on ground is evaluated at 1.1 10-15. This value is compatible with the expected accuracy budget of 3x10-16 when the clock will operate in microgravity. In the next step all the ACES instruments will be assembled for a launch scheduled on 2016.

Keywords: space clock, PHARAO, ACES, primary frequency standard, fundamental physics

11. ABSTRACT (IN ENGLISH)

12

Résumé (en francais)

La thèse présente les résultats expérimentaux obtenus au cours du développement et des essais au sol du modèle de vol de l'horloge atomes froids PHARAO. PHARAO est le premier étalon primaire de fréquence dédié à des applications spatiales. Il est développv par l'agence spatiale franaise CNES. PHARAO est un des principaux instruments de la mission spatiale de l'ESA: ACES (Atomic Clock Ensemble in Space). Le lancement est prévu en 2016. La mission est basée sur des comparaisons de très hautes performances en temps et en fréquence, entre PHARAO et un ensemble dhorloges basées au sol, pour effectuer des tests en physique fondamentale. La charge utile sera installée sur une palette extérieure de la Station spatiale internationale. Après une introduction sur les horloges atomiques et un résum de la mission ACES, l'architecture de PHARAO optimisée pour la microgravité et son fonctionnement sont décrits. Ensuite nous présentons les mesures et l'analyse de la stabilité de frquence. Au sol la stabilité de fréquence est mesurée à un niveau de 3,1x10-13 t-1/2. Cette valeur est en accord avec les différentes sources de bruit. En microgravité la stabilité atteindra 10-13 t-1/2. Pour terminer les principaux déplacements de fréquence sont analysés. Une étude détaillée est donnée sur les propriétés des blindages magnétiques, leurs hystérésis et la conception dune compensation magnétique active. L'objectif est de réduire l'incertitude sur leffet Zeeman du second ordre au niveau de quelques 10-17. La détermination de la température de lenvironnement des atomes est également analysée avec l'objectif d'atteindre une incertitude sur le déplacement de fréquence par le rayonnement du corps noir dans la gamme de 10-17. Un budget préliminaire sur lincertitude de fréquence de lhorloge au sol stablit 1,1x 10-15. Ce budget est compatible avec un objectif de 3x10-16 en microgravité. La prochaine étape verra lassemblage tous les autres instruments ACES pour un lancement prvu en 2016.

12. RÉSUMÉ (EN FRANCAIS)

Mots-clés: Horloge spatiale, PHARAO, ACES, étalon primaire de fréquence, physique fondamentale.

Bibliography

[1] Fritz Riehle. **Optical Atomic Clocks Could Redefine Unit of Time**. *Physics*, **5**:126, November 2012. vii, 4

[2] L. ESSEN and J. V. L. PARRY. **An Improved Cæsium Frequency and Time Standard**. *Nature*, **184**(4701):1791–1791, December 1959. 3

[3] T.W. Hänsch and A.L. Schawlow. **Cooling of gases by laser radiation**. *Optics Communications*, **13**(1):68–69, January 1975. 3

[4] **NIST-F1 Cesium Fountain Atomic Clock**. 3, 11, 42

[5] Ruoxin Li, Kurt Gibble, and Krzysztof Szymaniec. **Improved accuracy evaluation of the NPL-CsF2 primary frequency standard**. In *2011 Joint Conference of the IEEE International Frequency Control and the European Frequency and Time Forum (FCS) Proceedings*, pages 1–2. IEEE, May 2011. 3, 11, 42

[6] Jocelyne Guéna, Michel Abgrall, Daniele Rovera, Philippe Laurent, Baptiste Chupin, Michel Lours, Giorgio Santarelli, Peter Rosenbusch, Michael Tobar, Ruoxin Li, Kurt Gibble, Andre Clairon, and Sebastien Bize. **Progress in atomic fountains at LNE-SYRTE.** *IEEE transactions on ultrasonics, ferroelectrics, and frequency control*, **59**(3):391–410, March 2012. 3, 11, 42

[7] V Gerginov, N Nemitz, S Weyers, R Schröder, D Griebsch, and R Wynands. **Uncertainty evaluation of the caesium fountain clock PTB-CSF2**. *Metrologia*, **47**(1):65–79, February 2010. 3, 11, 42

[8] Philip Ball. **Precise atomic clock may redefine time**. *Nature*, July 2013. 4

[9] Alberto Battisti Marco Belloni. **ATOMIC CLOCKS CONTINUOUS DEVELOPMENT AT SELEX GALILEO FOR NAVIGATION SATELLITE SYSTEMS.** 2012. 5

[10] Ph. Laurent, M. Abgrall, Ch. Jentsch, P. Lemonde, G. Santarelli, A. Clairon, I. Maksimovic, S. Bize, Ch. Salomon, D. Blonde, J.F. Vega, O. Grosjean, F. Picard, M. Saccoccio, M. Chaubet, N. Ladiette, L. Guillet, I. Zenone, Ch. Delaroche, and Ch. Sirmain. **Design of the cold atom PHARAO space clock and initial test results**. *Applied Physics B*, **84**(4):683–690, August 2006. 5, 47

[11] L. Cacciapuoti, N. Dimarcq, G. Santarelli, P. Laurent, P. Lemonde, A. Clairon, P. Berthoud, A. Jornod, F. Reina, S. Feltham, and C. Salomon. **Atomic Clock Ensemble in Space: Scientific Objectives and Mission Status**. *Nuclear Physics B - Proceedings Supplements*, **166**:303–306, April 2007. 5, 30, 33

[12] Igor Moric and Philippe Laurent. **Status of the flight model of the cold atoms space clock PHARAO**. In *2013 Joint European Frequency and Time Forum & International Frequency Control Symposium (EFTF/IFC)*, pages 967–972. IEEE, July 2013. 6, 216

[13] Francois-Xavier Esnault, Olivier Grosjean, Christophe Delaroche, Didier Massonnet, Philippe Chatard, Charles-Marie de Graeve, Sebastien Telllier, Caroline Stepien, Lionel Fonta, Sabine Julien, Emilie Leynia de la Jarrige, Claude Escandes, Phillipe Gase, Andria Ratsimandresy, Serge Beraud, Thomas Basquin, Fabrice Buffe, Patrizia Torresi, Philippe Lariviere, Bernard Vivian, Benoit Faure, Thomas Leveque, David Valat, Frederic Picard, Sylvie Leon, Christian Sirmain, Jean-Francois Vega, Nadine Ladiette, Benoit Leger, Francois Gonzalez, Jean-Pierre Granier, Philippe Guillemot, Muriel Saccoccio, Didier Blonde, Isabelle Zenone, Clement Luitot, Michel Chaubet, Christophe Salomon, Michel Abgrall, Daniele Rovera, Igor Moric, and Philippe Laurent. **PHARAO flight model : Integration and "on ground" performances tests**. In *2014 IEEE International Frequency Control Symposium (FCS)*, pages 1–3. IEEE, May 2014. 6, 216

[14] Philippe LAURENT et Al. **PHARAO : le premier étalon primaire de fréquence, à atomes froids, spatial**. *Revue française de métrologie*, **n 34, Vol**, 2014. 6, 216

[15] Igor Moric, Philippe Laurent, Philippe Chatard, Charles-Marie de Graeve, Stephane Thomin, Vincent Christophe, and Olivier Grosjean. **Magnetic shielding of the cold atom space clock PHARAO**. *Acta Astronautica*, **102**:287–294, September 2014. 6, 153, 157, 216

[16] Igor Morić, Charles-Marie De Graeve, Olivier Grosjean, and Philippe Laurent. **Hysteresis prediction inside magnetic shields and application.** *The Review of scientific instruments*, **85**(7):075117, July 2014. 6, 140, 216

[17] Pierre Lemonde. *PHARAO: ÉTUDE D'UNE HORLOGE SPATIALE UTILISANT DES ATOMES REFROIDIS PAR LASER; RÉALISATION D'UN PROTOTYPE*. PhD thesis, November 1997. 8, 92, 93, 94

[18] Michel Abgrall. *Evaluation des performances de la fontaine atomique PHARAO, Participation à l'étude de l'horloge spatiale PHARAO*. PhD thesis, January 2003. 8, 47, 71, 92, 93, 94, 243, 244

[19] Yvan Sortais. **Construction d'une fontaine double à atomes froids de 87Rb et 133Cs ; Etude des effets dépendant du nombre d'atomes dans une fontaine**. December 2001. 8, 92, 93, 94, 205, 224, 230, 243

[20] Norman Ramsey. *Molecular Beams*. 1956. 10

[21] Norman F. Ramsey. **The method of successive oscillatory fields**. *Physics Today*, **66**(1):36, December 2013. 10

[22] I. Rabi, S. Millman, P. Kusch, and J. Zacharias. **The Molecular Beam Resonance Method for Measuring Nuclear Magnetic Moments. The Magnetic Moments of Li63, Li73 and F199**. *Physical Review*, **55**(6):526–535, March 1939. 10

[23] L. Essen and J. V. L. Parry. **The Caesium Resonator as a Standard of Frequency and Time**. *Philosophical Transactions of the Royal Society A: Mathematical, Physical and Engineering Sciences*, **250**(973):45–69, August 1957. 10

[24] M. Arditi and J.L. Picqué. **A cesium beam atomic clock using laser optical pumping. Preliminary tests**. *Journal de Physique Lettres*, **41**(16):379–381, August 1980. 10

[25] Steven Chu, Claude Cohen-Tannoudji, and William D. Phillips. **Nobel Prize in Physics 1997 website**. 11

[26] A. Clairon, P. Laurent, G. Santarelli, S. Ghezali, S.N. Lea, and M. Bahoura. **A cesium fountain frequency standard: preliminary results**. *IEEE Transactions on Instrumentation and Measurement*, **44**(2):128–131, April 1995. 11

[27] Peter W. Milonni and Joseph H. Eberly. *Laser Physics*. 2010. 11

[28] R Wynands and S Weyers. **Atomic fountain clocks**. *Metrologia*, **42**(3):S64–S79, June 2005. 12

[29] Mark Kasevich, Erling Riis, Steven Chu, and Ralph DeVoe. **RF spectroscopy in an atomic fountain**. *Physical Review Letters*, **63**(6):612–615, August 1989. 13

[30] A Clairon, C Salomon, S Guellati, and W. D Phillips. **Ramsey Resonance in a Zacharias Fountain**. *Europhysics Letters (EPL)*, **16**(2):165–170, September 1991. 13

[31] Jacques Vanier and Claude Audoin. *The quantum physics of atomic frequency standards*. 1989. 14, 69, 113, 114, 217, 225, 230

[32] Véronique Zehnlé and Jean Claude Garreau. **Doppler cooling to the recoil limit by means of sharp atomic transitions with controlled quenching**. *Journal of the Optical Society of America B*, **20**(5):931, July 2003. 16

[33] Daniel A. Steck. **Cesium D Line Data**. 2003. 16

[34] D. J. Wineland and Wayne M. Itano. **Laser cooling of atoms**. *Phys. Rev. A*, **20**(1521), 1979. 16

[35] Angharad Mair Thomas. *Ultra-cold Collisions and Evaporative Cooling of Caesium in a Magnetic Trap*. PhD thesis, 2004. 16

[36] Harold J. Metcalf and Peter van der Straten. *Laser Cooling and Trapping*, **1999**. 1999. 16, 17, 202

[37] Gilbert Grynberg Claude Cohen-Tannoudji, Jacques Dupont-Roc. *Atom-Photon Interactions: Basic Processes and Applications*. Wiley, 1998. 16

[38] J. Dalibard and C. Cohen-Tannoudji. **Laser cooling below the Doppler limit by polarization gradients: simple theoretical models**. *Journal of the Optical Society of America B*, **6**(11):2023, November 1989. 17, 32

[39] Steven Chu. **The manipulation of neutral particles Nobel lecture**, 1997. 17

[40] William D. Phillips. **Laser cooling and trapping of neutral atoms Nobel lecture**, 1997. 17

[41] N F Ramsey. **Experiments with separated oscillatory fields and hydrogen masers.** *Science (New York, N.Y.)*, **248**(4963):1612–9, June 1990. 18

[42] S. Kokkelmans, B. Verhaar, K. Gibble, and D. Heinzen. **Predictions for laser-cooled Rb clocks**. *Physical Review A*, **56**(6):R4389–R4392, December 1997. 18

[43] BIPM. **RECOMMENDED VALUES OF STANDARD FREQUENCIES FOR APPLICATIONS INCLUDING SECONDARY REPRESENTATIONS OF THE DEFINITION OF THE SECOND**, 2013. 19

[44] S.A. Diddams, A. Bartels, T.M. Ramond, C.W. Oates, S. Bize, E.A. Curtis, J.C. Bergquist, and L. Hollberg. **Design and control of femtosecond lasers for optical clocks and the synthesis of low-noise optical and microwave signals**. *IEEE Journal of Selected Topics in Quantum Electronics*, **9**(4):1072–1080, July 2003. 19

[45] R Le Targat, L Lorini, Y Le Coq, M Zawada, J Guéna, M Abgrall, M Gurov, P Rosenbusch, D G Rovera, B Nagórny, R Gartman, P G Westergaard, M E Tobar, M Lours, G Santarelli, A Clairon, S Bize, P Laurent, P Lemonde, and J Lodewyck. **Experimental realization of an optical second with strontium lattice clocks.** *Nature communications*, **4**:2109, January 2013. 19

[46] N Hinkley, J A Sherman, N B Phillips, M Schioppo, N D Lemke, K Beloy, M Pizzocaro, C W Oates, and A D Ludlow. **An atomic clock with 10(-18) instability.** *Science (New York, N.Y.)*, **341**(6151):1215–8, September 2013. 19, 42

[47] L. Cacciapuoti and C. Salomon. **ACES : Mission concept and scientific objectives**. 2007. 21

[48] M.P. Hess, L. Stringhetti, B. Hummelsberger, K. Hausner, R. Stalford, R. Nasca, L. Cacciapuoti, R. Much, S. Feltham, T. Vudali, B. Léger, F. Picard, D. Massonnet, P. Rochat, D. Goujon, W. Schäfer, P. Laurent, P. Lemonde, A. Clairon, P. Wolf, C. Salomon, I. Procházka, U. Schreiber, and O. Montenbruck. **The ACES mission: System development and test status**. *Acta Astronautica*, **69**(11-12):929–938, December 2011. 21

[49] **SpaceX website Falcon**. 21

[50] **SpaceX website Dragon**. 21

[51] ESA. **Research Announcement for ISS Experiments relevant to study Global Climate Change Annex 1: Additional technical Information on ISS capabilities and background information**. 2011. 23

[52] NASA. **Space Station Program Natural Environment Definition**. (SSP 30425, Revision B). 23

[53] NASA. **Overview of Attached Payload Accommodations and Environments on the International Space Station**. (TP2007214768), 2007. 23

[54] D. Goujon, P. Rochat, P. Mosset, D. Boving, A. Perri, J. Rochat, N. Ramanan, D. Simonet, X. Vernez, S. Froidevaux, and G. Perruchoud. **Development of the Space active Hydrogen Maser for the ACES Mission**. In *EFTF-2010 24th European Frequency and Time Forum*, pages 1–6. IEEE, April 2010. 31

[55] Joyce B Milliner. **Space Probe to Test Einstein's "Space-Time Warp" Theory**. 31

[56] PHARAO PROJECT TEAM. **PHARAO SYNTHESIS DOCUMENT**. 2010. 34, 47, 63

[57] Pacôme Delva, Peter Wolf, Frédéric Meynadier, Christophe LePoncin-Lafitte, and Philippe Laurent. **Time and frequency transfer with the ESA/CNES ACES-PHARAO mission**. *IAU Joint Discussion 7: Space-Time Reference Systems for Future Research at IAU General Assembly-Beijing. Online at http://referencesystems.info/iau-joint-discussion-7.html*, 2012. 35

[58] Sung Hoon Yang, Chang Bok Lee, Seung Woo Lee, Young Kyu Lee, and Youn Jeong Heo. **Assessment of Time Transfer Performance between TWSTFT and GPS Carrier Phase at KRISS**. In *2007 IEEE International Frequency Control Symposium Joint with the 21st European Frequency and Time Forum*, pages 942–945. IEEE, May 2007. 37

[59] Ivan Prochazka, Jan Kodet, Josef Blazej, Ulrich Schreiber, and Luigi Cacciapuoti. **Development of the European Laser Timing instrumentation for the ACES time transfer using laser pulses**. In *EFTF-2010 24th European Frequency and Time Forum*, pages 1–6. IEEE, April 2010. 38

[60] S. Reynaud, C. Salomon, and P. Wolf. **Testing General Relativity with Atomic Clocks**. *Space Science Reviews*, **148**(1-4):233–247, May 2009. 40

[61] C. SALOMON, L. CACCIAPUOTI, and N. DIMARCQ. **ATOMIC CLOCK ENSEMBLE IN SPACE: AN UPDATE**. *International Journal of Modern Physics D*, **16**(12b):2511–2523, December 2007. 40

[62] T. J. Quinn. *Recent Advance in Metrology and Fundamental Constants*. Ios Pr Inc, 2001. 41

[63] Guochang Xu. *Sciences of Geodesy - II: Innovations and Future Developments*. Springer Science & Business Media, 2012. 41

[64] T. Damour and A.M. Polyakov. **The string dilation and a least coupling principle**. *Nuclear Physics B*, **423**(2-3):532–558, July 1994. 41

[65] E Peik and Et al. **Limit on the Present Temporal Variation of the Fine Structure Constant**. *Phys. Rev. Lett.*, **93**(170801), 2004. 42

[66] V. Flambaum, D. Leinweber, A. Thomas, and R. Young. **Limits on variations of the quark masses, QCD scale, and fine structure constant**. *Physical Review D*, **69**(11):115006, June 2004. 42

[67] Michael E. Peskin and Dan V. Schroeder. *An Introduction To Quantum Field Theory (Frontiers in Physics)*. Westview Press; First Edition edition, 1995. 42

[68] J. D. Prestage, R. L. Tjoelker, and L. Maleki. **Atomic Clocks and Variations of the Fine Structure Constant**. *PHYSICAL REVIEW LETTERS*, 1995. 42

[69] Y. Fukuyama, T. Kurosu, G.A. Costanzo, and S. Ohshima. **Construction of Cs atomic fountain frequency standard at NRLM**. In *1998 Conference on Precision Electromagnetic Measurements Digest (Cat. No.98CH36254)*, page 18. IEEE. 42

[70] Ferenc Fuzesi, Mark D. Plimmer, Gregor Dudle, Jocelyne Guena, and Pierre Thomann. **Design Details of FOCS-2, an Improved Continuous Cesium Fountain Frequency Standard**. In *2007 IEEE International Frequency Control Symposium Joint with the 21st European Frequency and Time Forum*, pages 90–95. IEEE, May 2007. 42

[71] Nian-Feng Liu, Fang Fang, Wei-Liang Chen, Ping-Wei Lin, Ping Wang, Kun Liu, Rui Suo, and Tian-Chu Li. **Accuracy Evaluation of NIM5 Cesium Fountain Clock**. *Chinese Physics Letters*, **30**(1):010601, January 2013. 42

[72] F. Levi, L. Lorini, D. Calonico, and A. Godone. **Systematic shift uncertainty evaluation of IEN CSF1 primary frequency standard**. *IEEE Transactions on Instrumentation and Measurement*, **52**(2):267–271, April 2003. 42

[73] **NPL Rb Fountain**. 42

[74] W.H. Oskay, A. Bartels, S.A. Diddams, C.W. Oates, G. Wilpers, L. Hollberg, W.M. Itano, C.E. Tanner, and J.C. Bergquist. **The mercury-ion optical clock: Towards a measurement of the quadrupole shift**. pages 247–250. 42

[75] Sang Chung John D. Prestage. **Miniaturized Mercury Ion Clock for Ultra-Stable Deep Space Applications**. *38th Annual Precise Time and Time Interval (PTTI) Meeting*, 2006. 42

[76] D. Calonico, F. Levi, L. Lorini, G. Costanzo, M. Zoppi, M. Pizzocaro, A. Mura, E. K. Bertacco, and A. Godone. **Yb optical lattice clock at INRIM**. In *EFTF-2010 24th European Frequency and Time Forum*, pages 1–8. IEEE, April 2010. 42

[77] N. Huntemann, M. Okhapkin, B. Lipphardt, S. Weyers, Chr. Tamm, and E. Peik. **High-Accuracy Optical Clock Based on the Octupole Transition in ˆ{171}Ybˆ{+}**. *Physical Review Letters*, **108**(9):090801, February 2012. 42

[78] R.B. Warrington, P.T.H. Fisk, M.J. Wouters, M.A. Lawn, and C. Coles. **The CSIRO trapped /sup 171/Yb/sup +/ ion clock: improved accuracy through laser-cooled operation**. In *Proceedings of the 1999 Joint Meeting of the European Frequency and Time Forum and the IEEE International Frequency Control Symposium (Cat. No.99CH36313)*, **1**, pages 125–128. IEEE, 1999. 42

[79] S A King, R M Godun, S A Webster, H S Margolis, L A M Johnson, K Szymaniec, P E G Baird, and P Gill. **Absolute frequency measurement of the 2 S 1/2 2 F 7/2 electric octupole transition in a single ion of 171 Yb + with 10 15 fractional uncertainty**. *New Journal of Physics*, **14**(1):013045, January 2012. 42

[80] C. W. Chou, D. B. Hume, J. C. J. Koelemeij, D. J. Wineland, and T. Rosenband. **Frequency Comparison of Two High-Accuracy Alˆ{+} Optical Clocks**. *Physical Review Letters*, **104**(7):070802, February 2010. 42

[81] G. Kirchmair, J. Benhelm, F. Zähringer, R. Gerritsma, C. Roos, and R. Blatt. **High-fidelity entanglement of Ca+43 hyperfine clock states**. *Physical Review A*, **79**(2):020304, February 2009. 42

[82] **TOKYO RIKEN Quantum Metrology Laboratory**. 42

[83] A D Ludlow, T Zelevinsky, G K Campbell, S Blatt, M M Boyd, M H G de Miranda, M J Martin, J W Thomsen, S M Foreman, Jun Ye, T M Fortier, J E Stalnaker, S A Diddams, Y Le Coq, Z W Barber, N Poli, N D Lemke, K M Beck, and C W Oates. **Sr lattice clock at 1 x 10(-16) fractional uncertainty by remote optical evaluation with a Ca clock.** *Science (New York, N.Y.)*, **319**(5871):1805–8, March 2008. 42

[84] Xavier Baillard, Mathilde Fouché, Rodolphe Le Targat, Philip G. Westergaard, Arnaud Lecallier, Yann Le Coq, Giovanni D. Rovera, Sebastien Bize, and Pierre Lemonde. **Accuracy evaluation of an optical lattice clock with bosonic atoms**. *Optics Letters*, **32**(13):1812, 2007. 42

[85] Stephan Falke, Nathan Lemke, Christian Grebing, Burghard Lipphardt, Stefan Weyers, Vladislav Gerginov, Nils Huntemann, Christian Hagemann, Ali Al-Masoudi, Sebastian Häfner, Stefan Vogt, Uwe Sterr, and Christian Lisdat. **A strontium lattice clock with 3x10E-17 inaccuracy and its frequency**. page 20, December 2013. 42

[86] A. A. Madej, P. Dube, J.E. Bernard, G. Humphrey, M. Vainio, J. Jiang, and D.J. Jones. **Progress in the evaluation and operation of the NRC strontium single ion frequency standard as an optical atomic clock**. In *CPEM 2010*, pages 80–81. IEEE, June 2010. 42

[87] **NPL Strontium Ion Optical Frequency Standard website**. 42

[88] V. Kostelecký. **Gravity, Lorentz violation, and the standard model**. *Physical Review D*, **69**(10):105009, May 2004. 43

[89] Paul Stanwix, Michael Tobar, Peter Wolf, Clayton Locke, and Eugene Ivanov. **Improved test of Lorentz invariance in electrodynamics using rotating cryogenic sapphire oscillators**. *Physical Review D*, **74**(8):081101, October 2006. 43

[90] Lijing Shao and Norbert Wex. **New tests of local Lorentz invariance of gravity with small-eccentricity binary pulsars**. *Classical and Quantum Gravity*, **29**(21):215018, November 2012. 43

[91] M. C. Scholten. **Experimental Tests of Local Lorentz Invariance**. *SPECIAL TOPICS IN EXPERIMENTAL GRAVITATION*, 2007. 43

[92] Maxim Pospelov and Michael Romalis. **Lorentz invariance on trial**. *Physics Today*, 2004. 43

[93] **Survey Grade GNSS Equipment**. 44

[94] **GPS Differential Correction Methods**. 44

[95] A. Cazenave, K. Dominh, S. Guinehut, E. Berthier, W. Llovel, G. Ramillien, M. Ablain, and G Larnicol. **Sea level budget over 2003-2008: a reevaluation from GRACE space gravimetry, satellite altimetry and Argo**, 2008. 44

[96] P. Bengtsson, L., Koumoutsaris, S., Bonnet, R.-M., Herland, E.-A., Huybrechts, P., Johannessen, O.M., Milne, G., Oerlemans, J., Ohmura, A., Ramstein, G., Woodworth. **The Earth's Cryosphere and Sea Level Change**, 2011. 44

[97] Muriel Saccoccio, Jacques Loesel, Claude Coatantiec, Eric Simon, Philippe Laurent, Pierre Lemonde, I. Maksimovic, and M. Abgrall. **PHARAO space atomic clocks: new developments on the laser source**. *In: Proceedings of the 5th International Conference on Space Optics (ICSO 2004)*, 2004. 47, 58

[98] Kurt Gibble. **Scattering of cold atom coherences by hot atoms: Background gas collision shifts of primary fountain clocks**. In *2013 Joint European Frequency and Time Forum & International Frequency Control Symposium (EFTF/IFC)*, pages 46–47. IEEE, July 2013. 67

[99] WM Itano, JC Bergquist, JJ Bollinger, JM Gilligan, DJ Heinzen, FL Moore, MG Raizen, and DJ Wineland. **Quantum projection noise: Population fluctuations in two-level systems.** *Physical review. A*, **47**(5):3554–3570, May 1993. 92

[100] Giorgio Santarelli, Philippe Laurent, Pierre Lemonde, André Clairon, Anthony G. Mann, S. Chang, Andre N. Luiten, Christophe Salomon, and American Physical Society. **Quantum Projection Noise in an Atomic Fountain: A High Stability Cesium Frequency Standard**. *Phys. Rev. Lett.*, **82**(4619), 1999. 92

[101] Céline Vian. *Comparaison directe de fontaines atomiquesau niveau de 2X10-16 : tests de la cavité de vol de PHARAO.* PhD thesis, January 2006. 92, 93, 94, 98, 211

[102] G. J. Dick. **Local Oscillator Induced Instabilities in Trapped Ion Frequency Standards**. December 1987. 96

[103] J. D. Prestage G. J. Dick. **Local Oscillator Induced Degradation of Medium-Term Stability in Passive Atomic Frequency Standards**. 1990. 96

[104] Philip Westergaard, Jérôme Lodewyck, and Pierre Lemonde. **Minimizing the Dick effect in an optical lattice clock.** *IEEE transactions on ultrasonics, ferroelectrics, and frequency control*, **57**(3):623–8, March 2010. 96

[105] G. Breit and I. Rabi. **Measurement of Nuclear Spin**. *Physical Review*, **38**(11):2082–2083, December 1931. 114

[106] Andreas Bauch and Roland Schröder. **Frequency shifts in a cesium atomic clock due to Majorana transitions**. *Annalen der Physik*, **505**(5):421–449, 1993. 115, 125

[107] John. D. Jackson. *Classical Electrodynamics Third Edition*. Wiley; 3 edition, 1998. 117

[108] Richard Fitzpatrick. **Magnetic shielding lecture**, 2002. 117

[109] E. Della Torre. **A Preisach model for accommodation**. *IEEE Transactions on Magnetics*, **30**(5):2701–2707, 1994. 118

[110] T J Sumner, J M Pendlebury, and K F Smith. **Convectional magnetic shielding**. *Journal of Physics D: Applied Physics*, **20**(9):1095–1101, September 1987. 120

[111] J. Shilling and G. Houze. **Magnetic properties and domain structure in grain-oriented Si-Fe**. *IEEE Transactions on Magnetics*, **10**(2):195–223, June 1974. 121

[112] Giorgio Bertotti. *Hysteresis in Magnetism: For Physicists, Materials Scientists, and Engineers*. Gulf Professional Publishing, 1998. 121, 122, 158

[113] Alex Hubert and Rudolf Schäfer. *Magnetic Domains: The Analysis of Magnetic Microstructures*, **1998**. 1998. 121

[114] William D. Callister, Jr., and David G. Rethwisch. *Materials Science and Engineering: An Introduction*. 2009. 121

[115] J E L Bishop, P G Collar, and E W Lee. **Magnetic domain studies using permeability spectra III. Ni-Fe-Cu-Mo alloy**. *Journal of Physics D: Applied Physics*, **4**(8):1221–1234, August 1971. 121

[116] Salvatore Celozzi, Rodolfo Araneo, and Giampiero Lovat. *Electromagnetic Shielding*. John Wiley & Sons, 2008. 121, 140

[117] T.J. Yang, V. Gopalan, P. Swart, and U. Mohideen. **Experimental study of internal fields and movement of single ferroelectric domain walls**. *Journal of Physics and Chemistry of Solids*, **61**(2):275–282, February 2000. 121

[118] D U Gubser, S A Wolf, and J E Cox. **Shielding of longitudinal magnetic fields with thin, closely spaced, concentric cylinders of high permeability material.** *The Review of scientific instruments*, **50**(6):751, June 1979. 124

[119] O. BALTAG, D. COSTANDACHE, M. RAU, A. IFTEMIE, and I. RAU. **Dynamic shielding of the magnetic fields**. *Advances in Electrical and Computer Engineering*, **10**(4):135–142, 2010. 140

[120] D. Platzek, H. Nowak, F. Giessler, J. Rother, and M. Eiselt. **Active shielding to reduce low frequency disturbances in direct current near biomagnetic measurements**. *Review of Scientific Instruments*, **70**(5):2465, May 1999. 140

[121] K Kato, K Yamazaki, T Sato, A Haga, T Okitsu, K Muramatsu, T Ueda, K Kobayashi, and M Yoshizawa. **Active magnetic compensation composed of shielding panels.** *Neurology & clinical neurophysiology : NCN*, **2004**:68, January 2004. 140

[122] H.J.M. Brake, H.J. Wieringa, and H. Rogalla. **Improvement of the performance of a mu -metal magnetically shielded room by means of active compensation (biomagnetic applications)**, February 1991. 140

[123] F Resmer, H Nowak, F Giess ler, and J Haueisen. **Development of an active magnetic screen to allow a biomagnetometer to be used in an unshielded environment**. *Superconductor Science and Technology*, **17**(12):1365–1371, December 2004. 140

[124] I. D. Mayergoyz. *Mathematical Models of Hysteresis and Their Applications*. 2003. 141, 142

[125] Edward Della Torre. *Magnetic Hysteresis*. 2000. 142, 148, 158

[126] **Nodal regression explanation**. 150

[127] George B. Rybicki and Alan P. Lightman. *Radiative processes in astrophysics*. 1979. 161

[128] Wayne Itano, L. Lewis, and D. Wineland. **Shift of ˆ{2}S_{1/2} hyperfine splittings due to blackbody radiation**. *Physical Review A*, **25**(2):1233–1235, February 1982. 161

[129] E. Simon, P. Laurent, and A. Clairon. **Measurement of the Stark shift of the Cs hyperfine splitting in an atomic fountain**. *Physical Review A*, **57**(1):436–439, January 1998. 161

[130] S. Ulzega, A. Hofer, P. Moroshkin, R. Müller-Siebert, D. Nettels, and A. Weis. **Measurement of the forbidden electric tensor polarizability of Cs atoms trapped in solid ˆ{4}He**. *Physical Review A*, **75**(4):042505, April 2007. 161

[131] K Beloy, U I Safronova, and A Derevianko. **High-accuracy calculation of the blackbody radiation shift in the 133Cs primary frequency standard.** *Physical review letters*, **97**(4):040801, July 2006. 161

[132] E. Angstmann, V. Dzuba, and V. Flambaum. **Frequency Shift of the Cesium Clock Transition due to Blackbody Radiation**. *Physical Review Letters*, **97**(4):040802, July 2006. 161

[133] Eric Simon. **Vers une stabilité et une exactitude de 10-16 pour les horloges atomiques : - le rayonnement du corps noir - la détection optique**. October 1997. 161

[134] Krzysztof Szymaniec, Witold Chalupczak, Eite Tiesinga, Carl J. Williams, Stefan Weyers, and Robert Wynands. **Cancellation of the Collisional Frequency Shift in Caesium Fountain Clocks**. In *Conference on Coherence and Quantum Optics*, page CSuA13, Washington, D.C., 2007. OSA. 202, 205, 207

[135] Witold Chaupczak and Krzysztof Szymaniec. **Collisions in a ballistically expanding cloud of cold atoms in an atomic fountain**. *Journal of Physics B: Atomic, Molecular and Optical Physics*, **40**(2):343–350, January 2007. 202, 205, 207

[136] J. Guena, S. Bize, A. Clairon, R. Li, and K. Gibble. **Quantitative evaluation of distributed cavity phase shifts to improve the accuracy**

of SYRTE FO2. In *2011 Joint Conference of the IEEE International Frequency Control and the European Frequency and Time Forum (FCS) Proceedings*, pages 1–2. IEEE, May 2011. 210

[137] R. C. Mockler, R. E. Beehler, and C. S. Snider. **ATOMIC BEAM FREQUENCY STANDARDS**. *IRE TRANSACTIONS ON INSTRUMENTATION*, **I-9**(2), 1960. 221